Assessment of Cardiovascular Biomarkers Derived from Peripheral Pulse Waveforms Using Computational Blood Flow Modelling

Epstein, Sally Laura Tessier Banfill

Awarding institution:
King's College London

Assessment of Cardiovascular Biomarkers Derived from Peripheral Pulse Waveforms Using Computational Blood Flow Modelling

Sally Epstein

Department of Biomedical Engineering

King's College London

A thesis submitted for the degree of

Doctor of Philosophy

2016

Acknowledgements

I would like to thank the unwavering support of my supervisors Jordi Alastruey and Phil Chowienczyk, without them, this thesis would not have been possible. I would like to acknowledge the financial support of the Centre of Excellence in Medical Engineering (funded by the Wellcome Trust and EPSRC) and the National Institute for Health Research (NIHR) Biomedical Research Centre at Guys and St Thomas' NHS Foundation Trust in partnership with King's College London.

Our collaborators were also instrumental in this work and I would personally like to thank Dr Erik Erhardt, Dr Elena Allen and Dr Ries Robinson from Medici Tech Inc. for their assistance in this work.

Publications related to this thesis

Journal articles

Epstein, S., Willemet, M., Chowienczyk, P.J. and Alastruey, J., 2015. Reducing the number of parameters in 1D arterial blood flow modeling: less is more for patient-specific simulations. American Journal of Physiology-Heart and Circulatory Physiology, 309(1), pp.H222-H234.

Fok, H., Guilcher, A., Brett, S., Jiang, B., Li, Y., **Epstein, S.**, Alastruey, J., Clapp, B. and Chowienczyk, P., 2014. Dominance of the forward compression wave in determining pulsatile components of blood pressure similarities between inotropic stimulation and essential hypertension. Hypertension, 64(5), pp.1116-1123.

Epstein, S., Vergnaud, A.C., Elliott, P., Chowienczyk, P.

and Alastruey, J., 2014, August. Numerical assessment of the stiffness index. In 2014 36th Annual International Conference of the IEEE Engineering in Medicine and Biology Society (pp. 1969-1972). IEEE.

Published proceedings and abstracts

Li, Y., Fok, H., Jiang, B., **Epstein, S.**, Willemet, M., Alastruey, J., Parker, K. and Chowienczyk, P., 2015. Origins of the backward traveling wave in the arterial tree. Artery Research, 12, pp.42-43. Vancouver

Epstein, S., Alastruey, J. and Chowienczyk, P., 2014. Towards aortic pressure and flow waves modelling in the clinic. Artery Research, 8(4), p.162.

Li, Y., Fok, H., Jiang, B., **Epstein, S.**, Alastruey, J. and Chowienczyk, P., 2014. Do backward pressure waves arise

from reflections or from a reservoir?. Artery Research, 8(4), p.127.

Epstein, S., Fok, H., Chowienczyk, P. and Alastruey-Arimon, J., 2013. Effects of pharmacological drugs on the aortic pressure pulse: understanding mechanisms through modelling. Artery Research, 7(3), pp.159-160.

Abstract

The aim of this thesis is to investigate the ability of cardiovascular biomarkers calculated from peripheral pulse waveforms to estimate central properties of the cardiovascular system (*e.g.* aortic stiffness) using nonlinear one-dimensional (1-D) modelling of pulse wave propagation in the arterial network. To test these biomarkers, I have produced novel 1-D models of pulse wave propagation under normal and pathological conditions. In the first part of my thesis, I extended the modelling capabilities of the existing 1-D/0-D code to represent arterial blood flow under diabetes, hypertension, and combined diabetes and hypertension. Cardiac and vascular parameters of the 1-D model were tailored to best match data available in the literature to produce generalised hypertensive, diabetic, and combined diabetic and hypertensive population models. Using these models, I have shown that the pulse waveform at the finger is strongly affected by the aortic flow wave and the muscular artery stiffness and diameter. Furthermore the peak to peak time measured from the pulse waveform at the finger can identify hypertensive from diabetic patients.

In the second part, I developed a new methodology for optimising the number of arterial segments in 1-D modelling required to simulate precisely the blood pressure and flow waveforms at an arbitrary arterial

location. This is achieved by systematically lumping peripheral 1-D model branches into 0-D models that preserve the net resistance and total compliance of the original model. The methodology is important to simplify the computational domain while maintaining the precision of the numerical predictions – an important step to translate 1-D modelling to the clinic.

This thesis provides novel computational tools of blood flow modelling and waveform analysis for the design, development and testing of pulse wave biomarkers. These tools may help bridge the gap between clinical and computational approaches.

Contents

List of Figures

Chapter 1

Introduction

Diseases of the cardiovascular system are responsible for over four million deaths a year in Europe [Nichols *et al.*, 2013]. Cardiovascular disease (CVD) kills or seriously affects half the population of Britain [Wald & Law, 2003]. Globally, deaths from CVD are projected to reach 23.3 million by 2030 [Mathers & Loncar, 2006]. With the right diagnosis, CVD can be treated or delayed [Wald & Law, 2003].

These figures highlight the importance of developing efficient techniques to accurately diagnose and quantify the severity of diseases of the cardiovascular system. To achieve this objective a sound understanding of the physical origin of cardiovascular signals that can be easily acquired *in vivo* (ideally using non-invasive techniques) and used to diagnose and treat CVD needs to be accomplished. However, this understanding is hampered by the complex biological interactions of the cardiovascular system *in vivo*. This research focuses on the study of several indices that can be measured from the shape of pressure and flow pulse waveforms and which may be used to identify and classify CVD status. Numerical modelling

is used to study the interactions of physical characteristics of the cardiovascular system and how they contribute to changes in pulse waveforms at various arterial locations. Several cardiovascular conditions (*e.g.* hypertension, diabetes) significantly alter parameters found at the digital volume pulse (DVP) measured at the finger. How best to build a one-dimensional (1-D) model of blood flow in the systemic circulation that includes the larger arteries of the hand and represents the effect of these conditions on the DVP is explored within this work.

In this chapter we first provide a brief anatomical and physiological description of the cardiovascular system (Section 1.1) and an overview of diseases of the cardiovascular system relevant to this work (Section 1.2). We then define the difference between risk factors and risk markers, and provide examples of risk markers considered within this work (Section 1.3). This distinction is relevant to later chapters in which we extract possible biomarkers from arterial pulse waveforms. Furthermore, we provide a summary of the different haemodynamic models that exist in the literature (Section 1.4). We conclude with the aims of this thesis (Section 1.5) and a thesis outline.

1.1 The Cardiovascular System

The cardiovascular system encompasses the blood, systemic and pulmonary circulations, and the heart. We describe anatomical and physiological concepts of the heart and systemic circulation which are relevant to this work.

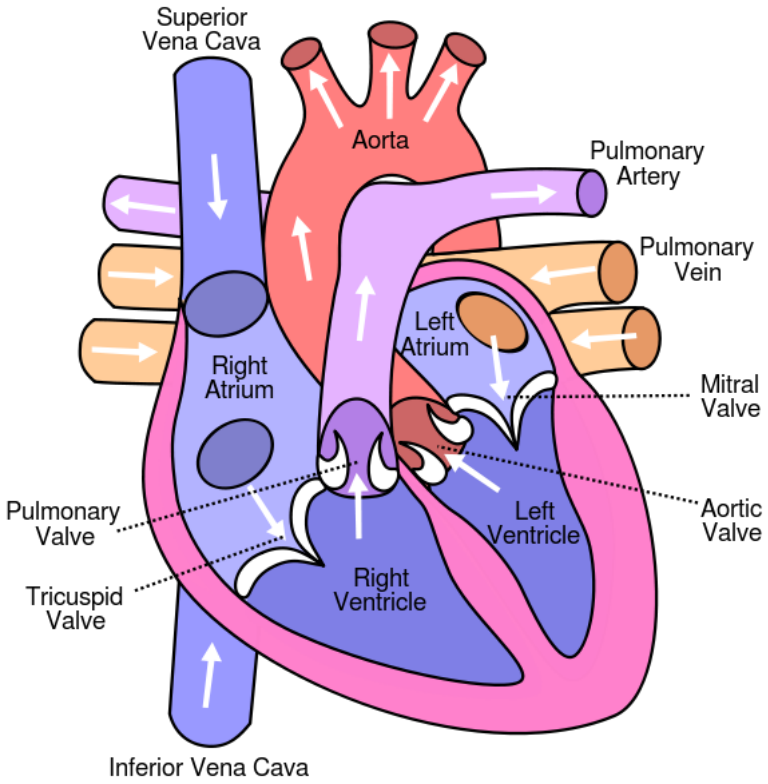

Figure 1.1: Structure of the human heart. The arrows indicate the path followed by the blood flow (Image from [Wikimedia Commons, 2015]).

1.1.1 The Heart

The heart is a hollow muscular organ found between the lungs. It consists of four main chambers. The large left and right ventricles are tasked with pumping blood to the systemic and pulmonary vasculatures, respectively (Fig. 1.1). Above each ventricle is the smaller, thin walled left and right atriam, which act as reservoirs for venous blood, from the pulmonary and systemic systems, respectively. The walls of the four chambers consist mainly of a thick layer of muscle known as the myocardium, surrounded on the outside by a layer of connective tissue and fat (the epicardium) and lined on the inside by a smooth membrane of endothelial

cells (endocardium) [Levick, 2003]. Located within the right atrium wall is the sinoatrial node (SN) which generates a small electrical pulse responsible for the coordinated contraction of the muscles of the heart, known as the cardiac cycle.

The cardiac cycle is segmented into two main phases. The diastolic phase occurs when the muscle wall is relaxed, and the valves separating the atrium and ventricle on both sides are open. Blood flows from the atriams into their respective ventricles. The electrical current from the SN passes through the atria wall causing it to contract, forcing the last of the blood into the ventricles; the interconnecting valves then shut to prevent any back flow. We then enter the latter stage of the cardiac cycle, known as systole. During this stage the ventricles contract increasing blood pressure and ejecting blood into the systemic and pulmonary vasculatures. Figure 1.2 shows an example of the flow waveform measured at the aortic root under normal physiological conditions.

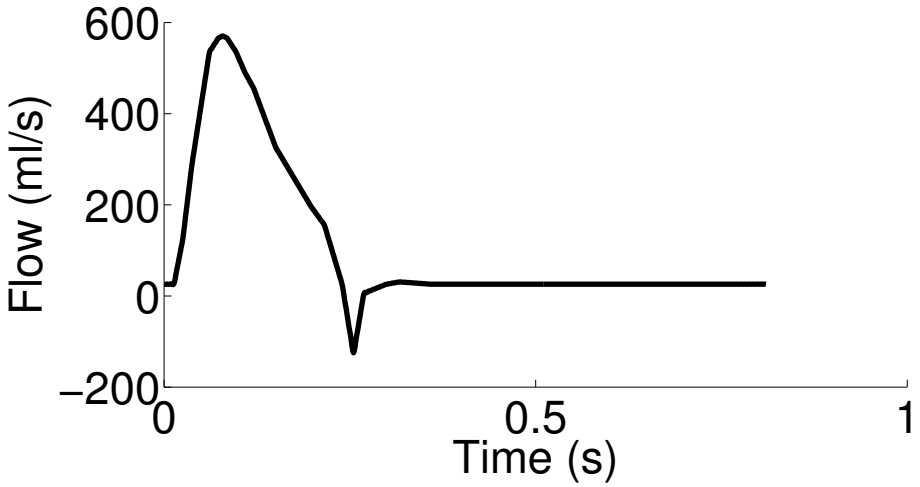

Figure 1.2: Flow waveform measured at the aortic root.

1.1.2 Vascular System

The vascular system is an elaborate highway of tapering curved elastic tubing that transforms the pulsatile flow of blood that exits the heart, into a continuous blood flow at the periphery. The component vessels of the system are categorised as follows: arteries, capillaries and veins. Arteries supply oxygenated blood around the body to the capillaries. The arterial pressure is kept high due to the distal end of the arterial system bifurcating into many vessels with small diameters, thus forming a large peripheral resistance [van de Vosse & Stergiopulos, 2011]. Within the capillaries is where the oxygen and carbon dioxide exchange occurs. The veins then collect the blood from the capillaries and return it to the heart. As the larger vessels of the arteries begin to branch into vessels with a smaller cross-sectional area, the total cross-sectional area of the vascular bed increases rapidly, as illustrated in Fig. 1.3. Thus, a large surface area is available to enable the efficient diffusion of oxygen and nutrients to the surrounding cells.

The walls of the veins and arteries consist of three layers, tunica intima, tunica media, and tunica adventia (see Fig. 1.4). The dimensions of the artery wall vary significantly through the cardiac cycle and the systemic vasculature, and even from person to person.

Smooth muscle cells, when contracted, are responsible for a stiffening of the vessel wall, and a reduction in the diameter. These cells are present in the tunica media in both arteries and veins. In arteries they are also present in the layer of elastic connective tissue lying immediately outside the tunica media, known as the external elastic lamina. In peripheral arteries the contraction of the artery by the smooth muscle cells has a more profound difference on the diameter of the

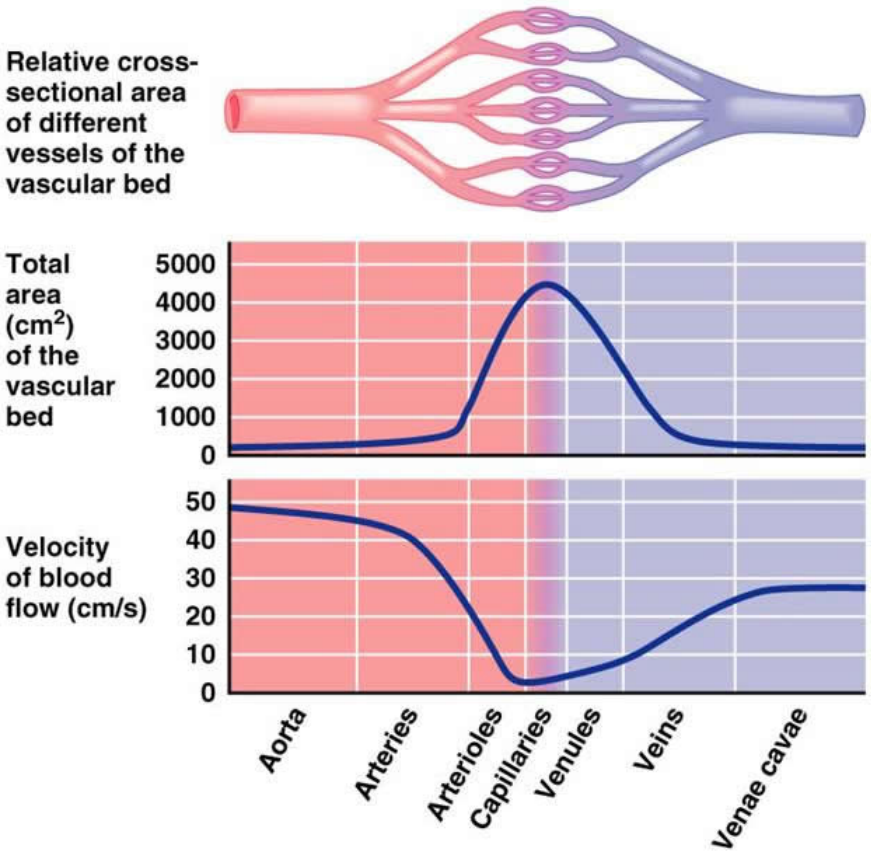

Figure 1.3: Relative cross-sectional area of different vessels (top); total area of vascular beds (middle); peak velocity of blood flow in vessels (bottom). (Taken from [Carter, 2015])

artery than at the central vessels. For instance, the femoral artery diameter can experience a 20% artery reduction, compared to only about 5% in the aorta [Caro *et al.*, 2011]. Due to the distensibility of the vessel, the walls expand and contract as the pulsatile motion of blood flows through. The distensibility of the vessel can be considered in part to be attributed to the amount of the elastin and collagen within the vessel wall.

The elastic nature of the vessels results in a phenomenon known as the Windkessel effect [Westerhof *et al.*, 2009]. Compliant vessels act as a buffer for the

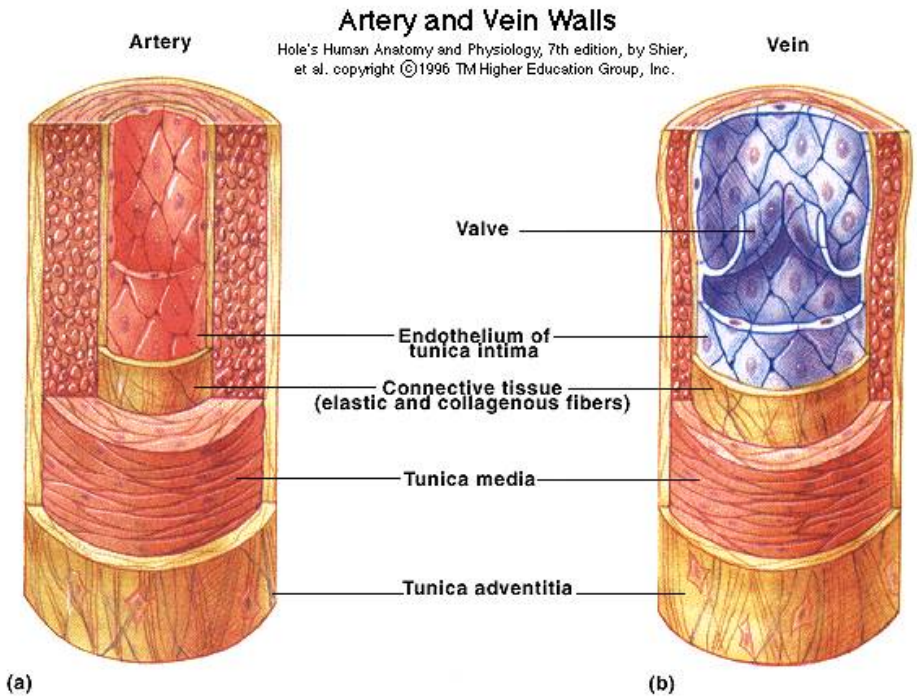

Figure 1.4: Cross section of a typical artery (left) and vein (right) [Shier *et al.*, 2003].

pulsatile blood flow from the heart, thus smoothing the flow wave in peripheral vessels (see Fig. 1.5).

1.1.3 The Pulse Wave

The ventricular ejection during systole creates a primary pulse wave that moves away from the heart along the arterial vessels. The speed that this pulse wave travels, which is called pulse wave velocity (PWV), is determined by the mechanical properties of the arterial walls. This forward-travelling wave is reflected at any point of discontinuity e.g. tapering, bifurcations or occlusions. The morphology of the measured pressure pulse waveform, at any given location, is the summation of the forward and reflected pressure pulse waveforms. Hence, the shape of the

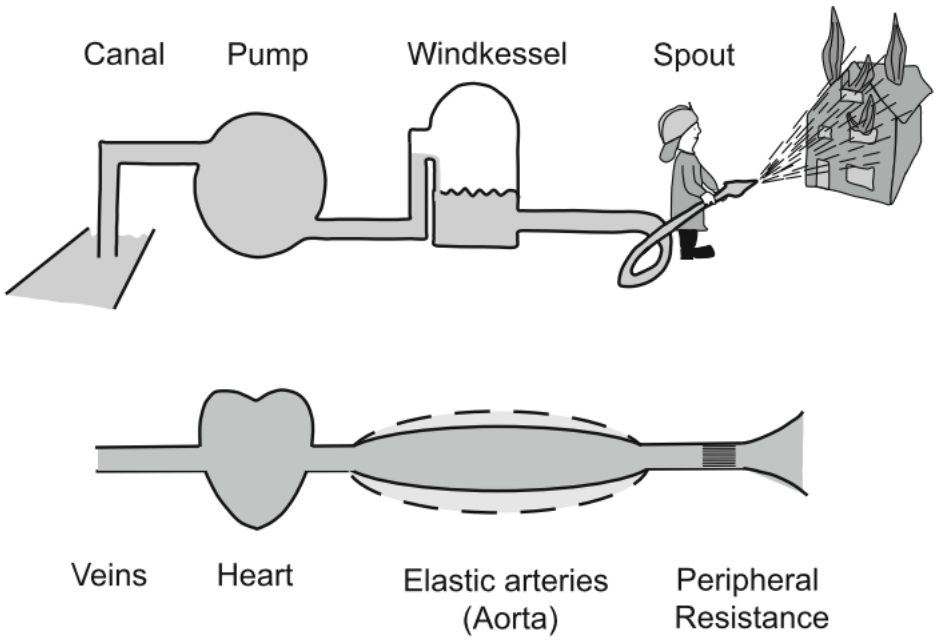

Figure 1.5: Windkessel phenomena, where the compliant vessel volume acts as a buffer for the pulsatile blood flow from the heart, similar to a traditional fire engine hose. Taken from Westerhof *et al.* [2009].

pressure waveform can be altered by changes in the arterial geometry [McDonald, 1974], vasoconstriction/vasodilation, and cardiac output [Murgo *et al.*, 1980]. For example, a stiffened artery creates a faster travelling pulse wave, and an earlier return of the incident wave at the aortic root. This may cause the reflective wave to arrive during the systolic period as opposed to the diastolic period. This early overlap of the forward- and backward-travelling wave creates a shoulder in the aortic pressure waveform in early systole.

Next we present two techniques available in the clinic to measure the pulse wave non-invasively.

1.1.3.1 Photoplethysmography

The pulse waveform at the digital artery in the finger can be measured using photoplethysmography (PPG). This technique uses an infrared optical transducer. The use of PPG has become a standard means of obtaining blood oxygenation data [Hertzman & Spealman, 1937]. The PPG device consists of a light source and light detector which is either positioned directly opposite (transmission plethysmography) or next to (reflective plethysmography) the light source.

Extensive research has been undertaken to understand exactly what the PPG signal is measuring. It is believed that the PPG waveform comes from the site of maximum pulsation within the arteriolar vessels, just before the level of the capillaries [Spigulis, 2005; Trefford & Lafferty, 1984]. It has been shown that the PPG is dependent not only on the blood volume (it is called digital volume pulse, DVP, in some studies), but the haematocrit (and haemoglobin concentration) [Challoner, 1979]. Zweifler *et al.* [1967] found, in individual subjects, the PPG wave to be directly proportional to the digital blood flow over a wide range of environmental conditions. Lindberg *et al.* [1991] compared PPG measurements at the radial artery against laser doppler flowmetry (LDF). They were able to show that LDF is more sensitive than PPG to changes in skin perfusion that follow a skin temperature change, even though both techniques are supposed to measure the same superficial blood perfusion of the skin. The velocity of blood flow affects the PPG, most likely due to the reorientation of red blood cells [D'Agrosa & Hertzman, 1967; Visser *et al.*, 1976]. The microvascular bed of the finger has capillaries and a large number of arteriovenous anastomoses (a vessel that shunts blood from an artery to a vein in order to bypass a capillary). Kim *et al.* [1986]; Secker & Spiers

[1997] have suggested that the signal from the PPG is from open arteriovenous anastomoses.

Different approaches have been taken to numerically model the PPG waveform: Johansson & Oberg [1999] generated a PPG signal as a linear combination of blood flow and pressure using a lumped parameter model; Hemalatha & Manivannan [2010]; Hemalatha *et al.* [2010]; Hou *et al.* [2011] generated PPG signals from the simulated pressure pulse; whereas Alastruey *et al.* [2009a]; Gircys *et al.* [2015] used changes in luminal cross-sectional area of the digital vessel to model the PPG signal.

The characteristics of the measured PPG depend on the measurement location, with different sites having differences in timings [Jago & Murray, 1988] and amplitude [Allen & Murray, 2000]. The pulsatile component of the DVP (*i.e.* the 'AC' component) has its fundamental frequency around 1Hz, depending on the heart rate [Allen, 2007]. During diastole the DVP exhibits a characteristic notch. This 'AC' component is highly sensitive to changes in the systemic circulation, such as changes in pulse wave reflections and pulse wave velocity of the large arteries [Chowienczyk *et al.*, 1999; Hayward *et al.*, 2002; Millasseau *et al.*, 2002a]. The 'AC' component is superimposed onto a 'DC' component. This 'DC' component varies slowly due to various functions; *e.g.* respiration [Lindberg *et al.*, 1992; Nilsson *et al.*, 2000], the autonomic nervous system [Nitzan *et al.*, 1998], and thermoregulation [Burton, 1937]. It has been suggested that the respiratory-induced changes to the waveform are caused by the movement of venous blood [Phillips *et al.*, 2012; Walton *et al.*, 2010]. Within this work, we will focus on the 'AC' component of the DVP. The amplitude of the PPG waveform is relative to each patient, and as such no standardisation procedure exists to compare the PPG amplitude between

patients [Shelley, 2007].

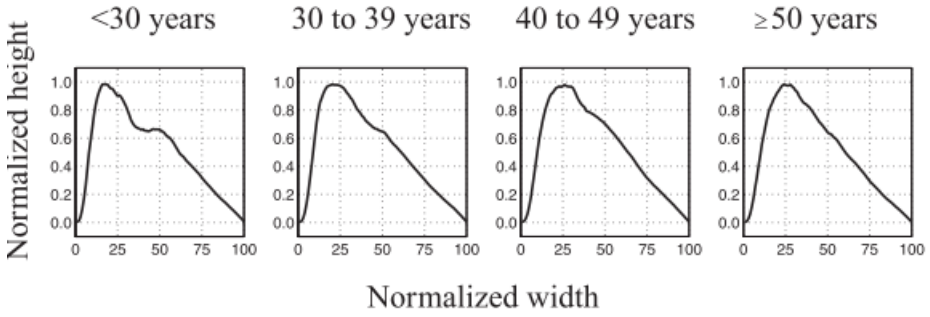

Figure 1.6: Normalised average of 116 subjects PPG waveform from the digital waveform. Subjects younger than 30 years (N=27), between 30 and 39 years (24), between 40 and 49 years (32), and 50 years of age or older (33). Adapted from Allen & Murray [2003]

In normotensive young patients, the shape of the DVP consists of an early peak during systole which is the result of a dominant forward pressure waveform from the left ventricle. A second, later diastolic peak is due to pulse wave reflections from sites of impedance mismatch. A dicrotic notch is seen during systole in patients with healthy compliant arteries [Dawber *et al.*, 1973; Elgendi, 2012]. As the patient ages there is an elongation in the time of arrival of the systolic peak and a smoothing of the amplitude of the second peak [Allen & Murray, 2003] (as seen in Fig. 1.6).

Work by Takazawa *et al.* [1998] has shown that the DVP closely resembles the carotid pressure waveform, even under the influence of vasodilator and vasoconstrictor drugs. Augmentation of the DVP is mainly influenced by changes in pressure wave reflections in the torso and lower body [McDonald, 1974]. Thus the DVP PPG waveform provides a noninvasive method to derive cardiovascular properties of the aorta and other central arteries.

PPG measurements at various locations can be used in the assessment of reactive hyperaemia [Simonson *et al.*, 1955], occlusions [Allen *et al.*, 2005; Lynch *et al.*, 1981; Oliva & Roztocil, 1983], and carotid artery disease [Barnes *et al.*, 1977].

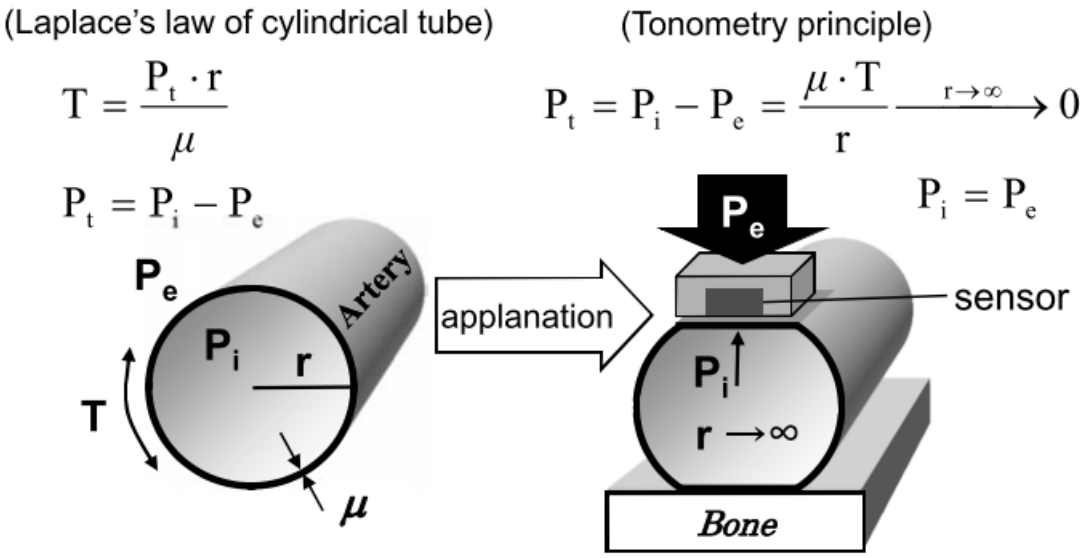

Figure 1.7: Applanation of artery where P_e =external pressure, P_i =internal pressure, P_t =transmural pressure, r =radius of curvature, T = wall tension and μ = wall thickness. Taken from Miyashita [2012].

1.1.3.2 Applanation Tonometry

Applanation tonometry is a technique that allows for a continuous non-invasive measurement of the arterial pressure waveform. If the artery is assumed to be a cylindrical thin walled vessel, then it is possible to apply Laplace's law to derive a measure of pressure (see Fig. 1.7). When a transducer applanates the vessel wall the radius of the wall curvature becomes infinite thus the internal pressure (P_i) is equal to the pressure applied by the transducer (P_e).

The successful applanation of the arterial wall is location dependent, the artery

considered must be superficial and supported by a bone structure beneath. It is noted that the brachial site is not suitable for applanation tonometry [O'Rourke & Adji, 2010]. Under optimal conditions, the applanation tonometry waveform measured non-invasively is nearly identical to the waveform measured invasively using a high-fidelity transducer [Chen *et al.*, 1996; Kelly *et al.*, 1989].

Applanation tonometry provides a continuous pressure waveform. However, the amplitude must be calibrated by means of an external method. The calibration method used is dependent on the measurement site. Pauca *et al.* [1992] have shown it is best to use the diastolic and mean pressure at the brachial cuff when calibrating the radial pressure waveform.

1.2 Diseases of the Cardiovascular System

CVD is a general term for all diseases of the heart and vascular system; *e.g.* stroke, cardiomyopathy, atrial fibrillation, congenital heart disease, venous thrombosis, aortic aneurysm, and coronary artery disease. Overall CVD is estimated to cost Europe €196 billion each year [Nichols *et al.*, 2013]. The underlying causes vary according to each condition.

Within this section we will present two cardiovascular diseases relevant to this thesis: diabetes and hypertension (Sections 1.2.1 and 1.2.2). Furthermore, we will look at the interactions between these two disease states (Section 1.2.3).

1.2.1 Hypertension

Hypertension is one of the most important preventable causes of premature morbidity and mortality in the UK. It affects a quarter of the adult population [Krause

et al., 2011]. The causes of hypertension can be environmental; alcohol, physical inactivity and diet related [Forman *et al.*, 2009; Hall, 2003; Saunders, 1987] or genetic [Beevers *et al.*, 2001]. Hypertension is characterised by left ventricular hypertrophy and arterial wall stiffening [Fouad *et al.*, 1984; Wolinsky, 1972]. Physical properties of the vasculature such as aortic stiffness affect cardiac mechanics (afterload) and, therefore, it is important to be able to quantify vascular properties to assess cardiac function.

In this thesis, hypertension is defined as having a blood pressure measured in the clinic of systolic pressure greater than 140 mmHg or diastolic pressure greater than 90 mmHg, as recommended by UK NICE guidelines [Krause *et al.*, 2011].

The non-invasive gold standard for clinical measurement of blood pressure has always been with a mercury sphygmomanometer at the brachial artery [Pickering *et al.*, 2005]. However as these antiquated devices are being phased out, the accuracy of newer devices has been questioned, with measured inaccuracies of aneroid spygmomanoeters ranging from 1% [Canzanello *et al.*, 2015; Yarows & Qian, 2001] to 44% [Mion & Pierin, 1998]. Thus, the importance of indices other than the traditional measurements of systolic, diastolic and mean pressure are highlighted.

In hypertension not only is the absolute value of blood pressure increased, but so is the shape of the pressure waveform. Stiffer arteries cause an earlier return of a larger reflected pulse wave which augments the systolic pressure waveform (as seen in Fig. 1.8). At peripheral locations, Hertzman & Spealman [1937] reported an increase in the crest time, loss of the rebound wave and triangulation of the DVP.

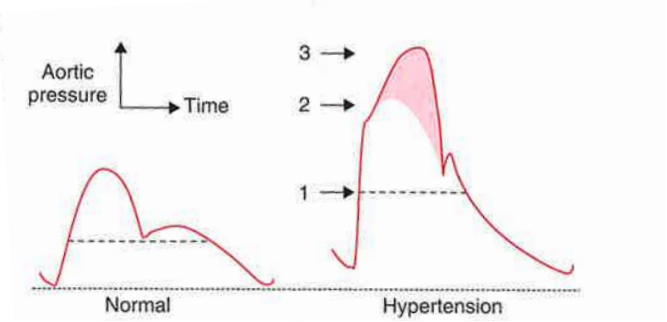

Figure 1.8: Normal (left) and hypertensive (right) pressure waveforms. Arrow 1 indicates the increase in mean pressure from the increased resistance in the small arteries. Arrow 2 indicates the increase in the systolic incident wave caused by reduced aortic compliance. Arrow 3 shows the augmentation of pressure from the arrival of an earlier reflected waveform. Taken from Levick [2003].

1.2.2 Diabetes

Diabetes is most prevalent in the Western Pacific Region (132 million), followed by Southeast Asia (71 million), Europe (53 million), North America and Caribbean (38 million), Middle East and North Africa (33 million), South and Central America (25 million), and Africa (15 million) [Whiting *et al.*, 2011]. The growing prevalence of the disease is partially due to the rise in obesity levels seen globally [Hossain *et al.*, 2007].

Diabetes mellitus (DM) is defined as a group of metabolic diseases primarily characterised by chronic hyperglycaemia (excess of glucose in the bloodstream) affecting both the macrocirculation and microcirculation [Alberti & Zimmet, 1998; American Diabetes Association, 2005]. The two categories of diabetes are type I, and type II. A patient with type I diabetes would be unable to produce insulin in the pancreas, and is treated with an insulin replacement. A type II patient would produce an insufficient amount of insulin and have an increase in insulin

resistance. Treatment in this case can be pharmacological, or involve modifications to diet and lifestyle.

Cardiovascular disease may predate diabetes (see Fig. 1.9) [Cruickshank & Wright, 1990; Cruickshank *et al.*, 2002; Haffner *et al.*, 1990, 2000; Paini *et al.*, 2006]. It is known that arterial stiffness is a predictor of diabetes before the onset of clinical diabetes [Atabek *et al.*, 2006; Giannattasio *et al.*, 1999; Haller *et al.*, 2004; Parikh *et al.*, 2000; Stakos *et al.*, 2005]. Diabetic microvascular disease is often explained as accelerated aging [McDonald, 1974]. Cameron *et al.* [2003] calculated an arterial age difference of 14 years between diabetic and their non diabetic counterparts.

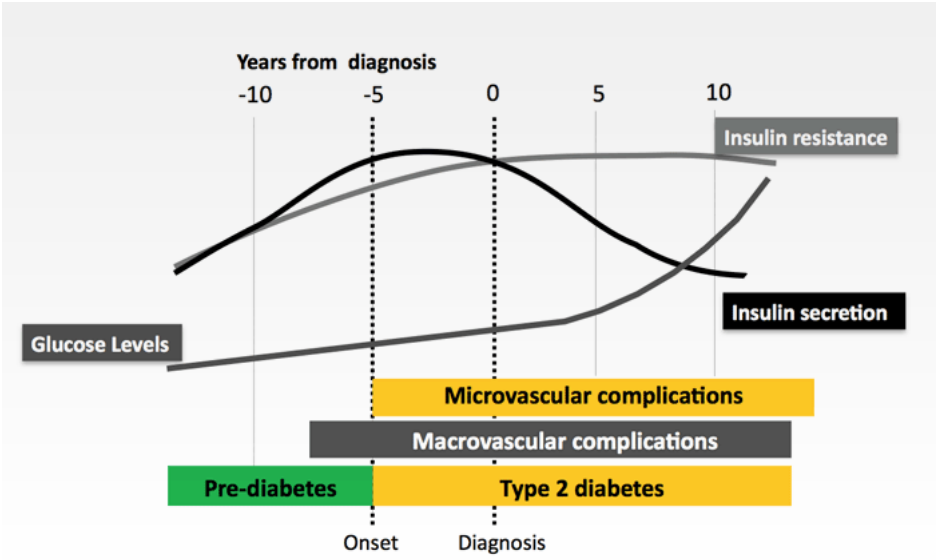

Figure 1.9: Pathophysiology of diabetes mellitus with time [Diabetes Advocates, 2015].

It has long been identified that patients with diabetes experience abnormalities in the pressure pulse waveform, such as diminished incident waves during diastole [Lax *et al.*, 1959] or reduced oscillatory compliance [McVeigh *et al.*, 1993]. The

augmentation index is a measure of arterial stiffness derived from the ascending aortic pressure waveform. Patients suffering from diabetes type I and type II may also have an increased augmentation index [Brooks *et al.*, 2001; Fukui *et al.*, 2003; Ravikumar *et al.*, 2002; Westerbacka *et al.*, 2005; Wilkinson *et al.*, 2000], as seen in Fig. 1.10. However Climie *et al.* [2013]; Lacy *et al.* [2004a]; Zhang *et al.* [2011] found that there was no correlation between the augmentation index and diabetes status when compared to age-matched non-diabetic counterparts.

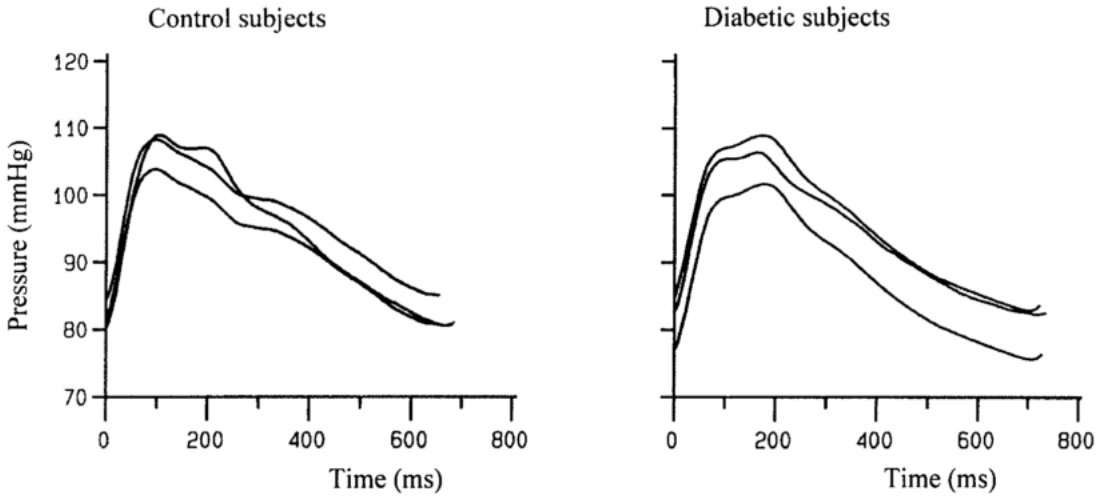

Figure 1.10: Typical synthesised aortic waveforms from diabetics (right) and in age and sex matched normotensive patients (left). Taken from Wilkinson *et al.* [2000].

1.2.3 Hypertension and Diabetes

Diabetes has long been associated with cardiovascular disease [Epstein & Sowers, 1992; Kannel & Castelli, 1979; Kannel & McGee, 1979; Pell & Alonzo, 1967]. A person with hypertension is almost 2.5 times more likely to develop type II diabetes than in their normotensive counterpart [Gress *et al.*, 2000]. Furthermore,

the risk of CVD is four-fold higher in patients with hypertension and diabetes compared to a non-diabetic normotensive subject [Hu *et al.*, 2007; Stamler *et al.*, 1993]. Arterial stiffness increases under both conditions, which often precedes microvascular events [Bella *et al.*, 2001; Benetos *et al.*, 1997]. The mechanisms by which vascular stiffness increases within the diabetic subgroup is not fully known [Franklin, 2002; Henry *et al.*, 2003; Schram *et al.*, 2004]. It has been hypothesised that type II diabetes mellitus worsens arterial stiffness in hypertensive patients through endothelium-related mechanisms [Bruno *et al.*, 2012].

1.3 Risk Factors and Risk Markers

Cardiovascular risk factors have been derived from epidemiological studies for over half a century. They help quantify the extent of CVD [Dawber *et al.*, 1961]. Risk factors are defined as having not only predictive but also causal value [Stampfer *et al.*, 2004]. The age of a patient is still the best determinant for CVD [Najjar *et al.*, 2005]. Other traditional risk factors are gender, family history, blood pressure, cholesterol lipid, weight, diet, hypertensive status, and smoking [Wang, 2008].

Risk markers (biomarkers) are distinct from risk factors, as they are not assumed to play a direct causal role in disease [Wang, 2008]. A large area of research is now focussed on finding new biomarkers that provide added value to the diagnostic clinician or reveal information on the underlying pathophysiology. A number of biomarkers have been identified so far, including carotid intima-media thickness [Leary, 1999], flow mediated dilation [Yeboah *et al.*, 2009], and arterial stiffness [Mitchell *et al.*, 2010]. In this section we will focus on vascular biomarkers relevant

to this thesis.

It is noted that additional tools exist to evaluate arterial stiffness. Wave intensity analysis (WIA) is derived by applying the method of characteristics to the 1-D equations of blood flow in elastic vessels [Parker & Jones, 1990]. WIA has been used to assess the working condition of the heart [Davies *et al.*, 2006].

1.3.1 Pulse Wave Velocity

Pulse wave velocity (PWV) is considered to be the gold standard method of assessing arterial stiffness [Laurent *et al.*, 2006]. PWV is a regional measure of arterial stiffness and is defined as the speed that the pressure and flow wavefronts travel within a flexible vessel when the velocity of blood flow is equal to zero. In general, the PWV is higher in more peripheral arteries. In the physiological setting, where vessel wall material properties are constantly varying, it is possible to take an average estimate of the PWV along a given vessel. The most common method of measuring PWV is to divide the distance between the carotid and femoral measurement sites across the body (measured using a tape) by the time delay between the arrival of pressure waveforms at the two sites [Mitchell *et al.*, 2008; Paini *et al.*, 2006; Vermeersch *et al.*, 2010] (see Fig. 1.11). Other possible measuring sites include the brachial-ankle, carotid-radial, and carotid-ankle [Gamella-Pozuelo *et al.*, 2015; Zhang *et al.*, 2011].

PWV has been shown to be dependent on age and to be driven by changes in blood pressure [McEniery *et al.*, 2010]. It has been shown to be an independent predictor of cardiovascular mortality [Blacher *et al.*, 1999; Cruickshank *et al.*, 2002; Laurent *et al.*, 2001, 2003; Mattace-Raso *et al.*, 2006; Meaume *et al.*, 2001; Safar

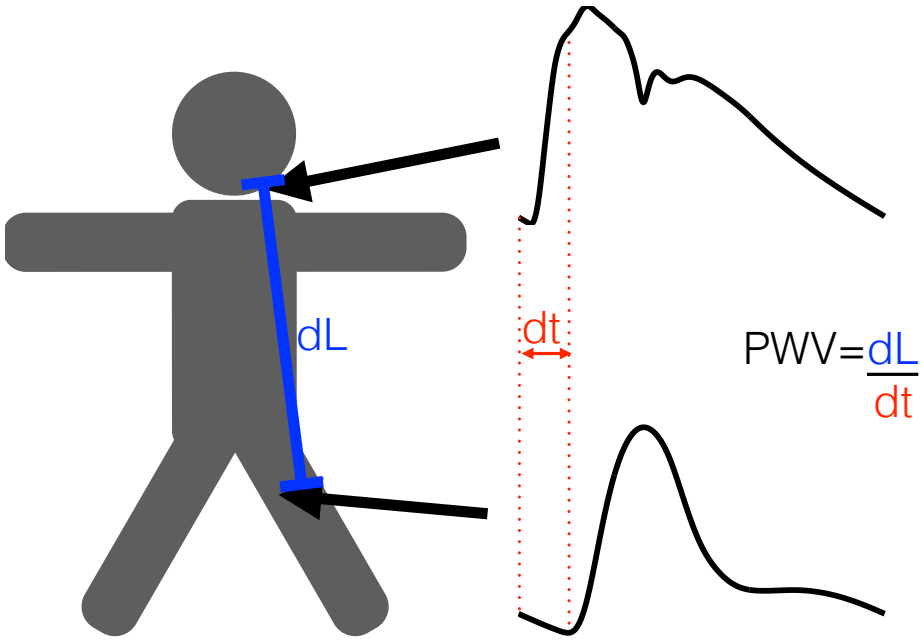

Figure 1.11: Pulse wave velocity determination for the carotid to femoral site by the foot-to-foot method. Where dL =distance travelled by waveform, and dt =time difference between the foot of the two waveforms.

et al., 2002; Sutton-Tyrrell *et al.*, 2005; Willum-Hansen *et al.*, 2006]. PWV is now included in the ESH/ESC guidelines for the management of arterial hypertension [Mancia & The Task Force for the management of arterial hypertension of the European Society of Hypertension (ESH) and of the European Society of Cardiology (ESC), 2013] and has been shown to be reliably reproducible in the clinical setting [Asmar *et al.*, 1995, 2001]. However, a reliable method for extracting central PWV from peripheral PPG signals must be developed, as of now, a robust methodology has not been determined [Elgendi, 2012].

1.3.2 Augmentation Index

The augmentation index (Aix) is primarily a measure of wave reflections at a given measuring site. It is commonly used as a surrogate for arterial stiffness since it is associated with PWV [Brown & Brown, 1999; Liang *et al.*, 1998]. Aix has also been shown to be influenced by left ventricular contractility [Jones & Sugawara, 1993; Laurent *et al.*, 2006] and heart rate [Brown & Brown, 1999; Cameron *et al.*, 1998; Segers *et al.*, 2006]. A schematic representation of how the Aix is calculated for different types of arterial pressure waveforms is given in Fig. 1.12. For the computation of Aix it is necessary to identify the time of arrival of the reflected pressure pulse for which either the shoulder or inflection point can be used [Segers *et al.*, 2007]. It is noted that the shoulder and inflection points are not always easily identifiable.

Aix has been shown to be an independent predictor of cardiovascular disease, coronary artery disease [Hayashi *et al.*, 2002; Patvardhan *et al.*, 2011], cardiovascular events such as myocardial infarction, death and restenosis [Weber *et al.*, 2005], and all-cause mortality [London *et al.*, 2001; Vlachopoulos *et al.*, 2010]. Additionally, Aix has been shown to correlate with the rate of restenosis after coronary stenting [Ueda *et al.*, 2004].

1.3.3 Stiffness Index

The stiffness index (SI) is derived from contour analysis of the peripheral pulse waveform; *e.g.* the DVP measured in the finger [Millasseau *et al.*, 2006]. SI is calculated by dividing the height of the patient by the time delay between the two characteristic peaks in the DVP waveform (see Fig. 1.13). The first peak of the

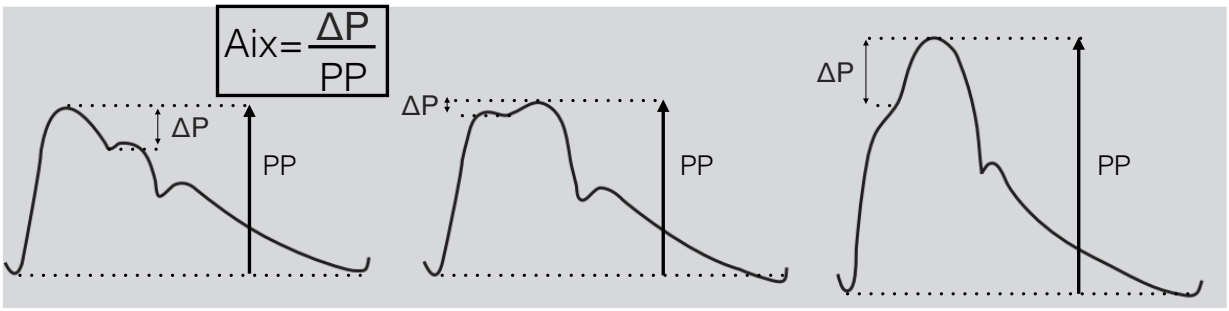

Figure 1.12: Calculation of augmentation index (ratio of peak height above the shoulder of the wave to the pulse pressure) in three types of aortic pressure waveforms generally seen in young (left), older (centre), and old adults (right). They are described as types A, B and C waveforms, respectively. Adapted from Rourke & Pauca [2004].

DVP is assumed to be related to a forward-travelling wave from the heart, and the second peak (the reflected wave) to be dependent on the PWV in the arterial system [Chowienczyk *et al.*, 1999; Millasseau *et al.*, 2002b; Morikawa, 1967].

SI has been correlated with birth weight [Broyd *et al.*, 2005], age [Millasseau *et al.*, 2003], body fat content [Wykretowicz *et al.*, 2007], and vascular disease [Chen *et al.*, 2005].

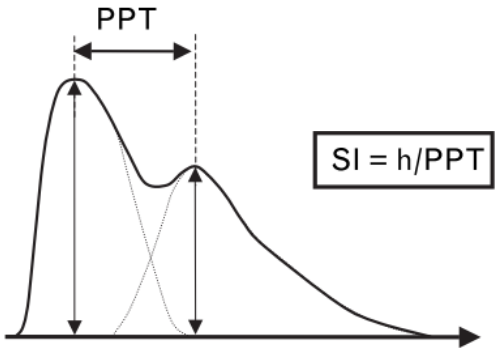

Figure 1.13: Measured DVP waveform with annotated time delay (PPT) between diastolic and systolic peaks. Stiffness Index (SI) calculated as: SI=h/PPT, where h is the height of the patient. Reproduced from Millasseau *et al.* [2006].

1.4 Numerical Modelling

Stemming from the concepts of conservation of mass and momentum, it is possible to mathematically model the pressure and flow waveforms within the cardiovascular system. Several modelling approaches can be used to simulate arterial haemodynamics. In this section we will outline the three-dimensional (3-D) (Section 1.4.1), one-dimensional (1-D) (Section 1.4.2), and zero-dimensional (0-D) (Section 1.4.3) formulations.

1.4.1 3-D Models

The governing equations of 3-D haemodynamics are based on the physical principles of conservation of mass and momentum within any given parcel of fluid. They are called the Navier-Stokes equations. The flexibility of the arterial wall needs to be simulated using a constitutive law. This method allows for an accurate portrayal of the geometry of the blood vessel and provides 3-D flow and pressures. For example, 3-D models enable computation of the shear stresses experienced at an artery wall [Perktold *et al.*, 1991], and the blood flow around obstacles within the vessel; *e.g.* around plaque [Jabbar *et al.*, 2012; Ohayon *et al.*, 2005]. Three-dimensional modelling has also been used extensively to simulate the forces experienced at an aneurysm (a balloon like bulge in the vessel wall) in order to improve treatment and care of the condition [Di Martino *et al.*, 2001; Groden *et al.*, 2001; Hatakeyama *et al.*, 2001; Vorp *et al.*, 1998], and to gain insight into the aortic haemodynamics of patients with aortic dissection [Alimohammadi *et al.*, 2014; Chen *et al.*, 2013; Karmonik *et al.*, 2008, 2010].

Due to the high computational cost of 3-D numerical models, only a portion of

the vasculature, or region of interest, is normally considered. Boundary conditions are typically provided in the form of 0-D or 1-D models.

1.4.2 1-D Models

Fluid flow in 1-D is governed by a reduced form of the incompressible continuity and Navier Stokes equations [Shi *et al.*, 2011]. 1-D models have the benefit of being able to capture the propagation of pressure and flow waveforms in the arterial network, with a modest computational cost.

Modelling of cardiovascular dynamics in 1-D can be solved by either frequency- or time-domain techniques. In the frequency domain the governing equations are linearised, hence the convective acceleration term is neglected. This term is relevant when there is tapering of the vessel well [Quick *et al.*, 2001; Westerhof *et al.*, 1969]. In the time domain, the method of characteristics can be applied to transform the nonlinear 1-D governing equations into a series of ordinary differential equations (ODE) solved along the characteristic paths [Whitham, 2011]. Alternatively, the governing equations can be solved using finite element methods [Reymond *et al.*, 2009; Sherwin *et al.*, 2003a; Smith *et al.*, 2002]. Further, a spectral method can be applied to solve the governing equations [Bessems *et al.*, 2008].

One-dimensional models are often focussed on the larger vessels of the arterial circulation [Blanco *et al.*, 2014; Hughes & Lubliner, 1973; Müller & Toro, 2013; Mynard & Nithiarasu, 2008; Olufsen, 1999; Reymond *et al.*, 2009; Sherwin *et al.*, 2003a; Stergiopulos *et al.*, 1992], but can also represent smaller subsections of the arterial vessels [Bessems *et al.*, 2008; Formaggia *et al.*, 2003; Leguy *et al.*, 2011;

Willemet *et al.*, 2013].

1.4.3 0-D Models

0-D models (or lumped parameter models) are useful in simulating the global haemodynamics of the arterial system with a relatively small computational cost. In 1899, Frank first applied a 0-D model to the arterial system – the two-element Windkessel – to describe the shape of the pressure waveform [Frank, 1899]. In this model, the entire arterial vasculature is simulated by a capacitor and a resistor. From this simple model, a huge array of lumped parameter models have been investigated ranging from the simple three-element Windkessel model of the aorta, used to calculate total compliance from pressure and flow measurements [Westerhof *et al.*, 2009], to other more extensive, multi-compartmental 0-D models used to represent the entire arterial system [Liang & Liu, 2005; Olufsen *et al.*, 2002; Pietrabissa *et al.*, 1996; Reisner & Heldt, 2013]. From these multi-compartmental models we can 1) gain a greater understanding of the role of heart and vascular properties in arterial haemodynamics; 2) learn about the nature of reflected waves contribution to pressure and flow waveforms; and 3) provide a model of haemorrhage, dehydration and other peripheral flow regulatory mechanisms [Avolio, 1980; Lanzarone *et al.*, 2007; Liang & Liu, 2005; Olufsen *et al.*, 2000; Reisner & Heldt, 2013; Westerhof *et al.*, 1969]. Lumped parameter models are not suitable for problems concerning spatially distributed parameters [Westerhof *et al.*, 2009].

1.5 Motivation and Objectives

The goal of this thesis is to assess computationally several cardiovascular biomarkers (or indices) that can be calculated from systemic pulse waveforms, focusing on the DVP waveform. By analysing pulse wave indices of cardiovascular health derived from large epidemiological studies, we observed that indices used clinically have regions of hypothesised origin which are too complicated to proof absolutely *in vivo*. In this thesis, we build confidence in using cardiovascular biomarkers through blood flow modelling. We create a novel 120-artery 1-D/0-D model of pulse wave propagation in the aorta and larger systemic arteries, including peripheral vessels of the head and upper limbs where the PPG wave can be measured. We validate this model qualitatively. We then perform an extensive sensitivity analysis to quantify the changes seen in the peripheral pulse wave due to variations in cardiac and vascular properties. We are then able to numerically quantify how PPG biomarkers relate to the underlying physical properties of the cardiovascular system. Several diseased states are simulated, including hypertension, diabetes, and combined hypertension and diabetes.

An important contribution of this thesis is the derivation of a novel methodology for optimising the number of arterial segments for a given 1-D model problem. This tool is motivated by the difficulty to measure all the parameters required to calibrate 1-D models in the clinic. This novel methodology could allow others to speed up their development process of 1-D blood flow simulations.

Within this work we will provide novel tools to help bridge the gap between clinical and computational approaches, and will investigate several clinically relevant applications of 1-D blood flow modelling.

1.6 Thesis Outline

Following this introduction, Chapter 2 describes the mathematical formulation of the 1-D/0-D numerical framework used in this thesis to simulate arterial blood flow in the systemic circulation. Chapter 3 presents the new 1-D/0-D model of arterial blood flow which simulates the DVP wave and forms the basis of the research carried out in Chapters 3 to 5. Chapter 3 also contains a local sensitivity analysis of the computed DVP wave at the finger to cardiovascular properties. In Chapter 4, the 1-D/0-D model is used to investigate whether the shape of the PPG waveform measured in the finger could be used to distinguish among subjects with diabetes, hypertension, and combined diabetes and hypertension. For this study, a virtual (computed) population of pulse waveforms is created, which includes healthy and diseased subjects. The population is parametrised using a global sensitivity approach. Chapter 5 provides a novel methodology to optimise the number of arterial segments for 1-D/0-D modelling. Lastly, Chapter 6 summarises the thesis contributions and suggests directions for future work.

Chapter 2

Mathematical Formulation

The application of numerical simulations to model blood flow in the human arterial system is now a widespread technique. The types of modelling approaches fall into three main categories: (1) 3-D models which solve a mixed set of nonlinear, partial differential equations known as the incompressible Navier Stokes equations which can be parabolic, hyperbolic or elliptical; (2) 1-D models which consist of a system of predominantly hyperbolic partial differential equations; and (3) 0-D models which are described by finite dimensional ordinary differential equations. Often the three model variants are coupled together to create a multi-scale computational frameworks; *e.g.* 3-D/0-D [Vignon-Clementel *et al.*, 2010], 3-D/1-D/0-D [Blanco *et al.*, 2012b], and 1-D/0-D [Willemet *et al.*, 2011].

A 1-D/0-D model has the benefits of containing vital information on the spatial geometry and material properties of vessels whilst maintaining a modest computational cost. For this work we have chosen this modelling approach; a well researched tool which has been validated against *in vitro* data (e.g. against a polyurethane vessel model in an open water filled container and an experimental

silicone tube model, mimicking the anatomy and physiology of the human vasculature in the arm) [Alastruey *et al.*, 2011; Bessems *et al.*, 2008; Boileau *et al.*, 2015; Huberts *et al.*, 2012c; Matthys *et al.*, 2007; Saito *et al.*, 2011], *in vivo* data (e.g. against data obtained from applanation tonometry, transcranial ultrasound and phase-contrast-MRI) [Bollache *et al.*, 2014; Leguy *et al.*, 2010; Mynard & Smolich, 2015; Olufsen *et al.*, 2000; Reymond *et al.*, 2011; Steele *et al.*, 2003; Stettler *et al.*, 1981], and 3-D simulations [Mynard & Nithiarasu, 2008; Xiao *et al.*, 2013].

This chapter details the 1-D mathematical formulation of blood pressure and flow in the arteries of the cardiovascular system. It begins by asserting the necessary assumptions to reduce an arterial segment to a 1-D model vessel Next, the physical principles of conservation of mass and momentum are applied to this vessel to derive the governing 1-D equations (Sections 2.1.2 and 2.1.3). To solve the system of equations it is then necessary to include changes in blood pressure and luminal cross-sectional area in the vessel (Section 2.1.4). The nonlinear governing equations are then manipulated to obtain the characteristic variables of the system (Section 2.2). The linearised 1-D equations are introduced in Section 2.3 and the Windkessel and other lumped parameter 0-D models utilised within this thesis are described in Section 2.4. We then describe the boundary and junction conditions required to create 1-D/0-D arterial networks (Section 2.5). This chapter concludes with a brief overview of numerical schemes used in the literature to solve the 1-D equations.

Different approaches have been taken to numerically model the PPG waveform, for the purpose of this study, we will assume that the PPG signal can be represented by the cross-sectional area at the digital artery.

2.1 1-D Governing Equations

Within this section we will derive the necessary equations to model blood flow in a system of arteries. Here we will derive the governing equations starting from a 1-D model control volume analysis. It is noted that the 1-D governing equations can also be obtained by integrating the 3-D Navier-Stokes equations over a given vessel cross-section [Formaggia *et al.*, 2001].

2.1.1 1-D Model Assumptions

To derive our 1-D blood flow equations we consider a vessel of length l, as seen in Fig. 2.1, which is independent of time, with centreline s($\mathbf{x}$). The cross-sectional area normal to the centreline is denoted by $A(s(\mathbf{x}), t)$, and the wall thickness by $h(s)$. We assume that the local curvature is small enough so that the axial direction can be described by $\mathbf{x} = (x, 0, 0)$. Along the centreline we define the area of each cross section as $A(x,t) = \int_S d\sigma$. Where S is the cross section and $d\sigma$ is a differential element of area. We do not consider the effect of gravity on the blood flow.

For the purpose of our study we have taken arterial wall thickness to be 10% of the internal artery radius [Caro *et al.*, 2011]. We define the blood flow velocity ($U(x,t)$) as an average over each cross section, hence $U(x,t) = \frac{1}{A}\int_S \hat{u}(x,\sigma,t)d\sigma$, where $\hat{u}(x,\sigma,t)$ is the velocity field within a fixed x position. Blood flow is considered to be laminar, which is a reasonable assumption due to the Reynolds number being below 2,000 through the arterial system, in normal conditions (when mean arterial flow is considered) [Zamir, 2000]. Additionally we define the average internal pressure over the cross section as $p(x,t) = \frac{1}{A}\int_S \hat{p}(x,\sigma,t)d\sigma$. Volume flux is defined along the x axis as $Q(x,t) = A(x,t)U(x,t)$. The fluid within the vessel

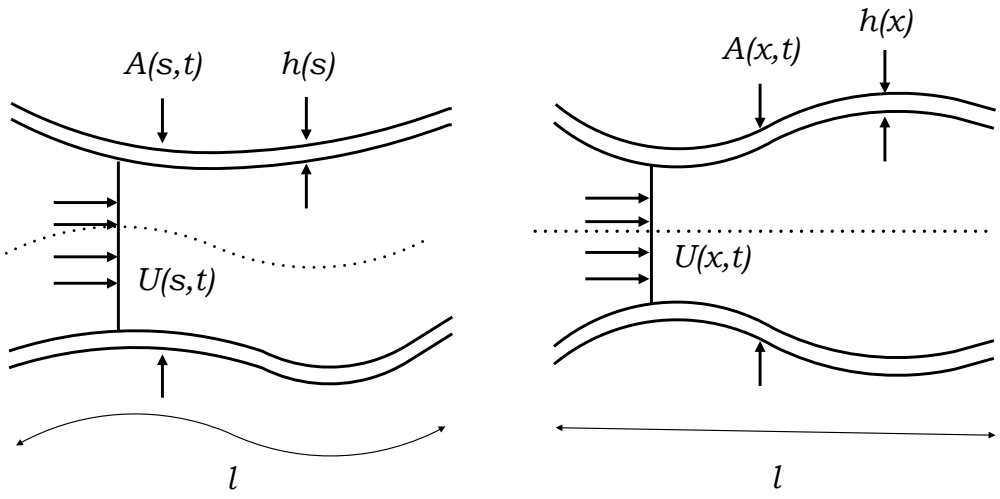

Figure 2.1: Layout of a simple compliant tube with cross-sectional area A, flow velocity U, vessel length l, and vessel wall thickness h. General orientation (left) and 1-D model orientation (right). Adapted from Alastruey [2006].

is assumed to be incompressible and Newtonian, with a uniform blood density [Khanafer *et al.*, 2006].

2.1.2 Mass Conservation

The rate of change of mass within the portion of vessel described in Section 2.1.1 is considered equal to the mass flux at the boundary. The volume is defined as $V(t) = \int_0^l A dx$, and we assume that there is no fluid loss at the vessel wall. Hence we have

$$\rho \frac{dV(t)}{dt} = \rho(Q(0,t) - Q(l,t)), \tag{2.1}$$

where ρ is the density of the blood. Similar to Alastruey [2006] we take $\rho = 1050$ Kg / m^3.

Additionally, $V(t) = \int_0^l A(x,t)dx$, and $Q(l,t) - Q(0,t) = \int_o^l \frac{\partial Q}{\partial x} dx$. Substituting

these known quantities into Eq. (2.1) yields

$$\rho \frac{d}{dt} \int_0^l A(x,t)dx = -\rho \int_0^l \frac{\partial Q}{\partial x} dx. \tag{2.2}$$

Assuming that the length l is independent of time (*i.e.* the vessel is tethered), we get

$$\rho \int_0^l \left(\frac{\partial A}{\partial t} + \frac{\partial Q}{\partial x} \right) dx = 0. \tag{2.3}$$

The integrand from Eq. (2.3) holds true for all values of $l \in \mathbb{R}$. Hence,

$$\frac{\partial A}{\partial t} + \frac{\partial Q}{\partial x} = 0. \tag{2.4}$$

2.1.3 Momentum Conservation

Considering the same vessel as in Section 2.1.2, we assume that there is no flux in the x-direction through the walls of the vessel. Conservation of momentum states that the rate of change of momentum within the control portion of a vessel plus the net flux of momentum out is equal to the applied forces on the control volume. Hence,

$$\frac{d}{dt} \int_0^l \rho Q dx + (\alpha \rho Q U)_l - (\alpha \rho Q U)_0 = F, \tag{2.5}$$

where F is the applied forces in the x-direction on the control volume, and α is a momentum flux correction factor which accounts for the nonlinear section integration of the local velocity $\hat{u}$;

$$\int_S \rho(\hat{u})^2 d\sigma = \alpha \rho U^2 A = \alpha \rho Q U. \tag{2.6}$$

The momentum flux correction factor (α), defined as

$$\alpha = \frac{1}{U^2 A} \int_S (\hat{u})^2 d\sigma, \tag{2.7}$$

allows for $\hat{u}$ to be non-constant across a given cross-sectional area: in a straight tube we would expect for the flow velocity to be highest in the centre of the tube, and lowest at the edges. To correct for this nonlinearity, we calculate α by assuming a shape of the velocity profile. For a uniform velocity profile, $\alpha = 1$; for a parabolic profile, $\alpha = \frac{4}{3}$. Within this thesis we will by default use $\alpha = 1.1$ as a compromise fit to experimental data [Smith *et al.*, 2002]. This assumption provides an axisymmetric and constant velocity profile that satisfies the no-slip condition.

The applied forces, F, are a pressure at either end of the vessel produced by the fluid, a pressure force at the wall boundary (the side of the vessels), and a frictional force per unit length, f; *i.e.*

$$F = (pA)_0 - (pA)_l + \int_0^l \int_{\partial S} \hat{p} n_x ds dx + \int_0^l f dx, \tag{2.8}$$

where ∂S is the boundary of a section S and n_x is the x component of the surface normal. The viscous term in Eq. (2.8) can be simplified by applying the divergence theorem and assuming uniform cross-sectional pressure and the tube being axisymmetric [Sherwin *et al.*, 2003a], which leads to

$$\int_0^l \int_{\partial S} \hat{p} n_x ds dx = \int_0^l p \frac{\partial A}{\partial x} dx. \tag{2.9}$$

By combining the above information we get

$$\frac{d}{dt}\int_0^l \rho Q dx + (\alpha\rho QU)_l - (\alpha\rho QU)_0 = (pA)_0 - (pA)_l + \int_0^l p\frac{\partial A}{\partial x}dx + \int_0^l f dx, \quad (2.10)$$

which can be rearranged as

$$\rho\int_0^l \left(\frac{\partial Q}{\partial t} + \frac{\partial(\alpha QU)}{\partial x}\right)dx = \int_0^l \left(-\frac{\partial(pA)}{\partial x} + p\frac{\partial A}{\partial x} + f\right)dx. \quad (2.11)$$

Additionally, by applying the partial derivative to the first term on the right hand side of Eq. (2.11),

$$\frac{\partial(pA)}{\partial x} = p\frac{\partial A}{\partial x} + A\frac{\partial p}{\partial x}. \quad (2.12)$$

Hence, the second term on the right hand side of Eq. (2.11) is cancelled out. Once again the interval (0,l) is arbitrary and our derivation will hold for any $l \in \mathbb{R}$. Thus, we can simplify Eq. (2.11) to

$$\frac{\partial Q}{\partial t} + \frac{\partial(\alpha QU)}{\partial x} + \frac{A}{\rho}\frac{\partial p}{\partial x} = \frac{f}{\rho}. \quad (2.13)$$

We can write Eq. (2.13) in terms of variables (A,U),

$$\frac{\partial(AU)}{\partial t} + \frac{\partial(\alpha AU^2)}{\partial x} + \frac{A}{\rho}\frac{\partial p}{\partial x} = \frac{f}{\rho}, \quad (2.14)$$

which is rearranged

$$U\left\{\frac{\partial A}{\partial t} + \frac{\partial(UA)}{\partial x}\right\} + (\alpha-1)U\frac{\partial(UA)}{\partial x} + A\left\{\frac{\partial U}{\partial t} + \alpha U\frac{\partial U}{\partial x}\right\} = -\frac{A}{\rho}\frac{\partial p}{\partial x} + \frac{f}{\rho}. \quad (2.15)$$

We note that the first bracketed expression is equal to the mass conservation

equations (Eq. (2.4)), hence rearranged we get

$$\frac{\partial U}{\partial t} + (2\alpha - 1)U\frac{\partial U}{\partial x} + (\alpha - 1)\frac{U^2}{A}\frac{\partial A}{\partial x} + \frac{1}{\rho}\frac{\partial p}{\partial x} = \frac{f}{\rho A}. \tag{2.16}$$

Following Brook *et al.* [1999] we neglect the convective inertia terms $(2\alpha - 2)U\frac{\partial U}{\partial x}$ and $(\alpha - 1)\frac{U^2}{A}\frac{\partial A}{\partial x}$. The convective inertia terms account for the fact that the velocity profile is not flat. These terms are much smaller than the rest of the terms in the momentum equation, especially in large arteries where the velocity profile is close to flat under normal physiological conditions, and hence, α is close to 1 [Caro *et al.*, 2011]. In more peripheral arteries the velocity profile becomes more parabolic ($\alpha = \frac{4}{3}$), and hence this assumption is less applicable. Hence, Eq. (2.16) is reduced to

$$\frac{\partial U}{\partial t} + U\frac{\partial U}{\partial x} + \frac{1}{\rho}\frac{\partial p}{\partial x} = \frac{f}{\rho A}. \tag{2.17}$$

The viscous term f is derived by integrating the incompressible 3-D Navier-Stokes equations [Smith *et al.*, 2002],

$$f = 2\mu\frac{A}{R}\left[\frac{\partial U}{\partial r}\right]_R, \tag{2.18}$$

where μ is the viscosity of the blood which we assume to be constant and equal to $4{\cdot}10^{-3} Pa \cdot s$. If we were to consider an inviscid fluid then we would set $f = 0$. In this work we assume a velocity profile adopted by Smith *et al.* [2002] which is of the form

$$\hat{u}(x, \sigma, t) = \frac{\gamma + 2}{\gamma}U\left[1 - \left(\frac{r}{R}\right)^{\gamma}\right], \tag{2.19}$$

where r is the radial component and γ is a constant for a particular flow profile.

Equation (2.19) defines a blunt axial velocity profile characteristic of oscillatory flow. Substituting Eq. (2.19) into Eq. (2.7) yields

$$\gamma = \frac{2-\alpha}{\alpha-1}. \tag{2.20}$$

Therefore, Eq. (2.19) can be expressed with respect to α as

$$\hat{u} = \frac{\alpha}{2-\alpha} U \left[1 - \left(\frac{r}{R}\right)^{\frac{2-\alpha}{\alpha-1}}\right]. \tag{2.21}$$

In this thesis $\gamma = 9$ ($\alpha = 1.1$) as a compromise fit to experimental data obtained at different points of the cardiac cycle [Smith *et al.*, 2002]. Substituting Eq. (2.21) into Eq. (2.18) yields

$$f = -22\mu\pi U. \tag{2.22}$$

2.1.4 Pressure-Area Relationship

To close the system of equations it is necessary to develop a relationship between pressure (p) and area (A). There are various tube law models that have been used in the literature: linear pressure-area models [Raines *et al.*, 1974], nonlinear pressure-area models [Čanić & Kim, 2003; Formaggia *et al.*, 2003; Olufsen, 1999; Payne, 2004; Sheng *et al.*, 1995; Sherwin *et al.*, 2003b; Smith *et al.*, 2002; Stergiopulos *et al.*, 1992; Urquiza *et al.*, 2006; Wan *et al.*, 2002] and nonlinear viscoelastic models accounting for the viscoelasticity of the vessel wall [Alastruey *et al.*, 2011; Formaggia *et al.*, 2003; Kitawaki & Shimizu, 2006; Reuderink *et al.*, 1989; Reymond *et al.*, 2011]. In Sections 2.1.4.1 and 2.1.4.2 an elastic and viscoelastic tube law model is introduced using a linear constitutive law resulting in a nonlinear

pressure-area relationship.

We present two different tube laws within this chapter, a nonlinear elastic tube law (used in Chapter 5) and a nonlinear visco-elastic tube law (used in Chapters 3 and 4). A viscoelastic tube law reduces the high frequency oscillations seen in a purely elastic tube laws; thus a better approximates human pressure and flow waveforms [Alastruey *et al.*, 2011]. However this benefit must be weighed against the added complexity when estimating additional parameters. Reymond *et al.* [2009] have shown the importance of using a viscoelastic term when simulating the cerebral circulation, hence why it is used in Chapters 3 and 4. The theory developed in Chapter 5 currently only extends to an elastic tube law.

2.1.4.1 Non-Linear Elastic Tube Law

We consider a cylindrical vessel with internal radius R_i and external radius R_e, and length l (as seen in Fig. 2.2). Wall thickness, h, is defined as $h = R_e - R_i$. There are two opposing forces: the force due to the circumferential stress, hlT_θ, and the force due to the intraluminal pressure, P_i, which acts against the external pressure, P_e. Since the sum of these two forces must be balanced, we get,

$$T_\theta = \frac{P_i R_i - P_e R_e}{h}. \tag{2.23}$$

In this work, we take the arterial vessel wall to be thin, thus $R_e \approx R_i$, and

$$T_\theta = \frac{(P_i - P_e) R_i}{h}. \tag{2.24}$$

To calculate the longitudinal stress T_x, we consider the forces in Fig. 2.2. The

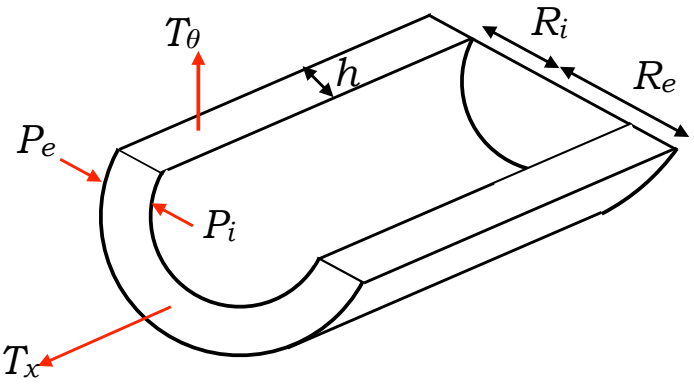

Figure 2.2: Relationship between vessel wall dimensions and stresses. The dimensions include inner radius R_i, external radius R_e, and wall thickness h. The stresses include circumferential stress T_θ, longitudinal stress T_z, intraluminal pressure P_i, and external pressure P_e.

stress T_x acts longitudinally and has a resultant force equal to $2\pi R_i h$, the internal pressure is a force equal to $(P_e - P_i)\pi R_i^2$. Hence the longitudinal stress, assuming the vessel wall is thin is

$$T_x = \frac{(P_e - P_i)R_i}{2h}. \tag{2.25}$$

Comparing Eqs. (2.24) and (2.25) we see that $2T_x = T_\theta$.

Poisson's ratio, ν, is the ratio between the strain in the circumferential direction to that in the longitudinal direction. Since the arterial wall is isotropic we set ν to be constant [Weizsacker & Pinto, 1988].

The blood vessel is composed of elastin and collagen fibres, which leads to a nonlinear stress-strain curve. At low strain levels there is a purely elastic response, but as the strain increases more collagen fibres are activated, causing a rise in the stress-strain curve. It is assumed that radial stress is equal to zero. For linearly elastic material we assume the material obeys Hooke's law, where the

stress is related to the strain in both the longitudinal and circumferential direction through the Young's modulus, E. The resultant circumferential strain, ϵ_θ, takes the following form,

$$\epsilon_\theta = \frac{1}{E}(T_\theta - \nu T_x). \tag{2.26}$$

Similarly the resultant longitudinal strain, ϵ_x, is

$$\epsilon_x = \frac{1}{E}(T_x - \nu T_\theta). \tag{2.27}$$

If we stipulate that the elongation of the tube is zero; *i.e.* the vessel is tethered in the longitudinal direction ($\epsilon_x = 0$), then the circumferential strain becomes

$$\epsilon_\theta = \frac{1}{E}(T_\theta(1 - \nu^2)). \tag{2.28}$$

Since the circumferential strain is defined as $\epsilon_\theta = \frac{R-R_0}{R_0} = \frac{\sqrt{A}-\sqrt{A_0}}{\sqrt{A_0}}$, we get

$$\frac{1}{E}(T_\theta(1 - \nu^2)) = \frac{\sqrt{A} - \sqrt{A_0}}{\sqrt{A_0}}. \tag{2.29}$$

Substituting Eq. (2.29) into Eq. (2.23) yields

$$\frac{1}{E}\left(\frac{(P_i - P_e)R_i}{h}(1 - \nu^2)\right) = \frac{\sqrt{A} - \sqrt{A_0}}{\sqrt{A_0}}. \tag{2.30}$$

Rearranging and allowing for $A_0 = \pi R_i^2$ we get

$$P_i = P_e + \frac{\beta}{A_o}(\sqrt{A} - \sqrt{A_0}), \qquad \beta = \frac{\sqrt{\pi} h_0 E}{(1 - \nu^2)}. \tag{2.31}$$

2.1.4.2 Non-Linear Viscoelastic Tube Law

Arterial walls exhibit viscoelastic behaviour which can be modelled with different mathematical forms [McDonald, 1974]. Hasegawa & Kanai [2004]; Learoyd & Taylor [1966] have shown the elastic modulus of the artery increases with frequency. The Kelvin-Voigt model has been shown to well model the viscoelastic properties of the canine aorta, and human femoral and carotid arteries [Armentano *et al.*, 1995a,b; Bauer *et al.*, 1979]. The Kelvin model is the simplest viscoelastic model that captures effects of creep, stress relaxation, and storage of strain energy at equilibrium [Valdez-Jasso *et al.*, 2009]. The resultant viscoelastic tube law is

$$P_i = P_e + \frac{\beta}{A_0}(\sqrt{A} - \sqrt{A_0}) + \frac{\Gamma}{A_0\sqrt{A}}\frac{\partial A}{\partial t}, \qquad \Gamma = \frac{1}{(1-\nu^2)}\sqrt{\pi}\varphi h, \tag{2.32}$$

where φ is the viscosity of the vessel wall.

2.2 Characteristic System

We are able to reduce the 1-D governing equations to a family of ordinary differential equations (ODE) using the method of characteristics. This method is only applicable when we consider the tube law for a purely elastic material, as described in Section 2.1.4.1. Once this method is applied we can derive the solution of the partial differential equation (PDE) by integrating along the ODE, if we have initial data prescribed on the boundary.

With the tube law Eq. (2.31) the pressure gradient term in the momentum

Eq. (2.17) takes the form

$$\frac{1}{\rho}\frac{\partial p}{\partial x} = \frac{1}{\rho}\left(\frac{\partial p}{\partial A}\frac{\partial A}{\partial x} + \frac{\partial p}{\partial \beta}\frac{d\beta}{dx} + \frac{\partial p}{\partial A_0}\frac{dA_0}{dx}\right). \tag{2.33}$$

Equations (2.4) and (2.17) can be written in a quasi-linear matrix form as

$$\frac{\partial \mathbf{U}}{\partial t} + \mathbf{H}\frac{\partial \mathbf{U}}{\partial \mathbf{x}} + \mathbf{C} = \mathbf{0}, \tag{2.34}$$

where $\mathbf{U} = \begin{bmatrix} A \\ U \end{bmatrix}$, $\mathbf{H} = \begin{bmatrix} U & A \\ \frac{1}{\rho}\frac{\partial p}{\partial A} & U \end{bmatrix}$, $\mathbf{C} = \begin{bmatrix} 0 \\ -\frac{1}{\rho}\left(\frac{f}{A} - \frac{\partial p}{\partial \beta}\frac{d\beta}{dx} - \frac{\partial p}{\partial A_0}\frac{dA_0}{dx}\right) \end{bmatrix}$. Matrix $\mathbf{H}$ has two real, distinct eigenvalues,

$$\lambda_{f,b} = u \pm c, \tag{2.35}$$

where

$$c = \sqrt{\frac{A}{\rho}\frac{\partial p}{\partial A}}, \tag{2.36}$$

where c is the pulse wave speed of the system. For the purely elastic tube law given by Eq. (2.31), Eq. (2.36) provides the following relationship between the pulse wave speed and the elastic property of the vessel β,

$$c = \sqrt{\frac{\beta}{2\rho A_0}}A^{1/4}. \tag{2.37}$$

At the reference area, A_0, we obtain the reference pulse wave velocity, c_0, given by

$$c_0 = \sqrt{\frac{\beta\sqrt{A_0}}{2\rho}} = \sqrt{\frac{hE}{2\rho R_0(1-\nu^2)}}. \tag{2.38}$$

If $c \neq 0$ then the PDE is strictly hyperbolic and the associated eigenvectors span $\mathbf{R}$. Under physiological flow c, is always greater than u. Therefore we know that $\lambda_f > 0$ and $\lambda_b < 0$.

Additionally the matrix $\mathbf{H}$ is diagonalisable since there exists an invertible matrix $\mathbf{L}$ such that

$$\mathbf{H} = \mathbf{L}^{-1}\mathbf{\Lambda}\mathbf{L}, \tag{2.39}$$

where $\mathbf{L} = \zeta \begin{bmatrix} \frac{c}{A} & 1 \\ -\frac{c}{A} & 1 \end{bmatrix}$, $\mathbf{\Lambda} = \zeta \begin{bmatrix} \lambda_f & 0 \\ 0 & \lambda_b \end{bmatrix}$, and ζ is a scaling factor [Alastruey, 2006]. By substituting the diagonalised matrix Eq. (2.39) into Eq. (2.34),

$$\mathbf{L}\frac{\partial \mathbf{U}}{\partial \mathbf{t}} + \mathbf{\Lambda}\mathbf{L}\frac{\partial \mathbf{U}}{\partial \mathbf{x}} + \mathbf{L}\mathbf{C} = \mathbf{0} \tag{2.40}$$

With the change of variable

$$\frac{\partial \mathbf{W}}{\partial \mathbf{U}} = \mathbf{L}, \tag{2.41}$$

where $\mathbf{W}$=$[W_f, W_b]^T$ is the vector of characteristic variables, Eq. (2.40) reduces to

$$\frac{\partial \mathbf{W}}{\partial \mathbf{t}} + \Lambda\frac{\partial \mathbf{W}}{\partial \mathbf{x}} + \mathbf{L}\mathbf{C} = \mathbf{0} \tag{2.42}$$

We define $\hat{x}$ as a parametric function in the (x, t) space, hence $\mathbf{W}$ along the path $\hat{x}(t)$ is

$$\frac{d\mathbf{W}(\hat{\mathbf{x}}(\mathbf{t}), \mathbf{t})}{dt} = \frac{\partial \mathbf{W}}{\partial t} + \frac{d\hat{x}}{dt}\mathbf{I}\frac{\partial \mathbf{W}}{\partial \hat{\mathbf{x}}}. \tag{2.43}$$

Thus, if we take $\frac{d\hat{x}}{dt}\mathbf{I} = \mathbf{\Lambda}$, then

$$\frac{d\mathbf{W}}{dt} = -\mathbf{L}\mathbf{C} \tag{2.44}$$

along $\hat{x}(t)$. We note that if $f = 0$ and β and A_0 are constant along x then $\mathbf{C} = \mathbf{0}$, Which enables us to solve Eq. (2.42) component wise:

$$\frac{\partial W_f}{\partial t} + \lambda_f \frac{\partial W_f}{\partial x} = 0 \tag{2.45a}$$

$$\frac{\partial W_b}{\partial t} + \lambda_b \frac{\partial W_b}{\partial x} = 0 \tag{2.45b}$$

Integrating provides an expression for W_f and W_b

$$W_{f,b} = U - U_0 \pm \int_{A_0}^{A} \left(\frac{c}{A}\right) dA, \tag{2.46}$$

where U_0 and A_0 are reference values.

To satisfy the Cauchy-Riemann condition $\frac{\partial^2 W_{f,b}}{\partial A \partial U} = \frac{\partial^2 W_{f,b}}{\partial U \partial A}$, the value of ζ in Eq. (2.39) must be constant. This thesis takes $\zeta = 1$. Characteristic variables are invariant (constant) along the characteristic curves, which are defined as $(t, Y_f(t))$ and $(t, Y_b(t))$ where,

$$\frac{dY_f}{dt} = \lambda_f, \tag{2.47}$$

$$\frac{dY_b}{dt} = \lambda_b. \tag{2.48}$$

2.3 Linearised 1-D Equations

Since the 1-D blood flow equations are only weakly nonlinear, it is possible to capture many characteristics of blood flow with the linearised system [Sherwin *et al.*, 2003a]. If we consider the viscoelastic tube law model and the mass and momentum equations (Eqs. (2.4), (2.14) and (2.32)) and linearise about the dias-

tolic conditions $(A, P, P_e, Q) = (A_d, 0, 0, 0)$, with β, A_d and Γ constant along x, yields [Alastruey *et al.*, 2012b]

$$\begin{aligned} C_{1-D}\frac{\partial p_e}{\partial t} + \frac{\partial q}{\partial x} &= 0, \\ L_{1-D}\frac{\partial q}{\partial t} + \frac{\partial p_e}{\partial x} - \gamma\frac{\partial^2 q}{\partial x^2} &= -R_{1-D}q, \\ p = p_e - \gamma\frac{\partial q}{\partial x}, \quad p_e = \frac{a}{C_{1-D}}, \quad \gamma &= \frac{\Gamma}{A_0^{3/2}}, \end{aligned}$$

where a, p, p_e and q are the perturbation variables for area, pressure, the elastic component of pressure, and flow rate, respectively. Additionally, per unit length of vessel,

$$C_{1-D} = \frac{2A_0^{3/2}}{\beta}, L_{1-D} = \frac{\rho}{A_0}, R_{1-D} = \frac{22\pi\mu}{A_0^2} \tag{2.49}$$

are the wall compliance, flow inertia, and resistance to blood flow due to blood viscosity, respectively.

2.4 Lumped Parameter Models

In this section we will describe the two lumped parameter (0-D) models used in this thesis: the classical two-element Windkessel (Section 2.4.1) and the three-element Windkessel (Section 2.4.2).

2.4.1 Two-Element Windkessel Model

Windkessel theory was first developed by Stephen Hales in 1733, then later advanced by Otto Frank in 1899 [Frank, 1899; Shi *et al.*, 2011] to explain how the pulsatile motion of blood from the heart is transformed to a continuous steady

flow at the peripheral blood vessels.

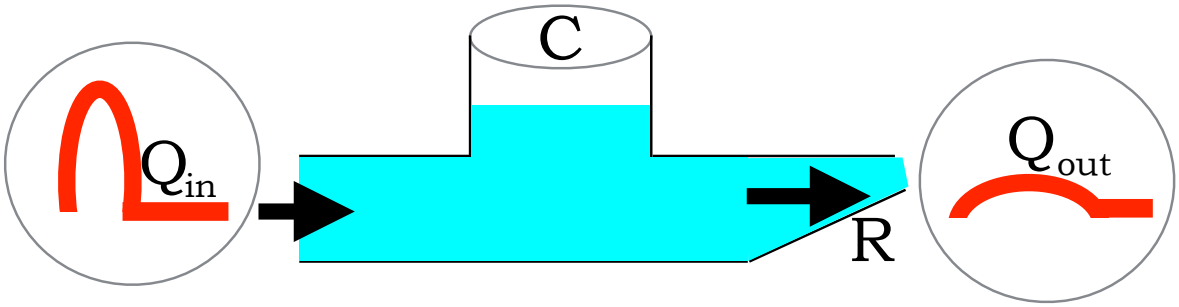

Figure 2.3: The two-element Windkessel model sketched in hydraulic form, with compliance, C, and resistance to blood flow, R.

We consider a Windkessel chamber filled at the inlet by a pulsatile flow of blood, Q_{in}, and with an outflow, Q_{out}, and resistance to flow, R at the outlet, as shown in Fig. 2.3. The compliance, C, of the elastic Windkessel chamber with blood volume, $V(t)$, and blood pressure, $P(t)$, is defined as

$$C = \frac{dV}{dP}. \tag{2.50}$$

The rate of change of volume is

$$\frac{dV}{dt} = \left(\frac{dV}{dP}\right)\frac{dP}{dt} = C\frac{dP}{dt}. \tag{2.51}$$

If we have a perfect system with no fluid losses, we can say that the rate of storage must be equal to the difference in inflow and outflow. Thus,

$$Q_{in}(t) - \frac{P - P_v}{R} = C\frac{dP}{dt}, \tag{2.52}$$

where P_v and R are the pressure and resistance of the peripheral vasculature,

respectively. Equation (2.52) has a solution of the form

$$P - P_v = (P_0 - P_v)e^{\frac{-t}{RC}} + \frac{1}{C}e^{\frac{-t}{RC}} \int_0^t Q_{in}(t')e^{\frac{t'}{RC}}dt', \tag{2.53}$$

where $P_0 = P(t = 0)$.

During diastole when $Q_{in} = 0$,

$$P - P_v = (P_0 - P_v)e^{\frac{-t}{RC}}. \tag{2.54}$$

Hence, during diastole when there is no inflow we see an exponential drop off in the pressure waveform. It is noted that the two-element Windkessel at high frequency pressure perturbations has an unrealistic flow response. Additionally, the model is not applicable to the arterial system as a whole since pressure waves are of different shapes and amplitude at different sites [McDonald, 1974].

2.4.2 Three-element Windkessel Model

The three-element Windkessel model (seen in Fig. 2.4) adds a resistive element to the two-element Windkessel model described in Section 2.4.1. The additional resistive term between the pump and the air chamber simulates resistance to blood flow to minimise oscillations in the blood pressure. The resultant 0-D equations are

$$\left(1 + \frac{R_1}{R_2}\right) Q(t) + CR_1\frac{dQ}{dt} = \frac{P(t) - P_v}{R_2} + C\frac{dP(t)}{dt}, \tag{2.55}$$

where the resistance R_1 is given by the characteristic impedance $Z_0 = \frac{\rho c_0}{A_0}$ in order to minimise wave reflections, the compliance C represents the change in vessel volume for a given pressure change, and R_2 represents the peripheral resistance.

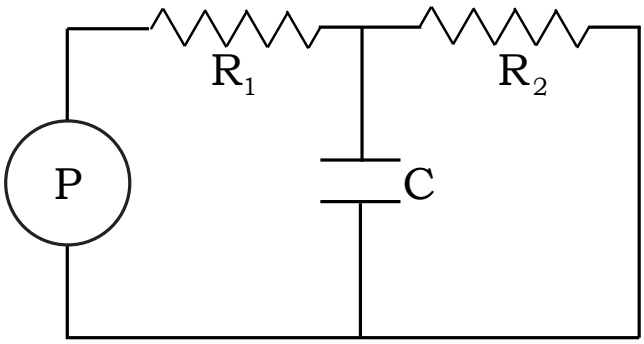

Figure 2.4: Representation of the electric circuit analogous to the three-element RCR Windkessel model.

The three-element Windkessel model is governed by a set of simultaneous ordinary differential equations. It will be used within this thesis as a boundary condition to our 1-D model to simulate blood flow in the peripheral vasculature.

2.5 1-D/0-D Model of Blood Flow in the Arterial Network

The arterial network has a tree like structure, with the heart at the root pumping blood into the system. At the periphery (leaves), we have the vascular bed, which can be simulated as a fractal-like asymmetric network of small arteries and arterioles [Taylor, 1966]. In order to simulate the arterial system, it is necessary to join the 1-D model arterial segments together to create a network. This is achieved by enforcing physical conditions at each boundary and junction, taking into account the forward- and backward-travelling characteristic wavefronts derived in Section 2.2.

In this section, first a description of how two or three segments of vessels are joined is given in Section 2.5.1. To this arterial model it is necessary to prescribe boundary conditions; both at the inlet and outlet of the model to simulate the heart and the peripheral vascular beds, respectively. Inlet and outlet boundary conditions are described in Section 2.5.2.

2.5.1 Vessel Junctions

At a bifurcation of a parent vessel into two daughter vessels it is necessary to resolve the characteristic variables at the given boundary (as shown in Fig. 2.5). We consider (A_1,P_1,U_1), (A_2,P_2,U_2) and (A_3,P_3,U_3) as the initial states of vessels 1 (parent), 2 and 3 (daughters), respectively at $t = t_n$. If we assume inviscid flow the system can be described in terms of forward and backward characteristic variables as

$$W_f(A_1^u, U_1^u) = W_f(A_1, U_1), \tag{2.56}$$

$$W_b(A_2^u, U_2^u) = W_b(A_2, U_2), \tag{2.57}$$

$$W_b(A_3^u, U_3^u) = W_b(A_3, U_3), \tag{2.58}$$

where W_f and W_b were defined in Section 2.2. Applying conservation of mass to the upwinded area and flow velocity variables (denoted by the superscript u), we have

$$A_1^u U_1^u = A_2^u U_2^u + A_3^u U_3^u. \tag{2.59}$$

Finally, applying Bernoulli's law (*i.e.* continuity of the sum of static and dynamic

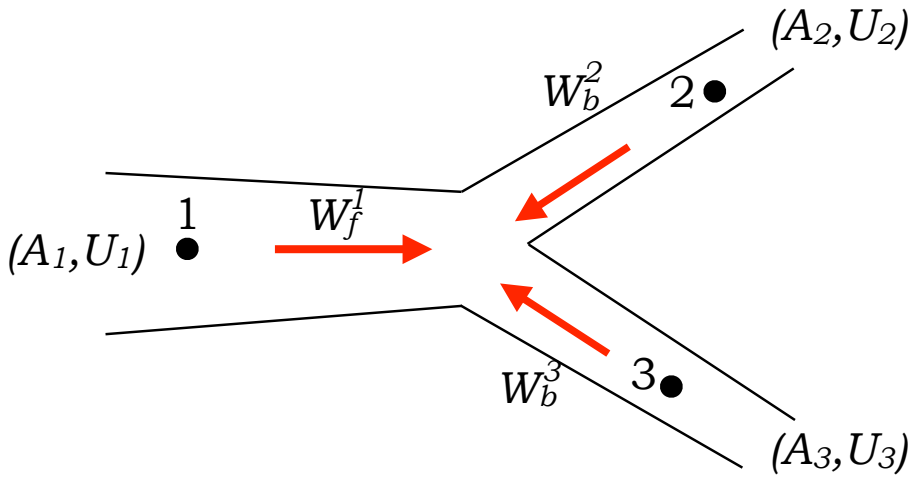

Figure 2.5: Layout of an arterial bifurcation.

pressures) we get [Alastruey *et al.*, 2012a]

$$P(A_1^u) + \frac{1}{2}\rho(U_1^u)^2 = P(A_2^u) + \frac{1}{2}\rho(U_2^u)^2, \tag{2.60}$$

$$P(A_1^u) + \frac{1}{2}\rho(U_1^u)^2 = P(A_3^u) + \frac{1}{2}\rho(U_3^u)^2. \tag{2.61}$$

The resulting nonlinear system of 6 equations (Eqs. (2.56) to (2.61)) are resolved using the Newton-Raphson method [Alastruey, 2006]. From this, the upwind flux at the junction is determined. Within this work the branching angle is neglected since experimental studies have suggested that the effect of the branch angle on the reflections at junctions is small [Westerhof *et al.*, 1969]. Trifurcations and merging flow are treated in a similar manner. I direct the reader to the work of Alastruey [2006] for a more thorough overview.

2.5.2 Inlet/Outlet Boundary Conditions

At the inlet and outlets of the arterial network it is necessary to enforce boundary conditions. It is assumed that the prescribed inlet to our model is located at the heart. It is possible to model the outflow from the heart using a lumped parameter model of the left ventricle [Mynard & Nithiarasu, 2008], the aortic valve [Matthys *et al.*, 2007; Sherwin *et al.*, 2003a], or the entire heart [Formaggia *et al.*, 2006; Reymond *et al.*, 2009].

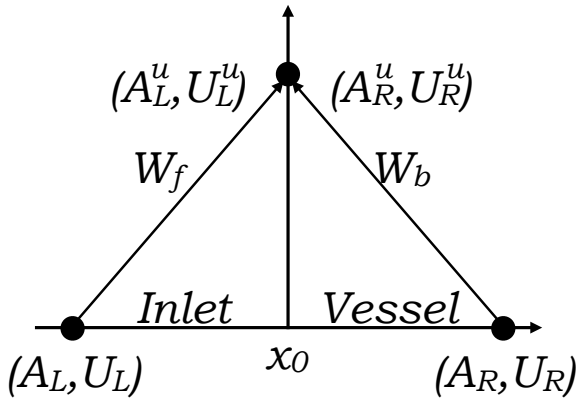

Figure 2.6: Layout of the Riemann problem at the inlet boundary to calculate the upwinded states. (A_L,U_L) represents the current variables in the dummy left hand region. (A_R,U_R) represents the initial state in the vessel region. (A_L^u,U_L^u) and (A_R^u,U_R^u) are the Riemann upwind variables. W_f and W_b are the forward and backward characteristic variables given by Eq. (2.46).

Within this work, a flow waveform ($Q_{bc} = A^u U^u$) is prescribed at the inlet of the ascending aorta. This type of inflow boundary condition has been widely used in the literature [Alastruey, 2006; Willemet *et al.*, 2015]. We consider the layout in Fig. 2.6 and assume the right side of the interface to be the 1-D model segment of the ascending aorta, and the left hand side to be the virtual inlet region. We further assume that $A_L = A_R$ and from the characteristic analysis in Section 2.2

we also have

$$W_f(A_L, U_L) = W_f(A_L^u, U_L^u), \tag{2.62}$$

and

$$W_b(A_R, U_R) = W_b(A_R^u, U_R^u). \tag{2.63}$$

A $W_f(A_L^u, U_L^u)$ is prescribed at each time step so that when combined with $W_b(A_R^u, U_R^u)$ leads to the desired flow boundary condition, $Q_{bc} = A^u U^u$.

At the outlet of our 1-D model we represent the downstream vasculature with a 0-D lumped parameter model. It is possible to model the peripheral vasculature bed using structured-tree outflow models [Olufsen, 1999], pure resistor conditions [Anliker *et al.*, 1971; Stettler *et al.*, 1981], or prescribe a pressure or flow rate [Brook & Pedley, 2002; Li & Cheng, 1993; Parker & Jones, 1990; Qureshi *et al.*, 2014; Wan *et al.*, 2002]. In this work we use the three-element Windkessel model described in Section 2.4.2. The three-element Windkessel model has been found to be a good fit to experimental data for the peripheral vasculature [Westerhof *et al.*, 2009]. This Windkessel model is coupled to each 1-D terminal segment by solving a first-order time discretisation of the conservation of mass in the capacitance [Alastruey, 2006].

2.6 Numerical Solution of the 1-D Equations

It is possible to solve the 1-D blood flow equations derived in Sections 2.1.2 to 2.1.4 using different numerical schemes. These include schemes based on the method of characteristics [Acosta *et al.*, 2015; Anliker *et al.*, 1971; Schaaf & Abbrecht., 1972; Wang & Parker, 2004], finite volumes [Montecinos *et al.*, 2014; Müller & Toro,

2013], finite differences [Azer & Peskin, 2007; Huo & Kassab, 2007; Liang *et al.*, 2009; Olufsen, 1999], and finite element methods [Blanco *et al.*, 2014; Formaggia *et al.*, 2003; Huberts *et al.*, 2012a; Mynard & Nithiarasu, 2008; Sherwin *et al.*, 2003a; Willemet *et al.*, 2013; Xiao *et al.*, 2013]. A comparison of these methods has shown a good agreement in their ability to capture the main features of pressure, flow and area waveforms in large arteries [Boileau *et al.*, 2015]. Within this work we use a finite element discontinuous Galerkin scheme with a spectral/hp spatial discretisation. To advance in time we use an explicit second-order Adams-Bashforth scheme. This method is appropriate to the equations derived in Sections 2.1.2 to 2.1.4 because it can propagate waves of varying frequencies without the drawback of excessive dispersion and diffusion errors [Karniadakis & Sherwin, 2013].

2.7 Concluding Remarks

This Chapter has detailed the mathematical formulation used within this Thesis to simulate blood flow in the arterial system. In Chapter 3 a local sensitivity analysis will be applied to a 1-D/0-D model of the full arterial network, focusing on the effect of cardiovascular properties on the computed DVP wave at the finger. Chapter 4 will use the 1-D formulation to investigate whether the shape of the PPG waveform measured in the finger could be used to distinguish among subjects with hypertension and diabetes. In Chapter 5, a novel methodology is described to optimise the number of arterial segments for 1-D/0-D modelling.

Chapter 3

A 1-D Model of Systemic Arterial Blood Flow: Validation and Sensitivity Analysis

Mathematical and numerical models are useful in expanding our understanding of cardiovascular function. As we discussed in Chapter 2, one-dimensional (1-D) blood flow models are well adapted at capturing arterial pulse wave propagation in the systemic vasculature.

In recent years, coupled 1-D/0-D models of the full arterial network [Blanco & Feijóo, 2013; Karamanoglu *et al.*, 1994; Olufsen *et al.*, 2000; Reymond *et al.*, 2009] and truncated network [Bode *et al.*, 2012; Huberts *et al.*, 2012a; Karamanoglu *et al.*, 1993; Leguy *et al.*, 2010; Watanabe *et al.*, 2013] have been developed. As well as considering healthy states, models under pathological conditions have also been developed, e.g. coronary disease [Blanco & Watanabe, 2015; Steele *et al.*, 2003; Willemet *et al.*, 2013] and hypertension [Reymond *et al.*, 2012]. The agreement

of these arterial models have been compared against *in vitro* [Alastruey *et al.*, 2005; Bessems *et al.*, 2008; Matthys *et al.*, 2007] and *in vivo* [Reymond *et al.*, 2011; Willemet *et al.*, 2013] measurements. These studies have shown that 1-D/0-D models offer good accuracy with considerably less computational cost than equivalent 3-D models [Mynard & Nithiarasu, 2008; Xiao *et al.*, 2013].

The first aim of this chapter is to produce a 120-vessel, nonlinear, visco-elastic 1-D/0-D model of pulse wave propagation in the larger arteries of the systemic circulation. The model will include the arteries of the head and hand, where the PPG pulse wave can be measured *in vivo*. This is the baseline model that will form the basis of the research carried out in Chapters 3 to 5 of this thesis. This baseline model will be qualitatively validated by comparing the shape of predicted blood pressure, flow and PPG waves at several arterial sites with that of corresponding *in vivo* waves from the literature. Computed luminal area waveforms at the digital artery in the finger will be compared against *in vivo* PPG waveforms under the assumption that the dynamic area waveform is analogous to the PPG wave at this site [Avolio, 2002]. The baseline model is described and qualitatively validated in Section 3.1.

The second aim of this chapter is to perform a local sensitivity analysis of the predicted 1-D model pulse waveforms to the model parameters. A local sensitivity analysis allows us to study the influence of input parameters of the model on pressure, flow and area waveforms when only one input parameter is varied at a time around an initial state [Ellwein *et al.*, 2008; Leguy *et al.*, 2010; Pope *et al.*, 2009; Willemet *et al.*, 2013]. The conclusions derived from a local sensitivity analysis are dependent on the initial state of the model, and do not account for the interactions between input variables. A global sensitivity analysis considers

the effect of each input parameter within the entire input space of parameters [Huberts *et al.*, 2013; Leguy *et al.*, 2011; Xiu & Sherwin, 2007].

Within this chapter we first present a local sensitivity analysis in order to analyse how changes of arterial stiffness, arterial cross-sectional diameter, peripheral resistance, and Windkessel outflow pressure change the shape of the measured PPG signal at the digital artery in the hand within a healthy population. We will vary input parameters of the model across a physiological range of values taken from the literature. This analysis is presented in Section 3.2. We then carry out a local sensitivity analysis of the PPG signal to the shape of the inflow waveform at the ascending aorta (Section 3.3). In the 1-D/0-D model, the inflow waveform at the ascending aorta is prescribed as the inlet boundary condition of the model. It is noted that in the literature the heart can be modelled using a lumped parameter model [Beyar *et al.*, 1987; Blanco & Feijóo, 2013; Blanco *et al.*, 2012a; Formaggia *et al.*, 2006; Guala *et al.*, 2015b; Mynard & Nithiarasu, 2008; Mynard & Smolich, 2015; Reymond *et al.*, 2009; Ursino, 1998]. Within this last section we will look at how changes of the prescribed inflow waveform at the ascending aorta propagate to the digital artery and affect the shape of the DVP signal.

3.1 Baseline 1-D Model of Systemic Arterial Blood Flow

The baseline 1-D model created in this thesis contains 120 arterial segments representing the larger arteries of the systemic circulation, including the vasculatures of the hand and head (Fig. 3.1). The nonlinear 1-D equations of an incompress-

ible fluid in a compliant and impermeable viscoelastic vessel network are solved in each arterial segment. At the inlet to our model (the aortic root) we prescribe the inflow waveform generated by cardiac contraction. At the periphery of each terminal vessel we couple a 3-element Windkessel model to simulate the peripheral vasculature (see Chapter 2).

Reymond *et al.* [2009] hypothesise that the cerebral circulation is necessary to obtain an accurate pressure and flow prediction at the carotid artery. It is for this reason that we have included the vasculature of the head within this work. The geometry of the hands taken from Epstein *et al.* [2015] has been added to the baseline model from Reymond *et al.* [2009]. The model from Reymond *et al.* [2009] is largely based on the work of Noordergraaf *et al.* [1963] and Westerhof *et al.* [1969], where the major systemic arteries were calculated for a subject with a height of 175cm and mass of 75kg. Unlike Reymond *et al.* [2009], we do not model the coronary tree as its inclusion is not necessitated by the aims of this thesis.

The model includes the circle of Willis, which is a ring like arterial structure within the head that supplies blood to the brain and surrounding structures. Many anatomical variations of the Circle of Willis exist. In this work we assume a complete arterial structure, which based on 150 MR angiograms accounts for 42% of the population [Krabbe-Hartkamp *et al.*, 1998].

Existing 1-D arterial models tend to be of younger patients; *e.g.* Reymond *et al.* [2011]- 30 years old, Mynard & Smolich [2015]- 20 to 30 years old, Guala *et al.* [2015b] 24 years old, Leguy [2010]- average 27 years old, Blanco *et al.* [2014] <30 years old, Leguy *et al.* [2010]- 21 to 34 years old. Notably Willemet *et al.* [2013] created numerical model for patients 72.7 $\pm$11.1 years old (mean $\pm$ SD),

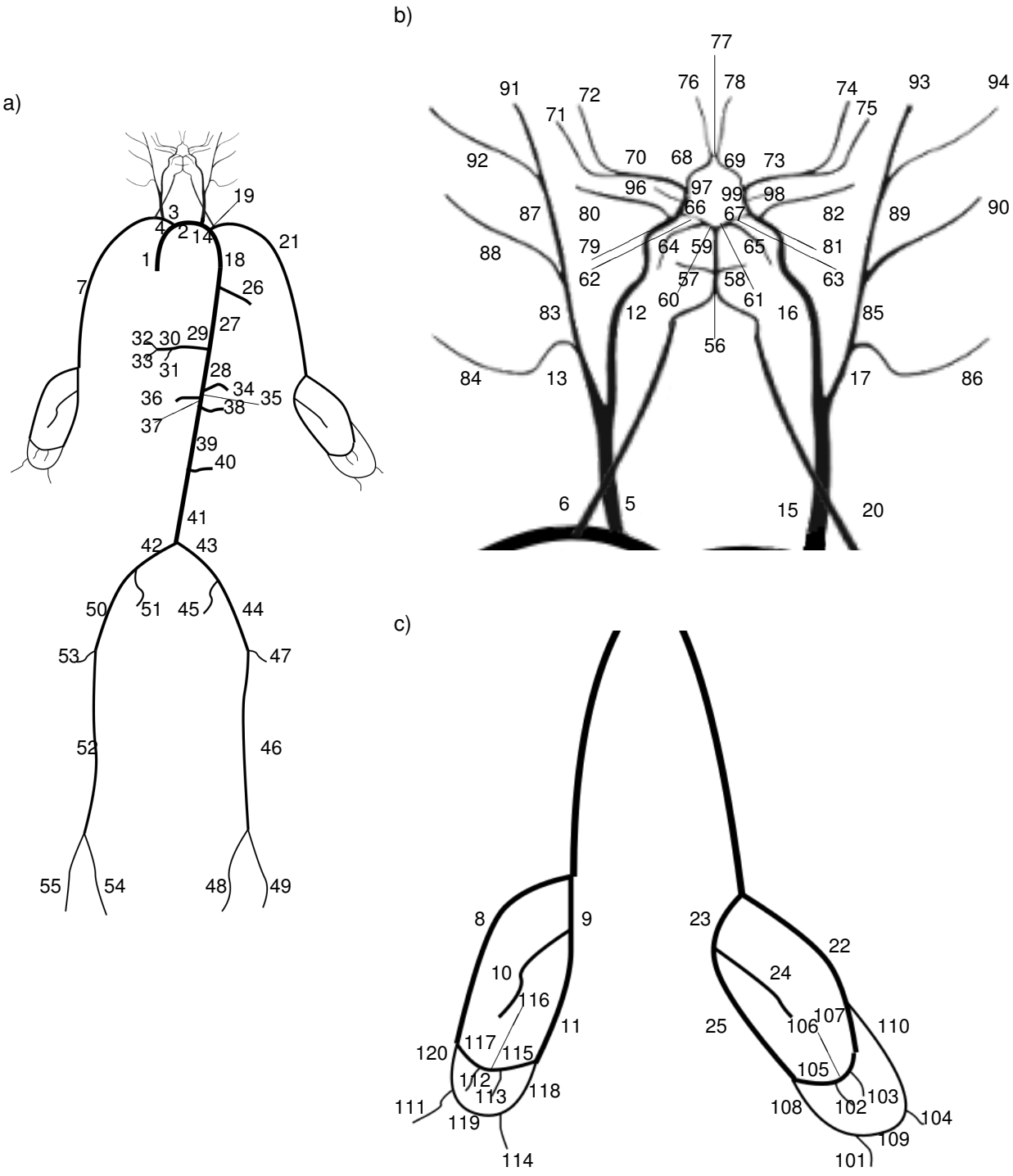

Figure 3.1: Schematic representation of the arterial tree. a) Main systemic arterial tree based on Reymond *et al.* [2009]. b) Detailed cerebral arterial tree also taken from Reymond *et al.* [2009]. c) Detail of the hand vasculature taken from Epstein *et al.* [2015].

and Caroli *et al.* [2013] simulated patients with a mean age 62 ± 16 years.

Several studies have investigated the role of ageing in numerical modelling. Previously Karamanoglu *et al.* [1995] aged their numerical model by adjusting the vascular stiffness, but maintaining all other parameters. Guala *et al.* [2015a] aged their numerical model by increasing the diameter, thickness and length of the aorta, the stiffness of the carotid, maximum elastance function of the heart, and the time of systole. The work of Liang *et al.* [2009] looked at ageing a closed-loop arterial model from 25 years to 85 years. In their study they increased the aortic stiffness, aortic radius, peripheral artery stiffness, peripheral resistance, and the left ventricular active elastance. Willemet *et al.* [2015] have created a fictive population that covers physiological features of patients aged < 30 to 70 years old by varying the elastic and muscular artery stiffness, elastic and muscular diameter, heart rate, stroke volume and peripheral resistance.

The 1-D systemic arterial network presented here (Fig. 3.1) is based on the studies cited above and incorporates several adjustments to match haemodynamic data from the literature, as described in the list below. We have adjusted the geometric and material properties of our model to better fit a middle aged patient (40-60 years). Where applicable we have included the mean age of the patients used within each reference study. To simplify the problem, arterial segments were divided into two subsets: 'elastic vessels' (vessels 1, 2, 5, 12, 13, 14, 15, 16, 17 18, 27, 28, 35, 37, 39, 41, 42 and 43 in Fig. 3.1) and 'muscular vessels' (all remaining segments). The following parameters were adjusted.

- **Aortic (elastic) diameter** scaled by 1.2042 to match the measured cross-sectional area at diastole based on data from Eren *et al.* [2004] (mean age

50 years).

- **Carotid diameter** scaled by 0.85 to ensure positive flow throughout the cardiac cycle [Mynard & Smolich, 2015].

- **Muscular diameter** scaled by 1.21 so that the pulse pressure better matched the data from Bella *et al.* [2001]; Lacy *et al.* [2004b]; Mitchell *et al.* [2003]; Tedesco *et al.* [2004] (i.e. 5333-7466 Pa) (mean ages 58, 54.5, 60, and 55 years).

- **Arterial stiffness**. In order to satisfy both the pulse pressure and carotid-femoral pulse wave velocity (PWV) taken from the literature it was necessary to iteratively change the global stiffness and the aortic stiffness concurrently. The aortic stiffness was scaled by 1.7, and the stiffness everywhere else by 0.94. Pulse pressure ranges from 5333-7466 Pa at baseline conditions [Bella *et al.*, 2001; Lacy *et al.*, 2004b; Mitchell *et al.*, 2003; Tedesco *et al.*, 2004] and carotid-femoral PWV between 7.7-9.4 m s^{-1} [Lacy *et al.*, 2004b; Mitchell *et al.*, 2003; Tedesco *et al.*, 2004].

- **Peripheral resistance** scaled by 0.655 so that the mean pressure corresponded to the measured mean pressure by Mitchell *et al.* [2003]; Tedesco *et al.* [2004] (*i.e.* 12.1-12.5 kPa).

- **Inflow** scaled by 0.9519 so that the mean flow rate matched the mean flow rate for a similar aged person of 106.76 $ml\ s^{-1}$ as found in de Simone *et al.* [1997] (age 33 years).

- **Outlet Windkessel** taken to be equal to the capillary pressure of 2.3 kPa measured in Fegan *et al.* [2003] (mean age 61 years).

The work of Bessems *et al.* [2008] has shown that wall viscoelasticity is necessary to model the attenuation of pressure and flow waves. Including a viscous term to the tube law enhances peripheral pressure and flow wave damping [Segers *et al.*, 1997]. Limited data are available on the viscoelastic properties of the artery. Here, for the largest 55 arteries of our arterial model the viscous modulus (Γ) is taken from Alastruey *et al.* [2012b]. For the remaining arterial segments in our model the wall viscous modulus values (Γ) are extrapolated from the existing data from arteries of similar sized radii. The nonlinear Voigt-type viscoelastic constitutive law for the arterial wall (see Section 2.1.4.2) is utilised to avoid high-frequency oscillations as obtained by a purely elastic tube law [Matthys *et al.*, 2007].

The 1-D model network was discretised into finite elements of 2 cm. Elements shorter than 2 cm were merged to the previous elements. A polynomial and quadrature order of 2 were applied everywhere apart from vessels 1, 95, 2, 14, 18, 27, 28, 35, 37, 39, 41, 42 and 43 (see Fig. 3.1), where an order of 3 was used to minimise numerical oscillations. Vessels 80 and 82 (left and right ophthalmic arteries) were a source of non-physical oscillations during elastic and visco-elastic simulations, this problem is sometimes seen when solving Taylor-Galerkin numerical schemes with a large discontinuity between two boundary edges [Formaggia *et al.*, 2003]. We were able to solve this problem by decreasing the time step of the solver, by increasing the length of the ophthalmic vessels to 2cm, and by increasing their cross-sectional area to 1.5mm and 1.3mm at the inlet and outlet of these vessels, respectively. A 2cm element size allows us to use quadrature rules and polynomial functions of order 3 combined with a time step of 0.1ms. To maintain the same time step for shorter elements, a quadrature and polynomial order of 2 were often required.

All model parameters are presented in Tables 3.1 to 3.4. The prescribed inflow waveform is shown in Fig. 3.2 A.

3.1.1 Qualitative Model Validation

Pressure and flow measurements in the main arterial segments (ascending aortic arch, left common carotid, right radial, left brachial, thoracic aorta, abdominal aorta, left external iliac artery) and PPG waveforms in the left digital artery are shown in Fig. 3.2. Figure 3.2 also includes typical pressure and flow waveforms taken from the literature.

Comparison of our simulated pressure and flow waveforms with published recorded data shows a good overall agreement in shape and amplitude at the compared sites. The model is able to well reproduce the main features of physiological pressure and flow waveforms in the large systemic arteries, and the PPG waveform at the digital artery in healthy patients. The model captures the following features seen from central to peripheral pressure waveforms found in clinical measurements by Kroeker & Wood [1955]: i, a gradual increase in pulse pressure and the systolic peak towards the periphery, ii, a systolic shoulder present in the aortic pressure waveform (A) but barely visible in the femoral waveform (G), and iii a dicrotic notch which is drawn out and deep in the brachial (D)/radial (C) waves, and is not visible in the femoral wave (G). There is a good agreement between the measured and predicted carotid (B) flow and pressure waveforms, with a similar notch in early diastole. At the radial (C) and brachial (D) sites, the period of backwards flow during early systole is slightly larger than in *in vivo* measurements. Flow waveforms at the thoracic (E) and abdominal aorta (F) well replicate *in vivo* data.

At the iliac artery the model is able to capture a period of backflow during early diastole, a known feature at this site [Reymond, 2011].

This study aimed to improve on the existing model used by Reymond *et al.* [2009] to include the vasculature of the hands and an alternative viscoelastic tube law. The inclusion of the hands to our 1-D numerical model will allow us to analyse the PPG signal at the digital artery, a common measurement site in clinical studies. It is necessary to include the cerebral circulation to well simulate the pressure and flow waveforms at the common and internal carotid artery [Blanco & Watanabe, 2015; Reymond, 2011].

There is a weak agreement in the shape of measured and predicted temporal flow waveforms. An unphysiological notch is present in early diastole which is not present to such a degree in the literature waveforms. This oscillation may be due to the viscosity parameter of the cerebral circulation being extrapolated from other similar sized vessels, which may not be an adequate assumption in this case. Due to the poor agreement of this waveform, we will not utilise the temporal artery to study PPG waveforms.

We further improved the model by altering the input parameters so the output parameters matched haemodynamic values from the literature for a given normotensive population of patients of age 50-60 years. Our model was then compared against literature waveforms of pressure and flow and PPG at the digital artery in healthy volunteers from the literature. We conclude that the 1-D/0-D model created in this section well reproduces the wave characteristics at the measured locations shown in Fig. 3.2, except for the PPG wave at the temporal artery.

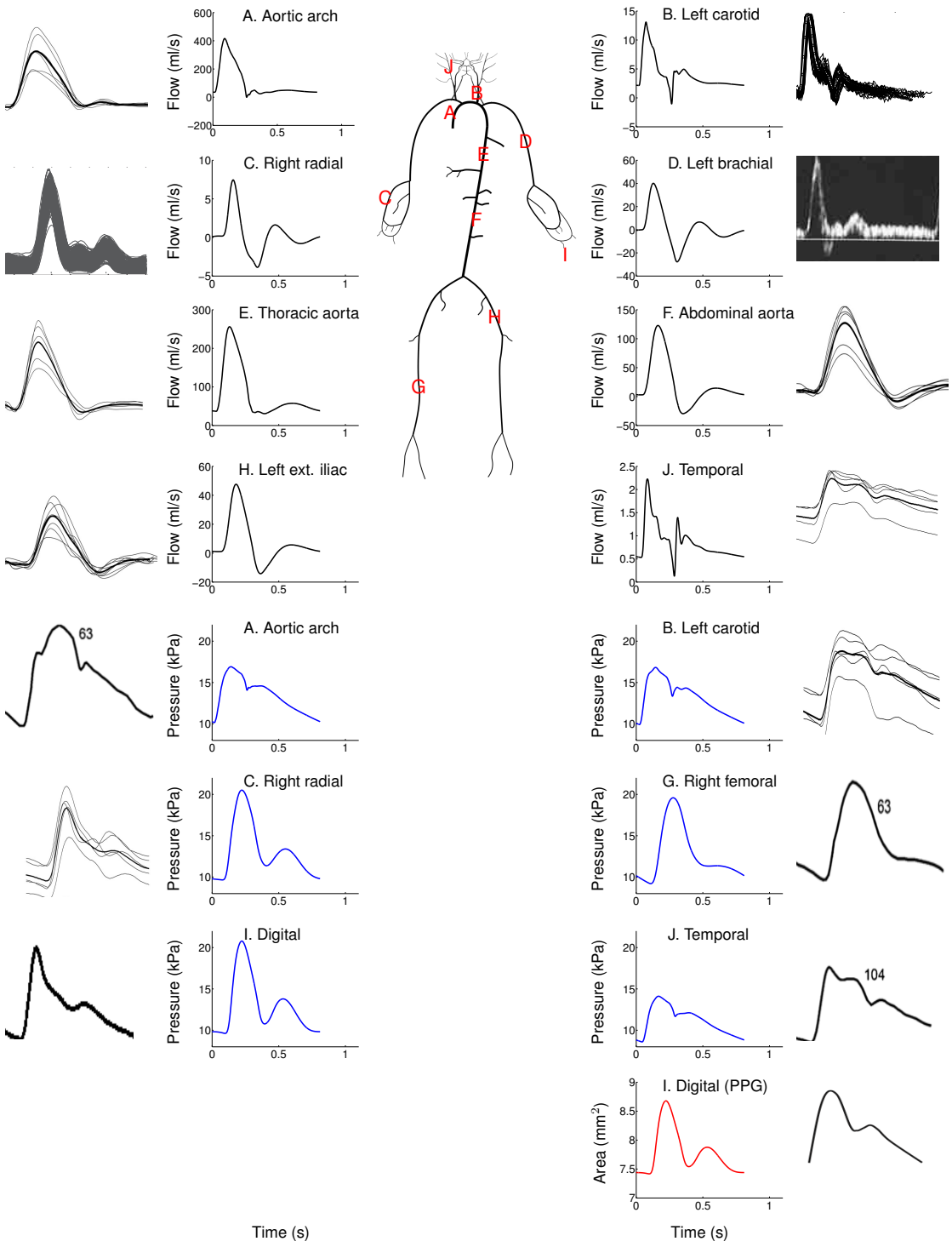

Figure 3.2: (first four rows) Numerical blood pressure (blue), flow (black) and area (red) waveforms in the (A) aortic arch, (B) left common carotid, (C) right radial, (D) left brachial, (E) thoracic aorta, (F) abdominal aorta, (G) right femoral, (H) left external iliac, (I) left digital artery, (J) temporal arteries. The first and last columns show non-dimensionalised *in vivo* waveforms measured at approximately the same locations as the corresponding numerical waveforms. *In vivo* waveforms were taken from Reymond *et al.* Reymond *et al.* [2009] for the aortic arch (flow), thoracic aorta, abdominal aorta, femoral (flow) and external iliac arteries; Holdsworth & Norley [1999] for the common carotid artery; Oseli *et al.* [2003] for the radial artery; Oates [2001] for the brachial artery; Millasseau *et al.* [2000] for the digital pressure; Mynard & Smolich [2015] for the aortic arch (pressure), the right femoral (pressure), and the right temporal (pressure); and Dawber *et al.* [1973] for the PPG signal (Class I).

Table 3.1: Parameters of the arterial tree (part I). $R_{in} \rightarrow R_{out}$: diastolic cross-sectional radii at the inlet and outlet of the arterial segment. $c_{in} \rightarrow c_{out}$: wave speed at the inlet and outlet of the arterial segment. $\Gamma_{in} \rightarrow \Gamma_{out}$: wall viscosity parameter at the inlet and outlet of the arterial segment. The characteristic impedance is given in brackets in 'Peripheral resistance'.

Vessel Name	Arterial segment	Length (cm)	$R_{in} \rightarrow R_{out}$ (mm)	$c_{in} \rightarrow c_{out}$ (m/s)	$\Gamma_{in} \rightarrow \Gamma_{out}$ (MPa s m^{-2})	Arterial compliance (10^{-10} m^3 Pa^{-1})	Arterial resistance (10^{10} Pa s m^{-3})	Peripheral resistance (10^{10} Pa s m^{-3})	Peripheral compliance (10^{-10} m^3 Pa^{-1})
Ascending Aorta 1	1	4	15.7 → 15.4	6.86 → 6.91	0.00149 → 0.00152	6.098	1.92e-06	-	-
Aortic arch A	2	2	13.6 → 13	7.24 → 7.35	0.00174 → 0.00182	1.984	1.806e-06	-	-
Brachiocepha	3	3.4	8.42 → 7.73	3.66 → 3.85	0.00431 → 0.00484	4.723	2.25e-05	-	-
Subclavian A.R	4	3.4	5.41 → 4.4	4.61 → 5.06	0.00757 → 0.00967	1.068	0.0001691	-	-
Common Carotid R	5	9.4	3.9 → 2.16	5.32 → 6.7	0.0555 → 0.107	0.806	0.00405	-	-
Vertebral R	6	14.9	1.98 → 1.53	6.91 → 7.59	0.141 → 0.187	0.268	0.04604	-	-
Subclavian R	7	42.2	4.02 → 2.47	5.26 → 6.37	0.0269 → 0.0463	4.288	0.01273	-	-
Radial R	8	23.5	1.98 → 1.68	6.91 → 7.34	0.141 → 0.168	0.470	0.05935	-	-
Ulnar A R	9	6.7	1.98 → 1.84	6.91 → 7.11	0.141 → 0.154	0.149	0.01416	-	-
Interosseous R	10	7.9	1.17 → 1.01	8.34 → 8.77	0.249 → 0.29	0.04	0.1606	5.534 (0.2574)	0.033
Ulnar B R	11	17.1	1.73 → 1.53	7.26 → 7.59	0.163 → 0.187	0.249	0.06818	-	-
I. Carotid R	12	17.8	1.79 → 1.37	7.18 → 7.89	0.132 → 0.174	0.239	0.08469	-	-
Ex Carotid 1 R	13	4.1	1.58 → 1.43	7.51 → 7.77	0.15 → 0.167	0.048	0.02246	-	-
Aortic arch B	14	3.9	11.7 → 11.4	7.63 → 7.7	0.00204 → 0.0021	2.635	6.202e-06	-	-
Common Carotid L	15	13.9	3.51 → 1.87	5.55 → 7.06	0.0625 → 0.125	0.867	0.009951	-	-
I. Carotid L	16	17.8	1.67 → 1.31	7.36 → 8.01	0.141 → 0.183	0.204	0.1058	-	-
Ex Carotid 1 L	17	4.1	1.49 → 1.37	7.66 → 7.89	0.159 → 0.174	0.042	0.02746	-	-
Thorac. aor. A	18	5.2	11 → 10.4	7.8 → 7.95	0.00219 → 0.00231	2.858	1.125e-05	-	-
Subclavian A.L	19	3.4	5.21 → 4.19	4.69 → 5.16	0.00791 → 0.0102	0.946	0.0002011	-	-
Vertebral L	20	14.8	1.98 → 1.53	6.91 → 7.59	0.141 → 0.187	0.266	0.04573	-	-
Subclavian L	21	42.2	4.02 → 2.47	5.26 → 6.37	0.0269 → 0.0463	4.288	0.01273	-	-
Radial L	22	23.5	1.89 → 1.53	7.05 → 7.59	0.149 → 0.187	0.389	0.07996	-	-
Ulnar A L	23	6.7	2.28 → 2.28	6.57 → 6.57	0.121 → 0.121	0.241	0.006952	-	-
Interosseous L	24	7.9	1.01 → 1.01	8.77 → 8.77	0.29 → 0.29	0.03	0.214	5.534 (0.2574)	0.033
Ulnar B L	25	17.1	2.18 → 1.98	6.68 → 6.91	0.127 → 0.141	0.482	0.0256	-	-
Intercostal	26	8	5.83 → 4.61	4.45 → 4.95	0.00345 → 0.00458	3.03	0.0003134	0.09168 (0.005611)	2.003
Thorac aorta B	27	10.4	9.14 → 7.23	8.31 → 9	0.00265 → 0.00339	2.828	6.787e-05	-	-
Abdominal Aor. A	28	5.3	6.85 → 6.85	9.17 → 9.17	0.00358 → 0.00358	0.886	6.73e-05	-	-
Celiac A	29	2	3.89 → 3.49	5.33 → 5.57	0.00558 → 0.00631	0.275	0.0003043	-	-
Celiac B	30	2	2.71 → 2.57	6.15 → 6.28	0.00837 → 0.00888	0.108	0.001157	-	-
Hepatic	31	6.6	2.8 → 2.33	6.07 → 6.52	0.0403 → 0.0495	0.33	0.004374	0.2384 (0.03295)	0.7669
Gastric	32	7.1	1.73 → 1.63	7.26 → 7.42	0.163 → 0.174	0.11	0.02479	0.3554 (0.07951)	0.5146
Splenic	33	6.3	2.23 → 2.08	6.62 → 6.79	0.124 → 0.134	0.20	0.008176	0.1519 (0.04349)	1.2
Superior Mes	34	5.9	3.93 → 3.58	5.3 → 5.51	0.011 → 0.0123	0.85	0.0008369	0.06112 (0.01096)	2.993

Table 3.2: Parameters of the arterial tree (part II). $R_{in} \rightarrow R_{out}$: diastolic cross-sectional radii at the inlet and outlet of the arterial segment. $c_{in} \rightarrow c_{out}$: wave speed at the inlet and outlet of the arterial segment. $\Gamma_{in} \rightarrow \Gamma_{out}$: wall viscosity parameter at the inlet and outlet of the arterial segment. The characteristic impedance is given in brackets in 'Peripheral resistance'.

Vessel Name	Arterial segment	Length (cm)	$R_{in} \rightarrow R_{out}$ (mm)	$c_{in} \rightarrow c_{out}$ (m/s)	$\Gamma_{in} \rightarrow \Gamma_{out}$ (MPa s m^{-2})	Arterial compliance (10^{-10} m^3 Pa^{-1})	Arterial resistance (10^{10} Pa s m^{-3})	Peripheral resistance (10^{10} Pa s m^{-3})	Peripheral compliance (10^{-10} m^3 Pa^{-1})
Abd. Aorta B	35	2	6.48 → 6.37	9.34 → 9.39	0.0038 → 0.00387	0.281	3.294e-05	-	-
Renal L	36	3.2	2.71 → 2.71	6.15 → 6.15	0.0418 → 0.0418	0.19	0.001662	0.07422 (0.02244)	2.463
Abd. Aorta C	37	2	6.64 → 6.64	9.26 → 9.26	0.00371 → 0.00371	0.307	2.885e-05	-	-
Renal R	38	3.2	2.71 → 2.71	6.15 → 6.15	0.0418 → 0.0418	0.19	0.001662	0.07422 (0.02244)	2.463
Abd.Aorta D	39	10.6	6.53 → 6.21	9.32 → 9.48	0.00377 → 0.00398	1.458	0.0001809	-	-
Inf Mesen	40	5	2.47 → 1.73	6.37 → 7.26	0.0463 → 0.068	0.15	0.007775	0.4514 (0.06854)	0.4046
Abd aorta	41	2	6.1 → 5.88	9.53 → 9.65	0.00405 → 0.0042	0.234	4.358e-05	-	-
Common Ilia R	42	5.9	4.51 → 4.01	10.5 → 10.9	0.0111 → 0.0125	0.279	0.0005066	-	-
Common Ilia L	43	5.9	4.51 → 4.01	10.5 → 10.9	0.0111 → 0.0125	0.279	0.0005066	-	-
Externa Iliac R	44	14.4	3.26 → 3.13	5.72 → 5.82	0.034 → 0.0357	1.323	0.003869	-	-
Inner Iliac R	45	5	2.13 → 2.13	6.73 → 6.73	0.131 → 0.131	0.15	0.006767	0.5212 (0.04103)	0.3508
Femoral R	46	44.3	2.71 → 2.03	6.15 → 6.85	0.1 → 0.137	1.815	0.04176	-	-
Deep Femoral R	47	12.6	2.13 → 1.98	6.73 → 6.91	0.131 → 0.141	0.34	0.01972	0.3135 (0.04908)	0.5836
Post tibial R	48	32.1	1.68 → 1.53	7.34 → 7.59	0.168 → 0.187	0.45	0.1355	0.3135 (0.09318)	0.5836
Ante tibial R	49	34.3	1.43 → 1.27	7.78 → 8.1	0.201 → 0.227	0.30	0.292	0.3667 (0.1465)	0.498
Externa Iliac L	50	14.4	3.26 → 3.13	5.72 → 5.82	0.034 → 0.0357	1.323	0.003869	-	-
Inner Iliac L	51	5	2.13 → 2.13	6.73 → 6.73	0.131 → 0.131	0.15	0.006767	0.5212 (0.04103)	0.3508
Femoral L	52	44.3	2.71 → 2.03	6.15 → 6.85	0.1 → 0.137	1.815	0.04176	-	-
Deep Fermoral L	53	12.6	2.13 → 1.98	6.73 → 6.91	0.131 → 0.141	0.34	0.01972	0.3135 (0.04908)	0.5836
Post tibial L	54	32.1	1.68 → 1.53	7.34 → 7.59	0.168 → 0.187	0.45	0.1355	0.3135 (0.09318)	0.5836
Ante tibial L	55	34.3	1.43 → 1.27	7.78 → 8.1	0.201 → 0.227	0.30	0.292	0.3667 (0.1465)	0.498
Basilar arte	56	2	2.13 → 1.94	6.73 → 6.98	0.131 → 0.145	0.053	0.003287	-	-
Super Cere R	57	1	0.955 → 0.793	8.93 → 9.51	0.307 → 0.373	0.00	0.04881	1.753 (0.4589)	0.0027
Super Cere L	58	1	0.955 → 0.793	8.93 → 9.51	0.307 → 0.373	0.00	0.04881	1.753 (0.4589)	0.0027
Basilar art 1	59	0.5	1.68 → 1.48	7.34 → 7.68	0.168 → 0.193	0.007	0.002253	-	-
Post cereb 1 R	60	0.2	1.06 → 1.06	8.62 → 8.62	0.275 → 0.275	0.001	0.004409	-	-
Post cereb 1 L	61	0.2	1.06 → 1.06	8.62 → 8.62	0.275 → 0.275	0.001	0.004409	-	-
Post commun R	62	0.4	0.684 → 0.684	9.99 → 9.99	0.435 → 0.435	0.001	0.05129	-	-
Post commun L	63	0.4	0.684 → 0.684	9.99 → 9.99	0.435 → 0.435	0.001	0.05129	-	-
Post cereb 2 R	64	5.9	1.11 → 1.01	8.48 → 8.77	0.261 → 0.29	0.03	0.1311	0.7029 (0.2574)	0.00435
Post cereb 2 L	65	5.9	1.11 → 1.01	8.48 → 8.77	0.261 → 0.29	0.03	0.1311	0.7029 (0.2574)	0.00435
ICA dist R	66	0.2	2.08 → 2.03	6.79 → 6.85	0.134 → 0.137	0.005	0.0003117	-	-
ICA dist L	67	0.2	2.08 → 2.03	6.79 → 6.85	0.134 → 0.137	0.005	0.0003117	-	-

Table 3.3: Parameters of the arterial tree (part III). $R_{in} \rightarrow R_{out}$: diastolic cross-sectional radii at the inlet and outlet of the arterial segment. $c_{in} \rightarrow c_{out}$: wave speed at the inlet and outlet of the arterial segment. $\Gamma_{in} \rightarrow \Gamma_{out}$: wall viscosity parameter at the inlet and outlet of the arterial segment. The characteristic impedance is given in brackets in 'Peripheral resistance'.

Vessel Name	Arterial segment	Length (cm)	$R_{in} \rightarrow R_{out}$ (mm)	$c_{in} \rightarrow c_{out}$ (m/s)	$\Gamma_{in} \rightarrow \Gamma_{out}$ (MPa s m^{-2})	Arterial compliance (10^{-10} m^3 Pa^{-1})	Arterial resistance (10^{10} Pa s m^{-3})	Peripheral resistance (10^{10} Pa s m^{-3})	Peripheral compliance (10^{-10} m^3 Pa^{-1})
Ant cerebral1 R	68	1.2	1.17 → 1.11	8.34 → 8.48	0.249 → 0.261	0.007	0.01984	-	-
Ant cerebral1 L	69	1.2	1.17 → 1.11	8.34 → 8.48	0.249 → 0.261	0.007	0.01984	-	-
Middle cere1 R	70	0.8	1.63 → 1.53	7.42 → 7.59	0.174 → 0.187	0.011	0.003581	-	-
MCA M2 sup R	71	7.1	1.11 → 0.573	8.48 → 10.6	0.261 → 0.522	0.02	0.5374	0.6566 (0.5909)	0.0021
MCA M2 inf R	72	7	1.11 → 0.573	8.48 → 10.6	0.261 → 0.522	0.02	0.5305	0.6566 (0.5909)	0.0021
Middle cere2 L	73	0.8	1.63 → 1.53	7.42 → 7.59	0.174 → 0.187	0.011	0.003581	-	-
MCA M2 sup L	74	7.1	1.11 → 0.573	8.48 → 10.6	0.261 → 0.522	0.02	0.5374	0.6566 (0.5909)	0.0021
MCA M2 inf L	75	7	1.11 → 0.573	8.48 → 10.6	0.261 → 0.522	0.02	0.5305	0.6566 (0.5909)	0.0021
Ant cereb A2 R	76	2.4	1.01 → 0.955	8.77 → 8.93	0.29 → 0.307	0.01	0.0725	0.7029 (0.2936)	0.003525
Ant commu	77	0.2	0.738 → 0.738	9.74 → 9.74	0.402 → 0.402	0.000	0.01884	-	-
Ant cereb A2 L	78	2.4	1.01 → 0.955	8.77 → 8.93	0.29 → 0.307	0.01	0.0725	0.7029 (0.2936)	0.003525
Int car sinus R	79	1.1	2.28 → 2.08	6.57 → 6.79	0.121 → 0.134	0.035	0.001365	-	-
Ophthalmic R	80	2	0.847 → 0.738	9.3 → 9.74	0.348 → 0.402	0.00	0.1435	1.753 (0.5442)	0.0003
Int car sinus L	81	1.1	2.28 → 2.08	6.57 → 6.79	0.121 → 0.134	0.035	0.001365	-	-
Ophthalmic L	82	2	0.847 → 0.738	9.3 → 9.74	0.348 → 0.402	0.00	0.1435	1.753 (0.5442)	0.0003
Exter. caro. 2 R	83	6.1	2.13 → 1.89	6.73 → 7.05	0.131 → 0.149	0.156	0.01061	-	-
Sup. thy. R	84	10.1	1.11 → 0.573	8.48 → 10.6	0.261 → 0.522	0.03	0.7843	1.97 (0.9949)	0.004425
Exter. caro. 2 L	85	6.1	2.13 → 1.89	6.73 → 7.05	0.131 → 0.149	0.156	0.01061	-	-
Sup. thy. L	86	10.1	1.11 → 0.573	8.48 → 10.6	0.261 → 0.522	0.03	0.7843	1.97 (0.9949)	0.004425
Super. tem. R	87	6.1	1.73 → 1.63	7.26 → 7.42	0.163 → 0.174	0.096	0.0213	-	-
Maxillary R	88	9.1	1.22 → 0.573	8.22 → 10.6	0.237 → 0.522	0.03	0.5995	1.641 (0.9949)	0.00375
Super. tem. L	89	6.1	1.73 → 1.63	7.26 → 7.42	0.163 → 0.174	0.096	0.0213	-	-
Maxillary L	90	9.1	1.22 → 0.573	8.22 → 10.6	0.237 → 0.522	0.03	0.5995	1.641 (0.9949)	0.00375
Superfi. R	91	10	1.22 → 0.793	8.22 → 9.51	0.237 → 0.373	0.04	0.3156	1.641 (0.4589)	0.00615
Superfi. pari.R	92	10.1	1.22 → 0.793	8.22 → 9.51	0.237 → 0.373	0.04	0.3188	1.641 (0.4589)	0.0057
Superfi. L	93	10	1.22 → 0.793	8.22 → 9.51	0.237 → 0.373	0.04	0.3156	1.641 (0.4589)	0.00615
Superfi. pari. L	94	10.1	1.22 → 0.793	8.22 → 9.51	0.237 → 0.373	0.04	0.3188	1.641 (0.4589)	0.0057
Acend. aorta 2	95	3.5	15.6 → 15.4	6.87 → 6.91	0.00149 → 0.00152	5.312	1.691e-06	-	-
Ant. choroid R	96	3.6	0.847 → 0.738	9.3 → 9.74	0.348 → 0.402	0.01	0.2588	1.313 (0.5442)	0.01155

Table 3.4: Parameters of the arterial tree (part IV). $R_{in} \rightarrow R_{out}$: diastolic cross-sectional radii at the inlet and outlet of the arterial segment. $c_{in} \rightarrow c_{out}$: wave speed at the inlet and outlet of the arterial segment. $\Gamma_{in} \rightarrow \Gamma_{out}$: wall viscosity parameter at the inlet and outlet of the arterial segment. The characteristic impedance is given in brackets in 'Peripheral resistance'.

Vessel Name	Arterial segment	Length (cm)	$R_{in} \rightarrow R_{out}$ (mm)	$c_{in} \rightarrow c_{out}$ (m/s)	$\Gamma_{in} \rightarrow \Gamma_{out}$ (MPa s m^{-2})	Arterial compliance (10^{-10} m^3 Pa^{-1})	Arterial resistance (10^{10} Pa s m^{-3})	Peripheral resistance (10^{10} Pa s m^{-3})	Peripheral compliance (10^{-10} m^3 Pa^{-1})
ICA distal R	97	0.2	2.03 → 2.03	6.85 → 6.85	0.137 → 0.137	0.005	0.000327	-	-
Ant. choroid L	98	3.6	0.847 → 0.738	9.3 → 9.74	0.348 → 0.402	0.01	0.2588	1.313 (0.5442)	0.01155
ICA distal L	99	0.2	2.03 → 2.03	6.85 → 6.85	0.137 → 0.137	0.005	0.000327	-	-
	100	0.1	1.94 → 1.94	6.98 → 6.98	0.145 → 0.145	0.002	0.0001997	-	-
Dig I L	101	2.5	1.43 → 1.43	7.78 → 7.78	0.201 → 0.201	0.03	0.01682	3.36 (0.1105)	0.159
Dig II L	102	3	1.49 → 1.49	7.66 → 7.66	0.192 → 0.192	0.03	0.01704	3.072 (0.09961)	0.174
Dig III L	103	3	1.45 → 1.45	7.74 → 7.74	0.198 → 0.198	0.03	0.01906	3.281 (0.1067)	0.163
Dig IV L	104	1.5	1.04 → 1.04	8.68 → 8.68	0.281 → 0.281	0.01	0.03586	6.549 (0.2387)	0.081
SPA I L	105	1	1.83 → 1.83	7.13 → 7.13	0.155 → 0.155	0.020	0.002523	-	-
SPA II L	106	1	1.26 → 1.26	8.12 → 8.12	0.229 → 0.229	0.007	0.01104	-	-
SPA III L	107	1	1.74 → 1.74	7.25 → 7.25	0.162 → 0.162	0.017	0.003022	-	-
DPA I L	108	3	1.43 → 1.43	7.78 → 7.78	0.201 → 0.201	0.030	0.02019	-	-
DPA II L	109	3	0.847 → 0.847	9.3 → 9.3	0.348 → 0.348	0.007	0.1631	-	-
DPA III L	110	3	1.04 → 1.04	8.68 → 8.68	0.281 → 0.281	0.013	0.07172	-	-
Dig I R	111	2.5	1.43 → 1.43	7.78 → 7.78	0.201 → 0.201	0.03	0.01682	3.36 (0.1105)	0.159
Dig II R	112	3	1.49 → 1.49	7.66 → 7.66	0.192 → 0.192	0.03	0.01704	3.072 (0.09961)	0.174
Dig III R	113	3	1.45 → 1.45	7.74 → 7.74	0.198 → 0.198	0.03	0.01906	3.281 (0.1067)	0.163
Dig IV R	114	1.5	1.04 → 1.04	8.68 → 8.68	0.281 → 0.281	0.01	0.03586	6.549 (0.2387)	0.081
SPA I R	115	1	1.83 → 1.83	7.13 → 7.13	0.155 → 0.155	0.020	0.002523	-	-
SPA II R	116	1	1.26 → 1.26	8.12 → 8.12	0.229 → 0.229	0.007	0.01104	-	-
SPA III R	117	1	1.74 → 1.74	7.25 → 7.25	0.162 → 0.162	0.017	0.003022	-	-
DPA I R	118	3	1.43 → 1.43	7.78 → 7.78	0.201 → 0.201	0.030	0.02019	-	-
DPA II R	119	3	0.847 → 0.847	9.3 → 9.3	0.348 → 0.348	0.007	0.1631	-	-
DPA III R	120	3	1.04 → 1.04	8.68 → 8.68	0.281 → 0.281	0.013	0.07172	-	-

3.2 Local Sensitivity Analysis

In order to better understand the 120-artery 1-D model produced in Section 3.1, we will investigate how variations in input parameters alter the pressure, velocity and cross-sectional area waveforms generated by the model. In particular, we will focus on how input parameters alter the shape of the digital pulse wave (DPV) at the digital artery in the hand.

Within this section, we will change the following input parameters: the peripheral Windkessel pressure and resistance, cross-sectional area of the elastic and muscular arteries, and the stiffness of the elastic and muscular arteries. The 6 parameters varied were chosen since they have been used in other sensitivity analysis for a normal healthy population. These parameters can all take a range of values under normal physiological conditions [Willemet *et al.*, 2015]. The work of Epstein *et al.* [2014]; Leguy *et al.* [2011]; Willemet *et al.* [2013] has shown that a change in arterial length and peripheral compliance has a very small change on arterial outputs. Thus, these two parameters will not be included in our sensitivity analysis.

According to the clinical literature, variations in arterial stiffness produce profound changes in the contour of the digital pulse wave (DPV). It has been hypothesised that the distinct two-peaked undulatory form of the DVP is due to pressure waves travelling from the left ventricle to the finger and later smaller reflections from internal mismatching, mainly in the lower body [Chowienczyk *et al.*, 1999]. But how other characteristics of the cardiovascular system interact at the digital artery remains relatively unknown.

Within this section we will first present the methodology of the sensitivity

analysis (Section 3.2.1) and then present the results of the analysis and discuss them in Sections 3.2.2 and 3.2.3, respectively.

3.2.1 Methods

The 120-artery model was used to study the effects on DVP of several physical properties of the system and investigate the role of wave reflections on the shape of the DVP contour. The DVP is simulated as the cross-sectional area waveform at the midlength point of the digital artery (Vessel 101) Fig. 3.1c.

We will first describe the changes in arterial (Section 3.2.1.1) and peripheral (Section 3.2.1.2) properties considered within this analysis. We will then describe the parameters that will be measured at the DVP to assess the effect of changes in these properties (Section 3.2.1.3).

3.2.1.1 Changes in Arterial Properties

We investigated the effects on the shape of the DVP of changes in peripheral resistances, Windkessel outflow pressure, elastic and muscular stiffness, and elastic and muscular cross-sectional diameter of the 120-artery model (Fig. Fig. 3.1 A) described above (hereinafter referred to as the *baseline model*). We considered the following six types of variations from the baseline model across a range of physiologically possible values.

- *Variation V1 – Changes in Windkessel outflow pressure*: The Windkessel pressure P_{out} was modified in all terminal Windkessel models by the same percentage, from -80% up to +100% of the baseline value): from 466.6 to 4666 Pa. Nine variations from the baseline model were considered. The

range of values chosen extends across measured capillary pressures in humans [McDonald, 1974; Parazynski *et al.*, 1993]. The baseline Windkessel pressure is 2333 Pa.

- *Variation V2 – Changes in peripheral resistance*: The resistance $R_1 + R_2$ was modified in all terminal Windkessel models by the same percentage, from -40% to 200% of the baseline value in order to simulate changes in net peripheral resistance from $5.22 \cdot 10^7$ to $2.61 \cdot 10^8$ Pa s m^{-3}. This range is based on the values reported in Jansen *et al.* [2001]. Twelve variations from the baseline model were considered. The baseline resistance is $8.71 \cdot 10^7$ Pa s m^{-3}.

- *Variation V3 – Changes in elastic vessel diameter*: The cross-sectional diameter of the elastic vessels was modified from -40% to 100% of the baseline values. At the aortic root, these percentages produce a range of diameters at diastolic pressures from 18.6 to 58.6 mm. Seven variations from the baseline model were considered. These variations covered the physiological range of cross-sectional areas measured at the aortic root by Roman *et al.* [1989]. The baseline diameter at the aortic root at diastolic pressure is 31.4 mm.

- *Variation V4 – Changes in muscular vessels diameter*: The cross-sectional diameter of the muscular vessels was modified from -60% to 60% of the baseline model. At the radial artery, this range equated to a diameter change from 1.6 to 5.8 mm, which corresponds to the physiological range of values measured by Yoo *et al.* [2005]. Eight variations from the baseline model were considered. The baseline diameter at the root of the radial artery at diastolic pressure is 3.8 mm.

- *Variation V5 – Changes in aortic stiffness*: The aortic stiffness was changed by -60% to +180% of the baseline values. A total of 12 variations from baseline values were considered. As a result, the carotid-femoral PWV changed from 5.4 to 9.1 m s^{-1}. This variation in carotid-femoral PWV corresponds to a physiologically possible range of values for a patient within the 30-50 year age range [The Reference Values for Arterial Stiffness' Collaboration, 2010].

- *Variation V6 – Changes in muscular stiffness*: The stiffness of the muscular vessels were changed by -40% to 180% of the baseline values. A total of 11 variations from baseline values were considered. As a result, local radial PWV changed from 5.2 to 13.2 m s^{-1}, where the baseline value was 7.1 m s^{-1}. The range of values for the radial PWV closely matches the range measured by Fulton & McSwiney [1930].

3.2.1.2 Changes in Peripheral Properties

We investigated the contribution to the baseline area waveform at the digital artery of wave reflections originating at the outlet of terminal branches, which we referred to as peripheral reflections. As described by Alastruey *et al.* [2009b], peripheral reflections can be eliminated from a terminal branch if the outflow three-element Windkessel model is replaced by a single resistance equal to the characteristic impedance at the outlet of the branch, so that any wave leaving the terminal branch is completely absorbed by the outlet. We applied completely absorbing boundary conditions to parts of the network. We divided the 120-artery network at the iliac bifurcation into two subsets: upper-body segments located above the iliac bifurcation and lower-body segments located below the iliac

bifurcation. We considered 4 combinations of the baseline Windkessel and the new absorbing boundary condition for the upper and lower body parts (Table 3.5)

Model	Upper Body	Lower Body
Baseline	Windkessel	Windkessel
P1	Absorbing	Absorbing
P2	Windkessel	Absorbing
P3	Absorbing	Windkessel

Table 3.5: Boundary conditions are either baseline RCR Windkessel or completely absorbing. The model is divided into upper- and lower-body arterial segments, as illustrated in Fig. 3.4a.

3.2.1.3 PPG Features

The DVP waveform is characterised by several distinct features. In Fig. 3.3 an example digital area waveform is annotated with the key features studied within this work. The features are as follows:

1) dT: Time between the first (systolic) and second (diastolic) peak of the DVP waveform. Timing is related to the time taken by the waveform to propagate from the heart to the periphery and back to the measurement site [Elgendi, 2012]. dT has been shown to be related to the central pulse pressure [Baruch *et al.*, 2014], and inversely related to a biomarker of arterial stiffness [Millasseau *et al.*, 2002a].

2) CT: Crest time. The time from the foot of the waveform until the first peak. Here we define the foot of the waveform to be the minimum of the waveform. Dillon & Hertzman [1941] showed that in patients with hypertension and arteriosclerosis the crest time is extended.

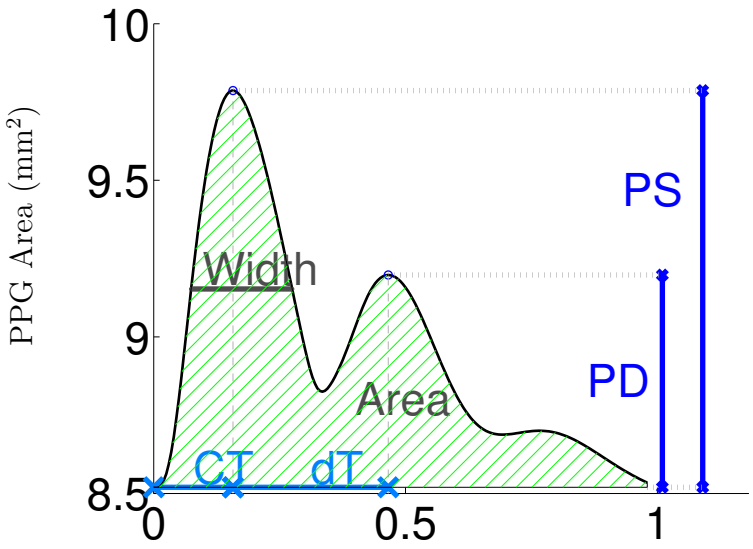

Figure 3.3: A typical cross-sectional area waveform at the digital artery and their characteristic parameters. dT= time between systolic and diastolic peaks; CT= crest time; Width= pulse width at half height of the systolic amplitude; PD= peak of diastole; PS= peak of systole. 'Area' is the hatched area in green.

3) *PS*: Pulse systole. The pulse amplitude between the minimum and maximum values of the DVP. It is an indicator of the pulsatile changes in blood volume by blood flow at the measurement site [Elgendi, 2012]. The work of Cannesson *et al.* [2007] has shown that is possible to predict fluid responsiveness in mechanically ventilated patients during general anaesthesia utilising this parameter.

4) *PD*: Pulse Diastole. The pulse amplitude of the second peak. Millasseau *et al.* [2002a] have shown that the pulse amplitude decreases with infusion of nitroglycerine in healthy subjects.

5) *Width*: The pulse width of the PPG waveform at half the height of the systolic amplitude. Awad *et al.* [2007] have shown that the width is sensitive to changes of systemic vascular resistance.

6) *Area*: The integrated area under the PPG waveform across one cardiac

cycle (limited by diastole). The work of McGrath *et al.* [2011a] has shown a high correlation between the area under the curve and ventricular stroke volume.

It is noted that additional parameters exist in the literature such as the stiffness index [Millasseau *et al.*, 2006], reflective index [Millasseau *et al.*, 2006], age index [Utami *et al.*, 2013], and further parameters extracted from the second derivative [Baek *et al.*, 2007; Elgendi, 2014; Takazawa *et al.*, 1998], but their application is not within the scope of the thesis aims.

3.2.2 Results

The effect of peripheral properties is shown in Fig. 3.4. Fig. 3.4c shows that two peaks are still present in the digital area waveform without a change in their arrival time when all peripheral reflections have been removed from the baseline model (model P1). This result suggests that both peaks are predominantly made up of wavefronts propagating from the aortic root and their reflections at arterial junctions, tapered vessels, and the aortic root. However, peripheral reflections do effect the arrival time of the first peak: it arrives 30 ms earlier when upper-body peripheral reflections are absent. Removing peripheral reflections from only the lower-body segments (P2) results in an area waveform with a greater magnitude than if peripheral reflections are removed from only upper-body segments (P3). This result indicates that peripheral reflections originating in the upper body have a greater contribution to the magnitude of the digital area waveform than do peripheral reflections originating in the lower body. The second peak arrives at approximately the same time in models P2 and P3, but the first peak arrives 52 ms earlier in model P3, suggesting that peripheral reflections in the upper body delay

the arrival time of the first peak. Additionally, the amplitude of the second peak is dependent on the existence of peripheral Windkessel sites in the upper body. It is noted that the difference in mean pressure waveforms is due to the total arterial resistance varying across each simulation [Leguy, 2010].

Figure 3.4b shows the pressure waveform at the aortic root. Similarly to the results described above for the DVP, the type of boundary conditions affects the time of arrival of the peak of systole by 20ms. Furthermore, during diastole the rate of decay is faster when all peripheral boundary conditions are absorbing (P1), compared to when just the upper body is an absorbing boundary conditions (P3). The diastolic pressure is modified by the absorbing boundary condition because we change the total peripheral resistance. The total peripheral resistance varies from 87.1, 0, 1.1 and 4.5 10^8 Pa s m^{-3} for model P1, P2, P3 and P4, respectively.

Figure 3.5 shows example pressure waveforms at the aortic root under changes in Windkessel outflow pressure, peripheral resistance, elastic and muscular cross-sectional diameter, or elastic and muscular stiffness variations (as defined in Section 3.2.1.1). Increasing Windkessel outflow pressure or peripheral resistance translates the mean pressure waveform up, but maintains the overall morphology of the pressure waveform. Changing the elastic and muscular diameter alters the shape of the pressure waveform in systole and diastole. Increasing the elastic diameter by 60% causes a 10% decrease in the peak pressure and introduces a delay in the arrival of systolic pressure of 7ms. During diastole the decay of the waveform is less steep. A 60% increase in muscular diameter decreases the peak pressure by 19%, similar to V3 the decay during diastole is less steep compared to the baseline model. Increasing elastic (V5) and muscular (V6) stiffness results in a faster decay of pressure during diastole and in an increase in peak pressure, when compared to

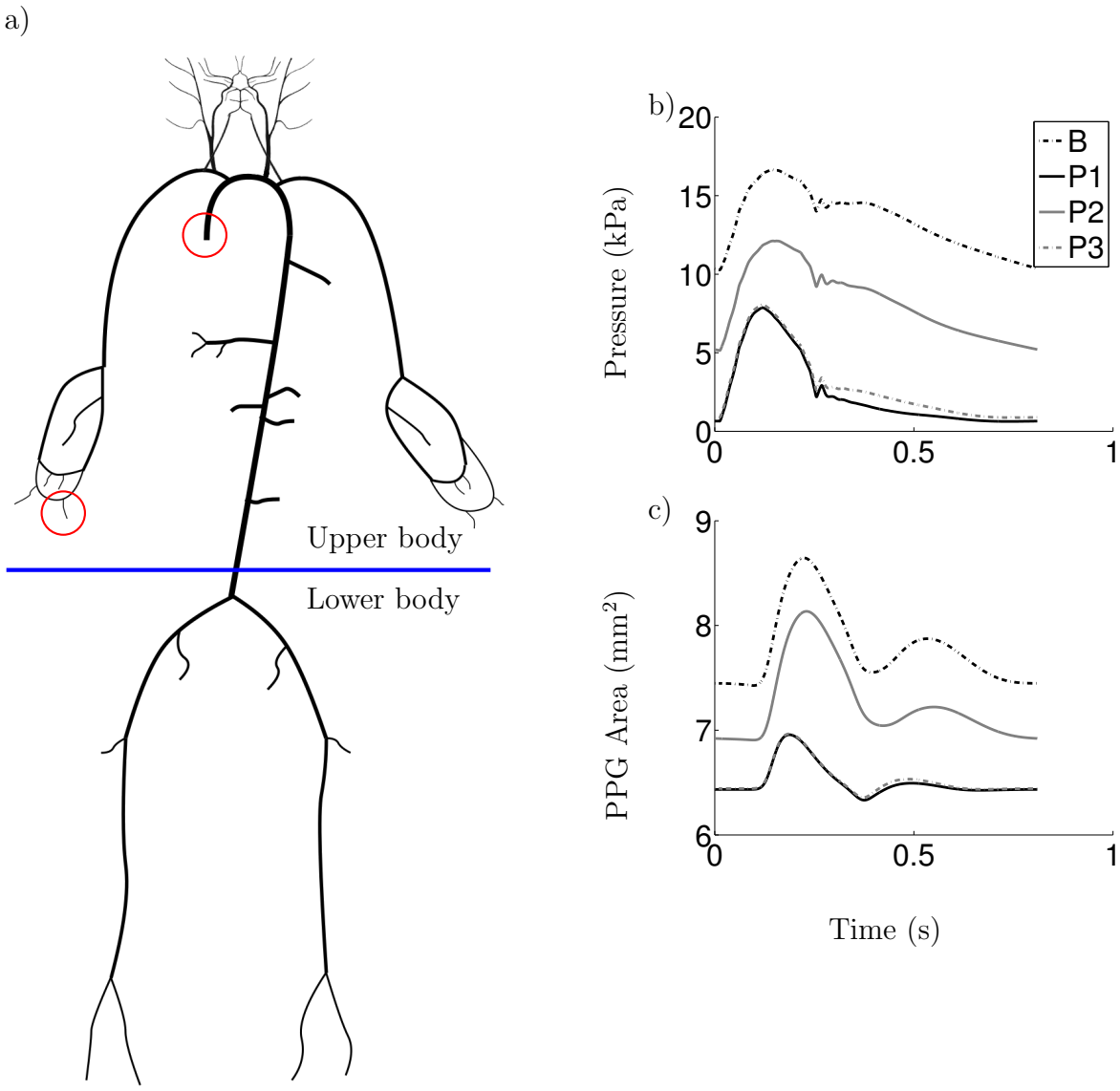

Figure 3.4: (a) Schematic representation of the 120-artery model modified from Epstein *et al.* [2014]. (b) Pressure waveform at the aortic root. (c) PPG waveform measured at the digital artery under the three different combinations of absorbing and Windkessel outflow boundary conditions described in Table 3.5.

the baseline model

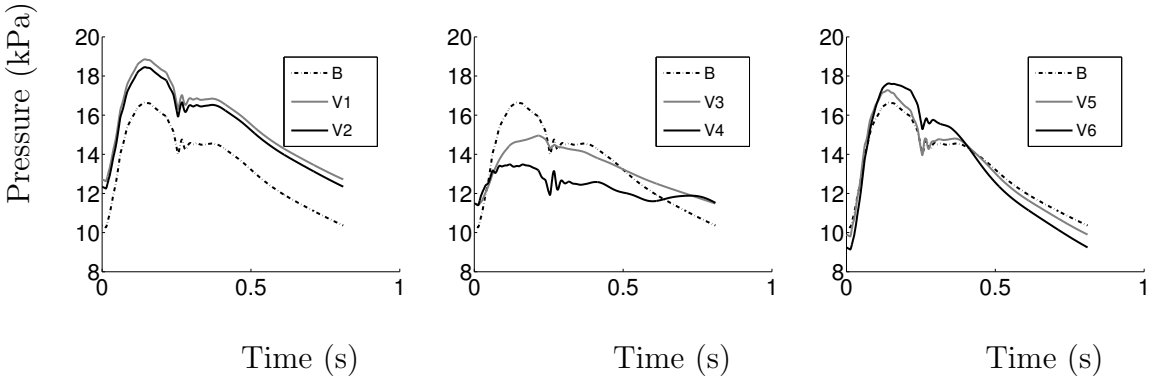

Figure 3.5: Pressure waveform at the aortic root under normal conditions (B), with a 200% increase in Windkessel outflow pressure (V1, left), a 120% increase in peripheral resistance (V2, left), a 60% increase in elastic diameter (V3, centre), a 60% increase in muscular diameter (V4, centre), a 200% increase in elastic stiffness (V5, right), or a 200% increase in muscular stiffness (V6, right).

Figure 3.6 shows the change in the DVP features dT, CT, PS and PD when Windkessel outflow pressure, peripheral resistance, elastic and muscular cross-sectional diameter, and elastic and muscular stiffness are varied. The least significant contributor to changes in dT, CT, PS and PD is V1 (variants of Windkessel outflow pressure). Similarly, V2 (changes in peripheral resistance) has a very small contribution. This is because peripheral resistances and Windkessel outflow pressure affect mainly the magnitude of the digital area waveform, without introducing considerable changes in the dT. These variations in DVP waveforms are in agreement with the well-known increase in mean blood pressure with increasing peripheral resistance and increasing Windkessel outflow pressure [McDonald, 1974]. Area and pressure changes follow a similar pattern because they are directly related through Laplace's law [Alastruey *et al.*, 2011; McDonald, 1974].

The time between the systolic and diastolic peaks, dT, has been shown to be inversely proportional to large artery stiffness [Millasseau *et al.*, 2002b]. Within

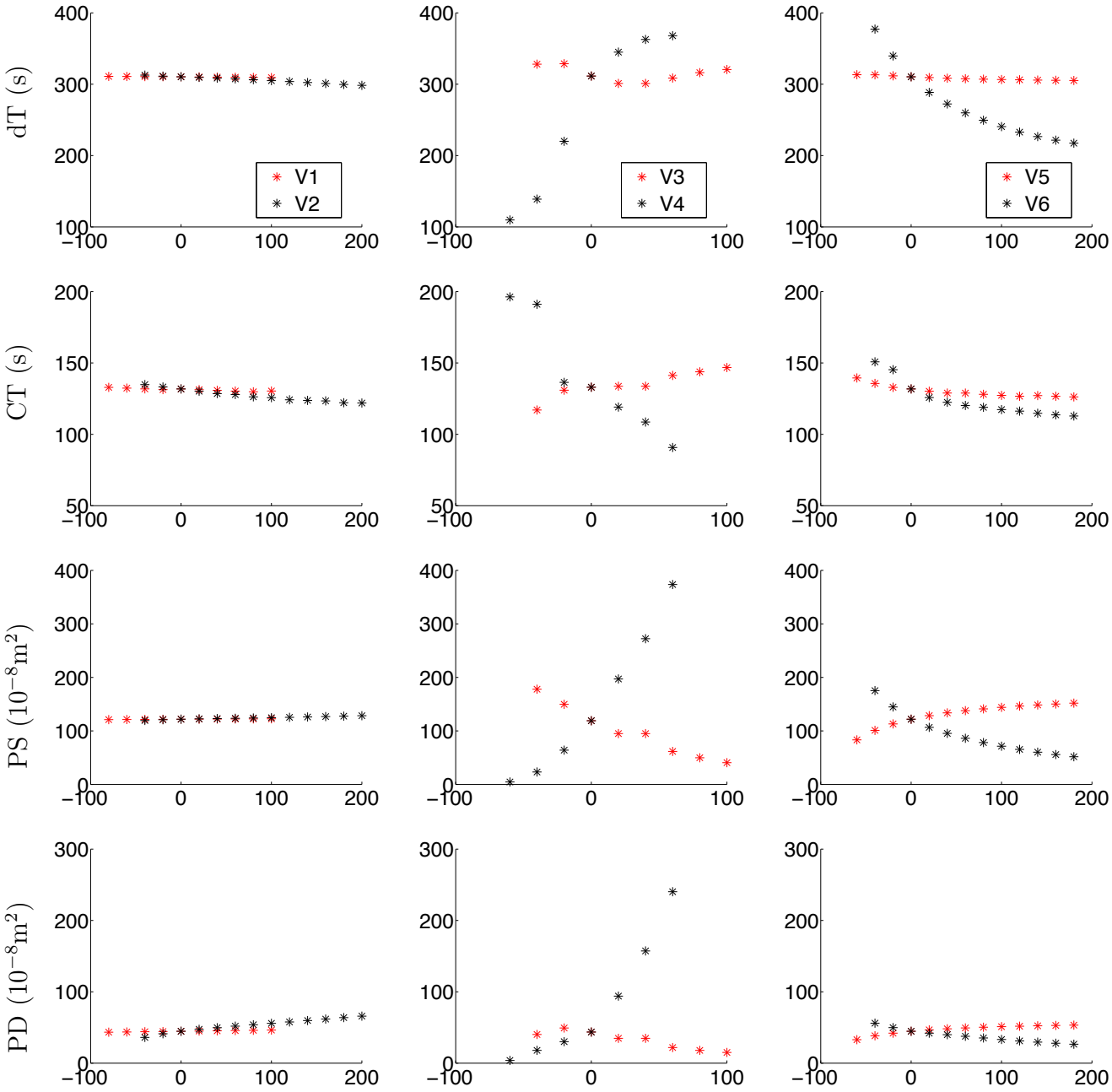

Figure 3.6: Change in dT, CT, PS, and PD at the DVP when Windkessel outflow pressure, peripheral resistance (left), elastic and muscular cross-sectional area (centre), and elastic and muscular stiffness (right) are varied from baseline conditions.

this sensitivity analysis, there is very little change to dT when alterations in the elastic stiffness (V5) are considered. However, with an increase of the stiffness of the muscular arteries (V6) there is a negative correlation to dT; hence the stiffness index ($SI = H/DT$, where H, is the height of the patient) would increase. An increase of muscular stiffness of 200% decreases dT by 30%, whereas a change of elastic stiffness of 200% decreases dT by less than 2%. Changes in elastic diameter (V3) created a nonlinear change in dT times, which suggests that dT results from a complex interaction of wave propagation and reflection within the 1-D domain.

The arrival of the crest of the waveform (CT) is negatively correlated to an increase in V5 and V6. Compared to baseline, an increase of elastic and muscular stiffness of 200% caused a decrease in CT of 5 and 19 ms, respectively.

Increasing elastic stiffness (V5) creates an increase in PS and PD. Whereas an increase in muscular stiffness (V6) causes a decrease in PS and PD. The opposing direction of correlation is due to the complex set of wave reflections that make up the area pulse waveform. An increase in aortic cross-sectional diameter (V3) has a negative influence on PS and PD.

The most significant contributor to changes in dT, CT, PS and PF is V4 (muscular cross-sectional diameter), this is due to the measurement site (the digital artery) being defined as a muscular artery. Thus, the characteristics of the measurement site are directly changed as part of the sensitivity analysis procedure. There is a strong positive correlation between PS, PD, and dT and V4. CT is negatively correlated with V4.

Figure 3.7 shows the change in PPG Width and Area with changes in V1, V2, V3, V4, V5 and V6. Similar to Fig. 3.7, changes in Windkessel outflow pressure and peripheral resistance (V1 and V2) have a negligible effect on PPG Width and

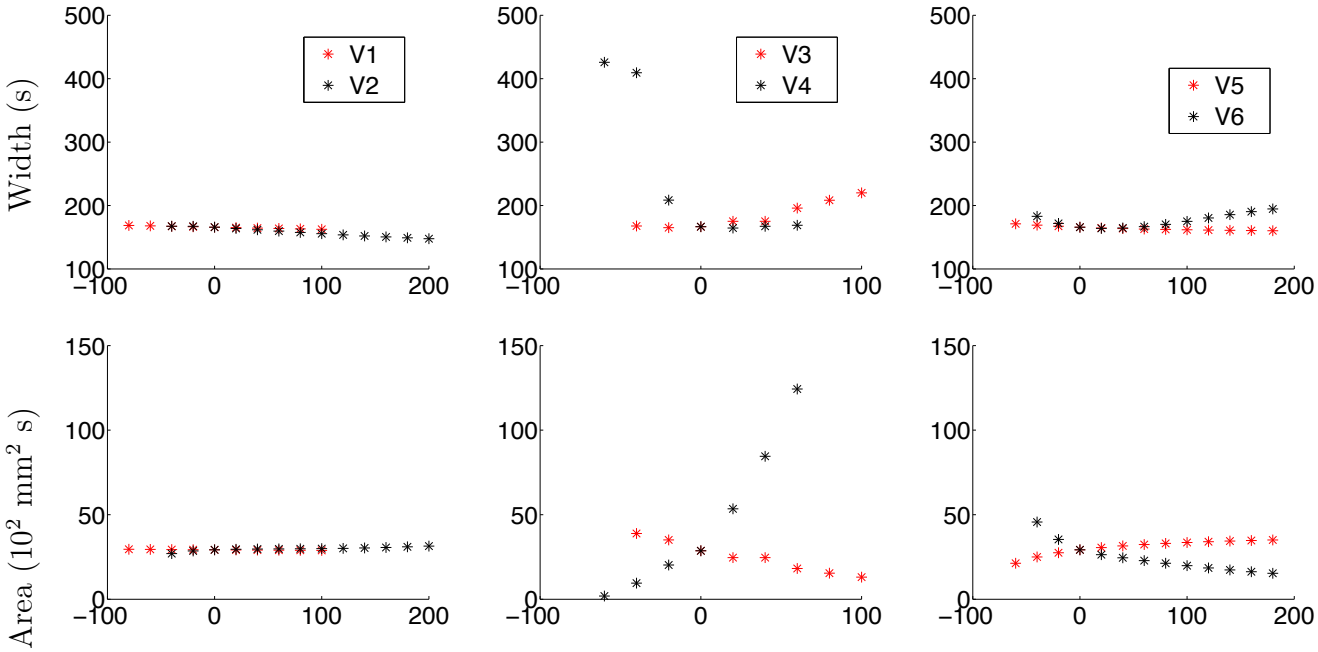

Figure 3.7: Change in Width and Area at the DVP PPG when Windkessel outflow pressure, peripheral resistance (left), elastic and muscular cross-sectional area (centre), and elastic and muscular stiffness (right) are varied from baseline conditions.

Area. There is an increase in PPG Width with increase in V3 and V6. Again, muscular diameter variation (V4) affects width and area significantly.

An increase of elastic stiffness of 200% created a 5 mm^2 increase in Area. However an increase in muscular arterial stiffness causes a smaller pulse amplitude at the digital artery, hence a decrease in the measured area. An increase in muscular stiffness of 200% caused a 14 mm^2 decrease in Area.

3.2.3 Discussion

The sensitivity analysis allows us to identify the parameters which influence significantly the model outputs. In our model the muscular cross-sectional diameter has a great influence on PPG waveform features. Within our methodology, by altering the muscular cross-sectional diameter we directly altered the characteristics at the measurement site (the digital artery). This result is similar to that found by Willemet [2012] when considering a femoral bypass.

One objective of the sensitivity analysis is to determine the parameters which do not influence the outputs significantly. In our model, Windkessel outflow pressure and peripheral resistance have a negligible influence on PPG waveforms.

Thiele *et al.* [2011] looked at the relation between PPG derived parameters and invasively-determined haemodynamic variables in 18 patients undergoing coronary artery bypass graft surgery. They found no significant relation between the peripheral resistance and the area or width of the PPG waveform. These findings are also seen within this sensitivity analysis.

Increase in arterial wall stiffness raises the amplitude, thus Area, of the digital area waveform due to an increase in pulse pressure caused by the Windkessel

effect, as described in Alastruey *et al.* [2014] using the 1-D formulation. Within this sensitivity analysis we found that an increased arterial stiffness resulted in a decreased CT. This is in contradiction to the work of Dillon & Hertzman [1941]; Wu *et al.* [2010] who found that CT increased in the presence of increased arterial stiffness. However, when considering the physics of the problem, it is reasonable to expect a faster arrival of the peak of the pulse waveform when the arterial network it is travelling through is stiffer (hence, pulse waveforms are transmitted faster).

The results from this sensitivity analysis suggest that it is not possible to quantify the elastic or muscular arterial stiffness of the arterial network from the amplitude of the digital pulse waveform from the parameters varied within this study. This is shown by considering the mixed effect of changes in elastic and muscular stiffness on PS, PD and Area. However, timings such as CT and DT may be useful in identifying the stiffness of the muscular arteries because of their sensitivity to such changes as seen in Fig. 3.6.

It is noted that one important consequence of using a local sensitivity analysis is that results depend on the initial state. In this analysis, the initial state is described in Section 3.1. One might consider more complex techniques such as global sensitivity analysis to overcome that simplification. But this is beyond the scope of this study.

Lastly, the inflow waveform remained unchanged in this study, which may explain the discrepancy between numerical and clinical results reported above. In the following section we address this limitation by investigating the effect of changes in inflow waveform variations on the DVP.

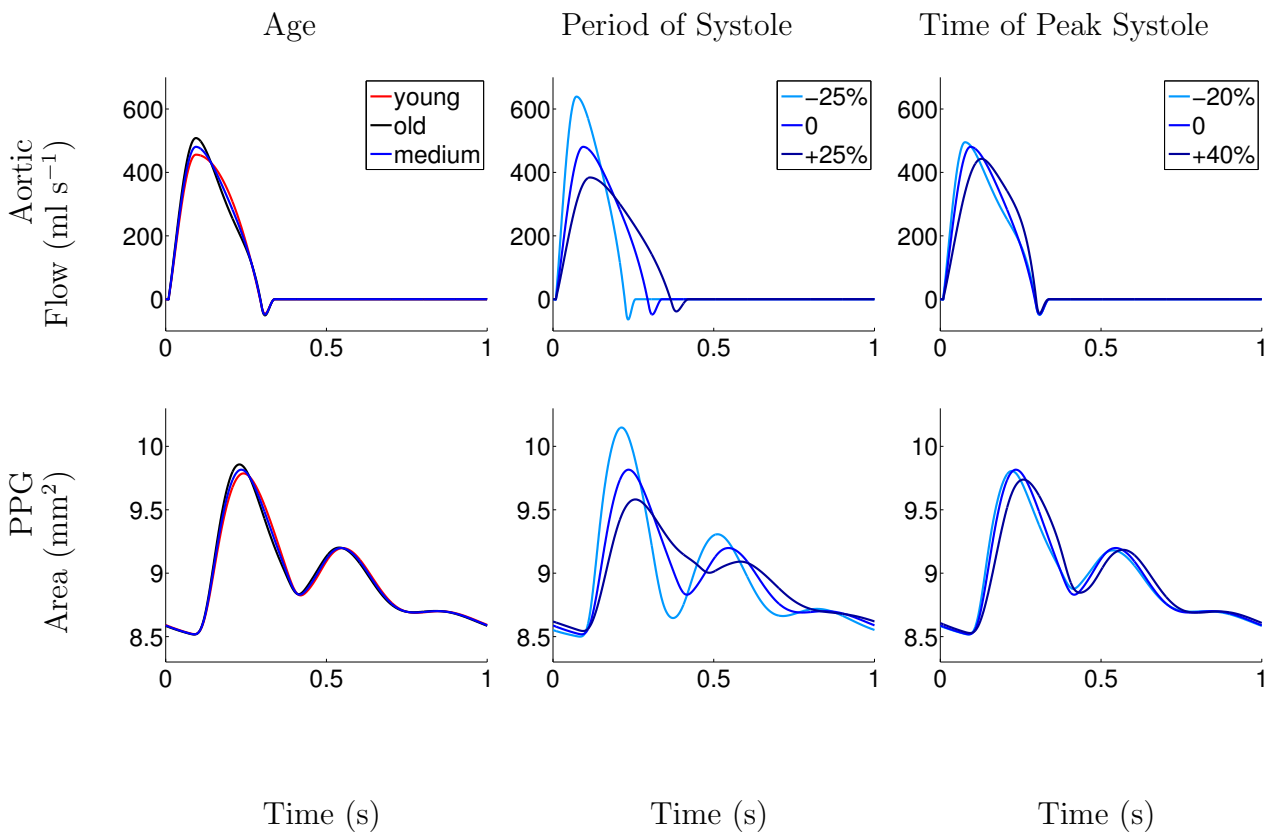

Figure 3.8: Flow waveform at the aortic root (top) and cross sectional area waveform at the digital artery (bottom), with change in age (left), period of systole (center) and time of peak systole (right). The central and right waveforms baseline conditions are of medium age.

3.3 Inflow Waveform Variations

In this section we aim to understand how changes in the aortic flow waveform modify the shape of the DVP waveform. We will prescribe 27 different aortic flow waveforms to the inlet of our 120-vessel nonlinear viscoelastic model and quantify the changes in the cross-sectional area at the digital artery.

The aortic inflow waveform can be separated into four main stages (see Fig. 3.8, top left): 1) An early rapid rise to a systolic peak at around 100ms after the arrival

of the foot of the wave; 2) a convex fall in flow until the end of systole at around 300ms; 3) a short period of back flow; and 4) a period of no flow for the rest of diastole [ORourke, 2009].

Within this study we systematically alter 3 dependent variables at flow waveform at the aortic root. The first is the shape of the flow waveform during systole, varying it from what would be found in a normal young, medium and old patient (left, Fig. 3.8). Secondly we vary the period of systole $\pm 25\%$ (center, Fig. 3.8). Finally varying the time of peak systole $-20\%, +40\%$ (right, Fig. 3.8). With each variation the mean flow is kept constant at 5 l min^{-1}, hence the peak systolic flow changes to maintain the mean flow.

The motivation for the change in flow waveform shape with age is taken from ORourke [2009]. The young flow waveform has a parabolic shape between the systolic peak and dicrotic notch, whereas the old waveform has an inflection point along the decreasing systolic edge which results in a convex curve. To cover a range of physiological values we vary the time of systole between 252-420 ms [Weissler *et al.*, 1961] and time of peak systole between 77-128 ms [Gardin *et al.*, 1984].

Within this section we will first describe aortic flow (Section 3.3.1) and aortic pressure (Section 3.3.2) parameters that are evaluated as part of this study. The measured PPG variables studied within this work are taken from Section 3.2.1.3 (see Fig. 3.3). We will then present the results of our analysis (Section 3.3.3). The last part of this section discusses the results and observations (Section 3.3.4).

3.3.1 Aortic Flow Features

The key features of the flow waveform at the aortic root are displayed in Fig. 3.9 and described next.

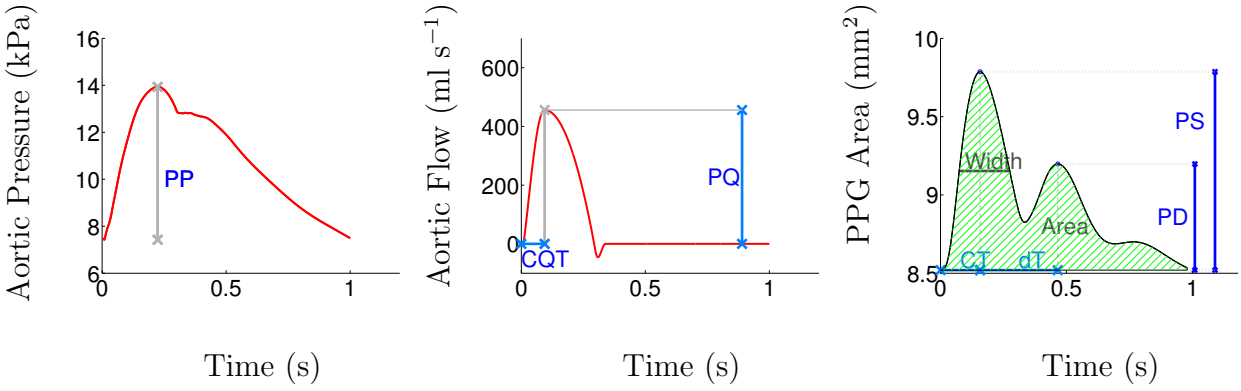

Figure 3.9: A typical pressure (left) and flow waveform (center) at the aortic root, and cross-sectional area waveform at the digital artery (right) and their characteristic parameters. Where PP= pulse pressure amplitude, CQT= crest flow time, PQ= peak flow,dT= time between systolic and diastolic peaks, CT=crest time, Width= pulse width at half height of the systolic amplitude, PD= peak of diastole, and PS= peak of systole.

1) *CQT*. Crest flow time. The time to peak aortic velocity. In healthy patients the CQT at the aorta is shown to vary between 80-120ms [Gardin *et al.*, 1983]. In this study we vary CQT between 61-159ms to cover the range of physiological values seen in a healthy population. These maximum and minimum values were selected as they were ± 37ms from the original value of 98ms. The timing of the crest is dependent on an early forward compression wave from the heart [Jones *et al.*, 2002]. CQT has been used to predict severe aortic stenosis [Kim *et al.*, 2014].

2) *PQ*. Peak flow at the aorta. PQ is an index of myocardial contractility [Rowland *et al.*, 1999]. Mitchell *et al.* [2003] found in normotensive male patients (n=19) a peak flow of 351±69 ml s^{-1} (mean ± SD). Nichols *et al.* [1977] found a

PQ value of 712±53 ml s^{-1} (mean ± SEM) in healthy patients undergoing cardiac catheterization. In this study we vary PQ between 343-723 ml s^{-1} in order to cover the full range of physiological values found in the literature. An increase in peak flow at the aortic root is seen in patients with a bicuspid aortic valve [Ferencik & Pape, 2003; Nkomo *et al.*, 2003], aortic regurgitation [Masuyama *et al.*, 1986], or increased body surface area [Gardin *et al.*, 1987].

3.3.2 Aortic Pressure Features

The arterial pressure at the aortic root is directly altered by changes in the aortic flow waveform. The work by Baruch *et al.* [2011] has found a correlation between pulse pressure at the aortic root and dT at the DVP. Thus, the key feature of the pressure waveform at the aortic root considered in this study is:

1) *PP*. Pulse pressure at the aortic root. Pulse pressure is correlated with the stroke volume of the aortic flow [Convertino *et al.*, 2006]. In our model, a change in the prescribed inflow boundary condition affects the measured pulse pressure at the aortic root. Within this study, PP is varied between 5.8-7.6 kPa, which covers a normal physiological range [Benetos *et al.*, 1998].

3.3.3 Results

We have modified the aortic flow waveform by (i) changing the shape during the downslope of systole to replicate the effect of ageing; (ii) altering the period of systole by ±25%; and (iii) altering the time of arrival of peak systole by −20% and +40% whilst preserving the overall period of systole. With each modulation the stroke volume, and heart rate are preserved. CQT and PQ vary between 61-

159 ms and 343-723 ml s^{-1} respectively. We have focussed on the haemodynamics of the digital artery as it can be easily measured continuously and non-invasively; *e.g.* by photopletysmography.

The influence of age on the DVP is shown in Fig. 3.8 (left). During the downslope of systole the shape of the older waveform is concave, whereas the younger waveform is flat. The medium waveform is an average between the other two. The resultant change to the DVP is small: with increasing age, the CT decreases.

The influence of time of systole on the DVP is more significant (Fig. 3.8, centre). Altering the timings by $\pm 25\%$ results in a significant change to the time of arrival and to the absolute values of the systolic and diastolic peaks. With each step increase in the time of peak systolic flow, the time of arrival for the DVP systolic peak increases by 20 ms, and the time of diastolic peak by 40 ms.

The impact of the timing of peak systolic flow is seen in Fig. 3.8 (right). The most noticeable change in the DVP is seen in the timing and absolute values of the systolic peak of the DVP. With decreasing time of CQT, from $+40\%$ to 0 to -20%, there is a decrease in CT at the DVP of 20 ms and 10 ms, respectively.

Figure 3.10 compares the change in CQT at the aortic root, to changes in dT, CT, PS, PD, Width and Area of the DVP in all 27 variations of the inflow waveform (as described in Section 3.3). For each pairing the linear regression equations ($y = ax+b$) and correlation coefficient ($r^{@}$) are shown in the top right hand corner. The coefficient of determination (r^2) vary from 0.09-0.91, the best correlation being CT against CQT (Fig. 3.10b). In Fig. 3.10b we see that the linear fit model underestimates the young waveforms, well matches the medium waveforms, and overestimates the old waveforms. There is a poor correlation between CQT and dT, PS, PS, Width and Area. Additionally, there is no clear pattern between the

simulated physiological age of the waveform and the dependent variables of dT, PS, PS, Width and Area. The outlier indicated in Fig. 3.10a is plotted in Fig. 3.13.

Figure 3.11 compares changes to the pulse amplitude of the input flow waveform to changes in dT, CT, PS, PD, Width and Area of the DVP. Correlation coefficients vary from 0.09-0.95. The correlation coefficient for dT, PS, PD, Width and Area against PQ is higher than in Figure 3.10. There is a very high correlation (0.95) for PS against PQ (Fig. 3.11c). The same outlier indicated in Fig. 3.11a is plotted in Fig. 3.13.

Figure 3.12 compares the changes to the PP at the aortic root to changes in dT, CT, PS, PD, Width and Area of the DVP. Correlation coefficients vary from 0.08 to 0.90. The two highest correlation coefficients are for PD and PS against PP, 0.89 and 0.9, respectively. When the outlier is removed from Fig. 3.10a, the correlation coefficient increases to 0.28. Similarly, when the outlier is removed from Fig. 3.11a and Fig. 3.12a the correlation coefficient increases to 0.62 and 0.79, respectively.

3.3.4 Discussion

In this study we have analysed how the shape of the prescribed inflow at the aortic root affects the simulated DVP. By systematically altering the shape of the inflow whilst maintaining the stroke volume constant, we have been able to assess how the DVP waveform changes independently of mean blood pressure changes. To carry out this study we have used a nonlinear, viscoelastic 1-D model of the larger 120 systemic arteries, including the vasculature of the hands and the head.

PPG has been shown to be useful in determining the heart rate [Lu *et al.*, 2008;

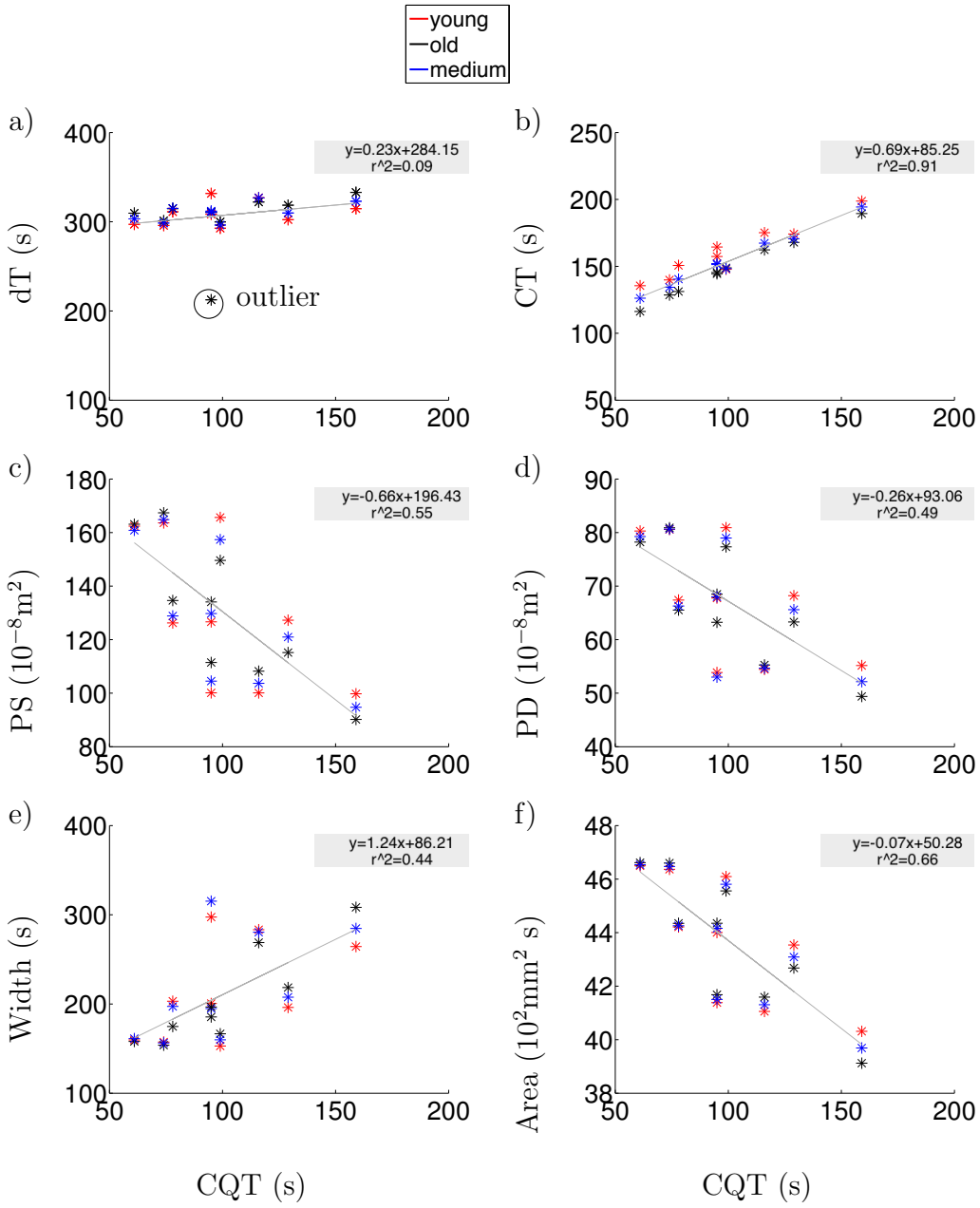

Figure 3.10: Plots comparing the crest flow time (CQT) at the aortic root against the time between the arrival of the systolic and diastolic shoulder (dT), crest time (CT), peak of systole (PS), peak of diastole (PD), width at half amplitude (Width), and area under the curve (Area) at the DVP. The age of the plotted inflow is defined as young (red), old (black) and medium (blue).

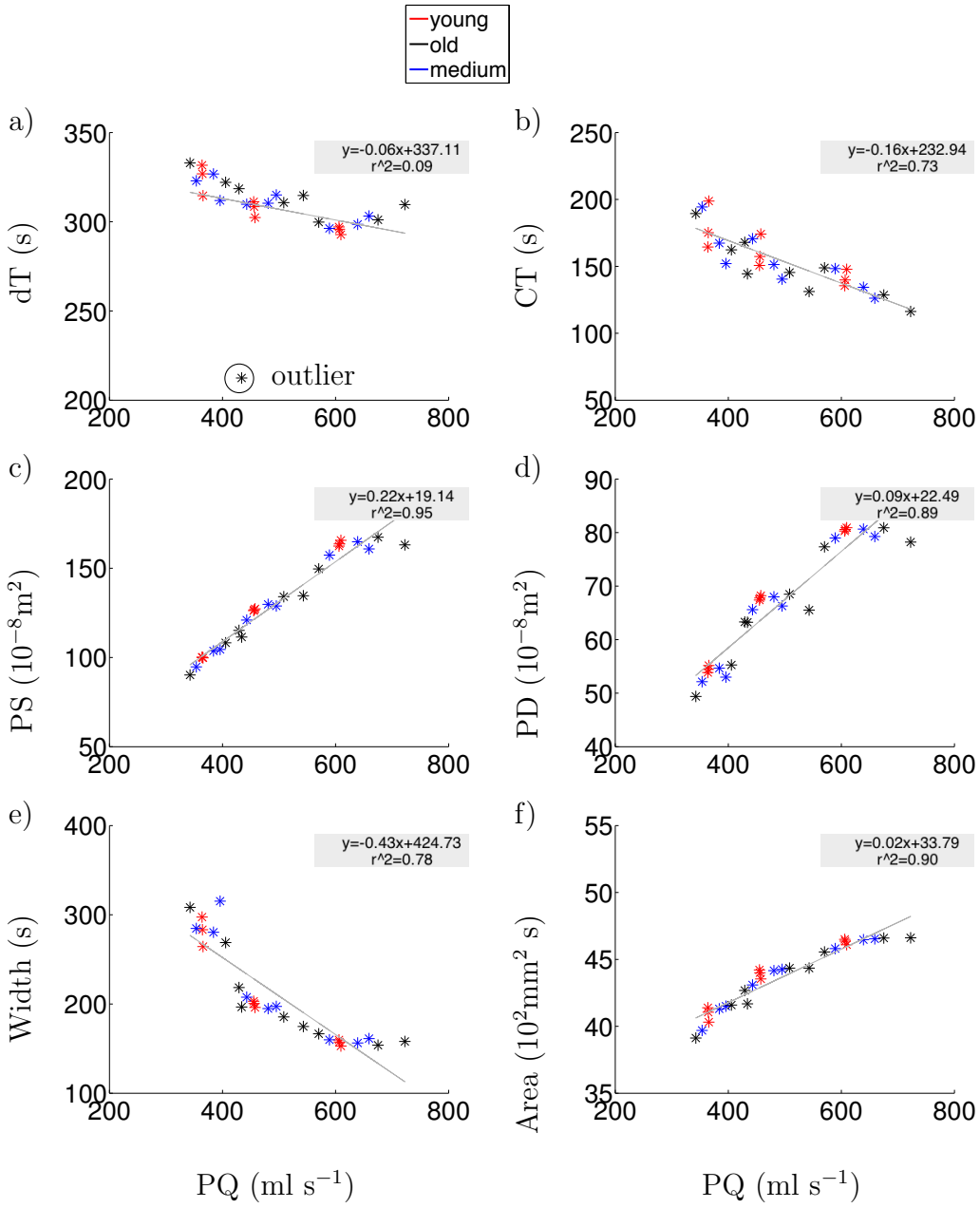

Figure 3.11: Plots comparing the peak flow (QP) at the aortic root against the time between the arrival of the systolic and diastolic shoulder (dT), crest time (CT), peak of systole (PS), peak of diastole (PD), width at half amplitude (Width), and area under the curve (Area) at the DVP. The age of the plotted inflow is defined as young (red), old (black) and medium (blue).

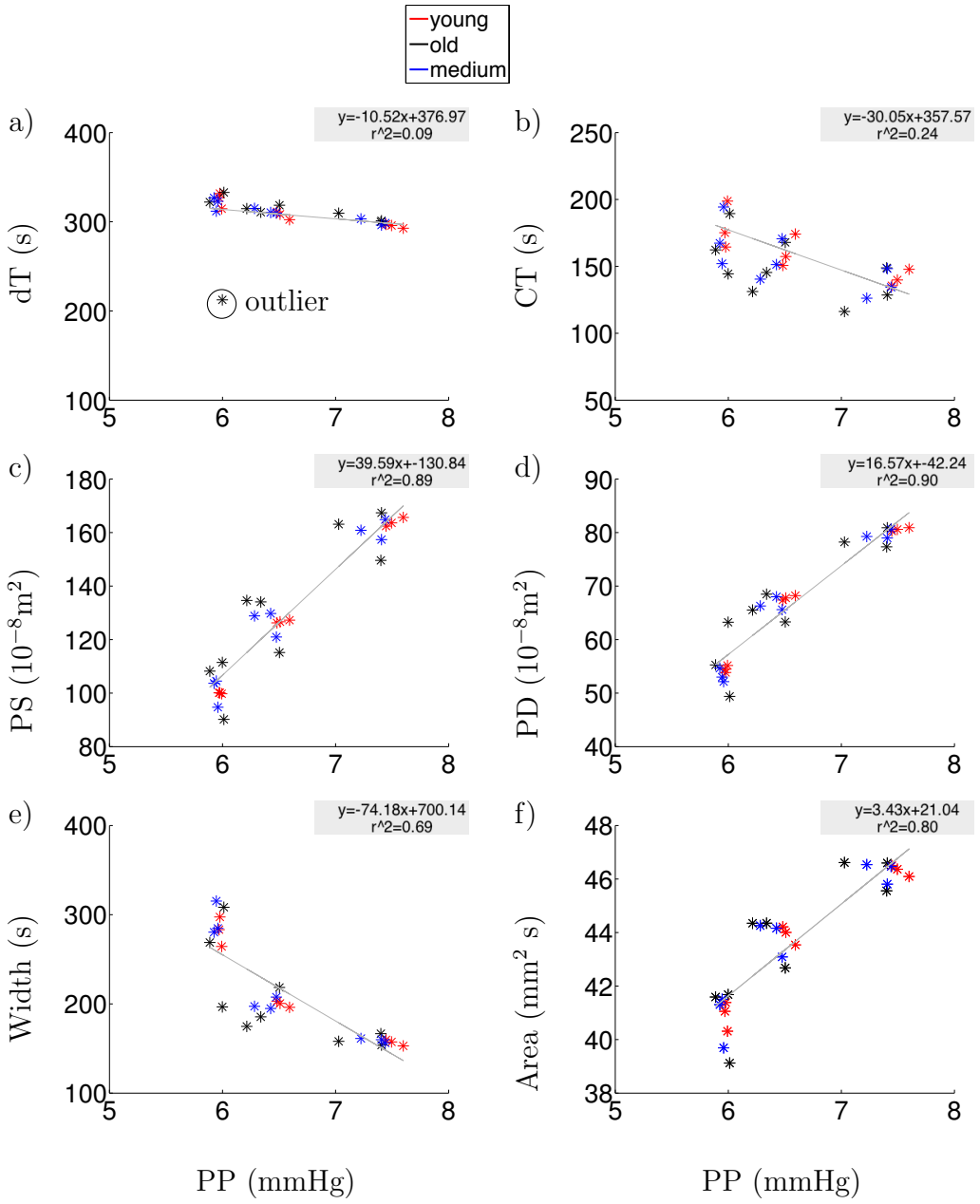

Figure 3.12: Plots comparing the pulse pressure (PP) at the aortic root against the time between the arrival of the systolic and diastolic shoulder (dT), crest time (CT), peak of systole (PS), peak of diastole (PD), width at half amplitude (Width), and area under the curve (Area) at the DVP. The age of the plotted inflow is defined as young (red), old (black) and medium (blue).

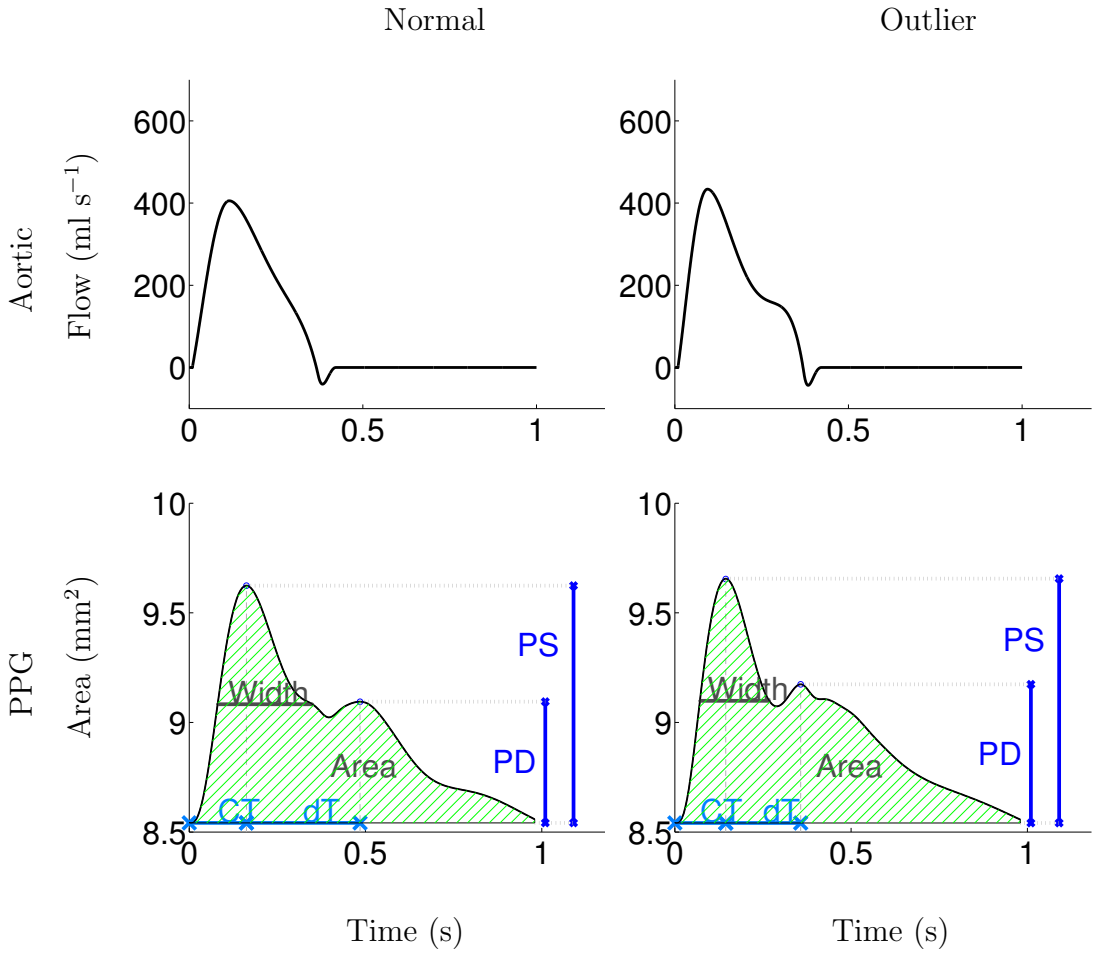

Figure 3.13: Two examples of a PPG waveform (bottom) and their respective inflow waveforms (top). Both waveforms have had an 'old' waveform with systolic period varied +25% prescribed to the inlet. The outlier (right) has had its time of peak systole decreased to 80% where as the normal (left) waveform time of peak systole is at baseline conditions (0%).

Nakajima *et al.*, 1996], systolic blood pressure [Talke *et al.*, 1990; Wallace *et al.*, 1987], and sympathetic tone [Tanaka *et al.*, 2000] of the cardiovascular system. The second derivative of the PPG waveform has been correlated with carotid artery distensibility [Imanaga *et al.*, 1998], age [Baek *et al.*, 2007], atherosclerosis [Bortolotto *et al.*, 2000], and coronary heart disease [Otsuka *et al.*, 2006]. However, there is little research on how changes in the heart timings and contractility alter the shape of the PPG waveform at the digital artery directly. Due to the complex nature of the cardiovascular system, it is difficult to change certain parameters independently. For example, within a given population if you wish to see the effect of time of the systolic period of the heart, then heart rate will also change, which would have to be adjusted for in any evaluation of the DVP [Weissler *et al.*, 1961]. The limitations seen *in vivo* can be overcome using our computational model.

There is a strong linear relationship between the CQT at the aortic inlet and CT at the finger. During early systole it is assumed there are no reflections from peripheral locations, thus there is only the forward travelling wave from the heart. Therefore, the time taken for the peak of the DVP waveform (CT) is equal to the time of the peak of the flow at the aortic root (CQT) plus the time it takes the wavelet to travel along the cardiovascular system to the site of the digital artery. The travel time is dependent on the PWV and distance of the path travelled by the forward travelling wave.

The high correlation coefficient (0.95) between PS at the DVP and PQ at the aortic root is best explained by considering pulse wave theory. During early systole we assume there are no reflected waves from peripheral locations, hence the time of peak systole of the pressure and flow waveform (hence area waveform) are linearly

related. This does not hold true for late systole and diastole where reflected waves interact with the forward waves. The complexity of interaction creates a nonlinear relation between pressure and flow. Therefore, the peak aortic flow is proportional to peak DVP.

The work by Baruch *et al.* [2011] has found a positive correlation between pulse pressure at the aortic root and dT at the DVP. With the removal of the outlier in Fig. 3.12 there is a strong correlation coefficient of 0.79, however the slope of the line is negative; whereas Baruch *et al.* [2011] found a positive relationship between the two parameters. It is noted that in the work by Baruch *et al.* [2011] they are studying negative body lower pressure, which creates changes in the peripheral vascular tone, which is not represented by our model. Hence the reason for the lowering of pulse pressure within their studies is due to a redistribution of blood throughout the cardiovascular system, whereas we are simulating a constant volume of blood at the inlet to our model with only slight changes in the shape of the inflow waveform. These, therefore, cause subtle changes to the pulse pressure due to the timings of the wave reflections.

Within this study, Width at the DVP is poorly correlated with PQ and CQT. Current literature suggests pulse width is dependent on heart rate [Hickey *et al.*, 2015] and stroke volume [Thiele *et al.*, 2011]. Both these variables are kept constant within this study.

The outlier indicated in Figs. 3.10a to 3.12a is the result of an old aortic inflow waveform with -20% arrival time of peak systole and a period of systole $+25\%$. Fig. 3.13 compares the inflow and DVP waveforms for this outlier with corresponding waveforms for a 'normal' case. Due to the fourth order polynomial fitted during the downslope of systole, a convex shape is seen with a steep secondary shoulder

This irregular bump causes a non-physiological peak at the DVP much earlier than the other inlet waveforms considered, indicated at dT in Fig. 3.13 (right).

To summarise, within this numerical study CT and PS at the DVP are strongly linearly related to CQT and PQ at the aortic root. When the stroke volume and heart rate are preserved, and only changes to the shape of the aortic flow waveform are considered, variations in CQT and PQ at the aortic root do not have a significant influence on the dT, PD, Width or Area of the DVP.

3.4 Concluding Remarks

Within this chapter we have studied the behaviour of a coupled visco-elastic 1-D/0-D model of blood flow in the major arterial vessels. The baseline model from Reymond *et al.* [2009] was extended to include the vasculature of the hands and cerebral circulation. A local sensitivity analysis has been carried out to study how the shape of the PPG signal at the digital artery in the hand is affected by changes in cardiovascular properties.

Comparison of the model simulations against *in vivo* measurements taken from the literature gives good results at the aorta, carotid, radial, brachial, femoral and digital arteries. We have compared the model qualitatively against the shape of pressure, flow and area waveforms from different sources. The generic model well predicted *in vivo* measurements from an average healthy population. Results have shown that the model is able to reproduce the main aspects of physiological flow in the large arteries, cerebral circulation and hands. Some improvements are necessary in order to obtain optimal reproduction of data at the temporal artery, since our model may produce unphysiological oscillations at this site. However,

waveforms in the head are more complex and exhibit more variations in their shape due to anatomical variation which may partially account for the discrepancy at this site [Reymond *et al.*, 2009].

In our model the arterial wall was simulated as a viscoelastic and incompressible material. It was necessary to estimate the viscous term in the Kelvin-Voigt model due to very little available data in the literature on the viscoelastic properties of the human arterial wall. The introduction of the viscous term has been shown to induce considerable variation in the shape of pressure and flow waves, especially in peripheral sites [Reymond *et al.*, 2009]. Inclusion of the viscous term reduces underdamped high-frequency oscillations. In our model we still experience high-frequency oscillations in the temporal arteries, which may be due to an incorrect estimate of vessel wall viscosity in the cerebral arteries.

Each vessel of our 120-artery model is represented as having a tapering cross-sectional area from the proximal to distal end. The effect of tapering vessels is important in determining the shape of pressure and flow waveforms [Segers & Verdonck, 2000]. However, within our model the vessels of the hand have a constant diameter, due to lack of data on arterial tapering at this site. Since the length of the vessels in the hand is small (less than 3cm), the difference between a tapered and non-tapered vessel is negligible [Myers & Capper, 2004].

In this work we have conducted a local sensitivity analysis. Results are based on the analysis from the baseline model validated at the beginning of this chapter. One objective of this sensitivity analysis has been to determine which parameters of the haemodynamic network influence outputs of the model. In this work we have focussed on the influence to the area waveform at the digital artery, which is analogous to the DVP PPG [Avolio, 2002].

To reduce the complexity of the sensitivity analysis, the arterial network was subdivided into muscular and elastic arteries. The elastic arteries consisted of the vessels of the aorta, the carotid arteries, and the iliac bifurcation. The muscular arteries were defined as all other remaining arteries. This subdivision was motivated by the opposing effects of ageing on central large arteries and on distal muscular medium-sized arteries [Boutouyrie *et al.*, 1992; O'Rourke, 2007]. The classification of the carotid artery as an elastic artery was motivated by *in vitro* [Gussenhoven *et al.*, 1989; Lockwood *et al.*, 1992] and *in vivo* [Boutouyrie *et al.*, 1992] studies. The vessels of the iliac bifurcation have been classified as 'musculo-elastic' [Rees, 1968], elastic [Cronenwett & Johnston, 2014; Fajardo *et al.*, 2001; Singh, 2010] and muscular [Gussenhoven *et al.*, 1989; Wilkinson *et al.*, 2002] within the literature; for the purpose of this thesis we have classified them as elastic. By classifying the iliac bifurcation as an elastic artery, the reflection coefficient (a parameter describing how much of a pulse wave is reflected) at the aortic-iliac bifurcation remained between -0.3 and 0.3, a physiologically applicable range [Greenwald *et al.*, 1990]. A similar classification was made in the work by Willemet *et al.* [2015], however they chose to classify the carotid artery as a muscular artery even though the carotid presents structural properties closer to the aorta (thus being an elastic artery). Additionally, Willemet *et al.* [2015] considered the iliac vessels as muscular, thus necessitating post-processing of the data to exclude unphysiological aortic-iliac reflection coefficients. Furthermore, we have considered different ranges of variation of the diameter and arterial stiffness for the elastic and muscular arteries; this difference was motivated by the available data found in the literature.

In our model, peripheral resistance and Windkessel outflow pressure have little influence on the shape of the PPG waveform. Notably the PPG waveform was

very sensitive to changes in diameter and stiffness in muscular arteries. The work of Willemet [2012] highlighted that the variation of the properties in one vessel are transmitted in all pressure waveforms but that the effects on velocity signals are more local. This would suggest the model sensitivity to changes in muscular arteries to be profound, since the the digital artery is classified as a muscular artery.

Central arterial stiffness has been identified as a important biomarker of health, however how best to measure this non-invasively is an area of considerable research [Laurent *et al.*, 2006]. Whether it is possible to accurately detect changes using PPG contour analysis presents a further challenge [Allen & Murray, 2003; Dillon & Hertzman, 1941; Hashimoto *et al.*, 2002; Millasseau *et al.*, 2002b; Takazawa *et al.*, 1998]. Our sensitivity analysis suggests that the most useful parameters at the digital PPG for assessing central arterial stiffness would be the crest time (CT) and the systolic pulse (PS).

The sensitivity analysis has also allowed us to analyse how the shape of the flow waveform from the heart transmits to the area waveform at the digital artery. Here we found a strong correlation between the time to peak flow (CQT) at the aortic root and the time to peak area (CT) at the digital artery. Similarly, there was a strong correlation between the pressure amplitude at systole (PQ) and the peak systolic amplitude of area at the digital artery (PS).

Similar to the work of Ellwein *et al.* [2008]; Leguy *et al.* [2010]; Willemet [2012], the local sensitivity analysis has shown the complex relationship between input parameters and boundary conditions to the model. Furthermore, as parameters act dependently on each other, it would be interesting to determine the correlation between parameters by applying global changes to the input parameter space. This

idea is investigated in more detail in Chapter 4.

3.4.1 Clinical Perspective

A central premise of this work is that cross-sectional area at the digital artery is analogous to the PPG waveform. PPG is widely used in the clinical setting and provides a continuous non-invasive circulatory signal with which to assess cardiovascular function.

One drawback of measuring the PPG signal is the inter-subject variability. The strength of the measured signal can be changed by the contact force from the device onto the finger [Teng & Zhang, 2004]. At the moment there is no calibration procedure to standardise the PPG amplitude to compare one patient to the next [Shelley, 2007]. A further drawback of this method is the intra-subject variability of the recording in pulse amplitude [Teng & Zhang, 2004]. The finger tip contains an abundance of alpha adregenic receptors which cause artery and vein vasoconstriction, thus causing the blood flow at the digital artery to be sensitive to sympathetic activity and changes to temperature [Hertzman & Roth, 1942; Schmid-Schönbein, 1981]. Additionally, when comparing our cross-sectional area at the digital artery to clinical PPG measurements it should also be noted that the derived signal from commercial devices are heavily processed and filtered [Feldman, 2006].

The numerical signal simulated within this thesis is free from all the inter- and intra-subject variability described above, and is recorded at a high frequency. Where possible we have compared any results derived from the PPG waveform to the existing literature in order to build confidence in the techniques used in this

chapter. However, further work needs to be done to apply the results from this numerical study to real clinical data.

Chapter 4

Classifying Hypertensive Vs Diabetic Subjects: a Virtual Population Study

Hypertension and diabetes are two of the most common chronic diseases in the western world, with a high rate of co-occurance [Bella *et al.*, 2001; Epstein, 1997; Epstein & Sowers, 1992; Franklin, 2002; Fuller, 1985; Kannel & McGee, 1979; Lago *et al.*, 2007; Megnien *et al.*, 1992; Sowers *et al.*, 2001; Stehouwer *et al.*, 2008]. Currently one-third of all people with type 2 diabetes may be undiagnosed [American Diabetes Association, 1999], and among US adults with hypertension, 17.3% were undiagnosed [Mozaffarian *et al.*, 2015]. There is a significant overlap in risk factors between the two cohorts, such as large artery stiffness and microvascular arterial changes appearing in hypertensive and diabetic patients [Yannoutsos *et al.*, 2016]. These studies suggest that there is significant room for improvement in the screening, prevention and management of diabetes, hypertension and combined diabetes

and hypertension.

The goal of this study is to use 1-D modelling to investigate whether the shape of the PPG waveform measured in the finger could be used to distinguish among subjects with diabetes, hypertension, and combined diabetes and hypertension. The 1-D model described in Chapter 3 will be used to create a virtual (computed) population of healthy and diseased subjects. A global sensitivity approach will be carried out to match the output parameters of the 1-D model to corresponding parameters from the literature data of patients with diabetes, hypertension, and combined diabetes and hypertension.

Patient-specific, 1-D simulations of blood flow have been shown to be useful in the estimation of arterial stiffness [Leguy *et al.*, 2010], guiding vascular surgery [Huberts *et al.*, 2012a; Willemet, 2012], and predicting aneurysm rupture [Blanco & Feijóo, 2013]. Additionally, 1-D models can be used to estimate clinically relevant parameters at sites that are inaccessible to measurements [Leguy *et al.*, 2010; Stergiopulos *et al.*, 1995, 1999]. The number of arterial segments used in 1-D modelling varies from a single vessel to 4 million arterial segments [Avolio, 1980; Blanco *et al.*, 2014; Campbell *et al.*, 1989; Mynard & Nithiarasu, 2008; Perdikaris *et al.*, 2014; Reymond *et al.*, 2009; Stergiopulos *et al.*, 1992]. The larger the arterial model, the more input parameters are needed. Since it is not always feasible to derive every input parameter from patient data, it is then necessary to estimate or extrapolate data from literature [Blanco *et al.*, 2014; Leguy, 2010]. The greater the complexity of the model, the more uncertainty there is in the results of the model [Quick *et al.*, 2001, 2006].

Most 1-D models of the systemic arterial tree are sourced from the work of Westerhof and Nordergraaf [Noordergraaf *et al.*, 1963; Westerhof *et al.*, 1969]. Ef-

forts have been made to personalise aspects of larger models [Bode *et al.*, 2012; Manini *et al.*, 2013; Mynard & Nithiarasu, 2008; Reymond *et al.*, 2011] or entire smaller models [Leguy *et al.*, 2010; Willemet, 2012] to patient-specific data. Sensitivity analysis approaches have been successful in personalising stiffness variables [Leguy *et al.*, 2010] and identifying the most influential input parameters [Huberts *et al.*, 2012b, 2013; Leguy *et al.*, 2011] in patients undergoing surgery. However, this approach has been limited to smaller data sets.

Previously, Willemet *et al.* [2015] created a database of numerical models using literature data for healthy patients by altering the vessel diameter and stiffness of elastic and muscular arteries, heart rate, stroke volume and total peripheral resistance. Kiselev *et al.* [2015] personalised a 1-D haemodynamic model by altering the total peripheral resistance, heart rate, stroke volume, cross-sectional area and stiffness of the upper and lower body to data of patients with mixed cardiovascular disease.

Large-scale patient trials are a rich source of data that has never been fully integrated into the field of 1-D blood flow modelling. Parameters such as diastolic pressure (DBP), systolic pressure (SBP), mean pressure (MAP), pulse pressure (PP), and heart rate (HR) have been shown to have significant value in the diagnosis or treatment of patient mortality disease risk [Franklin *et al.*, 1999; Kannel *et al.*, 1971, 1987; Meaume *et al.*, 2001]. Increasingly pulse wave velocity is being measured as a predictor of cardiovascular outcome and measured in patient trials [Laurent *et al.*, 2006; Willum-Hansen *et al.*, 2006]. However, the unique functional origin for changes of these variables remains an area of considerable research [Karamanoglu *et al.*, 1994]. A processing strategy is needed to make sense of the data available, and a statistical approach to manage the relevance of existing data

from the literature. It is possible to extract further information from the literature by creating a 1-D nonlinear model of pulse wave propagation to create a fictive population that matches the literature data. It is then possible to extract new information from the numerical model further to the existing literature data.

For the application of a diseased-population-specific simulation, a number of population specific input parameters are required. We have already completed a local sensitivity analysis in Chapter 3. The local sensitivity analysis allowed us to study the effect of each parameter from a specific initial state of the model by perturbing each input parameter around a nominal (baseline) value one at a time. This type of analysis has been used extensively [Ellwein *et al.*, 2008; Gul *et al.*, 2015; Huberts *et al.*, 2013; Leguy *et al.*, 2010; Pope *et al.*, 2009; Willemet, 2012]. However, the results from such an analysis are highly dependent on the initial state that the input parameters are perturbed from, and the same results cannot be extrapolated to other initial states without further analysis. A global sensitivity analysis assesses the interactions of the input parameters over the entire feasible region. Additionally, a global sensitivity analysis quantifies the impact between the input parameter and their output variable.

How best to select the input parameters to achieve this goal is not straight forward, and can be computationally very expensive. For this purpose we will use a Response Surface Methodology (RSM) to select physiologically feasible input parameters. RSM is a mathematical-statistical method used for studying the interactions between the input and output variables of a model. RSM has been used extensively to help researchers in the fields of drug delivery systems [Singh *et al.*, 2006], textile industry [Demirel & Kayan, 2012], and biodiesel production [Vicente *et al.*, 1998]. The objective of using RSM is to optimise the input variables to

attain the best match to the desired output variables of a given model.

Within this Chapter, we extend our results from those of a single patient-specific model of the cardiovascular system (as seen in Chapter 3) to create a population of blood flow models under different diseased states. The disease states studied are diabetes, hypertension, and combined diabetes and hypertension. Section 4.1 describes the methodology to create the population and analyse cardiovascular indices calculated from the pulse waveforms. Results are described in Section 4.2 and discussed in Section 4.3. [1]

4.1 Methodology

The series of diseased models explored in this chapter are designed using a RSM approach. RSM is composed of three main activities; the design of experiment, response surface estimation, and optimisation. The design phase consists of selecting a distribution of points in the input variable domain using a factorial design. Initially, a relatively coarse grid search over a physiological range of input parameters is considered. This helps us to understand the complex interactions between input parameters and the pressure and flow waveforms resulting from the numerical simulations. The eight varied input parameters are muscular and elastic diameter, muscular and elastic stiffness heart rate, stroke volume, total peripheral resistance and outflow pressure. The goal is to find the boundary over the input parameters resulting in jointly admissible output parameters.

[1] This study was conducted in collaboration with Medici Tech Ltd. The specific statistical design used in this study was conducted by Dr Erik Erhardt. Dr Erhardt designed the optimal input parameters for the numerical simulation to well represent a population of healthy and diseased subjects. The extensive literature review used to derive the input parameters, and all numerical simulations using 1-D modelling were conducted by myself. The methodology for the classification of the final fictive population into diseased states was created by Dr Erhardt.

From this initial run of simulations we are able to establish a relationship between input and output variables using a low order polynomial approximation. The relationship between input variables to output vectors is known as the *response surface*.

The optimisation phase of the RSM approach is an iterative process to find the best design variables to create a population of blood flow models that match characteristics of diseased cardiovascular systems. The results of the response surface are used to successively refine the input range for the simulations.

Within this section we describe the RSM (Section 4.1.1) used to create the fictive population. Section 4.1.2 briefly covers the random forest classification tool used to identify the disease state of the numerical model. In Section 4.1.3 we describe the search strategy of published cross-sectional studies looking at diabetic, hypertensive, and diabetic and hypertensive cohorts.

4.1.1 Response Surface Methodology (RSM)

Response surface methodology (RSM) combines experimental design, regression modelling, and optimisation techniques to relate one or more responses of a dependent variable to multiple inputs [Box & Wilson, 1951; Myers *et al.*, 2009]. RSM assists in finding the input region in which the optimal or target response(s) occurs.

In this work the input region (x) refers to the input parameters to the 1-D numerical model to simulate measured output parameters (y) such as systolic, diastolic pressure, and PWV. Since the 1-D model is governed by a system of nonlinear hyperbolic partial differential equations, the relationship between x and y is complex. It is possible to approximate this relationship using a low degree

polynomial of the form

$$y = f(x)\beta + \epsilon, \tag{4.1}$$

where $x = (x_1, x_2, ..., x_k)'$, $f(x)$ is a vector function of p elements that consists of powers and cross products of powers of $x_1, x_2, ..., x_k$ up to a given degree, β is a vector of p unknown constant coefficients, and ϵ is a random experimental error with assumed mean error of zero. An important assumption of the methodology is that the variables are continuous.

We use a second degree model of the form

$$y = \beta_0 + x'\beta_* + x'Bx + \epsilon, \tag{4.2}$$

where $x = (x_1, x_2, ..., x_k)'$,, $\beta_* = (\beta_1, \beta_2, ..., \beta_k)'$, and B is a symmetric matrix of order k, whose ith diagonal element is $\beta_{i,i}$ $(i = 1, 2, ..., k)$ and its (i, j)th off-diagonal element is $\frac{1}{2}\beta_{ij}$ $(i, j = 1, 2..., k\ i \neq j)$. Initially a first order polynomial was considered however it did not adequately model experimental responses. The second-order polynomial model was found to provide a good compromise between accuracy and computational cost.

The benefit of such a model is that it allows us to establish an approximate relationship between input and output parameters. Additionally, it helps us to identify the optimum setting of $x_1, x_2, ..., x_k$ that results in the desired output parameters, without running a large number of simulations (as would be needed in a Monte Carlo style approach; *e.g.* as used by Leguy *et al.* [2011]).

We created an experimental design based on a two-level fractional factorial of input parameters with centre points. This design samples from particular corner points of a hypercube for combinations of input parameters. This sampling strat-

egy has the advantage of requiring fewer iterations compared with a full factorial design (which would require, for an input vector of size m, 2^m runs).

A series of experiments were conducted to measure the response y for given x parameters. The goal is to find the boundary over the input parameters resulting in jointly admissible output parameters. The multidimensional space of input parameters is too large to perform a fine grid search over in order to find ranges for jointly admissible output values. Therefore, it is necessary to refine the choice of input parameters To simplify the possible input variables we clustered the 120-artery 1-D model into muscular and elastic arteries, as described in Chapter 3. We varied eight independent parameters of the 1-D model. These are the diameter of the muscular (MD) and elastic (ED) arteries; the heart rate (HR) and stroke volume (SV), which were varied by scaling the prescribed flow waveform at the aortic root; the arterial stiffness at the muscular (MS) and elastic (ES) arteries, which were varied according to the apparent pulse wave velocity (PWV). The muscular arteries consisted of the main aorta and the iliac bifurcation (see highlighted arteries in Fig. 5.1). Additionally, the total peripheral resistance (R) and outflow pressure (P_{out}) were changed. The compliance of the peripheral circulation and the length of the arteries were not changed, since it has been shown that these parameters do not significantly change the pressure and flow waveforms [Leguy *et al.*, 2011; Willemet *et al.*, 2013]. Initially, a coarse grid of variables was considered to explore the region of maximum response to identify a given disease set of output parameters.

We consider the following nine cardiovascular indices (output parameters): carotid-femoral PWV, carotid-radial PWV, carotid-brachial PWV, carotid-ankle PWV, systolic pressure, diastolic pressure, mean pressure, diastolic aortic diame-

ter, and systolic aortic diameter, as well as several indices derived from the PPG waveform. The units of each input parameter differ from one another hence they were transformed into coded variables. The mid value is defined as 1 and a low and high value correspond to -1 and $+1$, respectively. This method gives each predictor an equal share in determining the dominant predictor in the response surface. Initial low and high input parameters are shown in Table 4.1.

Parameter Name	low	mid	high
Muscular Artery Diameter	0.5	1	1.5
Elastic Artery Diameter	0.7	1	1.3
Heart Rate	0.705	1	1.295
Stroke Volume	0.6	1	1.4
Muscular Artery Stiffness	0.7	1	1.3
Elastic Artery Stiffness	0.78	1	1.22
Total Peripheral Resistance	0.8	1	1.2
Outflow Pressure	0.778	1	1.222

Table 4.1: Initial low, mid and high input parameters for experimental design.

The results of this grid search were used to define a range of input parameters with admissible outputs (i.e. outputs that are within a physiologically range). From this admissible range of input values several iterations of further simulations were performed sampling within the range. For this sub-sampling an estimate of the mean and variance of a Multivariate Normal (MVN) distribution was calculated from the admissible input range. MVN is a vector composed of elements that are each normally distributed. From the MVN distribution admissible sample input

points were drawn. Dr Erhardt designed an iterative process that repeatedly re-centered and reoriented (via covariance matrix) until sampling from a distribution centere in the applicable location and wide enough to cover the entire admissible range. This took a total of three iterations.

Statistical analysis was performed using a two-tail unpaired Student's t test with a significant difference being at the level of less than 0.05, 0.01 and 0.001.

4.1.2 Random Forest Classification

From the data set simulated in Section 4.1.1, we apply a classification framework to differentiate between normotensive, diabetic, hypertensive, and combined hypertensive and diabetic disease states. We used a random forest classification (RFC) tool which is an algorithm based on an ensemble of many classification trees [Breiman, 2001]. Each decision tree contains a subset of variables randomly selected from the original set. Classification predictions are made by the combined outcomes of the fully grown trees. This technique has the benefit of not over-fitting the data, and runs efficiently on large databases whilst allowing us to explore the relationship between the input variables. This type of classification has been used in predicting disease risk [Khalilia *et al.*, 2011] and guiding public health policy [Cushman *et al.*, 2010].

To model the relationship between the eight input variables and the nine output parameters, we implemented the 'randomForest' package [Liaw & Wiener, 2002] within the R enviroment [R Development Core Team, 2014]. From the original data set (*i.e.* the 120-artery 1-D model), 2,000 random tree samples were generated, with 3 variables considered at each split.

4.1.3 Search Strategy

Studies published up to September 2015 were searched manually in PubMed. Key words for the search were 'hypertension' and 'diabetes' and 'blood pressure' and 'PWV'.

The list of titles and abstracts was initially screened for relevancy. Articles were then excluded if they: (1) did not explicitly exclude or not provide information on whether diabetics were excluded from hypertensive cohorts, or hypertensive from diabetic cohorts; (2) included children or adolescents; (3) were animal studies; (4) were studies testing pharmacological agents; (5) were in languages other than English; (6) were *in vitro* or model-based studies; or (7) were review articles. Relevant articles were then checked in full to confirm eligibility and extract data.

Data extraction was standardized by use of a single form, which included publication date and author, sample size method of cfPWV measurement, blood pressure, variables relative to numerical models (either as input or output variables). These are summarised in Table 4.1. Not every study explicitly stated the distribution of participants between Type 1 and Type 2 diabetes; these are indicated by the symbol '?' in the 'Diabetes Status' column.

Reference	Diabetes Status	Sample n				Men %				Age				Measured Parameters
		Baseline	Diabetes	Hypertension	Combined	Baseline	Diabetes	Hypertension	Combined	Baseline	Diabetes	Hypertension	Combined	
Andersen *et al.* [2003]	20- DM1 25-DM2	45		45	45	69		53	69	52	-	53	55	SDP, DBP, HR, EJT
Bella *et al.* [2001]	?	1025	642	614	874	39	30	42	35	58	58	62	61	SDP, DBP, PP, HR,
Bruno *et al.* [2012]	DM2	82	-	175	84	57	-	60	58	55	-	54	57	SBP, DBP, PP, MBP, PWV (c-f), HR, CSBP, CPP
Eren *et al.* [2004]	DM2	27	24	25	18	41	38	40	28	50	51	55	54	SBP, DBP, PP, HR, ASD, ADD, PDC, Dis
Fegan *et al.* [2003]	DM2	-	13	-	13	-	38	-	38	-	61	-	61	SBP, DBP, MAP, Cap
Fegan *et al.* [2003]	DM2	-	-	19	19	-	53	-	53	-	67	-	63	SBP, DBP, MAP, Cap
Gamella-Pozuelo *et al.* [2015]	DM2	82	93	209	-	40	68	56	-	56	60	58	-	SBP, DBP, HR
Giannarelli *et al.* [2012]	DM2	45	48	90	-	44	60	58	-	43	58	50	-	SBP, DBP, MBP, HR, CarPP, CarDia, CarDi, CarDistens, CarStiff, PWV(c-f)
Grossman *et al.* [1992]	DM2	25	-	25	25	40	-	40	40	53	-	57	59	SBP, DBP, MAP, HR, SV, CO, TPR
Hildebrandt *et al.* [2005]	DM2	-	-	749	105	-	-	58	59	-	-	66	67	SBP, DBP, PP, HR, CO, CI, TPR
Isnard *et al.* [1989]	-	15	-	16	-	27	-	19	-	33	-	38	-	SBP, DBP, MAP, PP, HR, AADD, AASD, PWV (c-f)
Kulkarni *et al.* [2014]	DM2	30	28	31	55	47	54	48	45	52	52	55	59	SBP, DBP, PP, PWV (b-a), PWV(c-f), CPP, Aix
Lacy *et al.* [2004a]	25-DM1 41-DM2	66	66	-	-	64	64	-	-	55	55	-	-	SBP, DBP, MAP, PP, CPP, HR, PWV (c-f),T1, T2,EJT
Megnien *et al.* [1992]	DM2	11	9	9	-	100	100	100	-	43	48	47	-	SBP, DBP, MBP, Bdia, PWV(b-r), ArtComp
Mitchell *et al.* [2003]	-	19	-	60	-	100	-	100	-	60	-	60	-	SBP, DBP, PP, MAP, HR, CO, SV, PR, TAC, PWV(c-f), PWV(c-r), PWV(c-f),Aix,
Mitchell *et al.* [2003]	-	11	-	50	-	0	-	0	-	56	-	61	-	SBP, DBP, PP, MAP, HR, CO, SV, PR, TAC, PWV (c-f), PWV(c-r), PWV(c-b), Aix,
Paini *et al.* [2006]	DM2	94	-	243	126	74		62	58	53	-	53	63	SBP, DBP, MAP, PP, HR, CarPP, CarDD, PWV(c-f)
Ravikumar *et al.* [2002]	?	50	50	-	-	46	46	-	-	54	54	-	-	SBP, DBP, Aix
Tedesco *et al.* [2004]	DM2	35	50	50	85	60	68	60	39	52	55	53	55	SBP, DBP, PP, MBP, HR, PWV(c-f)
Triantafyllou *et al.* [2014]	-	86	-	137	-	52	-	71	-	43	-	45	-	SBP, DBP, HR, PWV, Aix
Wang *et al.* [2013]	?	639	58	312	54	48	62.	54	48	47	55	55	60	SBP,DBP,PP,HRR,CAVI
Wilkinson *et al.* [2000]	DM1	35	35	-	-	40	40	-	-	30	30	-	-	SBP, DBP, MAP, PP, Aix, CSBP, CDBP, CPP, EJT
Zhang *et al.* [2011]	DM2	79	79	-	-	49	49	-	-	60	60	-	-	SBP, DBP, PP, HR, PWV (c-f), PWV(c-r), PWV(c-a), Aix

Table 4.2: SBP, systolic blood pressure; DSP, diastolic blood pressure; PP, pulse pressure; MAP, mean arterial pressure; HR, heart rate; PWV (c-f), pulse wave velocity carotid to femoral; PWV (b-a), pulse wave velocity brachial to ankle; PWV (c-r), pulse wave velocity carotid to radial; PWV (c-b), pulse wave velocity carotid to bracial; EJT, ejection time; CSP, central systolic blood pressure; CPP, central pulse pressure; ASD, aortic systolic diameter; ADD, aortic diastolic diameter; PDC, aortic pulsatile diameter change; AADD, aortic arch diastolic diameter; AASD, aortic arch systolic diameter; CarPP, carotid pulse pressure; Cap, capillary pressure; TAC, total arterial compliance; Aix, augmentation index at the Dis, distensibility;

4.2 Results

4.2.1 Factorial Design and RSM Analysis

Relevant input variables for the simulations presented in this chapter were derived using the response surface methodology and random forest classification described in Sections 4.1.1 and 4.1.2, respectively. This experimental procedure was designed and conducted by the collaborating group, Medici Tech Inc, USA; thus only the subsequent results of the statistical design are presented in this chapter.

4.2.2 Fictive Population Simulations – Global Haemodynamic Biomarkers

Figures 4.1 and 4.2 present the measured PWV carotid-femoral, PWV carotid-radial, PWV carotid-brachial, PWV carotid-ankle, systolic pressure, diastolic pressure, mean pressure, diastolic diameter, and systolic diameter of the simulated database for the baseline, diabetic, combined diabetic and hypertensive, and hypertensive subgroups.

For the fictive baseline, diabetic, diabetic and hypertensive, and hypertensive subgroups no statistically significant difference was identified between the subgroups for the PWV carotid-femoral parameter. For all the subgroups, the maximum measured PWV was 9.8 m s^{-1} and the minimum 3.7 m s^{-1}. The lack of distinct differentiation between the diseased states does not match what is found in the literature: PWV carotid-femoral was elevated in patients with combined hypertensive and diabetic compared healthy controls [Kulkarni *et al.*, 2014].

For the carotid-radial PWV, it is possible to differentiate the hypertensive

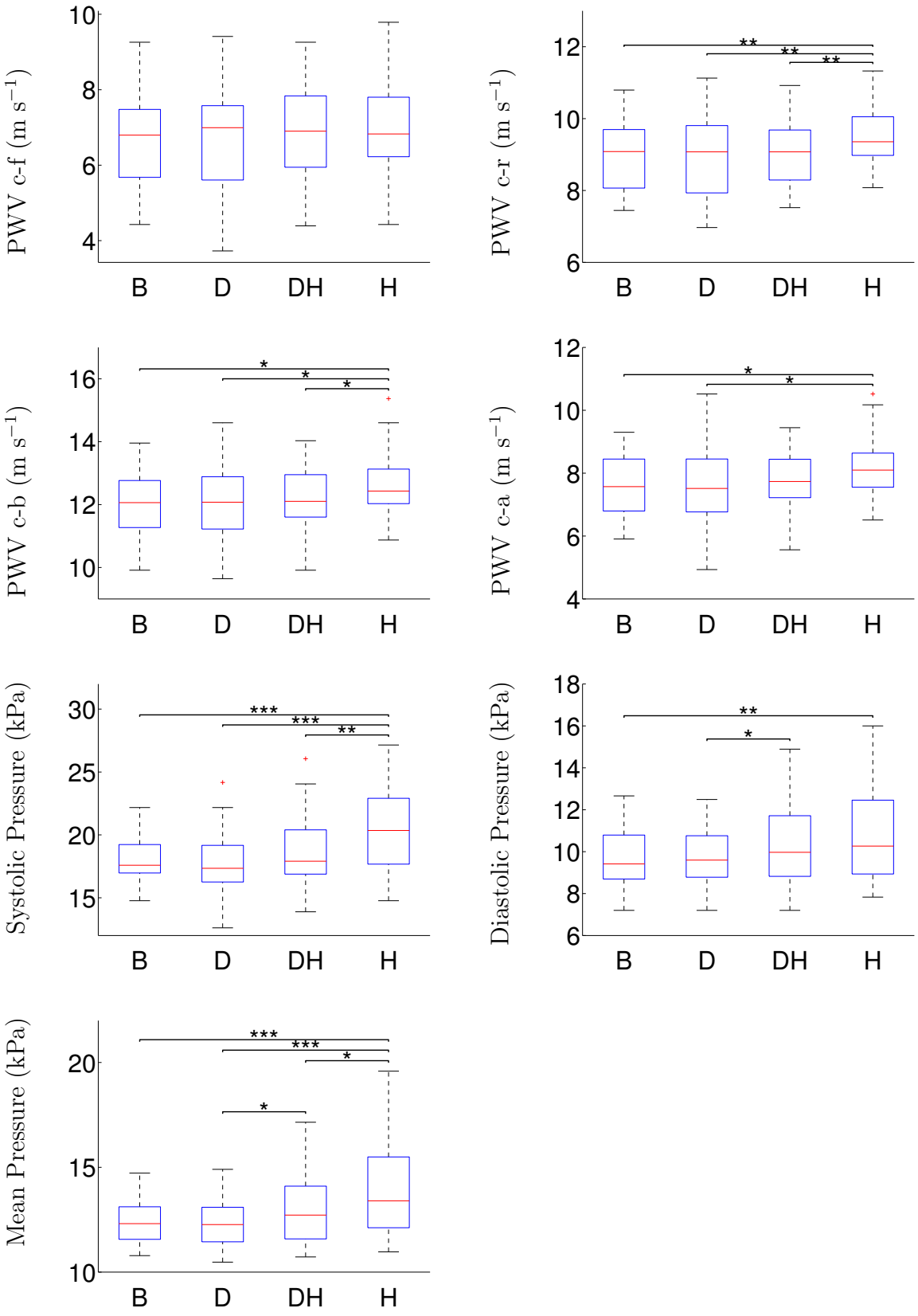

Figure 4.1: Boxplots of carotid-femoral, carotid-radial, carotid-brachial, and carotid-ankle PWV and systolic, diastolic, and mean pressure of the fictive population at baseline (B), diabetic (D), combined diabetic and hypertensive (DH), and hypertensive (H) conditions. On each box, the central mark is the median, the edges of the box are the 25th and 75th percentiles, the whiskers extend to the most extreme data points not considered outliers, and outliers are plotted individually. A t-test value of less than 0.05, 0.01 and 0.001 are indicated by *, **, and ***, respectively.

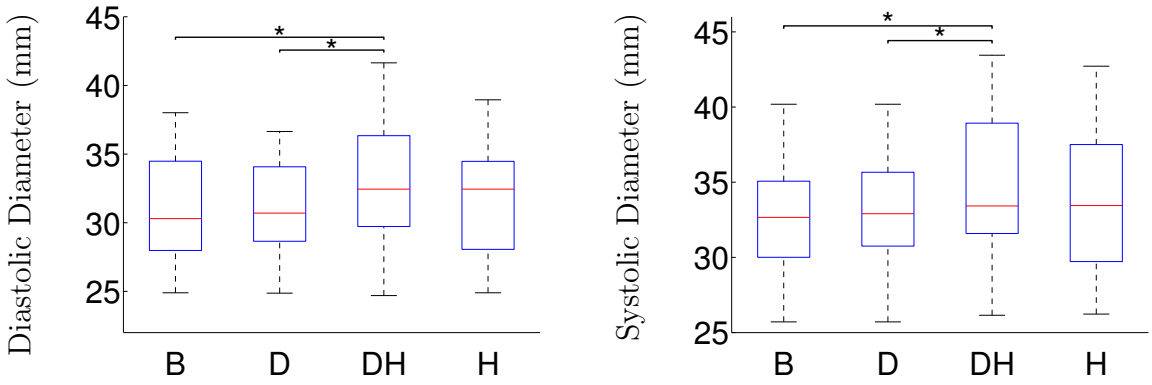

Figure 4.2: Boxplots of aortic diastolic and systolic diameter of the fictive population at baseline (B), diabetic (D), combined diabetic and hypertensive (DH), and hypertensive (H) conditions. On each box, the central mark is the median, the edges of the box are the 25th and 75th percentiles, the whiskers extend to the most extreme data points not considered outliers. A t-test value of less than 0.05, 0.01 and 0.001 are indicated by *, **, and ***, respectively.

subgroups from the baseline, diabetic, and the combined diabetic and hypertensive subgroup, with a t-test value <0.01. The median values of carotid-radial PWV for the baseline, diabetic, combined diabetic and hypertensive and hypertensive subgroups are 9.1, 9.1, 9.1 and 9.4 m s $^{-1}$, respectively. There were no outliers in any of the cohorts.

In Fig. 4.1 the baseline, diabetic, combined diabetic and hypertensive, and hypertensive subgroups measured a median carotid-brachial PWV value of 12.1, 12.1, 12.1 and 12.4 m s^{-1}, respectively. The minimum and maximum measured carotid-brachial PWV across all groups was 9.5 and 15.4 m s^{-1}, respectively. There was a statistical significant difference between the hypertensive subgroup and all other groups (p value <0.01).

The baseline, diabetic, combined diabetic and hypertensive, and hypertensive subgroups had a median carotid-ankle PWV of 7.6, 7.5, 7.7 and 8.1 m s^{-1}, re-

spectively. The minimum and maximum PWV across all groups was 4.9 and 10.5 m s^{-1}, respectively. There was a statistically significant difference between the hypertensive subgroup and the baseline and diabetic subgroups (p value < 0.01).

The baseline, diabetic, combined diabetic and hypertensive, and hypertensive subgroups had a median systolic pressure of 17.6, 17.3, 17.9 and 20.4 kPa, respectively. The minimum and maximum systolic pressure was 12.6 and 27.1 kPa, respectively. The hypertensive cohort was statistically significantly different from the combined diabetic and hypertensive subgroups ($p<0.01$). Additionally, the hypertensive subgroup was statistically different from the diabetic and baseline subgroups ($p<0.001$).

The baseline, diabetic, combined diabetic and hypertensive, and hypertensive subgroups had a median diastolic pressure of 9.4, 9.6, 10.0 and 10.3 kPa, respectively. The minimum and maximum diastolic pressure across the fictive population was 7.2 and 16 kPa, respectively. The hypertensive subgroup was statistically different from the baseline subgroup ($p<0.01$). The diabetic subgroup was significantly different from the combined diabetic and hypertensive subgroup ($p<0.05$).

The baseline, diabetic, combined diabetic and hypertensive, and hypertensive subgroups had a median mean pressure of 12.3, 12.3, 12.7 and 13.4 kPa, respectively. The minimum and maximum mean pressure across the fictive population was 10.5 and 19.6 kPa, respectively. The hypertensive subgroup was significantly different from the baseline ($p<0.001$), diabetic ($p<0.001$) and combined diabetic and hypertensive ($p<0.05$) subgroups. Additionally, the diabetic subgroup was statistically different from the combined diabetic and hypertensive subgroup ($p<0.05$).

In Fig. 4.2 the baseline, diabetic, combined diabetic and hypertensive, and

hypertensive subgroups had a median diastolic diameter of 30.3, 30.7, 32.5 and 32.5 mm. Within the fictive population the diastolic diameter ranges from 24.7 to 41.6 mm. The combined diastolic and hypertensive subgroup was significantly different from the baseline and diabetic subgroups ($p<0.05$).

The baseline, diabetic, combined diabetic and hypertensive, and hypertensive subgroups had a median diameter at systole of 32.6, 32.9, 33.4 and 33.4 mm, respectively. Within the fictive population the diastolic diameter ranges from 25.7 to 43.4 mm, respectively. The combined diastolic and hypertensive subgroup was significantly different from the baseline and diabetic subgroups ($p<0.05$).

4.2.3 Fictive Population Simulations – PPG Biomarkers

Figure 4.3 shows the PPG features (described in Section 3.2.1.3) of the virtual database of healthy patients (B) and patients with diabetes (D), diabetes and hypertension (DH), and hypertension (H). There is no statistical difference between the healthy and diseased patient groups for CT, PS, PD, With and Area.

The only statistically significant difference in subgroup datasets is found for the index dT: the time between the two peaks of the PPG waveform. The unpaired two-sample t-test analysis was used to determine whether the two sets of data are significantly different from each other. From our fictive population we are able to differentiate the hypertensive group from the diabetic and baseline subgroups, with a t-test value of 0.05 and 0.01, respectively. Compared to the hypertensive median value of 307 ms, the diabetic and hypertensive subgroups have a median value of 331 ms. In the literature dT is most often found in the form of the stiffness index, SI=H/dT, where H is the height of the patient.

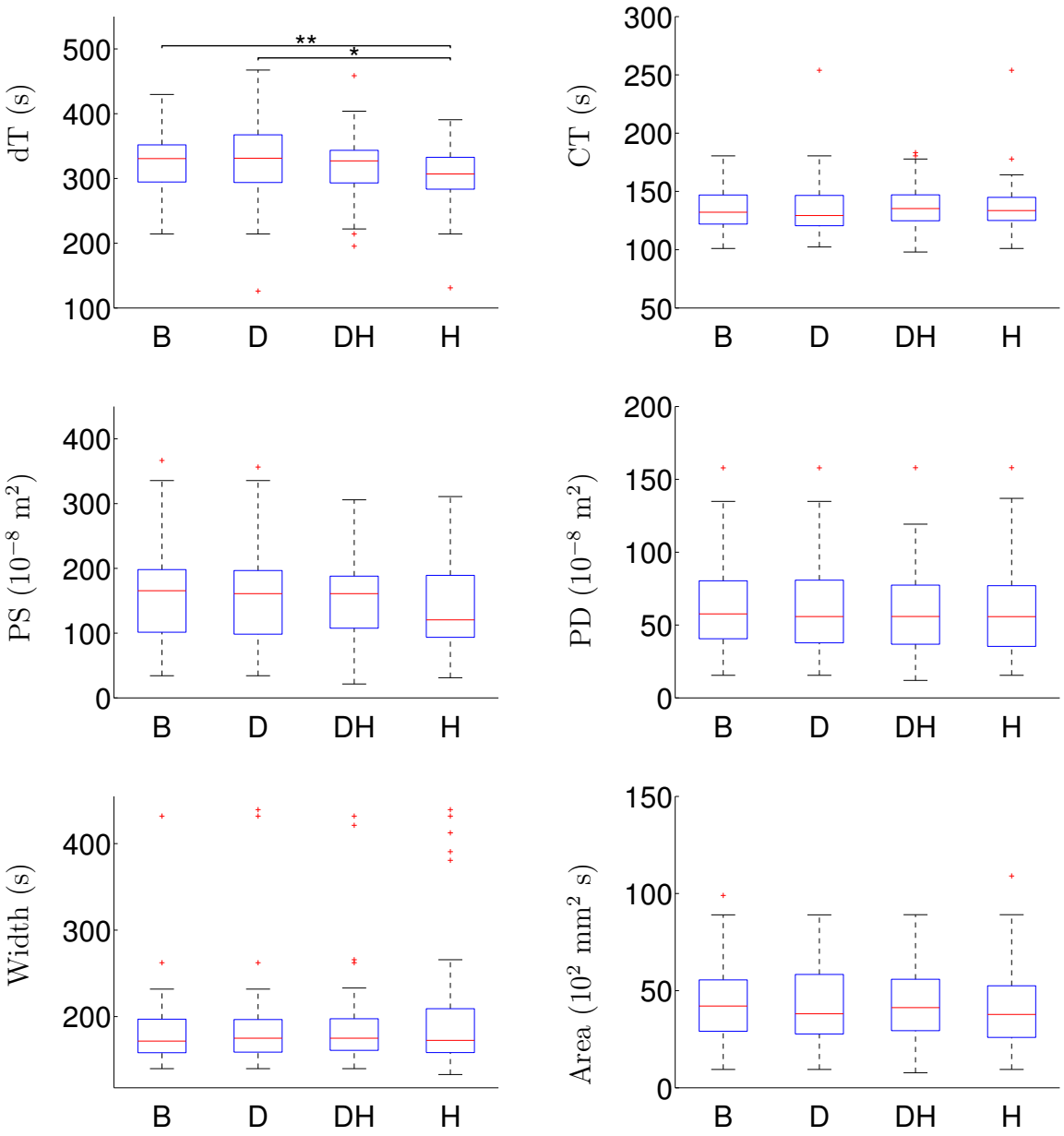

Figure 4.3: Boxplots of dT, CT, PS, PD, Width and Area of the PPG signal measured in the fictive population at baseline (B), diabetic (D), combined diabetic and hypertensive (DH), and hypertensive (H) conditions. On each box, the central mark is the median, the edges of the box are the 25th and 75th percentiles, the whiskers extend to the most extreme data points not considered outliers, and outliers are plotted individually. A t-test value of less than 0.05, 0.01 and 0.001 are indicated by *, **, and ***, respectively.

Eduardo & Gomes [2015] observed no statistically significant change in SI between patients with Type I diabetes and a control group. Boos *et al.* [2007] found a statistically significant increase of SI in patients with hypertension compared to a baseline group. Since dT and SI are inversely proportional, our results are in good agreement with the change found in the literature for a hypertensive cohort.

Notably, the mixed diabetic and hypertensive group is not statistically significantly different from any other of the diseased of healthy subgroups. No data could be found for dT or SI in the literature for a mixed hypertensive diabetic subgroup.

From the analysis of our fictive healthy and diseased population simulations we do not detect a statistically significant difference in the measured CT at the digital artery. The measured CT ranges from 98.0 to 253.9 ms. The baseline, diabetic, combined diabetic and hypertensive, and hypertensive subgroups had a median CT value of 132.2, 129.3, 135.3 and 133.6 ms, respectively.

The work of Liu *et al.* [2014] has found no statistical significant difference between CT of an aged matched diabetic and normal patient group. Jaryal *et al.* [2009] also found no correlation between diabetes and CT. However, they did not provide data on whether the patients were also hypertensive; thus no definitive conclusions can be drawn for the purpose of this analysis. A more recent study by Hubena *et al.* [2015] found, in aged matched patients, that CT was significantly higher in diabetic group compared to the control group. Dillon & Hertzman [1941] observed an increase in crest time in patients with hypertension from normal patients. However, it should be noted that the hypertensive cohort had an average age of 41 years, and the normal group an average age of 26 years. No study could be found analysing the crest time in patients with combined hypertension and

diabetes.

The baseline, diabetic, combined diabetic and hypertensive, and hypertensive had a median PS value of 165.5, 161.0, 161.0 and 120.4 (10^{-8}m^2), respectively. No statistically significant difference was identified between the subgroups. Across all groups the minimum measured PS was 21.4 and the maximum 366.7 (10^{-8}m^2). An outlier was identified in the baseline and diabetic subgroups. Hubena *et al.* [2015] found a significantly higher values of PS in the diabetic group in comparison with the control group, at statistically significant level $p < 0.05$. This finding is not observed in our fictive population.

The baseline, diabetic, combined diabetic and hypertensive, and hypertensive had a median PD value of 57.75, 55.8, 55.8 and 55.7 (10^{-8}m^2), respectively. No statistically significant difference was identified between the subgroups. Across all groups the minimum measured PD was 12.0 and the maximum 158.0 (10^{-8}m^2). An outlier was identified in each of the subgroups.

The baseline, diabetic, combined diabetic and hypertensive, and hypertensive had a median Width value of 171.7, 175.0, 175.0 and 172.6 s, respectively. No statistically significant difference was identified between the subgroups. Across all groups the minimum measured Width was 133.0 s and the maximum 439.3 s. For the baseline, diabetes, combined diabetes and hypertension, and hypertensive subgroups there were 2, 3, 4, and 5 outliers, respectively. Arza *et al.* [2013] has observed a relationship between PPG Width and systolic and diastolic pressure, however there is no direct study correlating Width and disease state.

The baseline, diabetic, combined diabetic and hypertensive, and hypertensive had a median Area value of 42.1, 38.1, 41.3 and 37.8 (10^2 mm^2 s), respectively. No statistically significant difference was identified between the subgroups. Across all

groups the minimum measured Area was 7.7 (10^2 mm^2 s) and the maximum 109.0 (10^2 mm^2 s). For the baseline, diabetes, combined diabetes and hypertension, and hypertensive subgroups there were 2, 3, 4, and 5 outliers, respectively.

Usman *et al.* [2013] looked at the area under the curve of the PPG waveform in 101 diabetic patients of Type 2, aged 50 to 70 years old. The results of this work show that an increased level of HbA1c (a measure of plasma glucose over a prolonged period) was related to a decrease in area under the curve. The authors suggested that changes in arterial properties can be non-invasively detected by analysing pulse shape characteristics. However, without a control group to compare the results to, it is difficult to extrapolate whether a diabetic subgroup would be statistically different from a baseline or hypertensive subgroup.

4.3 Discussion and Concluding Remarks

The main aim of this chapter was twofold. First, we have presented a novel methodology to optimise the input parameters of the 120-artery 1-D model developed in Chapter 3 in order to match biomarkers that have been reported in the literature. Second, we have analysed these simulated data sets to determine if additional parameters taken from the PPG waveform could be used to classify diabetes versus hypertension subjects.

To our knowledge, this is the first time that the RSM has been applied to the field of 1-D blood flow modelling in the larger systemic arteries. Elements of experimental statistical design are needed due to the complex relation between input and output conditions of the 1-D numerical model. We have attempted to match the following output parameters of the 1-D model using RSM: carotid-

femoral PWV, carotid-radial PWV, carotid-brachial PWV, carotid-ankle PWV, systolic pressure, diastolic pressure, mean pressure, aortic diastolic diameter, and aortic systolic diameter. Our methodology requires us to generate a database of virtual arterial waveforms using a 1-D modelling in the 120 larger systemic arteries, including the vasculature of the hands and head. The outputs of the set of 200 virtual subjects were assessed against literature data. The choice of sample size was identified by Dr Erdhardt as being large enough to draw statistically applicable results, but small enough to feasibly run several iterations within the given time. The simulation models built in this study are generic to each disease state, and do not attempt to match patient-specific data, but rather we followed a disease-centered approach.

Using our virtual population, we have assessed the cross-sectional area morphology by analysing 6 measurable parameters. We analysed our fictive population of healthy and diseased simulations to assess whether additional parameters extracted from the PPG waveform could be used in the identification and classification of disease. Our results suggest that the dT (the time between the two peaks of the PPG waveform) could be useful for this purpose. This observation is supported by *in vivo* trials from the literature that have shown that dT is related to aortic PWV [Millasseau *et al.*, 2002a].

While we varied elastic and muscular artery parameters across a range, we did not enforce a relation between their variations. Greenwald *et al.* [1990] found the reflection coefficient at the aorta-iliac bifurcation ranged from +0.3 in early life to −0.3 in old age. In the work of Willemet *et al.* [2015] numerical simulations with an aorta-iliac reflection coefficient outside of a physiological range were excluded from the dataset. The reflection coefficient for all simulations fell within

the physiological range for our data set.

Chapter 2 analyses the sensitivity to changes in the morphology of the flow profile (whilst the mean flow is preserved) to PPG parameters, showing that subtle changes of the shape of the flow profile result in significant changes in the morphology of the PPG waveform. Liu *et al.* [2001] presents the cardiovascular abnormalities associated with diabetes, combined diabetes and hypertension, and hypertension in a sample of middle-aged and older adults. Diabetes is associated with abnormal left ventricular relaxation and combined diabetes and hypertension with more severe abnormal left ventricular relaxation.

It is noted that the same healthy flow profile is imposed as the inflow boundary condition for simulating all disease states, but its time period and absolute value are scaled to match literature data. This simplification was one such limitation of our study and was necessary due to generalised disease specific continuous measurements of inflow.

The literature search study within this chapter was conducted using publicly available datasets. One such limitation is citation bias, where researchers may have not published null results, which may have found diabetes and hypertension to have no bearing on haemodynamic parameters. This unknown could have the effect of increasing the significance or disease state on certain haemodynamic parameters. Additionally, each study will be limited by varying degrees of information bias, including errors in study design, patient recruitment, device error, and differing device models. This statistical noise may hinder predictive performance developed within this work.

From our analysis, further work needs to be conducted to classify disease state from PPG measurement alone. The optimal classification model would combine

traditional parameters such as pressure or PWV with parameters extracted from the PPG waveform.

Chapter 5

Reducing the Number of Parameters in 1-D Arterial Blood Flow Modelling

Within Chapters 3 and 4 we have studied how input parameters influence the simulated pressure and flow waveforms using the 1-D/0-D model. Up until now we have lumped the input parameters into two subsets, muscular and elastic arteries. This has the benefit of drastically reducing the complexity of the problem. In this Chapter we approach the problem from a different perspective. We consider what would happen if we were to alter the geometry of the initial problem. The work of Alastruey *et al.* [2006, 2007] has looked at how anatomical variations influence local pressure and flow changes. We present a novel methodology to look at how the number of arterial segments included into a model affect the simulated pressure and flow waveform. By reducing the number of input segments we are able to decrease the overall number of input parameters of the model. Since it is not

always possible to personalise every input parameter of an haemodynamic model to a patient, we look to maximise the proportion of patient-specific parameters to literature or estimated parameters.

Patient-specific modelling has the potential to revolutionise how disease is treated in the clinical setting. Already it has been used to expand our understanding of the underlying pathophysiology of aortic rupture [Doyle *et al.*, 2009], cerebral aneurysm [Cebral *et al.*, 2009; Tezduyar *et al.*, 2008], and atherosclerosis in the carotid [Milner *et al.*, 1998]. Patient-specific modelling has also been used to to guide surgical planning [De Zelicourt *et al.*, 2011; Marsden *et al.*, 2009; Taylor *et al.*, 1999; Wilson *et al.*, 2005] and to provide cardiovascular biomarkers of cerebrovascular resistance [Olufsen & Nadim, 2004; Pope *et al.*, 2009]. However there are limitations to this technique due to factors such as operator uncertainty [Glor *et al.*, 2004a,b, 2005] and modelling assumptions [Lee *et al.*, 2008; Moyle *et al.*, 2006]. How best to parameterise a blood flow model remains challenging. One such approach is to perform a sensitivity analysis to find out which parameters are most vital to be personalised [Cebral *et al.*, 2005a; Huberts *et al.*, 2013; Leguy *et al.*, 2011].

Persistently elevated blood pressure (hypertension) is now identified as the most important single cause of mortality worldwide. By 2025 it is predicted that 1.56 billion people will have hypertension [Kearney *et al.*, 2005]. The correlation between hypertension and independent biomarkers has been extensively analysed [Laurent *et al.*, 2001; Wang *et al.*, 2007]. However, understanding how properties of the cardiovascular system affect the aortic blood pressure waveform and its relation to the pressure waveform in the upper limb (where blood pressure is routinely measured) has not yet been fully understood [Kakar & Lip, 2006]. One-dimensional

arterial blood flow modelling has the potential to improve this understanding of human haemodynamics.

Several studies have shown the ability of the nonlinear 1-D equations of blood flow in compliant vessels to capture the main features of pressure and flow waves in the aorta and other large arteries [Leguy *et al.*, 2010; Mynard & Nithiarasu, 2008; Olufsen, 1999; Reymond *et al.*, 2009; Willemet *et al.*, 2013]. However, a major drawback of 1-D modelling is that the determination of model input parameters from clinical data is a very challenging inverse problem [Quick *et al.*, 2001, 2006]. In the 1-D formulation, the arterial network is decomposed into arterial segments characterised by geometrical and structural properties. The larger the number of arterial segments in a given 1-D model, the greater the number of model input parameters that need to be estimated. Thus, a method of minimising the number of 1-D model arterial segments should help to maximise the percentage of input parameters that can be estimated from clinical measurements and, hence, that can be patient specific.

Patient-specific 1-D [Marchandise *et al.*, 2009; Steele *et al.*, 2003] and 3-D models [Ku *et al.*, 2002; Wilson *et al.*, 2005] have proven useful in predicting haemodynamic responses to medical interventions. Additionally, patient-specific modelling of haemodynamics requires extensive data to construct a personalised geometric model generated from MRI [Long *et al.*, 2000], or computed tomography [Antiga *et al.*, 2003] data. Patient-specific models also are beneficial in estimating parameters that cannot be measured *in vivo* [Cebral *et al.*, 2005b].

Within the field of multi-branched 1-D modelling, there has yet to be a consensus reached in terms of the optimum number of arterial segments necessary to obtain good quality pressure and flow measurements at the aorta. The number of

arterial segments used in 1-D modelling has increased in recent years from 55 to 4 million [Avolio, 1980; Blanco *et al.*, 2014; Mynard & Nithiarasu, 2008; Perdikaris *et al.*, 2014; Reymond *et al.*, 2009; Stergiopulos *et al.*, 1992]. Obviously, with an increasing number of arterial segments the more challenging it becomes to estimate a greater percentage of the total number of input parameters from available patient-specific data. Running a distributed 1-D model requires geometric and material properties for each arterial segment, a prescribed input blood volume flow waveform, and outflow boundary conditions for every terminal vessel. Thus, with each generation of bifurcations in the arterial tree the number of input parameters that need to be prescribed increases exponentially.

Lumped parameter models of the cardiovascular system are also commonly used to simulate arterial blood flow. They were introduced by Frank [1899] under the guise of a 'hydraulic Windkessel', which consists of a resistor and capacitor in series. The Windkessel model is adept at portraying the exponential decay in diastole, but it is less able to describe the pressure waveform during the systolic phase of the cardiac cycle [Segers *et al.*, 2008]. More elaborate combinations of resistors, capacitors and impedances have been suggested to improve fitting in systole [Kind *et al.*, 2010; Olufsen & Nadim, 2004; Stergiopulos *et al.*, 1999]. However, with the drop in the spatial dimension, the Windkessel model neither accounts for wave propagation and reflection, nor can it simulate the effect of pulse wave velocity (PWV), which is assumed to be infinite. Wave reflections play an important role in shaping the pressure waveform and central PWV has been identified as a highly valuable marker of arterial stiffness, which is being used in the classification and diagnosis of hypertension [Mancia & The Task Force for the management of arterial hypertension of the European Society of Hypertension (ESH) and of the

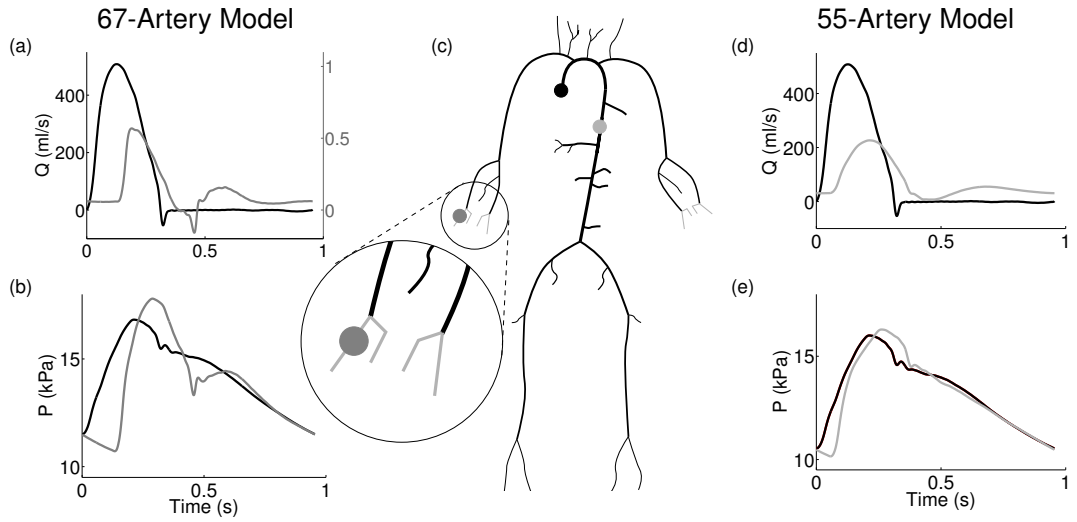

Figure 5.1: (c) Schematic representation of the 55-artery 1-D model (black). The circled region shows additional anatomical model of the hand included in the 67-artery model (grey), containing the superficial palmar arch and digital arteries. (a) Flow waveform prescribed at the aortic root as a reflective boundary condition (black), and simulated flow waveform at the digital artery (grey) for the 67-artery model. (b) Simulated pressure waveforms at the aortic root (black) and digital artery (grey) for the 67-artery model. (d) Flow waveform prescribed at the aortic root as a reflective boundary condition (black), and simulated flow waveform at the thoracic aorta (grey) for the 55-artery model. (e) Simulated pressure waveforms for the 55-artery model at the aortic root (black) and thoracic aorta (grey).

European Society of Cardiology (ESC), 2013]. Wave propagation and reflection can be studied using 1-D modelling [Willemet & Alastruey, 2014].

The aim of this study is to provide a new methodology for investigating the minimum number of tapered arterial segments required to simulate, using nonlinear 1-D modelling, the blood pressure and flow waveforms in the aorta and digital artery in the hand, where the upper limb pressure waveform is usually measured non-invasively. This is achieved by lumping peripheral 1-D model branches into Windkessel models that preserve the net resistance and total compliance of the original model. In addition, this methodology enables the analysis of the effect

of network topology and, hence, reflection sites on the shape of pressure and flow waves. Since the initial conditions of the problem will affect the results of any segment-reducing methodology, it is important to consider multiple initial conditions to the problem. Thus, our novel methodology is tested for the aorta of a 55-artery model under both normotensive and hypertensive conditions and for the digital artery of a 67-artery model under normotensive conditions (Fig. 5.1).

Section 5.1 describes the methodology to reduce the number of parameters in 1-D arterial blood flow modelling. In Section 5.2 the results of our novel methodology applied to different initial conditions area presented. Finally, Section 5.3 summarises and discusses results and observations.

5.1 Methods

We begin by describing the 55 and 67-artery models considered in this study (Sections 5.1.1 and 5.1.2). We then introduce our novel technique for lumping peripheral 1-D model branches into Windkessel models (Section 5.1.3). Lastly, we describe the error metrics used to analyse our results (Section 5.1.4).

5.1.1 55-artery model

The baseline 1-D arterial network considered in this work consists of the larger 55 arteries (Fig. 5.1c, black) with the properties of a normotensive human.

Until now in this thesis the geometry considered was a 120-vessel problem, which included the vasculature of the hand and head. One limitation of the methodology described in this chapter is that it cannot be applied to arterial loops; *i.e.* it cannot be applied to two vessels merging downstream from the heart

and hand. Thus why we consider an arterial geometry that excludes the vasculature of the head, which has a complex network of merging arteries. Additionally, unlike previous chapters, we consider a geometry of the hand that excludes a superficial palmar arch and deep palmar arch artery so that there are no arterial loops. Thus, we consider a 55 and a 67-artery model. The lengths of the arteries were not changed since previous studies have shown that this parameter does not change the pressure and flow waveforms significantly [Leguy *et al.*, 2011; Willemet *et al.*, 2013].

Figure 5.1d,e shows the flow and pressure waveforms at the aortic root and thoracic aorta of the 55-artery baseline model. We also considered a hypertensive model obtained by increasing arterial stiffness in all vessels of the baseline model and peripheral resistances in all Windkessel models. Both PWV and the total peripheral resistance in each terminal Windkessel ($R_1 + R_2$) are increased by a factor of 1.5.

5.1.2 67-artery model

We extended the baseline model by including the larger arteries of the hand using previously published data [Alastruey *et al.*, 2006, Table A1] (see Fig. 5.1c). Each hand consists of the superficial palmar arch and four digital arteries attached to the ulnar and radial arteries of the baseline model. Figure 5.1a,b shows the flow and pressure waveforms at the aortic root and digital artery of the 67-artery model. Pressure and flow in all four digital arteries are almost identical.

5.1.3 Reducing the number of arterial segments

The baseline model consists of the aorta and 5 generations of arterial bifurcations (Fig. 5.1c). We reduced the 55 arterial segments of this model using two procedures. In the first one, each successive reduction in the number of segments was achieved by decreasing the number of generations of bifurcations. For example, by eliminating the 5th generation of bifurcations, the arterial network is reduced to 53 arteries, since the right interosseous and right lower ulnar arteries (the only vessels at the 5th generation of bifurcations) are lumped into a single three-element Windkessel model coupled to the end point of the right upper ulnar.

In the second procedure, the number of arteries of the model containing the aorta up to the first generation of bifurcations was reduced by successively lumping each pair of the most peripheral vessels into a three-element Windkessel model (see Section 5.1.3.1). For example, the model up to the first generation of bifurcations (with 21 vessels) was reduced to 19 vessels by combining the left and right common iliac arteries into a three-element Windkessel model coupled to the lower abdominal aorta.

The 67-artery model (Fig. 5.1c, grey) was reduced to a model consisting of only the arterial segments of the upper right limb and ascending aorta, which is similar to the model of Karamanoglu *et al.* [1994]. Similarly to the 55-artery model, we reduced the number of arteries by first successively decreasing the number of generations of bifurcations and then systematically reducing the number of aortic segments. Thus, the 67-artery model was reduced up to the 19-artery model shown in Fig. 5.2f. This reduction enables the evaluation of a the digital artery (a peripheral measuring site) throughout the systematic reduction of arteries. The

maximum reduction of the 55-artery network gives a network of 1 artery (Fig. 5.3f).

5.1.3.1 Reducing a 1-D model terminal branch into an equivalent 0-D model

We describe our novel methodology to lump a single nonlinear 1-D model vessel of length l coupled with a linear three-element Windkessel model at the outlet (Fig. 5.4a) into a linear two-element Windkessel model (Fig. 5.4c). The vessel has a pressure and flow $p_{\text{in}}(t)$ and $q_{\text{in}}(t)$ at the inlet, and $p_{\text{out}}(t)$ and $q_{\text{out}}(t)$ at the outlet. The outlet forms the inlet boundary conditions of the Windkessel model, which has an outlet flow $\widehat{q_{\text{out}}}(t)$ and constant pressure $\widehat{p_{\text{out}}}$.

In previous derivations of the linear 0-D formulation from the nonlinear 1-D equations, it was assumed constant cross-sectional area and material properties along the length of the arterial segment or an average cross-sectional area [Alastruey *et al.*, 2008; Milišić & Quarteroni, 2004; Olufsen & Nadim, 2004]. In the following analysis we will not make such an assumption and will allow area and material properties to vary with the position along the vessel.

We consider the following linearised version of the 1-D equations [Alastruey *et al.*, 2012a],

$$\frac{A_{\text{d}}}{\rho c_{\text{d}}^2}\frac{\partial p}{\partial t} + \frac{\partial q}{\partial x} = 0, \tag{5.1a}$$

$$\frac{\partial q}{\partial t} + \frac{A_{\text{d}}}{\rho}\frac{\partial p}{\partial x} = \frac{-2(\xi+2)\pi\mu q}{\rho A_{\text{d}}}, \tag{5.1b}$$

where we have used $Q = UA$ and linearised about the diastolic conditions, (A, P, Q)= $(A_{\text{d}}+a, P_{\text{d}}+p, q)$, where $a(x,t)$, $p(x,t)$ and $q(x,t)$ are the perturbation variables for area, pressure and flow rate. The physiological conditions in the arterial system are only weakly nonlinear, thus many characteristics can be captured by the linearised

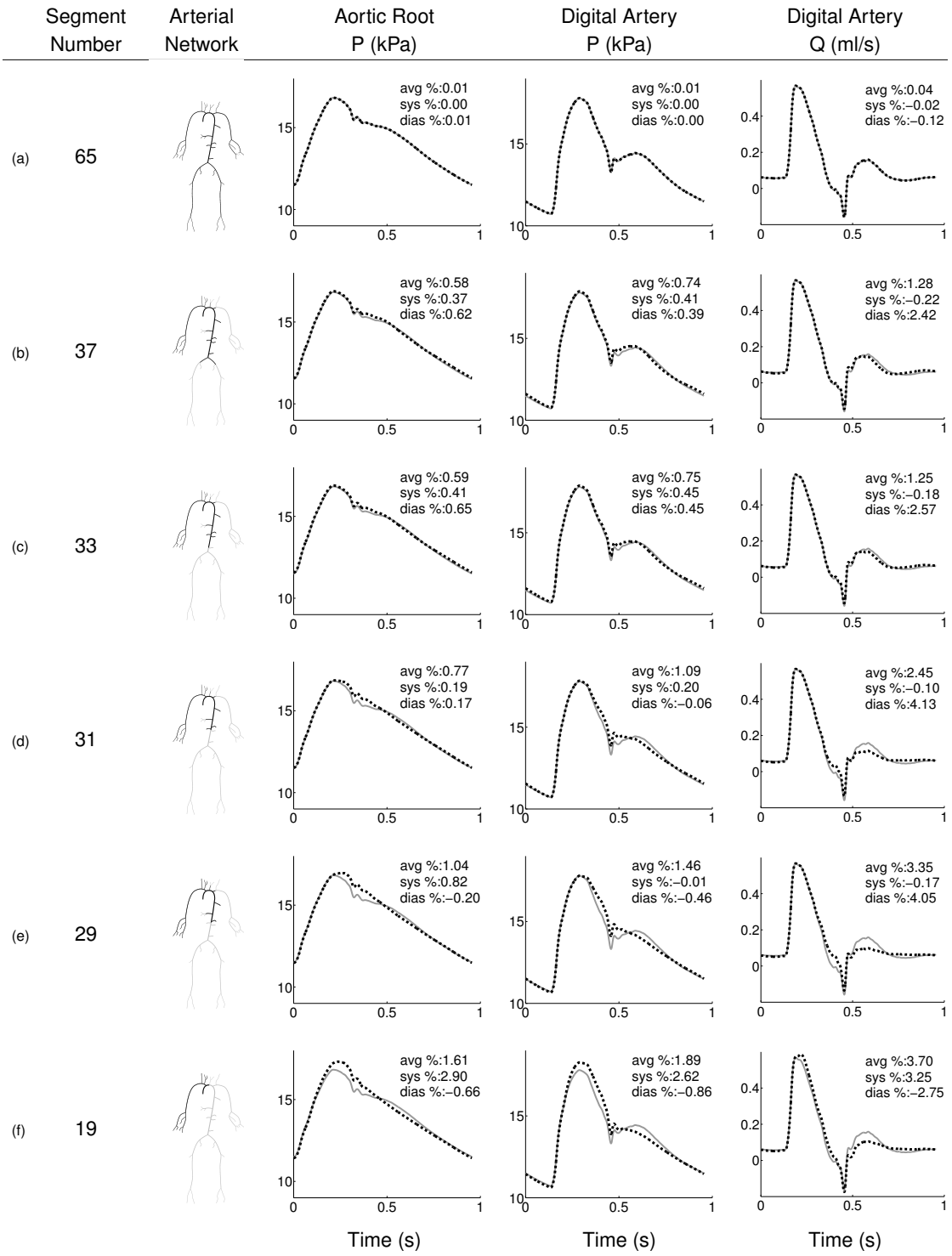

Figure 5.2: Pressure (P) and flow (Q) waveforms at the aortic root and midpoint of the digital artery of the 67-artery model (solid grey) and several reduced models (dashed black), one for each row. The number of segments and the arterial topology for each reduced model are given in the first two columns. Average (avg), systolic (sys) and diastolic (dias) relative errors are indicated in the top right corner of each plot.

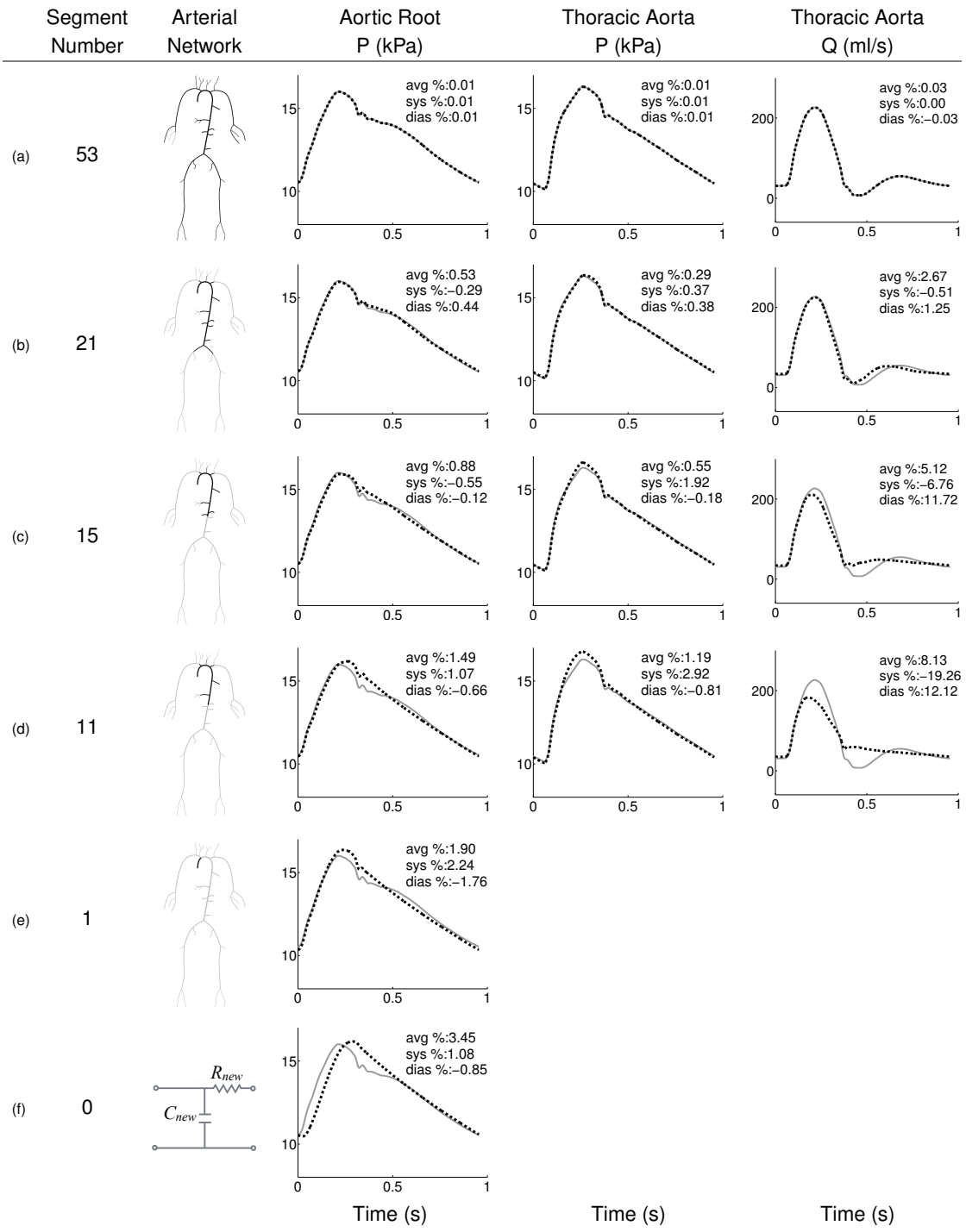

Figure 5.3: Pressure (P) and flow (Q) waveforms at the aortic root and midpoint of the thoracic aorta of the normotensive 55-artery model (solid grey) and several reduced models (dashed black), one for each row. The number of segments and the arterial topology for each reduced model are given in the first two columns. The aortic-root pressure waveform calculated by a two-element Windkessel model of the whole systemic circulation is shown in (f). Average (avg), systolic (sys) and diastolic (dias) relative errors are indicated in the top right corner of each plot.

system [Dick *et al.*, 1968]. To continue we introduce the following theorem:

Theorem 1. *Mean Value Theorem (MVT): Suppose* $f : [b_1, b_2] \to \Re$ *is continuous and suppose* $g \geq 0$ *is bounded and continuous on* $[b_1, b_2]$*, then there is* $\zeta \in [b_1, b_2]$ *such that*

$$\int_{b_1}^{b_2} f(x)g(x)dx = f(\zeta) \int_{b_1}^{b_2} g(x)dx, \tag{5.2}$$

and

$$f(\zeta) = \frac{\int_{b_1}^{b_2} f(x)g(x)dx}{\int_{b_1}^{b_2} g(x)dx}. \tag{5.3}$$

Integrating the linearised 1-D Eqs. (5.1a) and (5.1b) along the x-axis yields

$$\int_0^l \left(\underbrace{\frac{A_\mathrm{d}}{\rho c_\mathrm{d}^2} \frac{\partial p}{\partial t}}_{\mathrm{a}} + \underbrace{\frac{\partial q}{\partial x}}_{\mathrm{b}} \right) dx = 0, \tag{5.4a}$$

$$\int_0^l \left(\underbrace{\frac{1}{A_\mathrm{d}} \frac{\partial q}{\partial t}}_{\mathrm{c}} + \underbrace{\frac{1}{\rho} \frac{\partial p}{\partial x}}_{\mathrm{d}} \right) dx = - \int_0^l \underbrace{\frac{2(\xi + 2)\pi\mu q}{\rho A_\mathrm{d}^2}}_{\mathrm{e}} dx, \tag{5.4b}$$

where we have divided the last equation by $A_\mathrm{d}(x)$. We first evaluate both terms of Eq. (5.4a):

(a) $\int_0^l \frac{A_\mathrm{d}}{\rho c_\mathrm{d}^2} \frac{\partial p}{\partial t} dx = \frac{1}{\rho} \frac{dp(\zeta_1, t)}{dt} \int_0^l \frac{A_\mathrm{d}}{c_\mathrm{d}^2} dx$;

(b) $\int_0^l \frac{\partial q}{\partial x} dx = q_\mathrm{out} - q_\mathrm{in}$, with $q_\mathrm{out} = q(l, t)$ and $q_\mathrm{in} = q(0, t)$.

Since $p(x, t)$ is continuous and $\frac{A_\mathrm{d}}{c_\mathrm{d}^2}$ is bounded and continuous, with $A_\mathrm{d}(x) > 0$ and $c_\mathrm{d}(x) > 0$ under physiological conditions, we applied the MVT to (a), with $\zeta_1 \in [0, l]$.

We now evaluate each term of Eq. (5.4b):

(c) $\int_0^l \frac{1}{A_\mathrm{d}} \frac{\partial q}{\partial t} dx = \frac{dq(\zeta_2,t)}{dt} \int_0^l \frac{1}{A_\mathrm{d}} dx$;

(d) $\int_0^l \frac{1}{\rho} \frac{\partial p}{\partial x} = \frac{p_\mathrm{out} - p_\mathrm{in}}{\rho}$, with $p_\mathrm{out} = p(l,t)$ and $p_\mathrm{in} = p(0,t)$;

(e) $-\frac{2(\xi+2)\pi\mu}{\rho} \int_0^l \frac{q}{A_\mathrm{d}^2} dx = -\frac{2(\xi+2)\pi\mu}{\rho} q(\zeta_3,t) \int_0^l \frac{1}{A_\mathrm{d}^2} dx$.

Since $q(x,t)$ and $\frac{\partial q(x,t)}{\partial t}$ are continuous and $\frac{1}{A_\mathrm{d}}$ and $\frac{1}{A_\mathrm{d}^2}$ are bounded and continuous with $A_\mathrm{d}(x) > 0$ under physiological conditions, we can apply the MVT to (c) and (e) with ζ_2 and $\zeta_3 \in [0, l]$ [Milišić & Quarteroni, 2004].

Remark 1. *Pulse waves propagate rapidly within the cardiovascular system (with velocities of about 4-12 m s^{-1}), while arterial lengths can vary between few millimeters up to about 10 cm. As a result, pulse wave transit times within a vessel are small compared to the duration of the cardiac cycle. Thus at any given time the space averaged values will be close to the pointwise ones and $p(\zeta_1,t) = p_\mathrm{in}(t)$, $q(\zeta_2,t) = q_\mathrm{out}$ and $q(\zeta_3,t) = q_\mathrm{out}$ are reasonable [Milišić & Quarteroni, 2004].*

Equations (5.4a) and (5.4b) become

$$\underbrace{\frac{K_1}{\rho}\frac{dp_\mathrm{in}}{dt}}_{\mathrm{a}} + \underbrace{q_\mathrm{out} - q_\mathrm{in}}_{\mathrm{b}} = 0, \tag{5.5a}$$

$$\underbrace{K_2 \frac{dq_\mathrm{out}}{dt}}_{\mathrm{c}} + \underbrace{\frac{p_\mathrm{out} - p_\mathrm{in}}{\rho}}_{\mathrm{d}} = \underbrace{-\frac{2(\xi+2)\pi\mu}{\rho} K_3 q_\mathrm{out}}_{\mathrm{e}}, \tag{5.5b}$$

with

$$K_1 = \int_0^l \frac{A_\mathrm{d}}{c_\mathrm{d}^2} dx, \qquad K_2 = \int_0^l \frac{1}{A_\mathrm{d}} dx, \qquad K_3 = \int_0^l \frac{1}{A_\mathrm{d}^2} dx. \tag{5.6}$$

The term $C_\mathrm{v} = \frac{K_1}{\rho}$ is the integrated arterial compliance of the 1-D model vessel (Fig. 5.4b). We assume that the fluid inertia term $K_2 \frac{dq_\mathrm{out}}{dt}$ (Eq. (5.5b)) is negligible,

since peripheral inertias have a minor effect on flow waveforms [Alastruey *et al.*, 2008]. Thus Eqs. (5.5a) and (5.5b) become

$$C_{\mathrm{v}}\frac{dp_{\mathrm{in}}}{dt} + q_{\mathrm{out}} - q_{\mathrm{in}} = 0, \tag{5.7a}$$

$$p_{\mathrm{out}} - p_{\mathrm{in}} = -R_v q_{\mathrm{out}}, \tag{5.7b}$$

with

$$R_{\mathrm{v}} = 2(\xi+2)\pi\mu K_3, \tag{5.8}$$

where R_{v} is the integrated resistance of the 1-D model vessel (Fig. 5.4b).

We have shown that a 1-D arterial segment can be reduced to a two-element Windkessel model with resistance R_{v} and compliance C_{v}. To close the problem we must also consider the following equation for the three-element Windkessel model prescribed at the boundary (Fig. 5.4a),

$$\left(1+\frac{R_1}{R_2}\right)q_{\mathrm{out}} + CR_1\frac{dq_{\mathrm{out}}}{dt} = C\frac{dp_{\mathrm{out}}}{dt} + \frac{p_{\mathrm{out}} - \widehat{p_{\mathrm{out}}}}{R_2}, \tag{5.9}$$

where output values of pressure and flow from the Windkessel model are denoted as $\widehat{p_{\mathrm{out}}}$ and $\widehat{q_{\mathrm{out}}}(t)$, respectively. By substituting $q_{\mathrm{out}}(t)$ from Eq. (5.7a) and $p_{\mathrm{out}}(t)$ from Eq. (5.7b) into Eq. (5.9) we obtain

$$\left(1+\frac{R_1}{R_2}+\frac{R_{\mathrm{v}}}{R_2}\right)q_{\mathrm{in}} - \frac{p_{\mathrm{in}} - \widehat{p_{\mathrm{out}}}}{R_2} - \left(C_{\mathrm{v}}\left(1+\frac{R_1}{R_2}\right) + C + \frac{R_{\mathrm{v}}C_{\mathrm{v}}}{R_2}\right)\frac{dp_{\mathrm{in}}}{dt} + \frac{d(q_{\mathrm{in}} - C_{\mathrm{v}}\frac{dp_{\mathrm{in}}}{dt})}{dt}(CR_1 + CR_{\mathrm{v}}) = 0. \tag{5.10}$$

We make the assumption that the last term in Eq. (5.10) is of negligible size

compared to the other terms. This is deemed reasonable since

$$\frac{d(q_{\text{in}} - C_{\text{v}} \frac{dp_{\text{in}}}{dt})}{dt} = \frac{dq_{\text{out}}}{dt}, \tag{5.11}$$

according to Eq. (5.5a) and consistent with our previous assumption of the inertia term $K_2 \frac{dq_{\text{out}}}{dt}$ being negligible in physiological situations [Formaggia *et al.*, 2003]. Each arterial segment acts as a buffer, due to its compliance, hence the rate of change of flow at the outlet $\frac{dq_{\text{out}}}{dt}$ is small compared to the other terms in Eq. (5.10).

Rearranging Eq. (5.10) we get

$$q_{\text{in}} = \frac{p_{\text{in}} - \widehat{p_{\text{out}}}}{R_2 + R_1 + R_{\text{v}}} + \frac{1}{(R_2 + R_1 + R_{\text{v}})} \left(C_{\text{v}} R_2 + C_{\text{v}} R_1 + C R_2 + R_{\text{v}} C_{\text{v}}\right) \frac{dp_{\text{in}}}{dt}. \tag{5.12}$$

By comparing Eq. (5.12) to the two-element Windkessel equation [Frank, 1899; Westerhof *et al.*, 2009] we obtain

$$q_{\text{in}} = \frac{p_{\text{in}} - \widehat{p_{\text{out}}}}{R_{\text{new}}} + C_{\text{new}} \frac{dp_{\text{in}}}{dt}, \tag{5.13}$$

where $\widehat{p_{\text{out}}}$ is the value of pressure at which the outflow stops (most often approximated by the mean venous pressure), and Eqs. (5.14a) and (5.14b) for R_{new} and C_{new}. These denote the resistance and compliance of the two-element Windkessel (Fig. 5.4c) that describes blood flow in the original 1-D model vessel coupled to a three-element Windkessel (Fig. 5.4a).

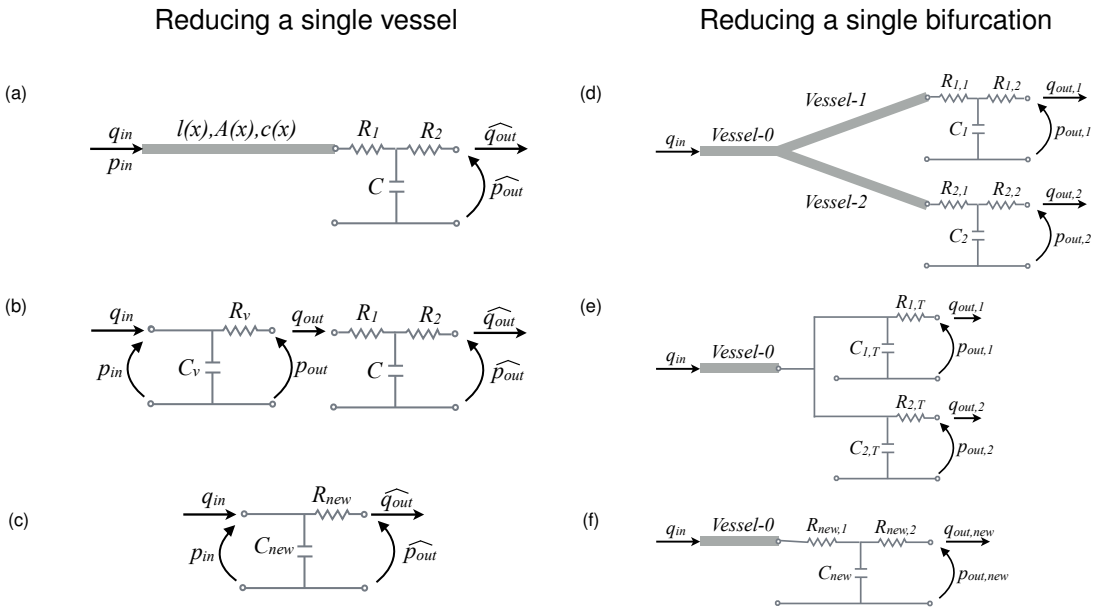

Figure 5.4: (left) Reduction of a nonlinear 1-D model single vessel attached to a three-element Windkessel model (R_1-C-R_2) (a) into a single two-element Windkessel model (R_{new}-C_{new}) (c), via an intermediary stage (b) in which the 1-D vessel is simplified into a two-element Windkessel model (R_{v}-C_{v}). The 1-D vessel is characterised by a length l, a cross-sectional area $A(x)$, and a pulse wave velocity $c(x)$. (right) Reduction of a nonlinear 1-D model single bifurcation coupled to three-element Windkessel models (R_1-C-R_2) (d) into a nonlinear 1-D model single vessel coupled to a three-element Windkessel model ($R_{\text{new},1}$-C_{new}-$R_{\text{new},2}$) (f). In the intermediary stage (e), the daughter vessels 1 and 2 and their outlet Windkessel model are transformed into two two-element Windkessel models (C_{T}-R_{T}). $q_{\text{in}}(t)$: inflow; $q_{\text{out}}(t)$: outflow; $p_{\text{in}}(t)$: inflow pressure; p_{out}: outflow pressure.

These are calculated as

$$R_{\text{new}} = R_2 + R_1 + R_{\text{v}} \tag{5.14a}$$

$$C_{\text{new}} = \frac{C_{\text{v}}R_2 + C_{\text{v}}R_1 + CR_2 + R_{\text{v}}C_{\text{v}}}{R_2 + R_1 + R_{\text{v}}}, \tag{5.14b}$$

where R_{v} and C_{v} are, respectively, the resistance and compliance of the 1-D model vessel (Fig. 5.4b).

5.1.3.2 Reducing a 1-D model single bifurcation into an equivalent 0-D model

We consider an arterial bifurcation with the parent vessel denoted by the index 0 and the daughter vessels by the indices 1 and 2 (Fig. 5.4d). Firstly, we apply the methodology described in Section 5.1.3.1 to transform each daughter vessel into two parallel RC-Windkessel models, with elements $R_{1,\mathrm{T}}$, $C_{1,\mathrm{T}}$ and $R_{2,\mathrm{T}}$, $C_{2,\mathrm{T}}$ for daughter vessels 1 and 2, respectively (Fig. 5.4e). We can then combine these two 0-D models into a single three-element Windkessel model, with resistances $R_{\mathrm{new},1}$ and $R_{\mathrm{new},2}$ and compliance C_{new} (Fig. 5.4f). The total peripheral resistance of the new 0-D model is calculated as

$$R_{\mathrm{new},1} + R_{\mathrm{new},2} = \frac{1}{\frac{1}{R_{1,\mathrm{T}}} + \frac{1}{R_{2,\mathrm{T}}}}, \tag{5.15}$$

where $R_{\mathrm{new},1}$ is set to be equal to the characteristic impedance of the parent vessel to minimise wave reflections [Alastruey *et al.*, 2008]. The total peripheral compliance of the new three-element Windkessel is calculated as

$$C_{\mathrm{new}} = C_{1,\mathrm{T}} + C_{2,\mathrm{T}}. \tag{5.16}$$

5.1.4 Error metrics

The pressure, area and flow waveforms generated by the reduced models were compared with those generated by the complete 55- or 67-models using the following

relative error metrics:

$$\begin{aligned}
\epsilon_{\mathrm{P,avg}} &= \frac{1}{N_t}\sum_{i=1}^{N_t}\left|\frac{P_i^{\mathrm{R}}-P_i^{\mathrm{C}}}{P_i^{\mathrm{C}}}\right|, & \epsilon_{\mathrm{Q,avg}} &= \frac{1}{N_t}\sum_{i=1}^{N_t}\left|\frac{Q_i^{\mathrm{R}}-Q_i^{\mathrm{C}}}{\max_j(Q_j^{\mathrm{C}})}\right|, \\
\epsilon_{\mathrm{P,sys}} &= \frac{\max_i(P_i^{\mathrm{R}})-\max_i(P_i^{\mathrm{C}})}{\max_i(P_i^{\mathrm{C}})}, & \epsilon_{\mathrm{Q,sys}} &= \frac{\max_i(Q_i^{\mathrm{R}})-\max_i(Q_i^{\mathrm{C}})}{\max_i(Q_i^{\mathrm{C}})}, \\
\epsilon_{\mathrm{P,dias}} &= \frac{\min_i(P_i^{\mathrm{R}})-\min_i(P_i^{\mathrm{C}})}{\min_i(P_i^{\mathrm{C}})}, & \epsilon_{\mathrm{Q,dias}} &= \frac{\min_i(Q_i^{\mathrm{R}})-\min_i(Q_i^{\mathrm{C}})}{\max_i(Q_i^{\mathrm{C}})},
\end{aligned} \tag{5.17}$$

with N_t the number of time points where the comparison is made. For each time point i, P_i^{C} and P_i^{R} are the pressures at the same spatial location of the complete (B) and reduced (R) model, respectively. The corresponding flows are Q_i^{C} and Q_i^{R}. The metrics $\epsilon_{\mathrm{P,avg}}$ and $\epsilon_{\mathrm{Q,avg}}$ are the average relative errors in pressure and the flow, respectively, over one cardiac cycle; $\epsilon_{\mathrm{P,sys}}$ and $\epsilon_{\mathrm{Q,sys}}$ are the errors for systolic pressure and flow; and $\epsilon_{\mathrm{P,dias}}$ and $\epsilon_{\mathrm{Q,dias}}$ are the errors for diastolic pressure and flow. To avoid division by small values of flow, we normalised the flow error by the maximum value of flow over the cardiac cycle, $\max_j(Q_j^{\mathrm{B}})$.

5.2 Results

We applied our method for reducing the number of 1-D model arterial segments described in Section 5.1.3 to the normotensive (Section 5.2.1) and hypertensive (Section 5.2.2) 55-artery models, as well as the normotensive 67-artery model (Section 5.2.3). In all cases we analysed the effect of decreasing the number of arterial segments on the pressure at the aortic root. For the 55-artery model we also investigated the pressure and flow at the midpoint of the thoracic aorta. For the 67-artery model we also studied the pressure and flow waveforms at the digital artery in the hand. The aortic-root flow is not studied for any model, since it is

enforced as the inflow boundary condition.

5.2.1 Normotensive 55-artery model

Figure 5.3 compares the aortic waveforms simulated by six reduced models (dashed black) with those produced by the baseline model (solid grey), under normotensive conditions. Average, systolic and diastolic errors are provided in each plot relative to the baseline model. For each reduced model in panels (a)-(e), the number of segments is shown in the first column and the model topology is illustrated in the second. Diastolic, systolic and average relative errors in aortic pressure are smaller than 3% for any reduced model, even for the single-vessel model shown in panel (e). Relative errors in the flow waveform at the thoracic aorta are greater than in pressure, but remain smaller than 20% (9% for the average relative error).

Considerable discrepancies between reduced and baseline models appear if 15 or less segments are included. These models, which do not include the superior mesenteric and renal arteries, lead to the following features of the aortic waveform not being captured as well as in the baseline model (Fig. 5.3c,d): the magnitude of the dicrotic notch and the time of peak systole at the root, and the magnitude of systolic pressure, the time and magnitude of the peak flow and the oscillatory flow in diastole at the thoracic aorta. However, all reduced models capture well the time and magnitude of the feet of baseline pressure and flow waves. Moreover, they produce pressure and flow waveforms in the second half of diastole that are similar to those simulated by the complete 55-artery model.

Figure 5.3f shows the aortic-root pressure waveform calculated by a two-element Windkessel model with a resistance and compliance equal to, respectively, the net

peripheral resistance and total compliance of the baseline model. The 0-D model is able to capture precisely the decay in aortic pressure in diastole, but is unable to describe well pressure in systole.

Figure 5.5 (left) shows systolic, diastolic and average relative errors in the pressure at the aortic root with the number of arterial segments. Errors remain smaller than 1% for models containing 53 to 21 segments; the latter consists of the aorta and first generation of bifurcations only (see topology in Fig. 5.3b). Further reductions in the number of segments yield a greater increase in the rate at which errors raise. Qualitatively similar progressions in relative errors are obtained for the flow and pressure at the thoracic aorta.

5.2.2 Hypertensive 55-artery model

Figure 5.6 compares the aortic pressure and flow waveforms produced by six reduced models (dashed black) with those simulated by the complete 55-artery model (solid grey), under hypertensive conditions. The topology of the reduced models and the format of the figure are the same as for the normotensive study above. Pulse and mean pressures are greater under hypertensive conditions: the pulse is doubled while the mean increases by about 50%. The amplitude and mean value of the flow change little with simulated hypertension.

Average relative errors in both pressure and the flow remain smaller than 2% for models containing 53 to 21 segments, in agreement with the normotensive results (Fig. 5.5a,b). However, eliminating segments of the aorta and first generation of bifurcations from the 21-artery model produces smaller errors under hypertensive conditions. Hypertensive reduced models are able to capture well all features of

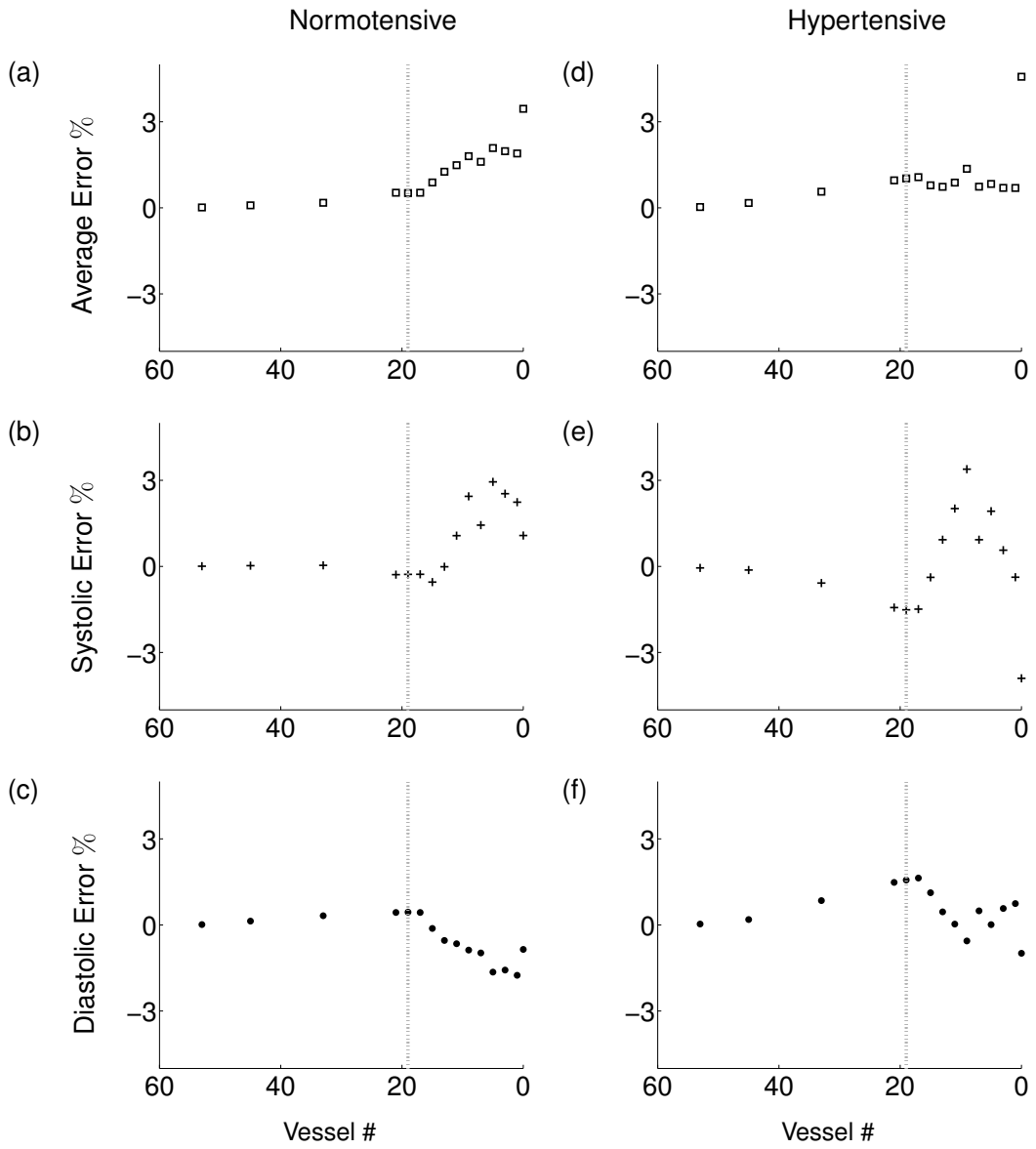

Figure 5.5: Evolution of the average (top), systolic (middle) and diastolic (bottom) relative errors in the pressure waveform at the aortic root of the 55-artery model with the number of arterial segments, under normotensive (left) and hypertensive (right) conditions. Vertical dashed lines correspond to the 19-artery model: arterial networks displayed on the left and on the line include a full aorta while those on the right only include portions of it.

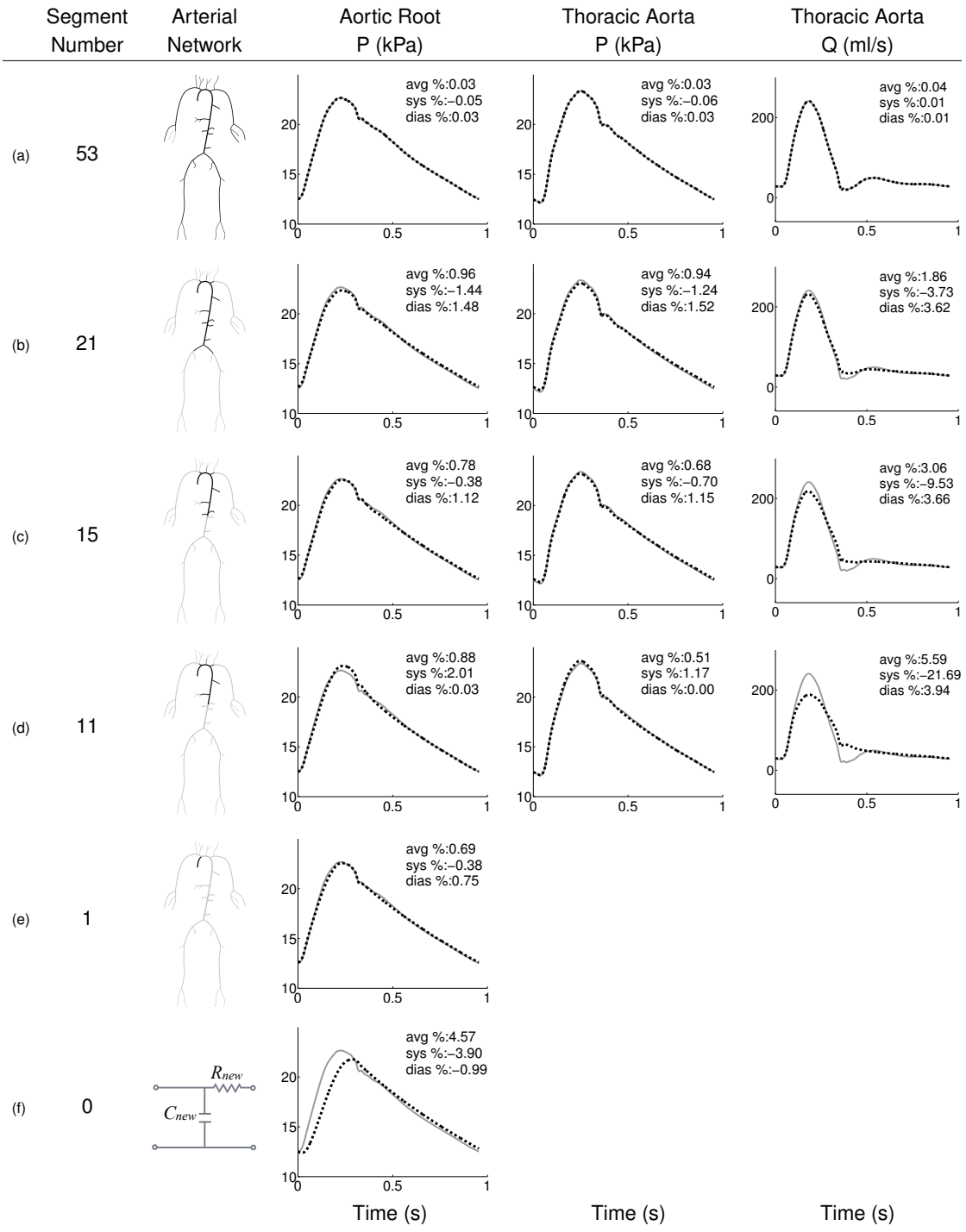

Figure 5.6: Pressure (P) and flow (Q) waveforms at the aortic root and midpoint of the thoracic aorta of the hypertensive 55-artery model (solid grey) and several reduced models (dashed black), one for each row. The number of segments and the arterial topology for each reduced model are given in the first two columns. The aortic-root pressure waveform calculated by a two-element Windkessel model of the whole systemic circulation is shown in (f). Average (avg), systolic (sys) and diastolic (dias) relative errors are indicated in the top right corner of each plot.

the aortic pressure waveform that normotensive reduced models were unable to reproduce (compare Figs. 5.3a-e and 5.6a-e). Discrepancies in aortic flow waveforms are similar under both normotensive and hypertensive conditions (compare last column in Figs. 5.3a-d and 5.6a-d). Moreover, similar evolutions of systolic and diastolic errors are observed under both normotensive and hypertensive conditions (Fig. 5.5).

In agreement with the normotensive results, the aortic-root pressure waveform calculated by the two-element Windkessel model of the whole systemic circulation is able to describe well the decay in pressure during diastole, but is unable to produce most of the features of the pressure wave in systole (Fig. 5.6f).

5.2.3 Normotensive 67-artery model

Figure 5.2 compares the aortic pressure and flow waveforms produced by six reduced models (dashed black) with those simulated by the complete 67-artery model (solid grey). Pulse and mean pressures differ from those of the baseline 55-artery model by -2.8% and 6.9% at the aortic root (Fig. 5.1). This is due to the total resistance and compliance being altered by the extended arterial network in the hands. With segment reductions, average systolic and diastolic relative errors of central aortic and digital arterial pressure remain smaller than 3% for models containing 65 to 19 segments. Relative errors of flow at the digital artery remain less than 5%.

Reduced 67-artery models with less than 33 vessels do not capture the following features at the central aorta: magnitude of the dicrotic notch and the time and magnitude of peak systole (Fig. 5.2d-f). At the digital artery these reduced

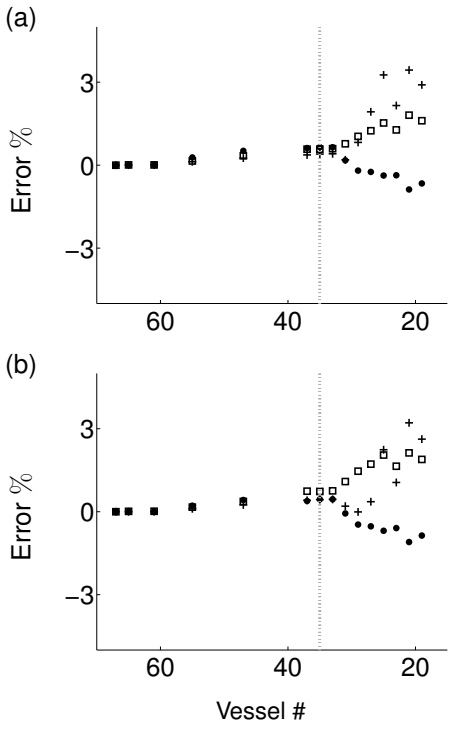

Figure 5.7: Evolution of the average (□), systolic (+) and diastolic (●) relative errors in the pressure waveform at the aortic root (a) and digital artery (b) with the number of arterial segments in the 67-artery model. Vertical dashed lines correspond to the 35-artery model: arterial networks displayed on the left and on the line include a full aorta while those on the right only include portions of it.

models no longer capture the time of arrival of the second pressure peak, the magnitude of the first pressure peak, and the oscillatory flow in diastole. Figure 5.7 shows average, systolic, and diastolic relative errors in the pressure at the aortic root (a) and digital artery (b) with the number of arterial segments. The largest divergence between the complete and reduced models is seen if less than 33 vessels are included; i.e. if aortic segments are lumped into Windkessel models.

5.3 Discussion

In this study we have presented a novel methodology for investigating the minimum number of arterial segments required to simulate precisely blood pressure and flow waveforms at multiple arterial sites using nonlinear 1-D modelling. By systematically lumping terminal 1-D model segments into 0-D Winkessel models that preserve the net resistance and total compliance of the original model (Fig. 5.4), we can study the effect on central and peripheral waveforms of reducing the number of arterial segments and, hence, input parameters. We have applied our methodology to investigate the effect of network topology (and hence reflection sites) on the shape of pressure and flow waves in the aorta and digital artery in the hand. To carry out this study we have used a nonlinear 1-D model of blood flow in the 55 larger systemic arteries of the human, under normotensive and hypertensive conditions, and an extended 67-artery model which includes the larger arteries in the hand, under normotensive conditions.

We have focussed on analysing (i) aortic haemodynamics, because central (aortic) pressure is an important determinant of cardiovascular function, and (ii) peripheral haemodynamics in the digital arteries, because pressure and volume at the digital artery can be measured continuously and non-invasively in the clinic; *e.g.* using the Finapres device [Imholz *et al.*, 1998] and photoplethysmopgraphy [Almond & Jones, 1988; Avolio, 2002], respectively. Our simulated aortic and digital pressure and flow waveforms contain the main features observed *in vivo* (Fig. 5.1).

5.3.1 Optimising arterial network topology

The 55-artery model consists of the aorta and other large arteries up to the fifth generation of bifurcations (Fig. 5.1) and contains 227 input parameters. The 67-artery model consists of the aorta and other large arteries up to the sixth generation of bifurcations (which include the palmar arch and digital arteries Fig. 5.1) and contains 271 input parameters. Each arterial segment is described by three parameters (length, luminal cross-sectional area at diastolic pressure and diastolic pulse wave velocity), while two additional parameters are required to model each peripheral arterial segment (peripheral resistance and compliance). The remaining parameters are the density and viscosity of blood, the shape of the velocity profile, the diastolic pressure, the inflow boundary condition and the outflow pressure at terminal Windkessel models.

By subsequently trimming the 55-artery model of generations of bifurcations, the number of arterial segments is reduced to 21, if only arterial vessels up to the first generation of bifurcations are simulated using 1-D modelling. As a result, the 227 input parameters of the initial model are reduced to 91. Such a considerable reduction in the number of parameters yields aortic pressure and flow waveforms which contain all the features of the 55-artery model with errors of up to only 4% relative to the initial model (Figs. 5.3b and 5.6b). Reducing the 67-artery model (271 input parameters) to the first generation of bifurcations (37 arteries, 171 parameters), with all segments of the right upper limb preserved, results in relative errors smaller than 1% in pressure at the central and peripheral measuring sites and smaller than 3% in the flow at the peripheral measuring site, with all errors relative to the initial model (Fig. 5.2b). These results suggest that our

original 55-artery (67-artery) models are over-parameterised for simulating aortic (and digital) waveforms.

The focus of previous studies using 1-D modelling [Avolio, 1980; Blanco *et al.*, 2014; Mynard & Nithiarasu, 2008; Perdikaris *et al.*, 2014; Reymond *et al.*, 2009; Stergiopulos *et al.*, 1992] was not confined to the simulation of aortic and upper-limb pulse . Our results favour the use of reduced models which consider only the arteries of interest; e.g. the model of Karamanoglu *et al.* [1994] for the ascending aorta and upper-limb vessels, and the model of Willemet *et al.* [2013] for the lower-limb vessels. This result has important implications for patient-specific 1-D modelling. A reduction in the number of 1-D model arterial segments decreases the number of input parameters that need to be prescribed, which should facilitate the estimation of a greater percentage of the total number of parameters from clinical measurements. Lowering the number of parameters, therefore, should increase the degree of patient-specific modelling that can be achieved to simulate central and upper-limb haemodynamics. However, it is important to note that the degree of applicability of 1-D models for patient-specific modelling remains at a pilot stage. As such, the task of clinical estimation of the 1-D model parameters may still be challenging, even if using the suggested lumping approach.

Our results also contribute towards understanding the role of pulse wave reflections in shaping the aortic (Section 5.3.2) and digital (Section 5.3.3) pressure and flow waves.

5.3.2 Effect of wave reflections on aortic pressure and flow waveforms

The excellent agreement between the 55-artery model and the reduced 21-artery model containing segments up to the first generation of bifurcations (Figs. 5.3b and 5.6b) suggests that the effect of multiple reflection sites downstream vessels of the first generation of bifurcations can be lumped into single reflection sites at the end of these vessels. Further reduction in the number of arterial segments by lumping aortic segments increases considerably relative errors once the superior mesenteric and renal arteries are removed (Fig. 5.3c-e). These observations are supported by *in vivo* studies showing that reflected waves generated artificially by total occlusions in the aorta distal to the renal arteries have no discernible influence on the pressure and flow waveforms at the ascending aorta [Khir & Parker, 2005; van den Bos *et al.*, 1976]. It is also in agreement with the outcome of numerical studies that used different tools of pulse wave analysis [Alastruey *et al.*, 2009b; Karamanoglu *et al.*, 1994]. Our numerical results are also consistent with the horizon effect hypothesis [Davies *et al.*, 2012], which states that aortic reflected waves are an amalgam of individual reflections from multiple reflection sites, with the nearer site contribution at full strength and sites further away having their contributions attenuated.

Further reductions in the number of 1-D model segments of the 55-artery model by lumping aortic segments and arteries that branch off the aorta into 0-D models – starting from the iliac bifurcation – yields relative errors in aortic flow and pressure smaller than 5% (Fig. 5.5). Relative errors in aortic-root pressure remain below 5% even if all the 55 segments of the baseline model are integrated into Frank

[1899] two-element Windkessel model of the entire arterial system (Figs. 5.3f and 5.6f). Removing aortic segments in the 55-artery model leads to discrepancies in the shape of aortic pressure and flow waveforms, in systole and early diastole, but does not in approximately the last half of diastole. This result suggests that the diastolic part of the pressure waveform along the aorta can be described by a lumped parameter model with only four parameters (the inflow from the left ventricle, the total compliance of the systemic circulation, the net resistance at the aortic root and the outflow pressure), which corroborates *in vivo* [Wang *et al.*, 2003; Westerhof *et al.*, 2009] and numerical [Willemet & Alastruey, 2014; Xiao *et al.*, 2013] studies showing that aortic pressure becomes space-independent with increasing time in diastole.

Lumping aortic segments of the 55-artery normotensive model yields reduced models that are unable to capture the main features of aortic pressure and flow waves in systole (Fig. 5.3c-f). Under hypertensive conditions, however, models with a reduced number of aortic segments maintain all features of the aortic-root pressure waveform with relative errors smaller than 2% (Fig. 5.6 c-e). This result suggests that individual distal reflection sites affect less the slope of the central pressure wave with hypertension. The following mechanism underlies this result. Greater PWVs in the hypertensive model make more valid the assumption of our reduction methodology of pulse wave transit times within each vessel being much smaller than the duration of the cardiac cycle. Our additional assumption of negligible inertia effects is also satisfied better in the hypertensive model, since increasing PWV (and hence decreasing arterial compliance) decreases the weight of the flow acceleration term in the conservation of momentum relative to the pressure gradient and viscous terms [Willemet & Alastruey, 2014].

5.3.3 Effect of wave reflections on digital pressure and flow waveforms

In the 67-artery model we systematically lumped aortic segments and branches off the aorta into 0-D models while preserving all arterial segments of the upper right limb. For any reduced models, we obtained relative errors for pressure and the flow at the aortic root and digital artery smaller than 4.5% (Figs. 5.2 and 5.7). The model with the least number of segments (19) contains only the ascending aorta and upper-right-limb vessels and has a topology similar to that used by Karamanoglu *et al.* [Karamanoglu *et al.*, 1994].

Results at the aortic root (Fig. 5.2) are in agreement with those obtained by the 55-artery model and confirm our conclusion that the effect of multiple reflection sites downstream vessels of the first generation of bifurcations can be lumped into single reflection sites at the end of these vessels.

Pressure and flow waveforms at the digital artery have two peaks, as observed *in vivo*. The second peak is progressively flattened as aortic segments are lumped (Fig. 5.2b-f). The greater change in shape occurs if the renal arteries are lumped into 0-D models (Fig. 5.2c-e). This result suggests that wave propagation in the thoracic aorta and renal arteries plays an important role in generating the second peak of the digital pressure and flow waves. This observation corroborates the conclusions from Baruch *et al.* [2014, 2011] and is also consistent with the hypothesis in Chowienczyk *et al.* [1999]; Millasseau *et al.* [2002a]: the second peak of the digital volume pulse (which is closely related to the pressure pulse) is due to pressure waves travelling from the left ventricle to the finger and later smaller reflections from internal mismatching, mainly in the lower body.

5.3.4 Perspective

We believe that our methodology could offer valuable insight into optimising the number of model input parameters that are needed to simulate pressure and flow waveforms in a given region of the systemic circulation other than the aorta and digital artery. This will be useful to identify which part of the arterial tree is responsible for shaping a particular pressure waveform and lessen the number of parameters that have to be estimated or taken from the literature to simulate that waveform using 1-D modelling. Other studies have considered truncated arterial networks, *e.g.* in the leg or arm, and have shown that arterial pressure and flow waveforms can be efficiently modelled without including the aorta in the computational domain [Leguy *et al.*, 2010; Raines *et al.*, 1974; Willemet *et al.*, 2013].

We have not proved that our reduction method produces the optimal result; *i.e.* other procedures may lead to more complex outflow 0-D models (*e.g.* those described in Jaeger *et al.* [1965]; Kind *et al.* [2010]; Olufsen [1999]; Stergiopulos *et al.* [1999]) that yield smaller relative errors for pressure and the flow if coupled to reduced 1-D models. It may not be possible to have a patient-specific model with all input parameters calculated from clinical measurements, but we need tools like the one presented here to eliminate unnecessary parameters and advance the usage of patient-specific simulations of arterial pressure and flow waveforms.

Within this chapter we have only considered an elastic arterial tube law model. In future work, it would be of interest to extend our reduction methodology to account for inertial effects (*e.g.* using inductance terms) and more sophisticated tube laws (*e.g.* as proposed by Valdez-Jasso *et al.* [2011]), which may be more

appropriate for hypertensive models [Armentano *et al.*, 1998].

Within this chapter we have considered the influence of a segment-reducing technique on two measuring sites. The differing responses of error between the two measuring sites raises an important issue of this technique. Pressure and flow waveforms are highly sensitive to local geometry changes, thus to apply this technique to another initial geometry careful consideration must be taken as to where the measuring sites that they wish to preserve are located.

Given the excellent agreement between 1-D and 3-D pressure and flow waves in the aorta, as reported by Xiao *et al.* [2013] under normal conditions, we believe that our methodology could be adapted to determine the size of the computational domain in 3-D blood flow modelling. This would require a methodology for lumping 3-D model vessels into 0-D models.

In future work the reduced parameters will not necessarily need to be derived from an original large arterial network but can be derived separately.

5.3.5 Concluding remarks

We have presented a new method for lumping peripheral 1-D vessels into 0-D Windkessel models that enables us to analyse the effect of network topology on pulse waveforms and determine a suitable number of arterial segments (and hence input parameters) required to simulate efficiently blood pressure and flow waveforms at multiple arterial sites which are relevant for a particular problem. This is important to simplify the computational domain while maintaining the precision of the numerical predictions.

Chapter 6

Conclusions and Future Work

We conclude with a summary of the work presented within this thesis. We also provide an overview of the wider implications of the work completed in this study. We highlight the hurdles that may be faced to apply the findings of this thesis to the clinical setting. We conclude with some directions of work for the future.

6.1 Summary of the Thesis Achievements

Previously extensive research has been conducted *in vivo* to investigate how changes in the properties of the cardiovascular system affect the shape of the PPG waveform [Allen *et al.*, 2005; Arza *et al.*, 2013; Awad *et al.*, 2006; Baek *et al.*, 2007; Baruch *et al.*, 2014, 2011; Boos *et al.*, 2007; Cannesson *et al.*, 2007; Dillon & Hertzman, 1941; Eduardo & Gomes, 2015; Elgendi, 2012; Hubena *et al.*, 2015; Jaryal *et al.*, 2009; Liu *et al.*, 2014; McGrath *et al.*, 2011b; Millasseau *et al.*, 2002a, 2006; Takazawa *et al.*, 1998; Usman *et al.*, 2013; Utami *et al.*, 2013]. Within this thesis we have used 1-D/0-D arterial blood flow modelling to investigate how changes in physical properties of the cardiovascular system affect the PPG waveform, focusing on the DVP.

The first part of this thesis has focused on the development of an 120-artery 1-D/0-D model, which includes the arterial vasculature of the hand and head. To this model we have applied a local sensitivity analysis, systematically altering peripheral Windkessel parameters, the cross-sectional area of the elastic and muscular arteries, and the stiffness of the elastic and muscular arteries, to study how characteristics of the cardiovascular system influence the morphology of the PPG waveform. We have then applied a global sensitivity analysis, the results of which have enabled us to create a fictive population of healthy and diseased (hypertension, diabetes, and combined hypertension and diabetes) arterial models. To this we have assessed the ability of existing and novel biomarkers to classify disease state. In the second part, a novel technique has been developed to help optimise the number of arterial segments included within an arterial model in order to achieve reasonable accuracy of predicted pulse waveforms.

The following subsections summarise the main three results of these thesis.

6.1.1 The digital PPG wave is strongly affected by the aortic flow wave and the muscular-artery stiffness and diameter

Validating a numerical model is a formidable task. There are many potential measurement sites to validate by comparison against *in vivo* data. The main aim of Chapter 3 was to create a generic arterial tree, representative of a healthy patient. Here we extended the existing geometrical model by Reymond *et al.* [2009] to include the vasculature of the hands [Epstein *et al.*, 2014] and an alternative viscoelastic tube law [Alastruey *et al.*, 2011]. Reymond *et al.* [2009] hypothesised

that the cerebral circulation is necessary to obtain an accurate pressure and flow waveform at the carotid artery; it is for this reason that we have included the vasculature of the head within this work. Photoplethysmography is a simple and cheap non-invasive technique that is extensively used. It consists of a small light source and photodetector most often measured at the digit. We wanted to use our new 1-D model to understand how changes of the cardiovascular system contribute to changes in the measured PPG signal. For this purpose we have included the vasculature of the hands, so that we can compare our results to measured PPG waveforms. Here we assume that the PPG signal can be represented by the cross-sectional area of the digital artery [Alastruey *et al.*, 2009a; Gircys *et al.*, 2015]. To our knowledge, this is the first study to link 1-D blood flow modelling and PPG signals in humans.

We have changed several inputs to the model (*e.g.* aortic diameter, carotid diameter, muscular diameter, arterial stiffness, peripheral resistance, etc) to match literature values. We have chosen to qualitatively compare pressure and flow waveforms at multiple measuring sites from a range of literature sources. We have compared flow at the aorta, carotid, radial, brachial, iliac and temporal arteries. Pressure at the aorta, carotid, radial, femoral, digital and temporal arteries have also been compared. Finally, we have compared the cross-sectional area at the finger to a measured PPG waveform. Results have shown that the model is able to produce the main features of physiological pressure and flow waveforms in the larger systemic arteries and digital circulation. Comparison at the cerebral circulation, where flow waveforms are more complex and exhibit more variation in their shape, have revealed an inadequacy of the model to replicate temporal arterial flow.

This study has strong clinical applications as it relates PPG waveform analysis (a non-invasive continuous measure of cardiovascular function) to known risk markers (e.g. PWV). The sensitivity methodology developed within this work provides a clear framework to investigate other variations in physical properties of the cardiovascular system and their influence on the PPG waveform. Due to the complexity of human physiology, this type of incremental sensitivity analysis would not be possible *in vivo*with pharmacological intervention .

A number of phenomena were not represented in this model, *e.g.* gravity. Payne [2004] has shown the influence of gravity to blood flow in an elastic axisymmetric vessel to be greater than the viscous effects or the momentum force. Gravitational forces are particularly important when studying the effect of postural changes [Olufsen *et al.*, 2005].

In the second part of Chapter 3 we have carried out a local sensitivity analysis. This is one method to evaluate how inputs of the model change the measured digital area waveforms, which is analogous to the PPG DVP. From this analysis we have shown that the measured PPG waveform is not very sensitive to changes in the peripheral resistance and Windkessel pressure. The parameters that influence the results the most are muscular stiffness and diameter. Notably, but to a lesser degree, the stiffness and diameter of the elastic vessels play an influential role in changes to the PPG waveform. We have chosen not to change the peripheral compliance or the length of the individual arteries based on the findings of Leguy *et al.* [2011]; Willemet *et al.* [2013].

In the final part of Chapter 3 we have evaluated how the shape of the flow waveform (prescribed as the inlet boundary condition) changes the area waveform at the digital artery. Here we have found a strong correlation between the systolic

peak at the area and the systolic peak at the aortic root. Similarly, the timings of the systolic peak at the aortic root and the area at the digital artery were strongly correlated.

6.1.2 The DVP peak-to-peak time can classify hypertensive vs diabetic subjects: a virtual population study

In Chapter 4 we have created a workflow to derive the necessary parameters from literature data to build a fictive population of healthy, diabetic, combined diabetic and hypertensive, and hypertensive subjects. Using this fictive blood flow simulations we have assessed traditional biomarkers (*e.g.* PWV and pressure) in addition to the indices calculated from the DVP wave investigated in Chapter 3.

We have developed a methodology to calculate physiological input parameters to our model which produce output parameters that well match healthy, diabetic, combined diabetic and hypertensive, and hypertensive populations taken from the literature. To calculate the input parameters we have used a global sensitivity approach, which has enabled us to assess how input parameters interact with one another, and the sensitivity of the output parameters to these changes. We have then performed several iterations of fictive numerical simulations, with each iteration providing a superior range of input parameters to match clinical data.

Only two known studies have looked at creating numerical simulations to represent a population of patients. Willemet *et al.* [2015] created a database of virtual healthy patients by varying 7 significant parameters of the 55-artery model within ranges that are representative of a healthy population from literature data. They varied the elastic arteries' stiffness and diameter, muscular arteries' stiffness and

diameter, heart rate, stroke volume, and peripheral vascular resistance. This resulted in a population of 3,325 virtual subjects. Kiselev *et al.* [2015] used patient data from a clinical trial of over 1,500 patients. They personalised the following parameters: upper body arterial stiffness and diameter, lower body stiffness and diameter, heart rate, stroke volume, and peripheral resistance. We have chosen to subdivide the arterial vessels into muscular and elastic arteries, similar to Willemet *et al.* [2015], with the adaptation of classifying the carotid and iliac-bifurcation arteries as elastic vessels. This adjustment was motivated by literature. Additionally, by classifying the vessels of the iliac-bifurcation as elastic vessels, the reflection coefficient remained within the physiological bounds of -0.3 to 0.3. Thus, unlike Willemet *et al.* [2015] we did not need to post-process the data to exclude unphysiological reflections coefficients. Since no data were provided on the characteristics of the excluded data set, it is difficult to evaluate whether removing a subset of the population skews the data, creating an unphysiological distribution of results.

We have extracted, from the literature, data on healthy, diabetic, hypertensive, and combined diabetic and hypertensive subjects. This process was by far the most labour intensive part of the study, due to often incomplete information in papers regarding the distribution of diabetic or hypertensives; often this information was entirely excluded from papers. Furthermore, some papers lacked the existence of a control group to compare the diabetic, combined diabetic and hypertensive, and hypertensives to. An additional limitation of this work is that different studies had different distributions of age within each sub group, and since age has a significant impact on cardiovascular function [De Angelis *et al.*, 2004; Kulkarni *et al.*, 2014; Lakatta & Schulman, 2004], this may create an inconsistent population model to derive conclusive results from.

The distribution of PWV, pressure and aortic diameter from the resultant simulated fictive population well match literature values found for diseased and healthy patients. Using this population we have investigated how parameters of the PPG waveform change under different healthy and diseased states. Moreover, we have compared our findings to studies from the literature where PPG parameters have been measured *in vivo* for the different diseases.

According to our results, the strongest indicator of disease state is the parameter dT (the time between the two peaks of the PPG). We have been able to use dT to differentiate the hypertensive group from the diabetic and baseline subgroups, with a t-test value of 0.05 and 0.01, respectively. In the literature, dT has already been associated to age [Millasseau *et al.*, 2003], vaso-active drugs [Millasseau *et al.*, 2002b, 2003], PWV [Millasseau *et al.*, 2002b; Padilla *et al.*, 2006], organ damage in untreated hypertension [Chen *et al.*, 2005], and metabolic risk factors [Veijalainen *et al.*, 2013]. Our results have shown that the parameters CT, PS, PD, Area and Width are not of statistical significance for the classification between healthy or diseased states.

6.1.3 A new method for optimising the number of input parameters in 1-D modelling: Less is more for patient-specific simulations

In Chapter 5 we have presented a novel methodology to optimise the number of arterial segments considered within a numerical model.

The number of arterial segments used in 1-D modelling has increased in recent years from 55 to 4 million[Avolio, 1980; Blanco *et al.*, 2014; Mynard & Nithiarasu,

2008; Perdikaris *et al.*, 2014; Reymond *et al.*, 2009; Stergiopulos *et al.*, 1992]. But little consideration has been given to the minimum number of arterial vessels that is needed to well simulate the pressure and flow waveforms at a given site.

In cases where there have been restrictions in the amount of *in vivo* data collected, smaller subsections of the vasculature have been studied, with good results [Gul *et al.*, 2015; Lafortune & Aris, 2012; Leguy *et al.*, 2011; Raines *et al.*, 1974; Willemet *et al.*, 2013]. Adaptions at the inlet boundary condition to these subsection models are needed since the heart is no longer part of the network [Bokov *et al.*, 2013; Willemet *et al.*, 2011]. How these smaller subsections of models relate to the larger cardiovascular system as a whole remains unclear.

Reymond *et al.* [2009] showed that in the presence of the detailed cerebral tree, the computed flow at the carotid is physiological, whereas in the absence of the cerebral tree the flow exhibits an abnormally high pulsatility. Otherwise, there are very few works in the field of 1-D modelling looking at what is the minimum geometry necessary around a given measuring site in order to simulate physiological pressure and flow waveforms.

Within this chapter we have presented a new methodology to systematically lump 1-D arterial domains into 0-D models Analysis has then been performed on sites of interest to determine how this systematic lumping affects local pressure and flow waveforms. For this purpose we have compared two sets of simulations. The first compares pressure and flow waveforms at two sites in the aorta, whilst lumping the vasculature peripheral to the aorta in a normotensive and hypertensive representation of the cardiovascular system. The second compares pressure and flow waveforms at the aorta and digital artery whilst lumping the peripheral vasculature towards the two sites of interest, in a normotensive model of the

cardiovascular system.

We believe that our methodology could offer valuable insight into optimising the number of model input parameters that are needed to simulate pressure and flow waveforms in a given region of the systemic circulation other than the aorta and digital artery. This will be useful to identify which part of the arterial tree is responsible for shaping a particular pressure waveform and lessen the number of parameters that have to be estimated or taken from the literature to simulate that waveform using 1-D modelling. Other studies have considered truncated arterial networks, *e.g.* in the leg or arm, and have shown that arterial pressure and flow waveforms can be efficiently modelled without including the aorta in the computational domain.

6.2 Directions for Future Research

Hypertension is a highly preventable risk factor for cardiovascular disease [World Health Organization, 2003], and is most prevalent in patients aged 40+ [Gu *et al.*, 2008]. Diabetes mellitus kills more people each year globally than malaria [Mathers & Loncar, 2006]. In developing countries there is a much greater predicted number of middle-aged patients than elderly patients with diabetes [King *et al.*, 1998]. But with the exception of Caroli *et al.* [2013]; Willemet [2012], existing 1-D blood flow models have been of young ($\leq$ 30 years) patients Blanco *et al.* [2014]; Guala *et al.* [2015b]; Leguy [2010]; Mynard & Smolich [2015]; Reymond *et al.* [2011], or do not provide information of the age of the patients being considered [Bode *et al.*, 2012]. For these reasons, we wanted our model to represent a middle-aged patient (with an approximate age of 40-60 years). We have scaled several parameters (*e.g.*

capillary pressure, inflow) to better match values from the literature for an older subject (age 50-60 years), apart from the inflow which has been scaled to a patient of age 33 years. An improvement to this model would be to better match the inflow to an older patient.

Ageing is associated with several physiological trends. Length, mean diameter and volume of the aorta are known to increase with age [Avolio *et al.*, 1983; Craiem *et al.*, 2012; Greenwald, 2007; Lakatta & Schulman, 2004; Levy, 2001; McEniery *et al.*, 2005; Nichols *et al.*, 1984]. Muscular artery stiffness is seen to increase with age but to a lesser degree than central aortic stiffness [Avolio *et al.*, 1983; McEniery *et al.*, 2005]. Stroke volume and cardiac output is known to decrease with increasing age [Nichols *et al.*, 1984] Furthermore, with ageing an increase in peripheral resistance is observed [Ferrari *et al.*, 2003]. It is noted that ageing is known to lengthen loosely tethered vessel, such as the abdominal aorta [Wenn & Newman, 1990], a parameter which was fixed within this thesis and the work of Karamanoglu *et al.* [1995]. Further refinement needs to be conducted on how to best represent an older subject in a numerical model.

Within our numerical model, the heart has been modelled as a boundary condition, which is limiting, especially when wishing to change specific characteristics of the cardiac function. Using a 0-D heart model, *e.g.* as proposed in Formaggia *et al.* [2006]; Mynard & Nithiarasu [2008]; Reymond *et al.* [2011], would allow a greater control over cardiac parameters (*e.g.* heart rate, contractility and filling). This would allow us to test independently how changes to the heart influence the shape of the PPG waveform. Furthermore, this would better match the inflow to a specific age group.

Another development of the current code would be to apply an external variable

pressure gradient to the vessels within the thoracic cavity to simulate breathing. A model of breathing already exists within the literature [Baretta *et al.*, 2012]. This improvement to the code would then simulate the DC component of the PPG waveform at the digital artery. It would be of particular interest to study how simulated breathing affects the measured PPG in different diseased models (*e.g.* diabetic or hypertensive).

To simulate blood flow it is necessary to have a law relating the pressure to the cross-sectional area of a vessel; *i.e.* a tube law. Within this thesis we have used a visco-elastic and an elastic tube law (see Chapter 2). There are several other linear and nonlinear tube law models that exist in the literature [Blanco & Feijóo, 2013; Bodley, 1971; Brook *et al.*, 1999; Kitawaki, 2012; Li & Cheng, 1993; Olufsen, 1999; Reymond *et al.*, 2009; Streeter *et al.*, 1963; Surovtsova, 2005]. The more complex the tube law, the more input parameters are needed. Further studies would therefore be needed to evaluate which tube law is best, and whether the gain in precision is compromised by any uncertainty of the parameter estimation.

The limitations of the Windkessel models in the cerebral circulation needs to be investigated further, since autoregulatory effects play an important role [David *et al.*, 2003; Ferrandez *et al.*, 2002; Moorhead *et al.*, 2004]. In this work we have matched the viscous term for the visco-elastic tube law of the cerebral circulation on the basis of similar sized vessels from elsewhere in the arterial system. This assumption needs to be validated against *in vivo* measurements of the cerebral circulation of the Kelvin-Voigt viscous term.

To simplify our sensitivity analysis we have subdivided all the arterial sections into muscular and elastic groups. In this work, the carotid artery has been assumed to be muscular. Since the carotid artery presents structural properties similar to

the aorta [Boutouyrie *et al.*, 1992], it may be more appropriate to consider the carotid as an elastic artery. One area of future work would be to refine how systemic arteries are classified into subgroups, it may even be interesting to subdivide the muscular arteries into two further subgroups based on cross-sectional area.

We have attempted to use an RSM method to create a hypertensive and diabetic population. The literature data gathered from diabetic, hypertensive, and combined diabetic and hypertensive subjects that exists is incomplete and measured using several different protocols, from different patient cohorts at different times. This could be improved by undertaking a clinical trial with a normotensive, diabetic, hypertensive, and combined diabetic and hypertensive aged match cohort. To this cohort it would then be possible to consistently measure parameters such as PWV, pressure and PPG signals, to better tailor the inputs to a new numerical model.

Ideally an assessment of performance for a classification tool (as used in Chapter 4) should be completed against a large independent data set that was not used in the training set. This was not possible within this study due to the lack of data available. An area of future work would be obtaining additional data sources to validate this classification tool.

Other classification methods other than that used in Chapter 4 exist such as boosted trees [Austin *et al.*, 2013], artificial neural networks [Das *et al.*, 2009], and support vector machines [Çomak *et al.*, 2007]. An area of future work would be investigating alternative tools in order to compare their strengths and weaknesses when applied to the field of 1-D blood flow modelling.

Alty *et al.* [2007] used a dual approach for the classification of arterial stiffness by utilising parameters based on physiology and information theory. From this

they were able to classify the arterial stiffness of a patient to a high degree of accuracy. A similar approach should be taken to help classify the diabetic, hypertensive, and combined diabetic and hypertensive population; utilising not just the parameters from within this thesis, but a combination of features from the PPG waveform.

Finally, within 1-D modelling a truncated arterial geometry presents many advantages. Considerably less input parameters are needed and there is less computational cost. However, by removing 1-D arterial segments we lose sites of reflection, something that is not straight forward to replicate in 0-D models. By applying the methodology described within Chapter 5, it could help during the early design phase of a 1-D numerical blood flow project to assess which segments are absolutely necessary to be included into the final network of segments. This could help to drastically reduce the complexity of personalising input parameters to a model. An extension of this work would be to apply the same methodology to a visco-elastic tube model. An interesting future study would be to look at the effects of this lumping methodology on measured biomarkers.

References

Acosta, S., Puelz, C., Rivière, B., Penny, D.J. & Rusin, C.G. (2015). Numerical method of characteristics for one-dimensional blood flow. *J. Comput. Phys.*, **294**, 96–109. 51

Alastruey, J. (2006). *Numerical Modelling of Pulse Wave Propogation in the Cardiovascular System: Devlopment, Validation and Clinical Applications*. Ph.D. thesis, Imperial College. xiv, 31, 42, 49, 50, 51

Alastruey, J., Parker, K., Peiro, J. & Sherwin, S. (2005). A one-dimensional simulation of the human conduit arteries compared to experimental data. In *Proceedings of the ASME Summer Bioengineering conference*. 54

Alastruey, J., Parker, K.H., Peiró, J. & Sherwin, S.J. (2006). Can the modified Allen's test always detect sufficient collateral flow in the hand? A computational study. *Comput. Methods Biomech. Biomed. Engin.*, **9**, 353–61. 125, 131

Alastruey, J., Parker, K.H., Peiró, J., Byrd, S.M. & Sherwin, S.J. (2007). Modelling the circle of Willis to assess the effects of anatomical variations and occlusions on cerebral flows. *J. Biomech.*, **40**, 1794–805. 125

Alastruey, J., Parker, K., Peiró, J. & Sherwin, S.J. (2008). Lumped parameter outflow models for 1-D blood flow simulations: effect on pulse waves and parameter estimation. *Commun. Math. Phys.*, **4**, 317–36. 133, 138, 141

Alastruey, J., Nagel, S.R., Nier, B.A., Hunt, A.A., Weinberg, P.D. & Peiró, J. (2009a). Modelling pulse wave propagation in the rabbit systemic circulation to assess the effects of altered nitric oxide synthesis. *J. Biomech.*, **42**, 2116–2123. 10, 159

Alastruey, J., Parker, K.H., Peiró, J. & Sherwin, S.J. (2009b). Analysing the pattern of pulse waves in arterial networks: a time-domain study. *J. Eng. Math.*, **64**, 331–51. 71, 152

Alastruey, J., Khir, A.W., Matthys, K.S., Segers, P., Sherwin, S.J., Verdonck, P.R., Parker, K.H. & Peiró, J. (2011). Pulse wave propagation in a model human arterial network: Assessment of 1-D visco-elastic simulations against in vitro measurements. *J. Biomech.*, **44**, 2250–8. 29, 36, 37, 77, 158

Alastruey, J., Parker, K. & Sherwin, S. (2012a). Arterial pulse wave haemodynamics. In *Anderson (Ed.) 11th International Conference on Pressure Surges, chapter 7*, 401–42, Virtual PiE Led t/a BHR Group. 49, 133

Alastruey, J., Passerini, T., Formaggia, L. & Peiró, J. (2012b). Physical determining factors of the arterial pulse waveform: theoretical analysis and calculation using the 1-D formulation. *J. Eng. Math.*, **77**, 19–37. 44, 60

Alastruey, J., Hunt, A.A.E. & Weinberg, P.D. (2014). Novel wave intensity analysis of arterial pulse wave propagation accounting for peripheral reflections. *Int. J. Numer. Meth. Biomed. Engng*, **30**, 249–79. 82

Alberti, K.G. & Zimmet, P.Z. (1998). Definition, diagnosis and classification of diabetes mellitus and its complications. Part 1: diagnosis and classification of diabetes mellitus provisional report of a WHO consultation. *Diabet. Med.*, **15**, 539–53. 15

Alimohammadi, M., Agu, O., Balabani, S. & Díaz-Zuccarini, V. (2014). Development of a patient-specific simulation tool to analyse aortic dissections: Assessment of mixed patient-specific flow and pressure boundary conditions. *Med. Eng. Phys.*, **36**, 275–84. 23

Allen, J. (2007). Photoplethysmography and its application in clinical physiological measurement. *Physiol. Meas.*, **28**, 1–39. 10

Allen, J. & Murray, A. (2000). Variability of photoplethysmography peripheral pulse measurements at the ears, thumbs and toes. *IEE Proc. Sci. Meas. Tech.*, **147**, 403–7. 10

Allen, J. & Murray, A. (2003). Age-related changes in the characteristics of the photoplethysmographic pulse shape at various body sites. *Physiol. Meas.*, **24**, 297–307. xii, 11, 98

Allen, J., Oates, C.P., Lees, T.A. & Murray, A. (2005). Photoplethysmography detection of lower limb peripheral arterial occlusive disease: a comparison of pulse timing, amplitude and shape characteristics. *Physiol. Meas.*, **26**, 811–21. 12, 157

Almond, N.E. & Jones, D.P. (1988). Noninvasive measurement of the human peripheral circulation: relationship between laser Doppler flowmeter and photoplethysmograph signals from the finger. *Angiology*, **39**, 819–29. 149

Alty, S.R., Angarita-Jaimes, N., Millasseau, S.C. & Chowienczyk, P.J. (2007). Predicting arterial stiffness from the digital volume pulse waveform. *IEEE T Bio-Med Eng*, **54**, 2268–75. 168

American Diabetes Association (1999). Standards of medical care for patients with diabetes mellitus. *Diabetes Care*, **22**, S32–S41. 101

American Diabetes Association (2005). Diagnosis and classification of diabetes mellitus. *Diabetes Care*, **27**, 55–60. 15

Andersen, N., Poulsen, S., Helleberg, K., Ivarsen, P., Knudsen, S. & Mogensen, C. (2003). Impact of essential hypertension and diabetes mellitus on left ventricular systolic and diastolic performance. *Eur. J. Echocardiography*, **4**, 306–12. 112

Anliker, B.M., Rockwell, R.L. & Ogden, E. (1971). Nonlinear analysis of flow pulses and shock waves in arteries. *ZAMP*, **22**, 217–46. 51

Antiga, L., Iordache, E.B. & Remuzzi, A. (2003). Computational geometry for patientspecic reconstruction and meshing of blood vessels from MR and CT angiography. *IEEE Trans. Med. Im.*, **22**, 674–84. 127

Armentano, R., Barra, J., Levenson, J., Simon, A. & Pichel, R. (1995a). Arterial wall mechanics in conscious dogs assessment of viscous, in-

ertial, and elastic moduli to characterize aortic wall behavior. *Circulation Research*, **76**, 468–78. 40

Armentano, R., Megnien, J., Simon, A., Bellenfant, F., Barra, J. & Levenson, J. (1995b). Effects of hypertension on viscoelasticity of carotid and femoral arteries in humans. *Hypertension*, **26**, 48–54. 40

Armentano, R., Graf, S., Barra, J., Velikovsky, G., Baglivo, H., Sanchez, R., Simon, A., Pichel, R.H. & Levenson, J. (1998). Carotid wall viscosity increase is related to intima-media thickening in hypertensive patients. *Hypertension*, **31**, 534–9. 156

Arza, A., Lazaro, J., Gil, E., Laguna, P., Aguilo, J. & Bailon, R. (2013). Pulse transit time and pulse width as potential measure for estimating beat-to-beat systolic and diastolic blood pressure. *CinC*, 887–90. 120, 157

Asmar, R., Benetos, A., Topouchian, J., Laurent, P., Pannier, B., Brisac, A.M., Target, R. & Levy, B.I. (1995). Assessment of arterial distensibility by automatic pulse qave velocity measurement: validation and clinical application studies. *Hypertension*, **26**, 485–90. 20

Asmar, R., Topouchian, J., Pannier, B., Benetos, A. & Safar, M. (2001). Pulse wave velocity as endpoint in large-scale intervention trial. The Complior study. Scientific, Quality Control, Coordination and Investigation Committees of the Complior Study. *J. Hypertens.*, **19**, 813–8. 20

Atabek, M.E., Kurtoglu, S., Pirgon, O. & Baykara, M. (2006). Arterial wall thickening and stiffening in children and adolescents with type 1 diabetes. *Diabetes. Res. Clin. Pr.*, **74**, 33–40. 16

Austin, P.C., Tu, J.V., Ho, J.E., Levy, D. & Lee, D.S. (2013). Using methods from the data-mining and machine-learning literature for disease classification and prediction: A case study examining classification of heart failure subtypes. *J. Clin. Epidemiol.*, **66**, 398–407. 168

Avolio, A. (2002). The finger volume pulse and assessment of arterial properties. *J. Hypertens.*, **20**, 2341–3. 54, 96, 149

Avolio, A.P. (1980). Multi-branched model of the human arterial system. *Med. Biol. Eng. Comput.*, **18**, 709–18. 25, 102, 128, 151, 163

Avolio, A.P., Chen, S.G., Wang, R.P., Zhang, C.L., Li, M.F. & O'Rourke, M.F. (1983). Effects of aging on changing arterial compliance and left ventricular load in a northern Chinese urban community. *Circulation*, **68**, 50–8. 166

Awad, A.a., Stout, R.G., Ghobashy, M.A.M., Rezkanna, H.a., Silverman, D.G. & Shelley, K.H. (2006). Analysis of the ear pulse oximeter waveform. *Journal of Clinical Monitoring and Computing*, **20**, 175–84. 157

Awad, A.a., Haddadin, A.S., Tantawy, H., Badr, T.M., Stout, R.G., Silverman, D.G. & Shelley, K.H. (2007). The relationship between the photoplethysmographic waveform and systemic vascular resistance. *J. Clin. Monitor. Comp.*, **21**, 365–72. 73

Azer, K. & Peskin, C.S. (2007). A one-dimensional model of blood flow in arteries with friction and convection based on the Womersley velocity profile. *Cardiovasc. Eng.*, **7**, 51–73. 52

Baek, H.J., Kim, J.S., Kim, Y.S., Lee, H.B. & Park, K.S. (2007). Second derivative of photoplethysmography for estimating vascular aging. *2007 6th International Special Topic Conference on IITAB*, **00**, 70–2. 74, 93, 157

Baretta, A., Corsini, C., Marsden, A.L., Vignon-Clementel, I.E., Hsia, T.Y., Dubini, G., Migliavacca, F. & Pennati, G. (2012). Respiratory effects on hemodynamics in patient-specific CFD models of the Fontan circulation under exercise conditions. *Eur. J. Mech. B-Fluid.*, **35**, 61–9. 167

Barnes, R.W., Clayton, J.M. & Bone, G.E. (1977). Supraorbital photoplethysmography. Simple, accurate screening for carotid occlusive disease. *J. Surg. Res.*, **22**, 319–27. 12

Baruch, M., Kalantari, K., Gerdt, D. & Adkins, C.M. (2014). Validation of the pulse decomposition analysis algorithm using central arterial blood pressure. *Biomed. Eng. Online*, **13**, 1–19. 72, 154, 157

Baruch, M.C., Warburton, D.E.R., Bredin, S.S.D., Cote, A., Gerdt, D.W. & Adkins, C.M. (2011). Pulse decomposition analysis of the digital arterial pulse during hemorrhage simulation. *Nonlinear Biomed. Phys.*, **5**, 1–15. 86, 94, 154, 157

Bauer, R.D., Busse, R., Schabert, A., Summa, Y. & Wetterer, E. (1979). Separate determination of the pulsatile elastic and viscous forces developed in the arterial wall in vivo. *Pfluegers Archiv*, **380**, 221–6. 40

Beevers, G., Lip, G. & O'Brien, E. (2001). ABC of hypertension. The pathophysiology of hypertension. *BMJ*, **322**, 912–16. 14

Bella, J., Devereux, R. & Roman, M. (2001). Separate and joint effects of systemic hypertension and diabetes mellitus on left ventricular structure and function in American Indians (the Strong Heart Study). *Am. J. Cardiol.*, **87**, 1260–5. 18, 59, 101, 112

Benetos, A., Laurent, S., Asmar, R.G. & Lacolley, P. (1997). Large artery stiffness in hypertension. *J. Hypertens.*, **15**, 89–97. 18

Benetos, A., Rudnichi, A., Safar, M. & Guize, L. (1998). Pulse pressure and cardiovascular mortality in normotensive and hypertensive subjects. *Hypertension*, **32**, 560–65. 86

Bessems, D., Giannopapa, C.G., Rutten, M.C.M. & van de Vosse, F.N. (2008). Experimental validation of a time-domain-based wave propagation model of blood flow in viscoelastic vessels. *J. Biomech.*, **41**, 284–91. 24, 29, 54, 60

Beyar, R., Hausknecht, M.J., Halperin, H.R., Yin, F.C. & Weisfeldt, M.L. (1987). Interaction between cardiac chambers and thoracic pressure in intact circulation. *Am. J. Physiol.*, **253**, 1240–52. 55

Blacher, J., Guerin, a.P., Pannier, B., Marchais, S.J., Safar, M.E. & London, G.M. (1999). Impact of aortic stiffness on survival in end-stage renal disease. *Circulation*, **99**, 2434–9. 19

Blanco, P.J. & Feijóo, R.a. (2013). A dimensionally-heterogeneous closed-loop model for the cardiovascular system and its applications. *Med. Eng. Phys.*, **35**, 652–67. 53, 55, 102, 167

Blanco, P.J. & Watanabe, S.M. (2015). An anatomically detailed arterial network model for one-dimensional computational hemodynamics. *IEEE Trans. Bio. Med. Eng.*, **62**, 736–53. 53, 62

Blanco, P.J., Trenhago, P.R., Fernandes, L.G. & Feijóo, R. (2012a). On the integration of the baroreflex control mechanism in a heterogenous model of the cardiovascular system. *Int. J. Numer. Meth. Biomed. Engng.*, **28**, 412–33. 55

Blanco, P.J., Urquiza, S.A. & Feijoo, R.A. (2012b). Assessing the influence of heart rate in local hemodynamics through coupled 3D-1D-0D models. *Int. J. Numer. Meth. Biomed. Engng.*, **28**, 72–86. 28

Blanco, P.J., Watanabe, S.M., Dari, E.A., Passos, M.A.R.F. & Feijóo, R.A. (2014). Blood flow distribution in an anatomically detailed arterial network model: criteria and algorithms. *Biomech. Model Mechanobiol.*, **13**, 1–28. 24, 52, 56, 102, 128, 151, 163, 165

Bode, A.S., Huberts, W., Bosboom, E.M.H., Kroon, W., van der Linden, W.P.M., Planken, R.N., van de Vosse, F.N. & Tordoir, J.H.M. (2012). Patient-specific computational modeling of upper extremity arteriovenous fistula creation: its feasibility to support clinical decision-making. *PloS one*, **7**, e34491. 53, 103, 165

Bodley, W.E. (1971). The non-linearities of arterial blood flow. *Phys. Med. Biol*, **16**, 663–72. 167

Boileau, E., Nithiarasu, P., Blanco, P.J., Müller, L.O., Fossan, F.E., Hellevik, L.R., Donders, W.P., Huberts, W., Willemet, M. & Alas-

TRUEY, J. (2015). A benchmark study of numerical schemes for one-dimensional arterial blood flow modelling. *Int. J. Numer. Meth. Biomed. Engng.*, **31**. 29, 52

BOKOV, P., FLAUD, P., BENSALAH, A., FULLANA, J.M. & ROSSI, M. (2013). Implementing boundary conditions in simulations of arterial flows. *Journal of biomechanical engineering*, **135**, 111004. 164

BOLLACHE, E., KACHENOURA, N., REDHEUIL, A., FROUIN, F., MOUSSEAUX, E., RECHO, P. & LUCOR, D. (2014). Descending aorta subject-specific one-dimensional model validated against in vivo data. *Journal of biomechanics*, **47**, 424–31. 29

BOOS, C.J., LANE, D.A., KARPHA, M., BEEVERS, D.G., HAYNES, R. & LIP, G.Y.H. (2007). Circulating endothelial cells, arterial stiffness, and cardiovascular risk stratification in hypertension. *Chest*, **132**, 1540–7. 119, 157

BORTOLOTTO, L.A., BLACHER, J., KONDO, T., TAKAZAWA, K. & SAFAR, M.E. (2000). Assessment of vascular aging and atherosclerosis in hypertensive subjects: Second derivative of photoplethysmogram versus pulse wave velocity. *Am. J. Hypertens.*, **13**, 165–71. 93

BOUTOUYRIE, P., LAURENT, S., BENETOS, A., GIRERD, X., HOEKS, A. & SAFAR, M. (1992). Opposing effects of ageing on distal and proximal large arteries in hypertensives. *J. Hypertens.*, **10**, 87–92. 97, 168

BOX, G.E. & WILSON, K.B. (1951). On the experimental attainment of optimum conditions. *J. Roy. Statist. Soc. Ser. B*, **13**, 1–45. 106

BREIMAN, L. (2001). Random Forests. *Machine Learning*, **45**, 5–32. 110

Brook, B.S. & Pedley, T.J. (2002). A model for time-dependent flow in (giraffe jugular) veins: Uniform tube properties. *J. Biomech.*, **35**, 95–107. 51

Brook, B.S., Falle, S.a.E.G. & Pedley, T.J. (1999). Numerical solutions for unsteady gravity-driven flows in collapsible tubes: evolution and roll-wave instability of a steady state. *J. Fluid Mech.*, **396**, 223–56. 35, 167

Brooks, B.a., Molyneaux, L.M. & Yue, D.K. (2001). Augmentation of central arterial pressure in type 2 diabetes. *Diabetic Medicine*, **18**, 374–80. 17

Brown, Y. & Brown, M. (1999). Similarities and differences between augmentation index and pulse wave velocity in the assessment of arterial stiffness. *Q. J. Med.*, **92**, 595–600. 21

Broyd, C., Harrison, E., Raja, M., Millasseau, L., Sandrine C Poston & Chowienczyk, P.J. (2005). Association of pulse waveform characteristics with birth weight in young adults. *J. Hypertens.*, **23**, 1391–6. 22

Bruno, R.M., Penno, G., Daniele, G., Pucci, L., Lucchesi, D., Stea, F., Landini, L., Cartoni, G., Taddei, S., Ghiadoni, L. & Del Prato, S. (2012). Type 2 diabetes mellitus worsens arterial stiffness in hypertensive patients through endothelial dysfunction. *Diabetologia*, **55**, 1847–55. 18, 112

Burton, A.C. (1937). The range and variability of the blood flow in the human fingers and the vasomotor regulation of body temperature. *Am. J. Physiol.*, **127**, 437–53. 10

Cameron, J.D., Mcgrath, B.P. & Dart, A.M. (1998). Use of radial artery applanation tonometry and a generalized transfer function to determine aortic

pressure augmentation in subjects with treated hypertension. *JACC*, **32**, 1214–20. 21

Cameron, J.D., Bulpitt, C.J., Pinto, E.S. & Rajkumar, C. (2003). The aging of elastic and muscular arteries a comparison of diabetic and nondiabetic subjects. *Diabetes Care*, **26**, 2133–8. 16

Campbell, K., Lee, L. & Frasch, H. (1989). Pulse reflection sites and effective length of the arterial system. *Am. J. Physiol. Heart. Circ. Physiol.*, **256**, 1684–9. 102

Čanić, S. & Kim, E.H. (2003). Mathematical analysis of the quasilinear effects in a hyperbolic model blood flow through compliant axi-symmetric vessels. *Math. Meth. Appl. Sci,*, **26**, 1161–86. 36

Cannesson, M., Attof, Y., Rosamel, P., Desebbe, O., Joseph, P., Metton, O., Bastien, O. & Lehot, J.J. (2007). Respiratory variations in pulse oximetry plethysmographic waveform amplitude to predict fluid responsiveness in the operating room. *Anesthesiology*, **106**, 1105–11. 73, 157

Canzanello, V.J., Jensen, P.L. & Schwartz, G.L. (2015). Are aneroid sphygmomanometers accurate in hospital and clinic settings? *Arch. Intern. Med.*, **161**, 729–31. 14

Caro, C.G., Pedley, T.J., Schroter, R. & Seed, W. (2011). *The mechanics of the circulation*. Cambridge University Press. 6, 30, 35

Caroli, A., Manini, S., Antiga, L., Passera, K., Ene-Iordache, B., Rota, S., Remuzzi, G., Bode, A., Leermakers, J., van de Vosse,

F.N., Vanholder, R., Malovrh, M., Tordoir, J. & Remuzzi, A. (2013). Validation of a patient-specific hemodynamic computational model for surgical planning of vascular access in hemodialysis patients. *Kidney Int.*, **84**, 1237–45. 58, 165

Carter, P. (2015). The Cardiovascular System: Blood Vessels. xii, 6

Cebral, J.R., Castro, M.A., Appanaboyina, S., Putman, C.M., Millan, D. & Frangi, A.F. (2005a). Efficient pipeline for image-based patient-specific analysis of cerebral aneurysm hemodynamies technique and sensitivity. *IEEE Trans. Med. Im.*, **24**, 457–67. 126

Cebral, J.R., Castro, M.A., Burgess, J.E., Pergolizzi, R.S., Sheridan, M.J. & Putman, C.M. (2005b). Characterization of cerebral aneurysms for assessing risk of rupture by using patient-specific computational hemodynamics models. *Am. J. Neuroradiol.*, **26**, 2550–9. 127

Cebral, J.R., Hendrickson, S. & Putman, C.M. (2009). Hemodynamics in a lethal basilar artery aneurysm just before its rupture. *American Journal of Neuroradiology*, **30**, 95–98. 126

Challoner, A. (1979). Photoelectric plethysmography for estimating cutaneous blood flow. *Non-invasive Physiol. Meas.*, **1**, 125–51. 9

Chen, C.H., Ting, C.T., Nussbacher, A., Nevo, E., Kass, D.A., Pak, P., Wang, S.P., Chang, M.S. & Yin, F.C. (1996). Validation of carotid artery tonometry as a means of estimating augmentation index of ascending aortic pressure. *Hypertension*, **27**, 168–75. 13

Chen, D., Müller-Eschner, M., Kotelis, D., Böckler, D., Ventikos, Y. & Von Tengg-Kobligk, H. (2013). A longitudinal study of Type-B aortic dissection and endovascular repair scenarios: Computational analyses. *Med. Eng. Phys.*, **35**, 1321–30. 23

Chen, J.Y., Tsai, W.C., Lin, C.C., Huang, Y.Y., Hsu, C.H., Liu, P.Y. & Chen, J.H. (2005). Stiffness index derived from digital volume pulse as a marker of target organ damage in untreated hypertension. *Blood Pressure*, **14**, 233–7. 22, 163

Chowienczyk, P.J., Kelly, R.P., Maccallum, H., Millasseau, S.C., Andersson, T.L.G., Gosling, R.G., Ritter, J.M. & Anggard, E.E. (1999). Photoplethysmographic assessment of pulse wave reflection. *J. Am. Coll. Cardiol.*, **34**, 2007–14. 10, 22, 68, 154

Climie, R.E., Nikolic, S.B., Otahal, P., Keith, L.J. & Sharman, J.E. (2013). Augmentation index and arterial stiffness inpatients with type 2 diabetes mellitus. *Artery Research*, **7**, 194–200. 17

Çomak, E., Arslan, A. & Türkoğlu, . (2007). A decision support system based on support vector machines for diagnosis of the heart valve diseases. *Comput. Biol. Med.*, **37**, 21–7. 168

Convertino, V.A., Cooke, W.H. & Holcomb, J.B. (2006). Arterial pulse pressure and its association with reduced stroke volume during progressive central hypovolemia. *J. Trauma*, **61**, 629–34. 86

Craiem, D., Chironi, G., Redheuil, A., Casciaro, M., Mousseaux, E., Simon, A. & Armentano, R.L. (2012). Aging impact on thoracic aorta 3D

morphometry in intermediate-risk subjects: Looking beyond coronary arteries with non-contrast cardiac CT. *Ann. Biomed. Eng.*, **40**, 1028–1038. 166

Cronenwett, J. & Johnston, K. (2014). *Rutherford's vascular surgery*. Elsevier Health Sciences. 97

Cruickshank, J. & Wright, J. (1990). Depressed aortic compliance in diabetics compared with verified controls for given levels of blood pressure over a wide range. *J. Hypertens.*, **8**, 1069. 16

Cruickshank, K., Riste, L., Anderson, S.G., Wright, J.S., Dunn, G. & Gosling, R.G. (2002). Aortic pulse-wave velocity and its relationship to mortality in diabetes and glucose intolerance: An integrated index of vascular function? *Circulation*, **106**, 2085–90. 16, 19

Cushman, W.C., Evans, G.W., Byington, R.P., Goff, D.C., Grimm, R.H., Cutler, J.A., Simons-Morton, D.G., Basile, J.N., Corson, M.A., Probstfield, J.L., Katz, L., Peterson, K.A., Friedewald, W.T., Buse, J.B., Bigger, J.T., Gerstein, H.C. & Ismail-Beigi, F. (2010). Effects of intensive blood-pressure control in type 2 diabetes mellitus. *N. Engl. J. Med.*, **362**, 1575–85. 110

D'Agrosa, L.S. & Hertzman, A.B. (1967). Opacity pulse of individual minute arteries. *J. Appl. Physiol.*, **23**, 613–20. 9

Das, R., Turkoglu, I. & Sengur, A. (2009). Effective diagnosis of heart disease through neural networks ensembles. *Expert Sys. Appl.*, **36**, 7675–80. 168

David, T., Brown, M. & Ferrandez, A. (2003). Auto-regulation and blood flow in the cerebral circulation. *Int. J. Numer. Meth. Fluids*, **43**, 701–13. 167

Davies, J.E., Whinnett, Z.I., Francis, D.P., Manisty, C.H., Aguado-Sierra, J., Willson, K., Foale, R.a., Malik, I.S., Hughes, A.D., Parker, K.H. & Mayet, J. (2006). Evidence of a dominant backward-propagating "suction" wave responsible for diastolic coronary filling in humans, attenuated in left ventricular hypertrophy. *Circulation*, **113**, 1768–78. 19

Davies, J.E., Alastruey, J., Francis, D.P., Hadjiloizou, N., Whinnett, Z.I., Manisty, C.H., Aguado-Sierra, J., Willson, K., Foale, R.a., Malik, I.S., Hughes, A.D., Parker, K.H. & Mayet, J. (2012). Attenuation of wave reflection by wave entrapment creates a "horizon effect" in the human aorta. *Hypertension*, **60**, 778–85. 152

Dawber, T., Thomas, H. & McNamara, P. (1973). Characteristics of the dicrotic notch of the arterial pulse wave in coronary heart disease. *Angiology*, 244–55. xv, 11, 63

Dawber, T.R., Kannel, W.B., Revotskie, N., Stokes, J., Kagan, A. & Gordon, T. (1961). Some factors associated with the development of coronary heart diseasesix years follow-up experience in the framingham study. *Ann. Intern. Med.*, **55**, 33–50. 18

De Angelis, L., Millasseau, S.C., Smith, A., Viberti, G., Jones, R.H., Ritter, J.M. & Chowienczyk, P.J. (2004). Sex differences in age-related stiffening of the aorta in subjects with type 2 diabetes. *Hypertension*, **44**, 67–71. 162

de Simone, G., Devereux, R.B., Daniels, S.R., Mureddu, G., Roman, M.J., Kimball, T.R., Greco, R., Witt, S. & Contaldo, F. (1997). Stroke volume and cardiac output in normotensive children and adults. *Circulation*, **95**, 1837–43. 59

De Zelicourt, D.A., Haggerty, C.M., Sundareswaran, K.S., Whited, B.S., Rossignac, J.R., Kanter, K.R., Gaynor, J.W., Spray, T.L., Sotiropoulos, F., Fogel, M.A. & Yoganathan, A.P. (2011). Individualized computer-based surgical planning to address pulmonary arteriovenous malformations in patients with a single ventricle with an interrupted inferior vena cava and azygous continuation. *J. Thorac. Cardiovasc. Surg.*, **141**, 1170–7. 126

Demirel, M. & Kayan, B. (2012). Application of response surface methodology and central composite design for the optimization of textile dye degradation by wet air oxidation. *IJIC*, **3**, 1–10. 104

Di Martino, E.S., Guadagni, G., Fumero, A., Ballerini, G., Spirito, R., Biglioli, P. & Redaelli, A. (2001). Fluid-structure interaction within realistic three-dimensional models of the aneurysmatic aorta as a guidance to assess the risk of rupture of the aneurysm. *Med. Eng. Phys.*, **23**, 647–55. 23

Diabetes Advocates (2015). American Diabetes Advocates (ADA) - National Diabetes Information Clearinghouse Home. xiii, 16

Dick, D.E., Kendrick, J.E., Matson, G.L. & Rideout, V.C. (1968). Measurement of nonlinearity in the arterial system of the dog by a new method. *Circ. Res.*, **22**, 101–11. 136

Dillon, J.B. & Hertzman, A.B. (1941). The form of the volume pulse in the finger pad in health, arteriosclerosis, and hypertension. *Am. Heart J.*, **21**, 172–90. 72, 82, 98, 119, 157

Doyle, B.J., Callanan, A., Burke, P.E., Grace, P.A., Walsh, M.T., Vorp, D.A. & McGloughlin, T.M. (2009). Vessel asymmetry as an additional diagnostic tool in the assessment of abdominal aortic aneurysms. *J. Vasc. Surg.*, **49**, 443–54. 126

Eduardo, P. & Gomes, B. (2015). Assessment of arterial stiffness in type 1 diabetes using digital pulse contour analysis: Is it a reliable method ? *Acta Diabetol*, **21**, 1–6. 117, 157

Elgendi, M. (2012). On the analysis of fingertip photoplethysmogram signals. *Curr. Cardiol. Rev.*, **8**, 14–25. 11, 20, 72, 73, 157

Elgendi, M. (2014). Detection of c, d, and e waves in the acceleration photoplethysmogram. *Comput. Methods Programs Biomed.*, **117**, 125–36. 74

Ellwein, L.M., Tran, H.T., Zapata, C., Novak, V. & Olufsen, M.S. (2008). Sensitivity analysis and model assessment: mathematical models for arterial blood flow and blood pressure. *Cardiovasc. Eng.*, **8**, 94–108. 54, 98, 104

Epstein, M. (1997). Diabetes and hypertension: the bad companions. *J. Hypertens.*, **15**, S55–S62. 101

Epstein, M. & Sowers, J. (1992). Diabetes mellitus and hypertension. *Hypertension*, **19**, 403–18. 17, 101

Epstein, S., Vergnaud, A.C., Elliot, P., Chowienczyk, P. & Alastruey, J. (2014). Numerical assessment of the stiffness index. In *Proc. 36th Annual International Conference of the IEEE Engineering in Medicine and Biology Society*, 1969–72. xvi, 68, 76, 158

Epstein, S., Willemet, M., Chowienczyk, P. & Alastruey, J. (2015). Reducing the number of parameters in 1D arterial blood flow modelling: Less is more for patient-specific simulations. *Am .J. Physiol. Heart. Circ. Physiol.*. xv, 56, 57

Eren, M., Gorgulu, S., Uslu, N., Celik, S., Dagdeviren, B. & Tezel, T. (2004). Relation between aortic stiffness and left ventricular diastolic function in patients with hypertension, diabetes, or both. *Heart*, 37–44. 58, 112

Fajardo, L.F., Berthrong, M. & Anderson, R.E. (2001). *Radiation pathology*. Oxford Univ Pr. 97

Fegan, P.G., Tooke, J.E., Gooding, K.M., Tullett, J.M., MacLeod, K.M. & Shore, A.C. (2003). Capillary pressure in subjects with type 2 diabetes and hypertension and the effect of antihypertensive therapy. *Hypertension*, **41**, 1111–7. 59, 112

Feldman, J.M. (2006). Can clinical monitors be used as scientific instruments? *Anesthesia and analgesia*, **103**, 1071–2. 99

Ferencik, M. & Pape, L.a. (2003). Changes in size of ascending aorta and aortic valve function with time in patients with congenitally bicuspid aortic valves. *Am. J. Cardiol.*, **92**, 43–46. 86

Ferrandez, A., David, T., Brown, M.D., A., F., T., D. & M.D., B. (2002). Numerical models of auto-regulation and blood flow in the cerebral circulation. *Comput. Methods Biomech. Biomed. Engin.*, **5**, 7–20. 167

Ferrari, A.U., Radaelli, A. & Centola, M. (2003). Aging and the cardiovascular system. 166

Formaggia, L., Gerbeau, J.F., Nobile, F. & Quarteroni, A. (2001). On the coupling of 3D and 1D Navier-Stokes equations for flow problems in compliant vessels. *Comput. Methods Appl. Mech. Engrg.*, **191**, 561–82. 30

Formaggia, L., Lamponi, D. & Quarteroni, A. (2003). One-dimensional models for blood flow in arteries. *J. Eng. Math.*, **47**, 251–76. 24, 36, 52, 60, 139

Formaggia, L., Lamponi, D., Tuveri, M. & Veneziani, A. (2006). Numerical modeling of 1D arterial networks coupled with a lumped parameters description of the heart. *Comput. Methods Biomech. Biomed. Engin.*, **9**, 273–88. 50, 55, 166

Forman, J., Stampfer, M. & Curhan, G. (2009). Diet and lifestyle risk factors associated with incident hypertension in women. *JAMA*, **302**, 401–11. 14

Fouad, F.M., Slominski, J.M. & Tarazi, R.C. (1984). Left ventricular diastolic function in hypertension: relation to left ventricular mass and systolic function. *JACC*, **3**, 1500–6. 14

Frank, O. (1899). Die grundform des arteriellen pulses. *Z Biol*, **37**, 483–526. 25, 44, 128, 139, 152

Franklin, S.S. (2002). Do diabetes and hypertension interact to accelerate vascular ageing? *J. Hypertens.*, **20**, 1693–6. 18, 101

Franklin, S.S., Khan, S.a., Wong, N.D., Larson, M.G. & Levy, D. (1999). Is pulse pressure useful in predicting risk for coronary heart disease? The Framingham heart study. *Circulation*, **100**, 354–60. 103

Fukui, M., Kitagawa, Y., Nakamura, N., Mogami, S., Ohnishi, M., Hirata, C., Ichio, N., Wada, K., Kamiuchi, K., Shigeta, M., Sawada, M., Hasegawa, G. & Yoshikawa, T. (2003). Augmentation of central arterial pressure as a marker of atherosclerosis in patients with type 2 diabetes. *Diabetes Res. Clin. Pract.*, **59**, 153–61. 17

Fuller, J.H. (1985). Epidemiology of hypertension associated with Diabetes mellitus. *Suppl II Hypertension*, **7**, 2–7. 101

Fulton, J.S. & McSwiney, B.A. (1930). The pulse wave velocity and extensibility of the brachial and radial artery in man. *J. Physiol.*, **69**, 386–92. 71

Gamella-Pozuelo, L., Fuentes-Calvo, I., Gómez-Marcos, M.a., Recio-Rodriguez, J.I., Agudo-Conde, C., Fernández-Martín, J.L., Cannata-Andía, J.B., López-Novoa, J.M., García-Ortiz, L. & Martínez-Salgado, C. (2015). Plasma cardiotrophin-1 as a marker of hypertension and diabetes-Induced target organ damage and cardiovascular risk. *Medicine*, **94**, 1–8. 19, 112

Gardin, J.M., Iseri, L.T., Elkayam, U., Tobis, J., Childs, W., Burn, C.S. & Henry, W.L. (1983). Evaluation of dilated cardiomyopathy by pulsed Doppler echocardiography. *Am. Heart J.*, **106**, 1057–65. 85

Gardin, J.M., Burn, C.S., Childs, W.J. & Henry, W.L. (1984). Evaluation of blood flow velocity in the ascending aorta and main pulmonary artery of normal subjects by Doppler echocardiography. *Am. Heart J.*, **107**, 310–9. 84

Gardin, J.M., Davidson, D.M., Rohan, M.K., Butman, S., Knoll, M., Garcia, R., Dubria, S., Gardin, S.K. & Henry, W.L. (1987). Relationship between age, body size, gender, and blood pressure and Doppler flow measurements in the aorta and pulmonary artery. *Am. Heart J.*, **113**, 101–9. 86

Giannarelli, C., Bianchini, E., Bruno, R.M., Magagna, A., Landini, L., Faita, F., Gemignani, V., Penno, G., Taddei, S. & Ghiadoni, L. (2012). Local carotid stiffness and intima-media thickness assessment by a novel ultrasound-based system in essential hypertension. *Atherosclerosis*, **223**, 372–7. 112

Giannattasio, C., Failla, M., Piperno, A., Grappiolo, A., Gamba, P., Paleari, F. & Mancia, G. (1999). Early impairment of large artery structure and function in Type I diabetes mellitus. *Diabetologia*, **42**, 987–94. 16

Gircys, R., Liutkevicius, A., Vrubliauskas, A. & Kazanavicius, E. (2015). Blood pressure estimation according to photoplethysmographic signal steepness. *Inf. Technol. Control*, 443–50. 10, 159

Glor, F.P., Ariff, B., Hughes, a.D., Crowe, L.a., Verdonck, P.R., Barratt, D.C., McG Thom, S.a., Firmin, D.N. & Xu, X.Y. (2004a). Image-based carotid flow reconstruction: a comparison between MRI and ultrasound. *Physiol. Meas.*, **25**, 1495–509. 126

Glor, F.P., Ariff, B., Hughes, a.D., Verdonck, P.R., Barratt, D.C., Augst, a.D., Thom, S.a.M. & Xu, X.Y. (2004b). Influence of head position on carotid hemodynamics in young adults. *Am. J. Physiol. Heart Circ. Physiol.*, **287**, 1670–81. 126

Glor, F.P., Ariff, B., Hughes, A.D., Verdonck, P.R., Thom, S.A.M., Barratt, D.C. & Xu, X.Y. (2005). Operator dependence of 3-D ultrasound-based computational fluid dynamics for the carotid bifurcation. *IEEE Trans. Med. Im.*, **24**, 451–6. 126

Greenwald, S.E. (2007). Ageing of the conduit arteries. *J. Pathol.*, **211**, 157–72. 166

Greenwald, S.E., Carter, a.C. & Berry, C.L. (1990). Effect of age on the in vitro reflection coefficient of the aortoiliac bifurcation in humans. *Circulation*, **82**, 114–23. 97, 122

Gress, T.W., Nieto, F.J., Shahar, E., Wofford, M.R. & Brancati, F.L. (2000). Hypertension and antihypertensive therapy as risk factors for type 2 diabetes mellitus. *N. Engl. J. Med.*, **342**, 905–12. 17

Groden, C., Laudan, J., Gatchell, S. & Zeumer, H. (2001). Three-dimensional pulsatile flow simulation before and after endovascular coil embolization of a terminal cerebral aneurysm. *J. Cereb. Blood Flow Metab.*, **21**, 1464–71. 23

Grossman, E., Shemesh, J., Shamiss, A., Thaler, M., Carroll, J. & Rsenthal, T. (1992). Left ventricular mass in Diabetes-Hypertension. *Arch. Intern. Med.*, **152**, 1001–4. 112

Gu, Q., Burt, V.L., Paulose-Ram, R. & Dillon, C.F. (2008). Gender differences in hypertension treatment, drug utilization patterns, and blood pressure control among US adults with hypertension: data from the National Health and Nutrition Examination Survey 1999-2004. *Am. J. Hypertens.*, **21**, 789–98. 165

Guala, A., Camporeale, C. & Ridolfi, L. (2015a). Compensatory effect between aortic stiffening and remodelling during ageing. *Plos One*, **10**, e0139211. 58

Guala, A., Camporeale, C., Tosello, F., Canuto, C. & Ridolfi, L. (2015b). Modelling and subject-specific validation of the heart-arterial tree system. *Ann. Biomed. Eng.*, **43**, 222–37. 55, 56, 165

Gul, R., Schutte, C. & Bernhard, S. (2015). Mathematical modeling and sensitivity analysis of arterial anastomosis in arm arteries. *Appl. Math. Model*, **22**. 104, 164

Gussenhoven, E.J., Essed, C.E., Lanc??e, C.T., Mastik, F., Frietman, P., van Egmond, F.C., Reiber, J., Bosch, H., van Urk, H., Roelandt, J. & Bom, N. (1989). Arterial wall characteristics determined by intravascular ultrasound imaging: An in vitro study. *JACC*, **14**, 947–52. 97

Haffner, S.M., Stern, M.P., Hazuda, H.P., Mitchell, B.D. & Patterson, J.K. (1990). Cardiovascular risk factors in confirmed prediabetic individuals. Does the clock for coronary heart disease start ticking before the onset of clinical diabetes? *JAMA*, **263**, 2893–8. 16

Haffner, S.M., Mykkänen, L., Festa, A., Burke, J.P. & Stern, M.P. (2000). Insulin-resistant prediabetic subjects have more atherogenic risk factors

than insulin-sensitive prediabetic subjects: implications for preventing coronary heart disease during the prediabetic state. *Circulation*, **101**, 975–80. 16

Hall, J.E. (2003). The kidney, hypertension, and obesity. *Hypertension*, **41**, 625–33. 14

Haller, M.J., Samyn, M., Nichols, W.W., Brusko, T., Wasserfall, C., Schwartz, R.F., Atkinson, M., Shuster, J.J., Pierce, G.L. & Silverstein, J.H. (2004). Radial artery tonometry demonstrates arterial stiffness in children with type 1 diabetes. *Clin. Res.*, **27**, 2911–7. 16

Hasegawa, H. & Kanai, H. (2004). Measurement of elastic moduli of the arterial wall at multiple frequencies by remote actuation for assessment of viscoelasticity. *Jpn. J. Appl. Phys.*, **43**, 3197–03. 40

Hashimoto, J., Chonan, K., Aoki, Y., Nishimura, T., Ohkubo, T., Hozawa, A., Suzuki, M., Matsubara, M., Michimata, M., Araki, T. & Imai, Y. (2002). Pulse wave velocity and the second derivative of the finger photoplethysmogram in treated hypertensive patients: their relationship and associating factors. *J. Hypertens.*, **20**, 2415–22. 98

Hatakeyama, T., Shigematsu, H. & Muto, T. (2001). Risk factors for rupture of abdominal aortic aneurysm based on three-dimensional study. *J. Vasc. Surg.*, **33**, 453–61. 23

Hayashi, T., Nakayama, Y., Tsumura, K., Yoshimaru, K. & Ueda, H. (2002). Reflection in the arterial system and the risk of coronary heart disease. *Am. J. Hypertens.*, **15**, 405–9. 21

Hayward, C., Kraidly, M., Webb, C.M. & Collins, P. (2002). Assessment of endothelial function using peripheral waveform analysis. *JACC*, **40**, 521–8. 10

Hemalatha, K. & Manivannan, M. (2010). Valsalva maneuver for the analysis of interaction hemodynamic model study. *2010 International Conference on Recent Trends in Information, Telecommunication and Computing*, **28**, 28–32. 10

Hemalatha, K., Suganthi, L. & Manivannan, M. (2010). Hybrid cardiopulmonary model for analysis of valsalva maneuver with radial artery pulse. *Ann. Biomed. Eng.*, **38**, 3151–61. 10

Henry, R.M.a., Kostense, P.J., Spijkerman, a.M.W., Dekker, J.M., Nijpels, G., Heine, R.J., Kamp, O., Westerhof, N., Bouter, L.M. & Stehouwer, C.D.a. (2003). Arterial stiffness increases with deteriorating glucose tolerance status: The Hoorn study. *Circulation*, **107**, 2089–95. 18

Hertzman, A.B. & Roth, L. (1942). The vasomotor components in the vascular reactions in the finger to cold. *Am. J. Physiol.*, **136**, 669–79. 99

Hertzman, A.B. & Spealman, C.R. (1937). Observations on the finger volume pulse recorded photoelectrically. *Am. J. Physiol.*, **119**, 3. 9, 14

Hickey, M., Phillips, J.P. & Kyriacou, P.A. (2015). Investigation of peripheral photoplethysmographic morphology changes induced during a hand-elevation study. *J. Clin. Monitor. Comp.*, 1–10. 94

Hildebrandt, P., Wachtell, K., Dahlöf, B., Papademitriou, V., Gerdts, E., Giles, T., Oikarinen, L., Tuxen, C., Olsen, M.H. & Devereux, R.B. (2005). Impairment of cardiac function in hypertensive patients with Type 2 diabetes: a LIFE study. *Diabetic Medicine*, **22**, 1005–11. 112

Holdsworth, D. & Norley, C. (1999). Characterization of common carotid artery blood-flow waveforms in normal human subjects. *Physiol. Meas.*, **20**, 219–40. xv, 63

Hossain, P., Kawar, B. & El Nahas, M. (2007). Obesity and diabetes in the developing world a growing challenge. *N. Engl. J. Med.*, **356**, 213–5. 15

Hou, L.x., Wei, M., Wang, X., Chen, X.z., Feng, Y. & Jiang, K. (2011). A novel non-iterative shape method for estimating the decay time constant of the finger photoplethysmographic pulse. *Journal of Zhejiang University SCIENCE A*, **12**, 438–45. 10

Hu, G., Jousilahti, P. & Tuomilehto, J. (2007). Joint effects of history of hypertension at baseline and type 2 diabetes at baseline and during follow-up on the risk of coronary heart disease. *Eur. Heart J.*, **28**, 3059–66. 18

Hubena, G., Osina, O., J, P.B. & Vasicko, T. (2015). Assessment of the peripheral blood flow of lower limbs in patients with diabetes mellitus with the use of digital photoplethysmography. *Acta Medica Martiniana*, **15**, 21–9. 119, 120, 157

Huberts, W., Bode, A., Kroon, W., Planken, R., Tordoir, J., van de Vosse, F. & Bosboom, E. (2012a). A pulse wave propagation model to sup-

port decision-making in vascular access planning in the clinic. *Med. Eng. Phys.*, **34**, 233–48. 52, 53, 102

Huberts, W., Donders, W.p., Delhaas, T. & van de Vosse, F.N. (2012b). Applicability of the polynomial chaos expansion method for personalization of a cardiovascular pulse wave propagation model. *Int. J. Numer. Meth. Biomed. Engng.*, **28**, 72–86. 103

Huberts, W., Van Canneyt, K., Segers, P., Eloot, S., Tordoir, J.H.M., Verdonck, P., van de Vosse, F.N. & Bosboom, E.M.H. (2012c). Experimental validation of a pulse wave propagation model for predicting hemodynamics after vascular access surgery. *J. Biomech.*, **45**, 1684–91. 29

Huberts, W., de Jonge, C., van der Linden, W.P.M., Inda, M.a., Tordoir, J.H.M., van de Vosse, F.N. & Bosboom, E.M.H. (2013). A sensitivity analysis of a personalized pulse wave propagation model for arteriovenous fistula surgery. Part A: Identification of most influential model parameters. *Med. Eng. Phys.*, **35**, 810–26. 55, 103, 104, 126

Hughes, T. & Lubliner, J. (1973). On the one-dimensional theory of blood flow in larger vessels. *Math. Biosci.*, **170**, 161–70. 24

Huo, Y. & Kassab, G.S. (2007). A hybrid one-dimensional/Womersley model of pulsatile blood flow in the entire coronary arterial tree. *Am. J. Physiol. Heart Circ. Physiol.*, **292**, 2623–33. 52

Imanaga, I., Hara, H., Koyanagi, S. & Tanaka, K. (1998). Correlation between wave components of the second derivative of plethysmogram and arterial distensibility. *Japanese Heart J.*, **39**, 775–84. 93

Imholz, B., Wieling, W., Montfrans, G. & Wesseling, K. (1998). Fifteen years experience with finger arterial pressure monitoring: assessment of the technology. *Cardiov. Res.*, **38**, 605–16. 149

Isnard, R.N., Pannier, B.M., Laurent, S., London, G.M., Diebold, B. & Safar, M.E. (1989). Pulsatile diameter and elastic modulus of the aortic arch in essential hypertension: A noninvasive study. *J. Am. Coll. Cardiol.*, **13**, 399–405. 112

Jabbar, A.U., Ali, R.U., Parvez, K. & Niazi, U.H.K. (2012). Three-dimensional numerical analysis of pulsatile blood flow around different plaque shapes in human carotid artery. *IJBBB*, **2**, 305–8. 23

Jaeger, G., Westerhof, N. & Noordergraaf, A. (1965). Oscillatory flow impedance in electrical analog of arterial system. *Circ. Res.*, **16**, 121–34. 155

Jago, J.R. & Murray, A. (1988). Repeatability of peripheral pulse measurements on ears, fingers and toes using photoelectric plethysmography. *Clin. Phys. Physiol. Meas.*, **9**, 319–29. 10

Jansen, J., Schreuder, J., Mulier, J., Smith, N., Settels, J. & Wesseling, K. (2001). A comparison of cardiac output derived from the arterial pressure wave against thermodilution in cardiac surgery patients. *Br. J. Anaesth.*, **2**, 212–22. 70

Jaryal, A.K., Selvaraj, N., Santhosh, J., Anand, S. & Deepak, K.K. (2009). Monitoring of cardiovascular reactivity to cold stress using digital volume pulse characteristics in health and diabetes. *J. Clin. Monitor. Comp.*, **23**, 123–130. 119, 157

Johansson, A. & Oberg, P.A. (1999). Estimation of respiratory volumes from the photoplethysmographic signal. Part 2: A model study. *Med. Biol. Eng. Comput.*, **37**, 48–53. 10

Jones, C.J.H. & Sugawara, M. (1993). Wavefronts in the aorta - implications for the mechanisms of left ventricular ejection and aortic valve closure. *Cardiov. Res.*, **27**, 1902–5. 21

Jones, C.J.H., Sugawara, M., Kondoh, Y., Uchida, K. & Parker, K.H. (2002). Compression and expansion wavefront travel in canine ascending aortic flow: wave intensity analysis. *Heart Vessels*, **16**, 91–8. 85

Kakar, P. & Lip, G.Y.H. (2006). Towards understanding the aetiology and pathophysiology of human hypertension: where are we now? *J. Hum. Hypertens.*, **20**, 833–6. 126

Kannel, W.B. & Castelli, P. (1979). Role of diabetes in congestive heart failure: the framingham study. *Am. J. Cardiol.*, **34**, 29–34. 17

Kannel, W.B. & McGee, D.L. (1979). Diabetes and cardiovascular disease: the Framingham study. *JAMA*, **241**, 2035–8. 17, 101

Kannel, W.B., Gordon, T. & Schwartz, M.J. (1971). Systolic versus diastolic blood pressure and risk of coronary heart disease. The Framingham study. *Am. J. Cardiol.*, **27**, 335–46. 103

Kannel, W.B., Kannel, C., Paffenbarger, R.S.J. & Cupples, L.A. (1987). Heart rate and cardiovascular mortality: the Framingham Study. *Am. Heart J.*, **113**, 1489–94. 103

Karamanoglu, M., O'Rourke, M.F., Avolio, a.P. & Kelly, R.P. (1993). An analysis of the relationship between central aortic and peripheral upper limb pressure waves in man. *Eur. Heart J.*, **14**, 160–7. 53

Karamanoglu, M., Gallagher, D., Avolio, A. & O'Rourke, M. (1994). Functional origin of reflected pressure waves in a multibranched model of the human arterial system. *Am. J. Physiol. Heart Circ. Physiol.*, **267**, 1681–8. 53, 103, 132, 151, 152, 154

Karamanoglu, M., Gallagher, D.E., Rourke, F.O. & Avolio, P. (1995). Pressure wave propagation of the human upper limb in a multibranched model. *Am. J. Physiol. Heart Circ. Physiol.*, **269**, H1363–H1369. 58, 166

Karmonik, C., Bismuth, J.X., Davies, M.G. & Lumsden, A.B. (2008). Computational hemodynamics in the human aorta: A computational fluid dynamics study of three cases with patient-specific geometries and inflow rates. *Technol. Health Care*, **16**, 343–54. 23

Karmonik, C., Bismuth, J., Redel, T., Anaya-Ayala, J.E., Davies, M.G., Shah, D.J. & Lumsden, A.B. (2010). Impact of tear location on

hemodynamics in a type B aortic dissection investigated with computational fluid dynamics. *Conf. Proc. IEEE Eng. Med. Biol. Soc.*, **2010**, 3138–41. 23

Karniadakis, G. & Sherwin, S. (2013). *Spectral/hp element methods for computational fluid dynamics*. Oxford University Press. 52

Kearney, P., Whelton, M. & Reynolds, K. (2005). Global burden of hypertension: analysis of worldwide data. *Lancet*, **365**, 217–23. 126

Kelly, R., Hayward, C., Avolio, a. & O'Rourke, M. (1989). Noninvasive determination of age-related changes in the human arterial pulse. *Circulation*, **80**, 1652–9. 13

Khalilia, M., Chakraborty, S. & Popescu, M. (2011). Predicting disease risks from highly imbalanced data using random forest. *BMC medical informatics and decision making*, **11**, 51. 110

Khanafer, K., Gadhoke, P., Berguer, R. & Bull, J. (2006). Modeling pulsatile flow in aortic aneurysms: effect of non-Newtonian properties of blood. *Biorheology*, **43**, 661–79. 31

Khir, A. & Parker, K. (2005). Wave intensity in the ascending aorta: effects of arterial occlusion. *J. Biomech.*, **38**, 647–55. 152

Kim, J.M., Arakawa, K., Benson, K.T. & Fox, D.K. (1986). Pulse oximetry and circulatory kinetics associated with pulse volume amplitude measured by photoelectric plethysmography. *Anesth. Analg.*, **65**, 1333–9. 9

Kim, S.H., Kim, J.S., Kim, B.S., Choi, J., Lee, S.C., Oh, J.K. & Park, S.W. (2014). Time to peak velocity of aortic flow is useful in predicting severe aortic stenosis. *Int. J. Cardiol.*, **172**, 443–6. 85

Kind, T., Faes, T.J.C., Lankhaar, J.W., Vonk-Noordegraaf, A. & Verhaegen, M. (2010). Estimation of three- and four-element windkessel parameters using subspace model identification. *IEEE Trans. Biomed. Eng.*, **57**, 1531–8. 128, 155

King, H., Aubert, R. & Herman, W. (1998). Global burden of diabetes, 19952025: prevalence, numerical estimates, and projections. *Diabetes Care*, **21**, 1414–31. 165

Kiselev, I., Kolpakov, F., Biberdorf, E., Baranov, V., Komlyagina, T., Suvorova, I., Melnikov, V. & Krivoschekov, S. (2015). Patient-specific 1D model of the human cardiovascular system. In *Biomedical Engineering and Computational Technologies (SIBIRCON), 2015 International Conference on*, 1, 76–81. 103, 162

Kitawaki, T. (2012). *Numerical simulation model with viscoelasticity of arterial wall*. INTECH Open Access Publisher. 167

Kitawaki, T. & Shimizu, M. (2006). Flow analysis of viscoelastic tube using one-dimensional numerical simulation model. *J Biomed. Sci. Eng.*, **1**, 183–94. 36

Krabbe-Hartkamp, M.J., Grond, J.V.d., Leeuw, F.D., Groot, J.D., Algra, A., Hillen, B., Breteler, M. & Mali, W. (1998). Circle of Willis:

morphologic variation on three-dimensional time-of-flight MR angiograms. *Radiology*, **207**, 103–11. 56

Krause, T., Lovibond, K., Caulfield, M., McCormack, T. & Williams, B. (2011). Management of hypertension: summary of NICE guidance. *BMJ (Clinical research ed.)*, **343**, 1–6. 13, 14

Kroeker, E.J. & Wood, E.H. (1955). Comparison of simultaneously recorded central and peripheral arterial pressure pulses during rest, exercise and tilted position in man. *Circ. Res.*, **3**, 623–32. 61

Ku, J.P., Draney, M.T., Arko, F.R., Lee, W.A., Chan, F.P., Pelc, N.J., Zarins, C.K. & Taylor, C.A. (2002). In vivo validation of numerical prediction of blood flow in arterial bypass grafts. *Ann. Biomed. Eng.*, **30**, 743–52. 127

Kulkarni, N.B., Ganu, M.U., Godbole, S.G. & Deo, S.S. (2014). Effect of age and blood pressure on surrogate markers of atherosclerosis in patients with type 2 Diabetes mellitus. *J. Clin. Diagn. Res.*, **8**, 08–11. 112, 113, 162

Lacy, P.S., O'Brien, D.G., Stanley, A.G., Dewar, M.M., Swales, P.P. & Williams, B. (2004a). Increased pulse wave velocity is not associated with elevated augmentation index in patients with diabetes. *J. Hypertens.*, **22**, 1937–44. 17, 112

Lacy, P.S., O'Brien, D.G., Stanley, A.G., Dewar, M.M., Swales, P.P. & Williams, B. (2004b). Increased pulse wave velocity is not associated with elevated augmentation index in patients with diabetes. *J. Hypertens.*, **22**, 1937–44. 59

Lafortune, P. & Aris, R. (2012). Coupled electromechanical model of the heart: parallel finite element formulation. *Int. J. Numer. Meth. Biomed. Engng.*, **28**, 72–86. 164

Lago, R.M., Singh, P.P. & Nesto, R.W. (2007). Diabetes and hypertension. *Nature clinical practice. Endocrinology & metabolism*, **3**, 667. 101

Lakatta, E. & Schulman, S. (2004). Age-associated cardiovascular changes are the substrate for poor prognosis with myocardial infarction. *JACC*, **44**, 35–7. 162, 166

Lanzarone, E., Liani, P., Baselli, G. & Costantino, M.L. (2007). Model of arterial tree and peripheral control for the study of physiological and assisted circulation. *Med. Eng. Phys.*, **29**, 542–55. 25

Laurent, S., Boutouyrie, P., Asmar, R., Gautier, I., Laloux, B., Guize, L., Ducimetiere, P. & Benetos, A. (2001). Aortic stiffness is an independent predictor of all-cause and cardiovascular mortality in hypertensive patients. *Hypertension*, **37**, 1236–41. 19, 126

Laurent, S., Katsahian, S., Fassot, C., Tropeano, A.I., Gautier, I., Laloux, B. & Boutouyrie, P. (2003). Aortic stiffness is an independent predictor of fatal stroke in essential hypertension. *Stroke*, **34**, 1203–6. 19

Laurent, S., Cockcroft, J., Van Bortel, L., Boutouyrie, P., Giannattasio, C., Hayoz, D., Pannier, B., Vlachopoulos, C., Wilkinson, I. & Struijker-Boudier, H. (2006). Expert consensus document on arterial stiffness: methodological issues and clinical applications. *Eur. Heart J.*, **27**, 2588–605. 19, 21, 98, 103

Lax, H., Feinberg, a.W. & Urban, W. (1959). Abnormalities of the arterial pulse wave in young diabetic subjects. *Circulation*, **20**, 1106–10. 16

Learoyd, B.M. & Taylor, M.G. (1966). Alterations with age in the viscoelastic properties of human arterial walls. *Circulation Research*, **18**, 278–92. 40

Leary, D., O (1999). Carotid-artery intima and media thickness as a risk factor for myocardial infarction and stroke in older adults. *N. Engl. J. Med.*, **340**, 14–22. 18

Lee, S.W., Antiga, L., Spence, J.D. & Steinman, D.A. (2008). Geometry of the carotid bifurcation predicts its exposure to disturbed flow. *Stroke*, **39**, 2341–47. 126

Leguy, C.A.D. (2010). *On the clinical estimation of the hemodynamical and mechanical properties of the arterial tree*. Ph.D. thesis, Eindhoven University of Technology. 56, 75, 102, 165

Leguy, C.A.D., Bosboom, E.M.H., Gelderblom, H., Hoeks, A.P.G. & van de Vosse, F.N. (2010). Estimation of distributed arterial mechanical properties using a wave propagation model in a reverse way. *Med. Eng. Phys.*, **32**, 957–67. 29, 53, 54, 56, 98, 102, 103, 104, 127, 155

Leguy, C.a.D., Bosboom, E.M.H., Belloum, a.S.Z., Hoeks, a.P.G. & van de Vosse, F.N. (2011). Global sensitivity analysis of a wave propagation model for arm arteries. *Med. Eng. Phys.*, **33**, 1008–16. 24, 55, 68, 103, 107, 108, 126, 131, 160, 164

Levick, J. (2003). *An introduction to cardiovascular physiology*. Hodder Arnold, London, 5th edn. xiii, 4, 15

Levy, B. (2001). Artery changes with aging: degeneration or adaptation? *Dialogues Cardiovasc. Med.*, **6**, 104–11. 166

Li, C.W. & Cheng, H.D. (1993). A nonlinear fluid model for pulmonary blood circulation. *J. Biomech.*, **26**, 653–64. 51, 167

Liang, F. & Liu, H. (2005). A closed-loop lumped parameter computational model for human cardiovascular system. *JSME Int J., Ser. C*, **48**, 484–93. 25

Liang, F.Y., Takagi, S., Himeno, R. & Liu, H. (2009). Biomechanical characterization of ventricular-arterial coupling during aging: A multi-scale model study. *J. Biomech.*, **42**, 692–704. 52, 58

Liang, Y.L., Teede, H., Kotsopoulos, D., Shiel, L., Cameron, J.D., Dart, A.M. & McGrath, B.P. (1998). Non-invasive measurements of arterial structure and function: repeatability, interrelationships and trial sample size. *Clin. Sci.*, **95**, 669–79. 21

Liaw, A. & Wiener, M. (2002). Classification and regression by randomForest. *R news*, **2**, 18–22. 110

Lindberg, L., Tamura, T. & Oberg, P. (1991). Photoplethysmography. Part 1. Comparison with laser Doppler flowmetry. *Med. Biol. Eng. Comput.*, 40–7. 9

Lindberg, L., Ugnell, H. & Öberg, P. (1992). Monitoring of respiratory and heart rates using a fibre-optic sensor. *MBEC*, **30**, 533–7. 10

Liu, A.B., Wu, H.T., Liu, C.W., Liu, C.C., Tang, C.J., Tsai, I.T. & Sun, C.K. (2014). Application of multiscale entropy in arterial waveform contour analysis in healthy and diabetic subjects. *Med. Biol. Eng. Comput.*, **53**, 89–98. 119, 157

Liu, J.E., Palmieri, V., Roman, M.J., Bella, J.N., Fabsitz, R., Howard, B.V., Welty, T.K., Lee, E.T. & Devereux, R.B. (2001). The impact of diabetes on left ventricular filling pattern in normotensive and hypertensive adults: the strong heart study. *JACC*, **37**, 1943–9. 123

Lockwood, G., Ryan, L., Gotlieb, A., Lonn, E., Hunt, J., Liu, P. & Foster, F. (1992). In vitro high resolution intravascular imaging in muscular and elastic arteries. *JACC*, **20**, 153–60. 97

London, G., Blacher, J. & Pannier, B. (2001). Arterial wave reflections and survival in end-stage renal failure. *Hypertension*, **38**, 434–9. 21

Long, Q., Xu, X.Y., Ariff, B., Thom, S.A., Hughes, A.D. & Stanton, A.V. (2000). Reconstruction of blood flow patterns in a human carotid bifurcation: a combined CFD and MRI study. *JMRI*, **11**, 299–311. 127

Lu, S., Zhao, H., Ju, K., Shin, K., Lee, M., Shelley, K. & Chon, K.H. (2008). Can photoplethysmography variability serve as an alternative approach to obtain heart rate variability information? *J. Clin. Monitor. Comp.*, **22**, 23–9. 88

Lynch, T.G., Wright, C.B. & Miller, E.V. (1981). Oculopneumoplethysmography, doppler examination, and supraorbital photoplethysmography. A

comparison of hemodynamic techniques in assessing cerebrovascular occlusive disease. *Annals of Surgery*, **194**, 731–36. 12

Mancia, G. & The Task Force for the management of arterial hypertension of the European Society of Hypertension (ESH) and of the European Society of Cardiology (ESC) (2013). 2013 ESH/ESC guidelines for the management of arterial hypertension. *Eur. Heart J.*, **34**, 2159–219. 20, 128

Manini, S., Passera, K., Huberts, W., Botti, L., Antiga, L. & Remuzzi, A. (2013). Computational model for simulation of vascular adaptation following vascular access surgery in haemodialysis patients. *Comput. Methods Biomech. Biomed. Engin.*, **17**, 37–41. 103

Marchandise, E., Willemet, M. & Lacroix, V. (2009). A numerical hemodynamic tool for predictive vascular surgery. *Medical Engineering & Physics*, **31**, 131–44. 127

Marsden, A.L., Bernstein, A.J., Reddy, V.M., Shadden, S.C., Spilker, R.L., Chan, F.P., Taylor, C.A. & Feinstein, J.A. (2009). Evaluation of a novel Y-shaped extracardiac Fontan baffle using computational fluid dynamics. *J. Thorac. Cardiovasc. Surg.*, **137**, 394–403. 126

Masuyama, T., Kodama, K., Kitabatake, A., Nanto, S., Sato, H., Uematsu, M., Inoue, M. & Kamada, T. (1986). Noninvasive evaluation of aortic regurgitation by continuous-wave Doppler echocardiography. *Circulation*, **73**, 460–6. 86

Mathers, C.D. & Loncar, D. (2006). Projections of global mortality and burden of disease from 2002 to 2030. *PLoS medicine*, **3**, 2011–30. 1, 165

Mattace-Raso, F.U.S., Van Der Cammen, T.J.M., Hofman, A., Van Popele, N.M., Bos, M.L., Schalekamp, M.a.D.H., Asmar, R., Reneman, R.S., Hoeks, A.P.G., Breteler, M.M.B. & Witteman, J.C.M. (2006). Arterial stiffness and risk of coronary heart disease and stroke: The Rotterdam Study. *Circulation*, **113**, 657–63. 19

Matthys, K.S., Alastruey, J., Peiro, J., Khir, A.W., Segers, P., Verdonck, P.R., Parker, K.H. & Sherwin, S.J. (2007). Pulse wave propagation in a model human arterial network: Assessment of 1-D numerical simulations against in vitro measurements. *J. Biomech.*, **40**, 3476–86. 29, 50, 54, 60

McDonald, D.A. (1974). *Blood flow in arteries*. Williams & Wilkins. 8, 11, 16, 40, 46, 70, 77

McEniery, C.M., Yasmin, Hall, I.R., Qasem, A., Wilkinson, I.B. & Cockcroft, J.R. (2005). Normal vascular aging: Differential effects on wave reflection and aortic pulse wave velocity. *JACC*, **46**, 1753–60. 166

McEniery, C.M., Maki-Petaja, K.M., McDonnell, B.J., Munnery, M., Hickson, S.S., Franklin, S.S., Cockcroft, J.R. & Wilkinson, I.B. (2010). The impact of cardiovascular risk factors on aortic stiffness and wave reflections depends on age: The Anglo-Cardiff collaborative trial (ACCT III). *Hypertension*, **56**, 591–7. 19

McGrath, S.P., Ryan, K.L., Wendelken, S.M., Rickards, C.a. & Convertino, V.a. (2011a). Pulse oximeter plethysmographic waveform changes in awake, spontaneously breathing, hypovolemic volunteers. *Anesth. Analg.*, **112**, 368–74. 74

McGrath, S.P., Ryan, K.L., Wendelken, S.M., Rickards, C.a. & Convertino, V.a. (2011b). Pulse oximeter plethysmographic waveform changes in awake, spontaneously breathing, hypovolemic volunteers. *Anesth. Analg.*, **112**, 368–74. 157

McVeigh, G., Brennan, G., Hayes, R., Cohn, J., Finkelstein, S. & Johnston, D. (1993). Vascular abnormalities in non-insulin-dependent diabetes mellitus identified by arterial waveform analysis. *Amer. J. Med.*, **95**, 424–30. 16

Meaume, S., Benetos, A., Henry, O.F., Rudnichi, A. & Safar, M.E. (2001). Aortic pulse wave velocity predicts cardiovascular mortality in subjects ¡ 70 years of age. *Arterioscler. Thromb. Vasc. Biol.*, **21**, 2046–50. 19, 103

Megnien, J., Simon, A., Valensi, P. & Flaud, P. (1992). Comparative effects of Diabetes Mellitus and hypertension on physical properties of human large arteries. *JACC*, **20**. 101, 112

Milišić, V. & Quarteroni, A. (2004). Analysis of lumped parameter models for blood flow simulations and their relation with 1D models. *ESAIM*, **38**, 613–32. 133, 137

Millasseau, S., Kelly, R., Ritter, J. & Chowienczyk, P. (2002a). Determination of age-related increases in large artery stiffness by digital pulse contour analysis. *Clin. Sci.*, **377**, 371–7. 10, 72, 73, 122, 154, 157

Millasseau, S.C., Guigui, F.G., Kelly, R.P., Prasad, K., Cockcroft, J.R., Ritter, J.M. & Chowienczyk, P.J. (2000). Nonivasive assessment of the digital volume pulse: comparison with the peripheral pressure pulse. *Hypertension*, **36**, 952–956. xv, 63

Millasseau, S.C., Kelly, R.P., Ritter, J.M. & Chowienczyk, P.J. (2002b). Determination of age-related increases in large artery stiffness by digital pulse contour analysis. *Clin. Sci.*, **377**, 371–7. 22, 77, 98, 163

Millasseau, S.C., Kelly, R.P., Ritter, J.M. & Chowienczyk, P.J. (2003). The vascular impact of aging and vasoactive drugs: Comparison of two digital volume pulse measurements. *AJH*, **16**, 467–72. 22, 163

Millasseau, S.C., Ritter, J.M., Takazawa, K. & Chowienczyk, P. (2006). Contour analysis of the photoplethysmographic pulse measured at the finger. *J. Hypertens.*, **24**, 1449–56. xiv, 21, 22, 74, 157

Milner, J., Moore, J., Rutt, B. & Teinman, D. (1998). Hemodynamics of human carotid artery bifurcation computational studies with models reconstructed from magnetic resonance imaging of normal subjects. *Vasc. Surg.*, **28**, 143–56. 126

Mion, D. & Pierin, a.M.G. (1998). How accurate are sphygmomanometers? *J. Hum. Hypertens.*, **12**, 245–8. 14

Mitchell, G.F., Lacourcière, Y., Ouellet, J.P., Izzo, J.L., Neutel, J., Kerwin, L.J., Block, A.J. & Pfeffer, M.a. (2003). Determinants of elevated pulse pressure in middle-aged and older subjects with uncomplicated systolic hypertension: the role of proximal aortic diameter and the aortic pressure-flow relationship. *Circulation*, **108**, 1592–8. 59, 85, 112

Mitchell, G.F., Conlin, P.R., Dunlap, M.E., Lacourcière, Y., Arnold, J.M.O., Ogilvie, R.I., Neutel, J., Izzo, J.L. & Pfeffer, M.a. (2008). Aortic diameter, wall stiffness, and wave reflection in systolic hypertension. *Hypertension*, **51**, 105–11. 19

Mitchell, G.F., Hwang, S.J., Vasan, R.S., Larson, M.G., Pencina, M.J., Hamburg, N.M., Vita, J.a., Levy, D. & Benjamin, E.J. (2010). Arterial stiffness and cardiovascular events: the Framingham Heart Study. *Circulation*, **121**, 505–11. 18

Miyashita, H. (2012). Clinical assessment of central blood pressure. *Current Hypertension Reviews*, **8**, 80–90. xiii, 12

Montecinos, G.I., Müller, L.O. & Toro, E.F. (2014). Hyperbolic reformulation of a 1D viscoelastic blood flow model and ADER finite volume schemes. *J. Comput. Phys.*, **266**, 101–23. 51

Moorhead, K.T., Doran, C.V., Chase, J.G. & David, T. (2004). Lumped parameter and feedback control models of the auto-regulatory response in the circle of willis. *Comput. Methods Biomech. Biomed. Engin.*, **7**, 121–30. 167

Morikawa, Y. (1967). Characteristic pulse wave caused by organic nitrates. *Nature*, **213**, 841–2. 22

Moyle, K.R., Antiga, L. & Steinman, D.a. (2006). Inlet conditions for image-based CFD models of the carotid bifurcation: is it reasonable to assume fully developed flow? *J. Biomech. Eng.*, **128**, 371–9. 126

Mozaffarian, D., Benjamin, E.J., Go, A.S., Arnett, D.K., Blaha, M.J., Cushman, M., De Ferranti, S., Després, J.P., Fullerton, H.J., Howard, V.J., Huffman, M.D., Judd, S.E., Kissela, B.M., Lackland, D.T., Lichtman, J.H., Lisabeth, L.D., Liu, S., Mackey, R.H., Matchar, D.B., McGuire, D.K., Mohler, E.R., Moy, C.S., Muntner, P., Mussolino, M.E., Nasir, K., Neumar, R.W., Nichol, G., Palaniappan, L., Pandey, D.K., Reeves, M.J., Rodriguez, C.J., Sorlie, P.D., Stein, J., Towfighi, A., Turan, T.N., Virani, S.S., Willey, J.Z., Woo, D., Yeh, R.W. & Turner, M.B. (2015). *Heart disease and stroke statistics-2015 update : A report from the American Heart Association*, vol. 131. 101

Müller, L.O. & Toro, E.F. (2013). Well-balanced high-order solver for blood flow in networks of vessels with variable properties. *Int. J. Numer. Meth. Biomed. Engng.*, **29**, 1388–411. 24, 51

Murgo, J.P., Westerhof, N., Giolma, J.P. & Altobelli, S.a. (1980). Aortic input impedance in normal man: relationship to pressure wave forms. *Circulation*, **62**, 105–116. 8

Myers, L.J. & Capper, W.L. (2004). Exponential taper in arteries: an exact solution of its effect on blood flow velocity waveforms and impedance. *Medical Engineering & Physics*, **26**, 147–55. 96

Myers, R.H., Montgomery, D.C. & Anderson-Cook, C.M. (2009). *Response surface methodology: process and product optimization using designed experiments*. John Wiley \& Sons. 106

Mynard, J.P. & Nithiarasu, P. (2008). A 1D arterial blood flow model incorporating ventricular pressure, aortic valve and regional coronary flow using the locally conservative Galerkin (LCG) method. *Commun. Numer. Meth. Engng.*, **24**, 367–417. 24, 29, 50, 52, 54, 55, 102, 103, 127, 128, 151, 163, 166

Mynard, J.P. & Smolich, J.J. (2015). One-dimensional haemodynamic modeling and wave dynamics in the entire adult circulation. *Ann. Biomed. Eng.*, **43**, 1443–60. xv, 29, 55, 56, 59, 63, 165

Najjar, S.S., Scuteri, A. & Lakatta, E.G. (2005). Arterial Aging: Is it an immutable cardiovascular risk factor? *Hypertension*, **46**, 454–62. 18

Nakajima, K., Tamura, T. & Miike, H. (1996). Monitoring of heart and respiratory rates by photoplethysmography using a digital filtering technique. *Med. Eng. Phys.*, **18**, 365–72. 93

Nichols, M., Townsend, N., Scarborough, P., Luengo-Fernandez, R., Leal, J., Gray, A. & Rayner, M. (2013). European cardiovascular disease statistics 4th edition 2012: EuroHeart II. *Eur. Heart J.*, **34**. 1, 13

Nichols, W.W., Conti, C.R., Walker, W.E. & Milnor, W.R. (1977). Input impedance of the systemic circulation in man. *Circ. Res.*, **40**, 451–8. 85

Nichols, W.W., Rourke, M.F.O., Avolio, A.P., Yaginuma, T., Murgo, J.P., Pepjne, C.J. & Conti, C.R. (1984). Effects of age on ventricular-vascular coupling. *Am. J. Cardiol.*, **55**, 1179–84. 166

Nilsson, L., Johansson, A. & Kalman, S. (2000). Monitoring of respiratory rate in postoperative care using a new photoplethysmographic technique. *J. Clin. Monitor.*, **16**, 309–15. 10

Nitzan, M., Babchenko, A., Khanokh, B. & Landau, D. (1998). The variability of the photoplethysmographic signal–a potential method for the evaluation of the autonomic nervous system. *Physiol. Meas.*, **19**, 93–102. 10

Nkomo, V.T., Enriquez-Sarano, M., Ammash, N.M., III, L.J.M., Bailey, K.R., Desjardins, V., Horn, R.A. & Tajik, A.J. (2003). Bicuspid aortic valve associated with aortic dilatation: A community-based study. *Arterioscler. Thromb. Vasc. Biol.*, **23**, 351–6. 86

Noordergraaf, A., Verdouw, D. & Boom, H.B. (1963). The use of an analog computer in a circulation model. *Prog. Cardiovasc. Des.*, **5**, 419–39. 56, 102

Oates, C. (2001). *Cardiovascular haemodynamics and doppler waveforms explained*. Greenwich Medical Media. xv, 63

Ohayon, J., Rioufol, G., Dubreuil, O. & Lyon, D. (2005). A three-dimensional finite element analysis of stress distribution in a coronary atherosclerotic plaque:. *Biomechanics Applied to Computer Assisted Surgery*, **661**, 225–41. 23

Oliva, I. & Roztocil, K. (1983). Toe pulse wave analysis in obliterating atherosclerosis. *Angiology*, **34**, 610–19. 12

Olufsen (1999). Structured tree outflow condition for blood flow in larger systemic arteries. *Am. J. Physiol. Heart Circ. Physiol.*, **276**, 257–68. 24, 36, 51, 52, 127, 155

Olufsen, M. & Nadim, A. (2004). On deriving lumped models for blood flow and pressure in the systemic arteries. *Math. Biosci. Eng.*, **1**, 61–80. 126, 128, 133

Olufsen, M.S. (1999). Structured tree outflow conditions for blood flow in larger systemic arteries. *Am. J. Physiol. Heart Circ. Physiol.*, **276**, 257–68. 167

Olufsen, M.S., Peskin, C.S., Kim, W.Y., Pedersen, E.M., Nadim, A. & Larsen, J. (2000). Numerical simulation and experimental validation of blood flow in arteries with structured-tree outflow conditions. *Ann. Biomed. Eng.*, **28**, 1281–99. 25, 29, 53

Olufsen, M.S., Nadim, A. & Lipsitz, L.a. (2002). Dynamics of cerebral blood flow regulation explained using a lumped parameter model. *Am. J. Physiol. Regulatory Integrative Comp. Physiol.*, **282**, 611–22. 25

Olufsen, M.S., Ottesen, J.T., Tran, H.T., Ellwein, L.M., Lipsitz, L.a. & Novak, V. (2005). Blood pressure and blood flow variation during postural change from sitting to standing: model development and validation. *Journal of applied physiology (Bethesda, Md. : 1985)*, **99**, 1523–37. 160

O'Rourke, M.F. (2007). Arterial aging: pathophysiological principles. *Vasc. Med.*, **12**, 329–41. 97

O'Rourke, M.F. & Adji, A. (2010). Clinical use of applanation tonometry: hope remains in Pandora's box. *J. Hypertens.*, **28**, 229–33. 13

Oseli, D., Bajec, I.L., Klemenc, M. & Zimic, N. (2003). Measurement and analysis of radial artery blood velocity in young normotensive subjects. *Informatica Medica Slovenica*, **8**, 15–9. xv, 63

Otsuka, T., Kawada, T., Katsumata, M. & Ibuki, C. (2006). Utility of second derivative of the finger photoplethysmogram for the estimation of the risk of coronary heart disease in the general population. *Circ. J.*, **70**, 304–10. 93

ORourke, M.F. (2009). Time domain analysis of the arterial pulse in clinical medicine. *Med. Biol. Eng. Comput.*, **47**, 119–29. 84

Padilla, J., Berjano, E., Saiz, J., Facila, L., Diaz, P. & Merce, S. (2006). Assessment of relationships between blood pressure, pulse wave velocity and digital volume pulse. *Comput. Cardiol.*, 893–6. 163

Paini, A., Boutouyrie, P., Calvet, D., Tropeano, A.I., Laloux, B. & Laurent, S. (2006). Carotid and aortic stiffness: determinants of discrepancies. *Hypertension*, **47**, 371–6. 16, 19, 112

Parazynski, S.E., Tucker, B.J., Aratow, M., Crenshaw, A. & Hargens, A.R. (1993). Direct measurement of capillary blood pressure in the human lip. *J. Appl. Physiol.*, **74**, 946–50. 70

Parikh, a., Sochett, E.B., McCrindle, B.W., Dipchand, A., Daneman, A. & Daneman, D. (2000). Carotid artery distensibility and cardiac function in adolescents with type 1 diabetes. *J. Pediatr.*, **137**, 465–9. 16

Parker, K.H. & Jones, C.J.H. (1990). Forward and backwards running waves in the arteries: analysis using the method of characteristics. *J. Biomech. Eng.*, **112**, 322–26. 19, 51

Patvardhan, E., Heffernan, K.S., Ruan, J., Hession, M., Warner, P., Karas, R.H. & Kuvin, J.T. (2011). Augmentation index derived from peripheral arterial tonometry correlates with cardiovascular risk factors. *Cardiol. Res. Pract.*, **2011**, 1–6. 21

Pauca, A.L., Wallenhaupt, S.L., Kon, N.D. & Tucker, W.Y. (1992). Does radial artery pressure accurately reflect aortic pressure? *CHEST Journal*, **102**, 1193–8. 13

Payne, S.J. (2004). Analysis of the effects of gravity and wall thickness in a model of blood flow through axisymmetric vessels. *Med. Biol. Eng. Comput.*, **42**, 799–806. 36, 160

Pell, S. & Alonzo, C.A.D. (1967). Some aspects of hypertension in diabetes mellitus. *JAMA*, **202**, 10–6. 17

Perdikaris, P., Grinberg, L. & Karniadakis, G.E. (2014). An effective fractal-tree closure model for simulating blood flow in large arterial networks. *Ann. Biomed. Eng.*, 1–11. 102, 128, 151, 164

Perktold, K., Resch, M. & Peter, R. (1991). Three-dimensional numerical analysis of pulsatile flow and wall shear stress in the carotid artery bifurcation. *J. Biomech.*, **24**, 409–20. 23

Phillips, J.P., Belhaj, A., Shafqat, K., Langford, R.M., Shelley, K.H. & Kyriacou, P.a. (2012). Modulation of finger photoplethysmographic traces during forced respiration: Venous blood in motion? *Conf. Proc. IEEE Eng. Med. Biol. Soc.*, 3644–47. 10

Pickering, T.G., Hall, J.E., Appel, L.J., Falkner, B.E., Graves, J., Hill, M.N., Jones, D.W., Kurtz, T., Sheps, S.G. & Roccella, E.J. (2005). Recommendations for blood pressure measurement in humans and experimental animals: Part 1: blood pressure measurement in humans: a statement for professionals from the Subcommittee of Professional and Public Education of the American Heart Association Cou. *Hypertension*, **45**, 142–61. 14

Pietrabissa, R., Mantero, S., Marotta, T. & Menicanti, L. (1996). A lumped parameter model to evaluate the fluid dynamics of different coronary bypasses. *Med. Eng. Phys.*, **18**, 477–84. 25

Pope, S.R., Ellwein, L.M., Zapata, C.L., Novak, V., Kelley, C.T. & Olufsen, M.S. (2009). Estimation and identification of parameters in a lumped cerebrovascular model. *Math. Biosci. Eng.*, **6**, 93–115. 54, 104, 126

Quick, C.M., Young, W.L. & Noordergraaf, A. (2001). Infinite number of solutions to the hemodynamic inverse problem. *Am. J. Physiol. Heart Circ. Physiol.*, **280**, 1472–9. 24, 102, 127

Quick, C.M., Berger, D.S., Stewart, R.H., Laine, G.a., Hartley, C.J. & Noordergraaf, A. (2006). Resolving the hemodynamic inverse problem. *IEEE Trans. Biomed. Eng.*, **53**, 361–8. 102, 127

Qureshi, M.U., Vaughan, G.D.a., Sainsbury, C., Johnson, M., Peskin, C.S., Olufsen, M.S. & Hill, N.a. (2014). Numerical simulation of blood flow and pressure drop in the pulmonary arterial and venous circulation. *Biomech. Model Mechanobiol.*, **13**, 1137–54. 51

R Development Core Team (2014). R: A language and environment for statistical computing. Vienna: R foundation for statistical computing. 110

Raines, J.K., Jaffrin, M.Y. & Shapiro, A.H. (1974). A computer simulation of arterial dynamics in the human leg. *J. Biomech.*, **7**, 77–91. 36, 155, 164

Ravikumar, R., Deepa, R., Shanthirani, C.S. & Mohan, V. (2002). Comparison of carotid intima-media thickness, arterial stiffness, and brachial artery flow mediated dilatation in diabetic and nondiabetic subjects (The Chennai urban population study [CUPS-9]). *Am. J. Cardiol.*, **90**, 702–7. 17, 112

Rees, P.M. (1968). Electron microscopical observations on the architecture of the carotid arterial walls , with special reference to the sinus portion. *J. Anat.*, **103**, 35–47. 97

Reisner, A.T. & Heldt, T. (2013). A computational model of hemorrhage and dehydration suggests a pathophysiological mechanism: Starling-mediated protein trapping. *Am .J. Physiol. Heart. Circ. Physiol.*, **304**, 620–31. 25

Reuderink, P.J., Hoogstraten, H.W., Sipkema, P., Hillen, B. & Westerhof, N. (1989). Linear and nonlinear one-dimensional models of pulse wave transmission at high Womersley numbers. *J. Biomech.*, **22**, 819–27. 36

Reymond, P. (2011). *Pressure and flow wave propagation in patient-specific models of the arterial tree*. Ph.D. thesis. 62

Reymond, P., Merenda, F., Perren, F., Rufenacht, D. & Stergiopulos, N. (2009). Validation of a one-dimensional model of the systemic arterial tree. *Am. J. Physiol. Heart Circ. Physiol.*, **297**, 208–22. xv, 24, 37, 50, 53, 55, 56, 57, 62, 63, 95, 96, 102, 127, 128, 151, 158, 164, 167

Reymond, P., Bohraus, Y., Perren, F., Lazeyras, F. & Stergiopulos, N. (2011). Validation of a patient-specific one-dimensional model of the systemic arterial tree. *Am. J. Physiol. Heart Circ. Physiol.*, **301**, 1173–82. 29, 36, 54, 56, 103, 165, 166

Reymond, P., Westerhof, N. & Stergiopulos, N. (2012). Systolic hypertension mechanisms: effect of global and local proximal aorta stiffening on pulse pressure. *Ann. Biomed. Eng.*, **40**, 742–9. 53

Roman, M.J.D., Devereux, R.B., Kramer-Fox, R. & O'Loughlin, J. (1989). Two-dimensional echocardiographic aortic root dimensions in normal children and adults. *Am. J. Cardiol.*, **64**, 507–12. 70

Rourke, M.F.O. & Pauca, A.L. (2004). Augmentation of the aortic and central arterial pressure waveform. *Blood Press. Monit.*, **9**, 179–85. xiii, 22

Rowland, T., Potts, J., Potts, T., Son-Hing, J., Harbison, G. & Sandor, G. (1999). Cardiovascular responses to exercise in children and adolescents with myocardial dysfunction. *Am. Heart J.*, **137**, 126–33. 85

Safar, M.E., Blacher, J., Pannier, B., Guerin, A.P., Marchais, S.J., Guyonvarc'h, P.M. & London, G.M. (2002). Central pulse pressure and mortality in end-stage renal disease. *Hypertension*, **39**, 735–8. 19

Saito, M., Ikenaga, Y., Matsukawa, M., Watanabe, Y., Asada, T. & Lagree, P.Y. (2011). One-dimensional model for propagation of a pressure wave in a model of the human arterial network: Comparison of theoretical and experimental results. *J. Biomech. Eng.*, **133**, 121005. 29

Saunders, J. (1987). Alcohol: an important cause of hypertension. *BMJ*, **294**, 1045–6. 14

Schaaf, B.W. & Abbrecht., P.H. (1972). Digital computer simulation of human systemic arterial pulse wave transmission: a nonlinear model. *J. Bio*, **5**, 345–64. 51

Schmid-Schönbein, H. (1981). *Clinical aspects of blood viscosity and cell deformability*. Springer London. 99

Schram, M.T., Henry, R.M.A., van Dijk, R.A.J.M., Kostense, P.J., Dekker, J.M., Nijpels, G., Heine, R.J., Bouter, L.M., Westerhof, N. & Stehouwer, C. (2004). Increased central artery stiffness in impaired glucose and type 2 diabetes. *Hypertension*, **43**, 176–81. 18

Secker, C. & Spiers, P. (1997). Accuracy of pulse oximetry in patients with low systemic vascular resistance. *Respirology*, **52**, 127–130. 9

Segers, P. & Verdonck, P. (2000). Role of tapering in aortic wave reflection: hydraulic and mathematical model study. *J. Biomech.*, **33**, 299–306. 96

Segers, P., Stergiopulos, N., Verdonck, P. & Verhoeven, R. (1997). Assessment of distributed arterial network models. *Med. Biol. Eng. Comput.*, **35**, 729–36. 60

Segers, P., De Backer, J., Devos, D., Rabben, S.I., Gillebert, T.C., Van Bortel, L.M., De Sutter, J., De Paepe, A. & Verdonck, P.R. (2006). Aortic reflection coefficients and their association with global indexes of wave reflection in healthy controls and patients with Marfan's syndrome. *Am. J. Physiol. Heart Circ. Physiol.*, **290**, 2385–92. 21

Segers, P., Rietzschel, E.R., De Buyzere, M.L., De Bacquer, D., Van Bortel, L.M., De Backer, G., Gillebert, T.C. & Verdonck, P.R. (2007). Assessment of pressure wave reflection: Getting the timing right! *Physiol. Meas.*, **28**, 1045–56. 21

Segers, P., Rietzschel, E.R., De Buyzere, M.L., Stergiopulos, N., Westerhof, N., Van Bortel, L.M., Gillebert, T. & Verdonck, P.R. (2008). Three- and four-element Windkessel models: Assessment of their fitting performance in a large cohort of healthy middle-aged individuals. *Proc. Inst. Mech. Eng. H*, **222**, 417–28. 128

Shelley, K.H. (2007). Photoplethysmography: Beyond the calculation of arterial oxygen saturation and heart rate. *Anesth. Analg.*, **105**, 31–6. 11, 99

Sheng, C., Sarwal, S.N., Watts, K.C. & Marble, a.E. (1995). Computational simulation of blood flow in human systemic circulation incorporating an external force field. *Med. Biol. Eng. Comput.*, **33**, 8–17. 36

Sherwin, S., Franke, V., Peiró, J. & Parker, K. (2003a). One-dimensional modelling of a vascular network in space-time variables. *J. Eng. Math.*, **47**, 217–50. 24, 33, 43, 50, 52

Sherwin, S.J., Formaggia, L. & Peirã, J. (2003b). Computational modelling of 1D blood flow with variable mechanical properties and its application to the simulation of wave propagation in the human arterial system. *Int. J. Numer. Meth. Fluids*, **700**, 673–700. 36

Shi, Y., Lawford, P. & Hose, R. (2011). Review of 0-D and 1-D models of blood flow in the cardiovascular system. *Biomed. Eng. Online*, **10**, 3476–86. 24, 44

Shier, D., Butler, J. & Lewis, R. (2003). *Anatomy & physiology*. McGraw-Hill. xii, 7

Simonson, E., Koff, S., Keys, A. & Minckler, J. (1955). Contour of the toe pulse, reactive hyperemia, and pulse transmission velocity: group and repeat variability, effect of age, exercise, and disease. *Am. Heart J.*, **50**, 260–79. 12

Singh, B., Chakkal, S.K. & Ahuja, N. (2006). Formulation and optimization of controlled release mucoadhesive tablets of atenolol using response surface methodology. *AAPS PharmSciTech*, **7**, 1–10. 104

Singh, I. (2010). *Textbook of human histology: With colour atlas & practical guide*. Jaypee Brothers Publishers. 97

Smith, N.P., Pullan, A.J. & Hunter, P.J. (2002). An anatomically based model of transient coronary blood flow in the heart. *SIAM J. Appl. Math.*, **62**, 990–1018. 24, 33, 35, 36

Sowers, J.R., Epstein, M. & Frohlich, E.D. (2001). Diabetes, hypertension, and cardiovascular disease an update. *Hypertension*, **37**, 1053–9. 101

Spigulis, J. (2005). Optical noninvasive monitoring of skin blood pulsations. *Applied Optics*, **44**, 1850–7. 9

Stakos, D.a., Schuster, D.P., Sparks, E.a., Wooley, C.F., Osei, K. & Boudoulas, H. (2005). Cardiovascular effects of type 1 diabetes mellitus in children. *Angiology*, **56**, 311–7. 16

Stamler, J., Vaccaro, O., Neaton, J. & Wentworth, D. (1993). Diabetes, other risk factors, and 12-yr cardiovascular mortality for men screened in multiple risk factor intervention trial. *Diabetes Care*, **16**, 434–44. 18

Stampfer, M.J., Ridker, P.M. & Dzau, V.J. (2004). Risk factor criteria. *Circulation*, **109**, IV–3. 18

Steele, B.N., Wan, J., Ku, J.P., Hughes, T.J.R. & Taylor, C.a. (2003). In vivo validation of a one-dimensional finite-element method for predicting blood flow in cardiovascular bypass grafts. *IEEE Trans. Biomed. Eng.*, **50**, 649–56. 29, 53, 127

Stehouwer, C.D.a., Henry, R.M.a. & Ferreira, I. (2008). Arterial stiffness in diabetes and the metabolic syndrome: A pathway to cardiovascular disease. *Diabetologia*, **51**, 527–39. 101

Stergiopulos, N., Young, D.F. & Rogge, T.R. (1992). Computer simulation of arterial flow with applications to arterial and aortic stenoses. *J. Biomech.*, **25**, 1477–88. 24, 36, 102, 128, 151, 164

Stergiopulos, N., Meister, J.J. & Westerhof, N. (1995). Evaluation of methods for estimation of total arterial compliance. *Am. J. Physiol.*, **268**, 1540–8. 102

Stergiopulos, N., Westerhof, B.E. & Westerhof, N. (1999). Total arterial inertance as the fourth element of the windkessel model. *Am. J. Physiol. Heart Circ. Physiol.*, **276**, 81–8. 102, 128, 155

Stettler, J.C., Niederer, P. & Anliker, M. (1981). Theoretical analysis of arterial hemodynamics including the influence of bifurcations. Part I: mathematical models and prediction of normal pulse patterns. *Ann. Biomed. Eng.*, **9**, 145–64. 29, 51

Streeter, V.L., Keitzer, W.F. & Bohr, D.F. (1963). Pulsatile pressure and flow through distensible vessels. *Circ. Res.*, **13**, 3–20. 167

Surovtsova, I. (2005). Effects of compliance mismatch on blood flow in an artery with endovascular prosthesis. *J. Biomech.*, **38**, 2078–86. 167

Sutton-Tyrrell, K., Najjar, S.S., Boudreau, R.M., Venkitachalam, L., Kupelian, V., Simonsick, E.M., Havlik, R., Lakatta, E.G., Spur-

geon, H., Kritchevsky, S., Pahor, M., Bauer, D. & Newman, A. (2005). Elevated aortic pulse wave velocity, a marker of arterial stiffness, predicts cardiovascular events in well-functioning older adults. *Circulation*, **111**, 3384–90. 20

Takazawa, K., Tanaka, N., Fujita, M., Matsuoka, O., Saiki, T., Aikawa, M., Tamura, S. & Ibukiyama, C. (1998). Assessment of vasoactive agents and vascular aging by the second derivative of photoplethysmogram waveform. *Hypertension*, **32**, 365–70. 11, 74, 98, 157

Talke, P., Nichols, R.J. & Traber, D.L. (1990). Does measurement of systolic blood pressure with a pulse oximeter correlate with conventional methods? *J. Clin. Monitor.*, **6**, 5–9. 93

Tanaka, G., Sawada, Y. & Yamakoshi, K. (2000). Beat-by-beat double-normalized pulse volume derived photoplethysmographically as a new quantitative index of finger vascular tone in humans. *Eur. J. Appl. Physiol.*, **81**, 148–54. 93

Taylor, C.a., Draney, M.T., Ku, J.P., Parker, D., Steele, B.N., Wang, K. & Zarins, C.K. (1999). Predictive medicine: computational techniques in therapeutic decision-making. *Comput. Aided Surg.*, **4**, 231–47. 126

Taylor, M. (1966). The input impedance of an assembly of randomly branching elastic tubes. *Biophys. J.*, **6**, 29–51. 47

Tedesco, M.A., Natale, F., Di Salvo, G., Caputo, S., Capasso, M. & Calabró, R. (2004). Effects of coexisting hypertension and type II diabetes mellitus on arterial stiffness. *J. Hum. Hypertens.*, **18**, 469–73. 59, 112

Teng, X.F. & Zhang, Y.T. (2004). The effect of contacting force on photoplethysmographic signals. *Physiol. Meas.*, **25**, 1323–35. 99

Tezduyar, T.E., Sathe, S., Schwaab, M. & Conklin, B.S. (2008). Arterial fluid mechanics modeling with the stabilized space time fluid structure interaction technique. *Int. J. Numer. Meth. Fluids*, 601–629. 126

The Reference Values for Arterial Stiffness' Collaboration (2010). Determinants of pulse wave velocity in healthy people and in the presence of cardiovascular risk factors: 'establishing normal and reference values'. *Eur. Heart J.*, **31**, 2338–50. 71

Thiele, R.H., Colquhoun, D.a., Patrie, J., Nie, S.H. & Huffmyer, J.L. (2011). Relationship between plethysmographic waveform changes and hemodynamic variables in anesthetized, mechanically ventilated patients undergoing continuous cardiac output monitoring. *J. Cardiothorac. Vasc. Anesth.*, **25**, 1044–50. 81, 94

Trefford, J.d. & Lafferty, K. (1984). What does photoplethysmography measure? *Med. Biol. Eng. Comput.*, 479–80. 9

Triantafyllou, A., Anyfanti, P., Gavriilaki, E., Zabulis, X., Gkaliagkousi, E., Petidis, K., Triantafyllou, G., Gkolias, V., Pyrpasopoulou, A. & Douma, S. (2014). Association between retinal vessel caliber and arterial stiffness in a population comprised of normotensive to early-stage hypertensive individuals. *Am. J. Hypertens.*, **27**, 1472–8. 112

Ueda, H., Hayashi, T., Tsumura, K., Yoshimaru, K., Nakayama, Y. & Yoshikawa, J. (2004). The timing of the reflected wave in the ascending aortic

pressure predicts restenosis after coronary stent placement. *Hypertens. Res.*, **27**, 535–40. 21

Urquiza, S., Blanco, P., Vénere, M. & Feijóo, R. (2006). Multidimensional modelling for the carotid artery blood flow. *Comput. Methods Appl. Mech. Engrg.*, **195**, 4002–17. 36

Ursino, M. (1998). Interaction between carotid baroregulation and the pulsating heart: a mathematical model. *Am. J. Physiol. Heart Circ. Physiol.*, **275**, 1733–47. 55

Usman, S., Reaz, M. & Ali, M. (2013). Repeated measurement analysis of the area under the curve of photoplethysmogram among diabetic patients. *Life Science Journal*, **10**, 1–4. 121, 157

Utami, N., Setiawan, A.W., Zakaria, H., Mengko, T.R. & Mengko, R. (2013). Extracting blood flow parameters from Photoplethysmograph signals: A review. *2013 3rd International Conference on ICICI-BME*, 403–7. 74, 157

Valdez-Jasso, D., Banks, H.T., Haider, M.a., Bia, D., Zocalo, Y., Armentano, R.L. & Olufsen, M.S. (2009). Viscoelastic models for passive arterial wall dynamics. *Adv. Appl. Math. Mech.*, **1**, 151–65. 40

Valdez-Jasso, D., Bia, D., Zócalo, Y., Armentano, R.L., Haider, M.a. & Olufsen, M.S. (2011). Linear and nonlinear viscoelastic modeling of aorta and carotid pressure-area dynamics under in vivo and ex vivo conditions. *Ann. Biomed. Eng.*, **39**, 1438–56. 155

van de Vosse, F.N. & Stergiopulos, N. (2011). Pulse wave propagation in the arterial tree. *Annu. Rev. Fluid Mech.*, **43**, 467–99. 5

van den Bos, G., Westerhof, N., Elzinga, G. & Sipkema, P. (1976). Reflection in the systemic arterial system: Effects of aortic and carotid occlusion. *Cardiov. Res.*, **10**, 565–73. 152

Veijalainen, A., Tompuri, T., Laitinen, T., Lintu, N., Viitasalo, A., Laaksonen, D.E., Jääskeläinen, J. & Lakka, T.a. (2013). Metabolic risk factors are associated with stiffness index, reflection index and finger skin temperature in children. *Circulation J.*, **77**, 1281–8. 163

Vermeersch, S.J., Dynamics, B. & Society, L. (2010). Determinants of pulse wave velocity in healthy people and in the presence of cardiovascular risk factors: 'establishing normal and reference values'. *Eur. Heart J.*, **31**, 2338–50. 19

Vicente, G., Coteron, A. & Aracil, J.M.M. (1998). Application of the factorial design of experiments and response surface methodology to optimize biodiesel production. *Ind. Crop. Prod.*, **8**, 29–35. 104

Vignon-Clementel, I., Figueroa, C., Jansen, K. & Taylor, C. (2010). Outflow boundary conditions for 3D simulations of non-periodic blood flow and pressure fields in deformable arteries. *Comput. Methods Biomech. Biomed. Engin.*, **13**, 625–40. 28

Visser, K., Lamberts, R., Korsten, H. & Zijlstra, E. (1976). Observations on blood flow related electrical impedance changes in rigid tubes. *Pflügers Arch.*, **366**, 289–91. 9

Vlachopoulos, C., Aznaouridis, K., O'Rourke, M.F., Safar, M.E., Baou, K. & Stefanadis, C. (2010). Prediction of cardiovascular events and all-cause mortality with central haemodynamics: A systematic review and meta-analysis. *Eur. Heart J.*, **31**, 1865–71. 21

Vorp, D.a., Raghavan, M.L. & Webster, M.W. (1998). Mechanical wall stress in abdominal aortic aneurysm: influence of diameter and asymmetry. *J. Vasc. Surg*, **27**, 632–9. 23

Wald, N. & Law, M. (2003). A strategy to reduce cardiovascular disease by more than 80%. *BMJ*, **326**, 1–6. 1

Wallace, C.T., Baker, J.D.I.I.I., Alpert, C.C., Tankersley, S.J., Conroy, J.M. & Kerns, R.E. (1987). Comparison of blood pressure measurement by Doppler and by pulse oximetry techniques. *Anesth. Analg.*, **66**, 1018–9. 93

Walton, Z.D., Kyriacou, P.A., Silverman, D.G. & Shelley, K.H. (2010). Measuring venous oxygenation using the photoplethysmograph waveform. *J. Clin. Monitor. Comp.*, **24**, 295–303. 10

Wan, J., Steele, B., Spicer, S.a., Strohband, S., Feijoo, G.R., Hughes, T.J. & Taylor, C.a. (2002). A one-dimensional finite element method for simulation-based medical planning for cardiovascular disease. *Comput. Methods Biomech. Biomed. Engin.*, **5**, 195–206. 36, 51

Wang, H., Liu, J., Zhao, H., Fu, X., Shang, G., Zhou, Y., Yu, X., Zhao, X., Wang, G. & Shi, H. (2013). Arterial stiffness evaluation by cardio-ankle vascular index in hypertension and diabetes mellitus subjects. *J. Am. Soc. Hypertens.*, **7**, 426–31. 112

Wang, J. & Parker, K. (2004). Wave propagation in a model of the arterial circulation. *J. Biomech.*, **37**, 457–70. 51

Wang, J.J., O'Brien, A.B., Shrive, N.G., Parker, K.H. & Tyberg, J.V. (2003). Time-domain representation of ventricular-arterial coupling as a windkessel and wave system. *Am. J. Physiol. Heart Circ. Physiol.*, **284**, 1358–68. 153

Wang, T.J. (2008). New cardiovascular risk factors exist, but are they clinically useful. *Eur. Heart J.*, **29**, 441–4. 18

Wang, T.J., Gona, P., Larson, M.G., Levy, D., Benjamin, E.J., Tofler, G.H., Jacques, P.F., Meigs, J.B., Rifai, N., Selhub, J., Robins, S.J., Newton-Cheh, C. & Vasan, R.S. (2007). Multiple biomarkers and the risk of incident hypertension. *Hypertension*, **49**, 432–8. 126

Watanabe, S.M., Blanco, P.J. & Feijóo, R.a. (2013). Mathematical model of blood flow in an anatomically detailed arterial network of the arm. *ESAIM: M2AN*, **47**, 961–85. 53

Weber, T., Auer, J., O'Rourke, M.F., Kvas, E., Lassnig, E., Lamm, G., Stark, N., Rammer, M. & Eber., B. (2005). Increased arterial wave reflections predict severe cardiovascular events in patients undergoing percutaneous coronary interventions. *Eur. Heart. J.*, **26**, 2657–63. 21

Weissler, A.M., Peeler, R.G. & Roehll, W.H. (1961). Relationships between left ventricular ejection time, stroke volume, and heart rate in normal individuals and patients with cardiovascular disease. *Am. Heart J.*, **62**, 367–78. 84, 93

Weizsacker, H.W. & Pinto, J.G. (1988). Isotropy and anisotropy of the arterial wall. *J. Biomech.*, **21**, 477–87. 38

Wenn, C. & Newman, D. (1990). Arterial tortuosity. *Australas. Phys. Eng. Sci. Med.*, **13**, 67–70. 166

Westerbacka, J., Leinonen, E., Salonen, J.T., Salonen, R., Hiukka, A., Yki-Järvinen, H. & Taskinen, M.R. (2005). Increased augmentation of central blood pressure is associated with increases in carotid intimamedia thickness in type 2 diabetic patients. *Diabetologia*, **48**, 1654–62. 17

Westerhof, N., Bosman, F., De Vries, C.J. & Noordergraaf, A. (1969). Analog studies of the human systemic arterial tree. *J. Biomech.*, **2**, 121–43. 24, 25, 49, 56, 102

Westerhof, N., Lankhaar, J.W. & Westerhof, B.E. (2009). The arterial windkessel. *Med. Biol. Eng. Comput.*, **47**, 131–41. xii, 6, 8, 25, 51, 139, 153

Whitham, G.B. (2011). *Linear and Nonlinear Waves*. John Wiley & Sons. 24

Whiting, D.R., Guariguata, L., Weil, C. & Shaw, J. (2011). IDF diabetes atlas: global estimates of the prevalence of diabetes for 2011 and 2030. *Diabetes Res. Clin. Pr.*, **94**, 311–21. 15

Wikimedia Commons (2015). http://simple.wikipedia.org/wiki/Heart. xii, 3

Wilkinson, I., MacCallum, H., Roojimans, D., Murray, G., Cockcroft, J.R., McKnight, J. & Webb, D. (2000). Increased augmentation index and systolic stress in type 1 diabetis mellitus. *Q. J. Med.*, **93**, 441–8. xiii, 17, 112

Wilkinson, I.B., Qasem, A., McEniery, C.M., Webb, D.J., Avolio, A.P. & Cockcroft, J.R. (2002). Nitric oxide regulates local arterial distensibility in vivo. *Circulation*, **105**, 213–217. 97

Willemet, M. (2012). *Blood flow modeling for patient-specific bypass surgery in lower-limb arteries*. Ph.D. thesis, Universite Catholique de Louvain. 81, 98, 102, 103, 104, 165

Willemet, M. & Alastruey, J. (2014). Arterial pressure and flow wave analysis using time-domain 1-D hemodynamics. *Ann. Biomed. Eng.*, **43**, 1–17. 129, 153

Willemet, M., Lacroix, V. & Marchandise, E. (2011). Inlet boundary conditions for blood flow simulations in truncated arterial networks. *J. Biomech.*, **44**, 897–903. 28, 164

Willemet, M., Lacroix, V. & Marchandise, E. (2013). Validation of a 1D patient-specific model of the arterial hemodynamics in bypassed lower-limbs: simulations against in vivo measurements. *Med. Eng. Phys.*, **35**, 1573–83. 25, 52, 53, 54, 56, 68, 108, 127, 131, 151, 155, 160, 164

Willemet, M., Chowienczyk, P. & Alastruey, J. (2015). A database of virtual healthy subjects to assess the accuracy of foot-to-foot pulse wave velocities for estimation of aortic stiffness. *Am. J. Physiol. Heart Circ. Physiol.*, **309**, 663–75. 50, 58, 68, 97, 103, 122, 161, 162

Willum-Hansen, T., Staessen, J.a., Torp-Pedersen, C., Rasmussen, S., Thijs, L., Ibsen, H. & Jeppesen, J. (2006). Prognostic value of aortic pulse

wave velocity as index of arterial stiffness in the general population. *Circulation*, **113**, 664–70. 20, 103

Wilson, N.M., Arko, F.R. & Taylor, C.a. (2005). Predicting changes in blood flow in patient-specific operative plans for treating aortoiliac occlusive disease. *Comput. Aided Surg.*, **10**, 257–77. 126, 127

Wolinsky, H. (1972). Long-term effects of hypertension on the rat aortic wall and their relation to concurrent aging changes. Morphological and chemical studies. *Circ. Res.*, **30**, 301–9. 14

World Health Organization (2003). 2003 World Health Organization (WHO)/ International Society of Hypertension (ISH) statement on management of hypertension World Health Organization , International Society of Hypertension Writing Group. *J. Hypertens.*, 1983–92. 165

Wu, H.T., Liu, C.C., Lin, P.H., Chung, H.M., Liu, M.C., Yip, H.K., Liu, A.B. & Sun, C.K. (2010). Novel application of parameters in waveform contour analysis for assessing arterial stiffness in aged and atherosclerotic subjects. *Atherosclerosis*, **213**, 173–7. 82

Wykretowicz, A., Adamska, K., Guzik, P., Krauze, T. & Wysocki, H. (2007). Indices of vascular stiffness and wave reflection in relation to body mass index or body fat in healthy subjects. *Clin. Exp. Pharmacol. Physiol.*, **34**, 1005–9. 22

Xiao, N., Alastruey, J. & Alberto Figueroa, C. (2013). A systematic comparison between 1-D and 3-D hemodynamics in compliant arterial models. *Int. J. Numer. Meth. Biomed. Engng.*, **30**, 204–31. 29, 52, 54, 153, 156

Xiu, D. & Sherwin, S.J. (2007). Parametric uncertainty analysis of pulse wave propagation in a model of a human arterial network. *J. Comput. Phys.*, **226**, 1385–407. 55

Yannoutsos, A., Ahouah, M., Tubiana, C.D., Topouchian, J., Touboul, C., Safar, M.E. & Blacher, J. (2016). Hemodynamic parameters in hypertensive diabetic patients. *J. Hypertens.*, 1123–1131. 101

Yarows, S.A. & Qian, K. (2001). Accuracy of aneroid sphygmomanometers in clinical usage: University of Michigan experience. *Blood Press. Monit.*, **6**, 101–6. 14

Yeboah, J., Folsom, A.R., Burke, G.L., Johnson, C., Polak, J.F., Post, W., Lima, J.a., Crouse, J.R. & Herrington, D.M. (2009). Predictive value of brachial flow-mediated dilation for incident cardiovascular events in a population-based study: The multi-ethnic study of atherosclerosis. *Circulation*, **120**, 502–9. 18

Yoo, B.S., Yoon, J., Ko, J.Y., Kim, J.Y., Lee, S.H., Hwang, S.O. & Choe, K.H. (2005). Anatomical consideration of the radial artery for transradial coronary procedures: Arterial diameter, branching anomaly and vessel tortuosity. *Int. J. Cardiol.*, **101**, 421–7. 70

Zamir, M. (2000). *The physics of pulsatile flow*. Springer, New York. 30

Zhang, M., Bai, Y., Ye, P., Luo, L., Xiao, W., Wu, H. & Liu, D. (2011). Type 2 diabetes is associated with increased pulse wave velocity measured at different sites of the arterial system but not augmentation index in a Chinese population. *Clin. Cardiol.*, **34**, 622–7. 17, 19, 112

Zweifler, A., Cushing, G. & Conway, J. (1967). The relationship between pulse volume and blood flow in the finger. *Angiology*, **18**, 591–8. 9